

Mobility and homogeneity effects on the power conversion efficiency of solar cells

Von der Fakultät Informatik, Elektrotechnik und Informationstechnik
der Universität Stuttgart zur Erlangung der Würde eines
Doktor-Ingenieurs (Dr.-Ing.) genehmigte Abhandlung

Vorgelegt von

Julian Mattheis

geboren am 14.12.1975 in Hannover

Hauptberichter: Prof. Dr. rer. nat. habil. J. H. Werner

Mitberichter: Prof. Dr. rer. nat. habil. U. Rau

Prof. Dr. E. Kasper

Tag der Einreichung: 20.06.2007

Tag der mündlichen Prüfung: 08.01.2008

Institut für Physikalische Elektronik der Universität Stuttgart

2008

Contents

Abstract	v
Zusammenfassung	vii
1 Introduction	1
1.1 Structure	2
2 Efficiency limits of solar cells	4
2.1 Classification of solar cell models	5
2.1.1 Classification scheme	7
2.2 Current-voltage characteristic of solar cells	9
2.3 Radiative efficiency limit	9
2.3.1 Complete carrier collection	10
2.3.2 Incomplete carrier collection	14
2.4 Classical diode theory	15
2.4.1 Incomplete carrier collection	15
2.4.2 Complete carrier collection	16
3 Generalized efficiency limit	18
3.1 Radiative recombination and photon recycling	19
3.2 Photon recycling in the literature	20
3.3 Diffusion equation with reabsorption	22
3.3.1 Parameter normalization	24
3.3.2 Free parameters	26
3.4 Results with constant absorption coefficient	27
3.4.1 Radiative efficiency limit	28

3.4.2	Non-radiative recombination	32
3.5	Photon recycling and detailed balance	35
3.5.1	Radiation balance in equilibrium	35
3.5.2	Non-equilibrium concentration profile	40
3.5.3	Radiation balance in non-equilibrium	42
3.5.4	Reciprocity between solar cell and light emitting diode	47
3.6	Critical mobility	49
3.6.1	High mobility limit - absorptance	50
3.6.2	Low mobility limit	52
3.6.3	Critical mobility in the radiative recombination limit	55
3.6.4	Critical mobility for non-radiative recombination	57
3.7	Analytical approximation	57
3.7.1	Analytical approximations in the literature	59
3.7.2	Two-layer model	61
3.7.3	Modified-lifetime model	61
3.7.4	Evaluation of the approximation	64
3.8	Energy-dependent absorption coefficient	71
3.8.1	Thickness-dependent current enhancement	75
3.8.2	Thickness-dependent efficiency enhancement	77
3.8.3	Maximum open circuit voltage	79
3.9	Maximum efficiencies of real materials	80
3.9.1	Analytical approximation	82
3.9.2	Critical mobility	89
3.9.3	Discussion	91
3.10	Limitations to the model	95
3.11	Conclusion	96
4	Band gap fluctuations	98
4.1	Disorder and band gap fluctuations	101
4.2	Band gap fluctuations model	101
4.2.1	Light absorption	103
4.2.2	Light emission	104
4.2.3	Discussion	113

4.3	Numerical approach	115
4.3.1	Formulation of the problem	116
4.3.2	Correlated band gap sequence	118
4.3.3	Discussion	119
4.4	Experimental results	121
4.5	Discussion	124
4.5.1	Length-scale of band gap fluctuations	124
4.5.2	Origin of band gap fluctuations	128
4.5.3	Model refinements	130
4.5.4	Implications for solar cell performance	133
4.6	Conclusions	134
5	Outlook	136
A	Radiative efficiency limit with energy-dependent absorptance	138
A.1	Inhomogeneous band gap	138
A.2	Optimal absorptance	140
B	Derivation and numerical implementation of the photon recycling scheme	144
B.1	Exponential Integrals	144
B.2	Diffusion equation with reabsorption	146
B.2.1	Linear matrix formalism	146
B.2.2	Transport	149
B.2.3	Recombination	149
B.2.4	Direct internal generation	150
B.2.5	Internal generation after multiple reflections	153
B.2.6	External generation	160
B.3	Generation terms	162
B.3.1	Internal generation	163
B.3.2	External generation	166
B.4	Diffusion operator	168
B.5	Boundary conditions	169
B.5.1	Back contact	169

B.5.2	Junction	170
B.6	Discussion	170
B.6.1	Reabsorption matrix	170
B.6.2	Energy superposition	171
B.7	Numerical error sources	171
B.7.1	Optical limitations - absorption length	171
B.7.2	Electrical limitations - diffusion length	173
C	Derivation of the two-layer model	174
	Nomenclature	179
	Bibliography	184
	Curriculum Vitae	194
	List of Publications	195
	Danksagung	197

Abstract

The thesis on hand investigates the interplay between detailed radiation balances and charge carrier transport. The first part analyzes the role of limited carrier transport for the efficiency limits of pn -junction solar cells. The second part points out the influence of transport on the absorption and emission of light in inhomogeneous semiconductors.

By incorporating an integral term that accounts for the repeated internal emission and reabsorption of photons (the so-called photon recycling) into the diffusion equation for the minority carriers, the first part of the thesis develops a self-consistent model that is capable of describing the power conversion efficiencies of existing devices as well as of devices in the radiative recombination limit. The model thus closes the gap between the classical diode theory and the Shockley Queisser detailed balance efficiency limit. While the model converges towards the Shockley Queisser limit when recombination is exclusively radiative and the minority carrier mobility is infinity, it converges towards the classical diode theory once the minority carrier lifetime is dominated by non-radiative recombination. It is shown that the classical diode theory without the inclusion of photon recycling produces accurate results only if the minority carrier lifetime is at least ten times smaller than the radiative lifetime. The thesis shows that even in the radiative recombination limit, charge carrier transport is extremely important. The efficiency is reduced drastically once the minority carrier mobility drops below a critical mobility even under otherwise most ideal conditions. A closed-form expression is derived for this critical mobility, which depends on the absorption coefficient and the doping concentration. The thesis thus presents a universal criterion that needs to be fulfilled by any photovoltaic material in order to obtain high power conversion efficiency. The numerical results are analyzed and compared to an analytical approximation. This approximation is capable of describing the efficiency of solar cells with assumed energy-independent absorption coefficient. While it also accurately predicts

the open circuit voltage of solar cells with energy-dependent absorption coefficient, it is only a rough estimate for the short circuit current. The thesis applies the developed model to solar cells made of crystalline silicon, amorphous silicon and Cu(In,Ga)Se_2 (CIGS). It shows that crystalline silicon solar cells neither have transport problems in the radiative recombination limit nor in existing devices. In Cu(In,Ga)Se_2 solar cells, mobilities are at most two orders of magnitude above the critical mobility and guarantee complete carrier collection only close to the radiative limit. Existing devices utilize graded band gaps equally as a means of passivating the back contact and for increasing carrier collection in the bulk. Amorphous silicon solar cells, however, not only need to overcome insufficient carrier collection in existing devices by means of built-in electric fields, but also come close to being limited by carrier collection even in the radiative limit.

The second part of the thesis investigates the role of carrier transport for the absorption and emission of light in semiconductors with band gap fluctuations. The chapter develops an analytical statistical model to describe the absorption and emission spectra of such inhomogeneous semiconductors. Particular emphasis is placed on the role of the length-scale of the band gap fluctuations. As it turns out, the crucial quantity with respect to the emission spectrum is the ratio of the charge carrier transport length and the length-scale of the band gap fluctuations. Both, absorption edge and emission peak are broadened by band gap fluctuations. While the absorption spectrum is not influenced by the length scale of the fluctuations, the developed model shows that the spectral position of the emission peak relative to the absorption edge depends on the ratio of fluctuation length and transport length. Comparison with numerical simulations underlines the importance of the fluctuation length in relation to the diffusion length and also points out the influence of the magnitude of the band gap fluctuations in terms of the standard deviation of the fluctuations. The model is applied to experimental absorption and photoluminescence data of Cu(In,Ga)Se_2 thin films with varying gallium content. The ternary compounds CuInSe_2 and CuGaSe_2 exhibit the smallest magnitude of fluctuations with standard deviations in the range of 20 – 40 meV. The fact that the quaternary compounds show standard deviations of up to 65 meV points to alloy disorder as one possible source of band gap fluctuations. All observed fluctuations occur on a very small length scale that is at least ten times smaller than the electron diffusion length of approximately $1\text{ }\mu\text{m}$.

Zusammenfassung

Die vorliegende Arbeit untersucht das Zusammenspiel von detaillierten Strahlungsgleichgewichten mit dem Transport von Ladungsträgern. Der erste Teil analysiert die Bedeutung von begrenztem Ladungsträgertransport für die Wirkungsgradgrenzen von pn -Übergang Solarzellen. Der zweite Teil zeigt den Einfluss von Transport auf die Absorption und Emission von Licht in inhomogenen Halbleitern auf.

Zur Berücksichtigung der wiederholten internen Emission und Reabsorption von Photonen (des sog. Photon Recyclings) baut der erste Teil der Arbeit einen Integralterm in die Diffusionsgleichung für die Minoritätsladungsträger ein. Dadurch wird ein selbstkonsistentes Modell entwickelt, das in der Lage ist, den Wirkungsgrad von realen Solarzellen ebenso zu beschreiben wie den idealen Wirkungsgrad im Limit strahlender Rekombination. Das Modell schließt somit die Lücke zwischen der klassischen Diodentheorie und dem aus der detaillierten Bilanz abgeleiteten Shockley Queisser Wirkungsgrad Limit. Während das Modell gegen das Shockley Queisser Limit konvergiert, wenn Rekombination ausschließlich strahlend und die Minoritätsträger Beweglichkeit unendlich ist, geht es in die klassische Diodentheorie über, wenn die Minoritätsträgerlebensdauer durch nicht-strahlende Rekombination dominiert wird. Es wird gezeigt, dass die klassische Diodentheorie ohne die Berücksichtigung von Photon Recycling nur hinreichend genaue Resultate produziert, wenn die Minoritätsträgerlebensdauer mindestens zehnmal kleiner ist als die strahlende Lebensdauer. Die Arbeit zeigt, dass Ladungsträgertransport sogar im strahlenden Wirkungsgrad Limit von höchster Wichtigkeit ist. Selbst unter ansonsten idealen Bedingungen wird der Wirkungsgrad drastisch reduziert, sobald die Minoritätsträgerbeweglichkeit kleiner als eine kritische Beweglichkeit ist. Es wird ein einfacher analytischer Ausdruck für die kritische Beweglichkeit hergeleitet, die vom Absorptionskoeffizienten und der Dotierung abhängt. Damit präsentiert diese Arbeit ein universales Kriterium, das von jedem

photovoltaischen Material erfüllt werden muss, um einen hohen Wirkungsgrad zu erreichen. Die numerischen Resultate werden analysiert und mit einem analytischen Modell verglichen. Dieses analytische Modell ist in der Lage, den Wirkungsgrad von Solarzellen mit energieunabhängigem Absorptionskoeffizienten zu beschreiben. Während es ebenso die Leerlaufspannung von Solarzellen mit energieabhängigem Absorptionskoeffizienten korrekt approximiert, erbringt das analytische Modell in diesem Fall jedoch nur eine ungefähre Näherung für den Kurzschlussstrom. Die Arbeit wendet das entwickelte Modell auf Solarzellen aus kristallinem und amorphem Silizium und aus Cu(In,Ga)Se_2 an. Es zeigt sich, dass Solarzellen aus kristallinem Silizium weder im strahlenden Limit noch in existierenden Solarzellen durch eine zu kleine Beweglichkeit begrenzt sind. In Solarzellen aus Cu(In,Ga)Se_2 sind die Mobilitäten nur maximal zwei Größenordnungen größer als die kritische Beweglichkeit und garantieren vollständige Ladungsträgersammlung daher nur sehr dicht am strahlenden Limit. Real existierende Zellen nutzen gradierte Bandlücken zur Sammlungsunterstützung im Volumen ebenso wie zur Rückseitenpassivierung. Solarzellen aus amorphem Silizium hingegen müssen nicht nur in realen Bauelementen eingebaute elektrische Felder zur Sammlungsunterstützung einsetzen. Auch im Grenzfall rein strahlender Rekombination sind die Mobilitäten in der Nähe der kritischen Mobilität und somit unter Umständen nicht ausreichend, um eine vollständige Ladungsträgersammlung zu gewährleisten.

Der zweite Teil der Arbeit untersucht die Bedeutung von Ladungsträgertransport für die Absorption und Emission von Licht in Halbleitern mit Bandlückenfluktuationen. Dieses Kapitel entwickelt ein analytisches statistisches Modell zur Beschreibung von Absorptions- und Emissionsspektren solch inhomogener Halbleiter. Besonderes Augenmerk wird dabei auf die Rolle der Längenskala von Bandlückenfluktuationen gelegt. Wie sich herausstellt, ist die entscheidende Größe in Bezug auf das Emissionsspektrum das Verhältnis aus der charakteristischen Ladungsträger Transportlänge und der Fluktuationslänge der Bandlückenfluktuationen. Sowohl Absorptionskante als auch der Emissionspeak werden durch Bandlückenfluktuationen verbreitert. Während das Absorptionsspektrum jedoch unbeeinflusst von der Längenskala der Fluktuationen ist, zeigt das entwickelte Modell, dass die spektrale Position des Emissionspeaks relativ zur Lage der Absorptionskante von dem Verhältnis aus Transportlänge und Fluktuationslänge abhängt. Der Vergleich mit numerischen Simulationen unterstreicht die Bedeutung der Fluktuationslänge im Vergleich zur Transportlänge. Aufgezeigt wird

außerdem der Einfluss der Fluktuationshöhe, ausgedrückt durch die Standardabweichung der Fluktuationen. Das Modell wird auf experimentelle Absorptions- und Photolumineszenzdaten von Cu(In,Ga)Se_2 Filmen mit verschiedenem Galliumgehalt angewandt. die ternären Verbindungen CuInSe_2 und CuGaSe_2 weisen die geringsten Fluktuationen mit Standardabweichungen zwischen 20 und 40 meV auf. Der Umstand, dass die quaternären Systeme Standardabweichungen von bis zu 65 meV besitzen, deutet darauf hin, dass Unordnung infolge der Legierung eine mögliche Ursache der Bandlückenfluktuationen darstellen. Alle beobachteten Fluktuationen besitzen eine sehr kurze Fluktuationslänge, die mindestens zehnmal kleiner ist als die Elektronen Diffusionslänge von ca. $1\text{ }\mu\text{m}$.

Chapter 1

Introduction

Today, the biggest share of the world output of solar cells is made of crystalline silicon. This dominance of crystalline silicon is owed to the long history of experience in silicon microelectronics [1]. From a perspective based on the suitability of silicon as a photovoltaic absorber material, however, this dominance seems rather astonishing. In particular, the low absorption coefficient seems to disqualify the indirect semiconductor silicon as the photovoltaic material of choice.

Therefore, a lot of effort has been put in the investigation of new high-absorption thin-film materials [2–4], such as amorphous silicon [5], Cu(In,Ga)Se_2 [6], organic semiconductors [7], or organic dyes [8]. However, so far, these so-called second generation [9] thin-film solar cells have not yet lived up to expectations. They all fall short of achieving the efficiencies reached with conventional first-generation silicon solar cells.

Of course, the absorption of light is only the first step to the successful conversion of optical into electrical energy. The photo-generated charge carriers also need to be separated before they recombine. Obviously, this requires high carrier lifetimes. However, one factor which is often overlooked in this context is the importance of charge carrier transport. High lifetimes guarantee high open circuit voltages. Additional high mobilities are needed to achieve high short circuit current. While many of the new materials under consideration, in particular the organic materials, feature excellent lifetimes and open circuit voltages, most of them suffer from low short circuit currents caused by insufficient carrier mobilities.

This problem is well known in existing devices. Means to improve carrier collection include the application of *pin* structures in amorphous silicon, graded band gaps in

Cu(In,Ga)Se_2 , or enlarged junction areas in the case of dye-sensitized solar cells.

However, up to now it remains unclear, what influence carrier transport has on the efficiency limits of solar cells. Such efficiency limits have only been calculated for devices with assumed complete carrier collection. The efficiency limits of photovoltaic energy conversion are reached when all heat-dissipating loss-mechanisms are avoided. In accordance with the principle of detailed balance, the only unavoidable loss mechanism is radiative recombination. This is because in thermodynamic equilibrium all thermal radiation from outside the solar cell needs to be balanced by an equal radiation flux from within the cell. Hence, a general treatment of solar cell efficiencies needs to address radiation balances as well as charge carrier transport.

An extra dimension is added to the problem by inhomogeneous material parameters, such as the fundamental band gap. While the laws governing the radiative interaction between the solar cell and its ambience, i.e., the reciprocity between light absorption and emission, are still valid locally on a microscopic scale, they need to be modified on a macroscopic level. Once again, the description of the macroscopic radiation balances needs to take into account transport phenomena.

1.1 Structure

This thesis investigates the role of carrier transport and inhomogeneous band gaps for the radiation balances between absorbed and emitted radiation, which determine the efficiency limits of *pn*-junction solar cells. The thesis is structured as follows:

Chapter 2 delineates existing theories to describe the efficiencies of solar cells. It classifies solar cells according to complete and incomplete collection of photo-generated carriers and points out the shortcomings of the existing theories when it comes to describe the efficiencies of solar cells with incomplete carrier collection.

Chapter 3 is the main chapter of this thesis. It develops a generalized numerical model that combines issues of carrier transport and radiation balances which is capable of describing solar cell efficiencies for all combinations of radiative or non-radiative recombination and complete or incomplete carrier collection. The chapter points out the importance of carrier transport for the solar cell efficiency even under otherwise most ideal conditions. It shows that the efficiency is reduced sharply once the mobility drops below a critical mobility. Subsequently, the chapter develops an analytical approxima-

tion of the numerical model. It closes with the efficiency limits of real pn junction solar cells made from crystalline silicon, amorphous silicon, and $\text{Cu}(\text{In,Ga})\text{Se}_2$.

Chapter 4 develops an analytical model to describe light absorption and emission in semiconductors with fluctuations of the fundamental band gap. It focusses on the relationship between carrier transport and the length-scale of band gap fluctuations. The model is applied to $\text{Cu}(\text{In,Ga})\text{Se}_2$ layers with different gallium content. It is shown that the gallium content influences the extent of band gap fluctuations and that all observed fluctuations occur on a length-scale which is much smaller than the electron diffusion length.

Chapter 2

Efficiency limits of solar cells

Abstract: This chapter discusses existing solar cell theories. It categorizes the theories along the dimensions of charge carrier recombination and charge carrier transport (carrier collection). The detailed balance efficiency limit presented by Shockley and Queisser describes the radiative recombination limit with complete carrier collection. The classical diode theory in turn holds for non-radiative recombination and incomplete as well as complete carrier collection. For the case of complete carrier collection, a simple combination of the detailed balance theory with the classical diode theory is given by adding up radiative and non-radiative recombination currents.

In very general terms, there are three pillars that constitute a solar cell's photovoltaic ability to convert solar energy into electrical energy:

- (i) Carrier generation,
- (ii) Carrier recombination, and
- (iii) Carrier transport.

This chapter analyzes the influence of these three pillars on the power conversion efficiency of a solar cell. It shortly delineates the two main currently existing theories describing solar cell efficiencies. Subsequently, the chapter presents a classification scheme to distinguish solar cell modelling approaches according to the ideality of carrier recombination and carrier transport. By placing the two theories into the classification scheme, it points out, where they fail to converge.

Until now, there existed two completely different approaches to calculate the efficiency of ideal and non-ideal solar cells. For the ideal case Shockley and Queisser (SQ) [10] developed their detailed balance theory as described in section 2.3.1. The efficiency of non-ideal *pn*-junction solar cells on the other hand is based on the solution of the continuity equation as described by Shockley's diode equation [11], which is recapitulated in section 2.4.

2.1 Classification of solar cell models

Shockley-Queisser (SQ) theory

Shockley and Queisser regard the solar cell as a black box as sketched in Fig. 2.2 and base their derivation of the current/voltage characteristic on the radiation balance between the solar cell and its ambience. In their view, the cell consists only of a light absorbing and emitting surface with two electrical terminals. They do not account for internal (microscopic) processes; only externally visible (macroscopic) quantities are considered. Their idealized conception of the three pillars outlined above is structured as follows:

- (i) Carrier generation is completely defined by the macroscopic absorptance a which ideally depends only on the band gap energy E_g (cf. Eq. (2.5)) and the photon flux of solar and ambient black body irradiation impinging on the surface of the solar cell.
- (ii) Carrier recombination is exclusively radiative. Due to the required balance of absorbed and emitted radiation in thermodynamic equilibrium, radiative recombination cannot be prevented and is described by the macroscopic radiative recombination current which equals the emitted photon flux. The radiative recombination current depends only on the absorptance a , the cell temperature T , and the voltage V at the terminals.
- (iii) Carrier transport is a microscopic phenomenon taking place within the black box. In the SQ theory, carrier collection is assumed to be ideal, and the concept of transport therefore simply does not exist.

Summing up, the radiative SQ efficiency limit of a solar cell depends only on the magnitude and spectral distribution of the solar irradiation, the cell temperature, and the band gap energy of the absorber material.

Classical diode theory (CDT)

In contrast to the SQ theory, the classical diode theory does not treat the solar cell as a black box. Instead, it looks at the interior, replacing the macroscopic quantities by microscopic quantities that describe the local opto-electronic phenomena within the solar cell.

- (i) Carrier generation is described by Lambert-Beer's law of absorption. The absorptance $a(E)$ is replaced by the absorption coefficient $\alpha(E)$.
- (ii) Carrier recombination is described by the local recombination rate, which under low level injection conditions is determined by the minority carrier lifetime τ .
- (iii) Carrier transport is determined by the gradient of the electro-chemical potential of the minority carriers. In the case of a homogeneous material without electrical field, carrier transport is exclusively diffusive.

As pointed out above, the classical diode theory consists of solving the continuity equation for the minority carriers. The approach is thereby explicitly based on carrier transport, which had been completely disregarded in the SQ approach.

The emission of photons, however, which is essential to the SQ theory is not being tagged by the classical diode theory. Without accounting for the photons emitted by the solar cell, though, the compliance of the detailed radiation balance between the solar cell and its ambience becomes intrinsically impossible.

Therefore, it is intuitively obvious that the classical diode theory does not result in the same maximum efficiencies as the SQ theory.

Unified model

Consequently, a model that unifies the SQ theory with the classical diode theory needs to tackle the question of how to incorporate the detailed radiation balance of absorbed and emitted photons into a microscopic transport approach.

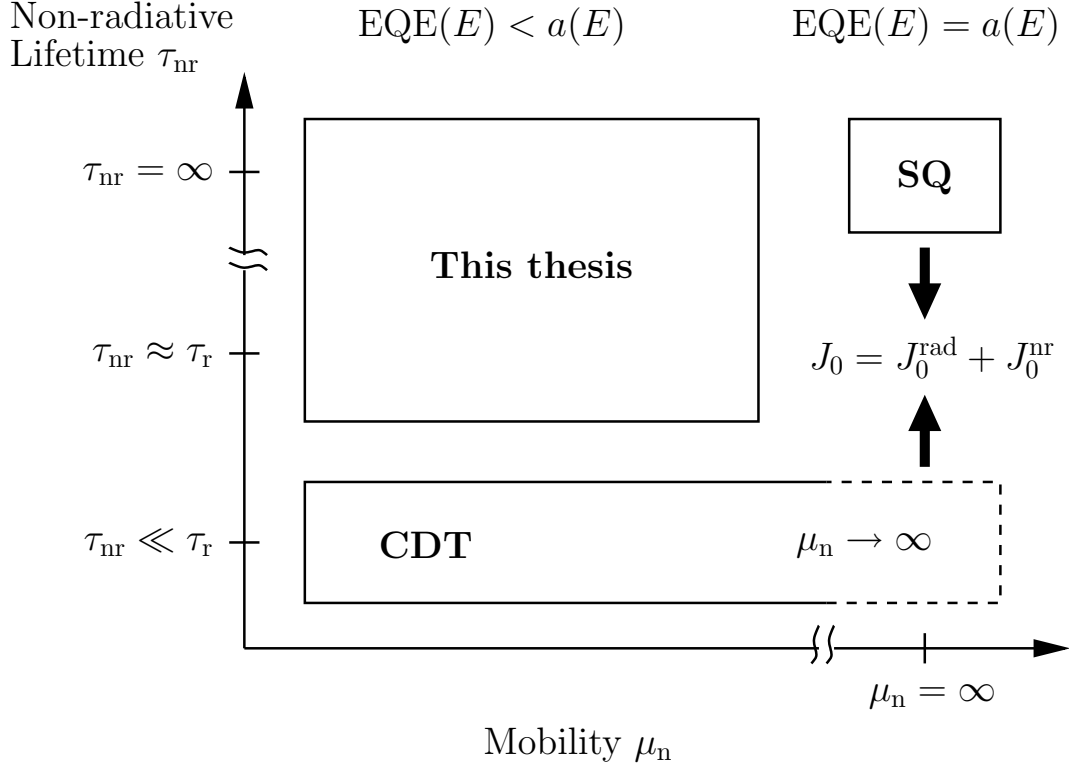


Fig. 2.1: Classification of solar cell models in the two-dimensional space of carrier recombination and carrier transport. The Shockley-Queisser (SQ) theory describes the case with only radiative recombination where it holds $\tau_{nr} \gg \tau_r$, i.e. $\tau = \tau_r$. The SQ theory is a macroscopic theory that assumes complete carrier collection with $\mu_n \rightarrow \infty$, which leads to $EQE(E) = a(E)$. In contrast, the classical diode theory (CDT) is a microscopic theory that covers the case $\tau_{nr} \ll \tau_r$ and includes incomplete carrier collection. The CDT can easily be extended to comprise infinite carrier mobility. At the macroscopic level with $\mu_n \rightarrow \infty$, it can also be combined with the SQ theory to cover the whole lifetime range. However, on the microscopic level with incomplete carrier collection, such an easy combination of the two theories is not possible.

Moreover, with the solar cell no longer being a black box, the radiation balance not only has to be fulfilled with respect to the external radiative interaction between the solar cell and its ambience but also within the solar cell.

2.1.1 Classification scheme

Figure 2.1 systemizes the above considerations. It divides solar cells according to the 'idealization' of carrier recombination and carrier transport.

With respect to recombination, the ideal case is reached, when carriers only recombine radiatively. The crucial parameter for recombination is the minority carrier lifetime, which consists of a radiative lifetime τ_r and a lifetime τ_{nr} for non-radiative processes and is computed with $1/\tau = 1/\tau_r + 1/\tau_{nr}$.

The second dimension is the dimension of carrier transport as expressed by the minority carrier mobility μ_n . Ideally, μ_n is infinity. Then, the spatial resolution of the solar cell becomes obsolete, since all generated carriers are collected independent of the position of the generation. In this case, a macroscopic solar cell model is sufficient to describe the cell's efficiency.

The ideal carrier transport also makes a spatial resolution of carrier generation unnecessary. The solar cell is completely defined by macroscopic quantities, such as the absorptance spectrum $a(E)$, where E is the photon energy.

As a consequence of the infinite mobility, the probability to collect an absorbed photon under short circuit conditions becomes unity. Therefore, the external quantum efficiency $\text{EQE}(E)$ as defined by the number of collected electrons divided by the number of incident photons under short circuit conditions equals the absorptance $a(E)$.

Non-ideal transport requires a spatial resolution in the direction of current transport. The macroscopic approach has to be replaced by a microscopic approach that includes the spatial resolution of carrier generation, recombination, and transport. Not all absorbed photon are collected and it holds $\text{EQE}(E) < a(E)$.

The SQ theory assumes only radiative recombination, i.e. $\tau = \tau_r$, and also complete carrier collection, i.e. $\mu_n \rightarrow \infty$. Conversely, the classical diode theory (CDT) is suited for solar cells with non-ideal recombination and non-ideal carrier collection. While the diode theory can easily be extended to comprise complete carrier collection, such an extension is not so straightforward when recombination is dominated by radiative recombination.

The existing theories are well equipped to describe the case of complete carrier collection, where the solar cell is only described as a black box with macroscopic properties. However, they fail to describe the combination of incomplete carrier collection with radiative recombination.

In the following, I recapitulate the SQ theory and the diode theory. The next chapter will then address the task of providing the missing link between the theories.

2.2 Current-voltage characteristic of solar cells

Throughout this thesis, all solar cells are considered ideal insofar that their series resistance is zero and their parallel resistance is infinity. Therefore, they exhibit the current/voltage characteristic

$$J(V) = J_0 \left(\exp \left(\frac{qV}{k_B T} \right) - 1 \right) - J_{sc}, \quad (2.1)$$

where J_0 is the saturation current density and J_{sc} is the short circuit current density. The applied voltage is V , q is the elementary charge, k_B is Boltzmann's constant, and T is the absolute temperature.

From the saturation current J_0 and the short circuit current J_{sc} one obtains the open circuit voltage

$$V_{oc} = \frac{k_B T}{q} \ln \left(\frac{J_{sc}}{J_0} + 1 \right), \quad (2.2)$$

the fill factor with the phenomenological expression [12]

$$FF = \frac{u_{oc} - \ln(u_{oc} + 0.72)}{u_{oc} + 1} \quad (2.3)$$

with $u_{oc} = qV_{oc}/(k_B T)$, and the efficiency

$$\eta = \frac{qJ_{sc}V_{oc}FF}{P_{in}}, \quad (2.4)$$

where P_{in} is the areal power density of the illumination. Throughout this thesis I use the global AM1.5g spectrum scaled to $P_{in} = 100 \text{ mW/cm}^2$ from Ref. [13].

2.3 Radiative efficiency limit

This section discusses the maximum power conversion efficiency of a single junction solar cell, as determined by the detailed radiation balance between the solar cell and its ambience. This maximum efficiency is called detailed balance efficiency limit or radiative efficiency limit. In the radiative efficiency limit, radiative recombination is the only loss mechanism. As will be shown below, such radiative recombination cannot be circumvented.

Section 2.3.1 analyzes the radiative efficiency limit of solar cells with infinite mobility and the resulting consequences as described above. Section 2.3.2 discusses the implications of a non-ideal quantum efficiency for the detailed balance efficiency, which constitutes the basis for the detailed analysis presented in chapter 3.

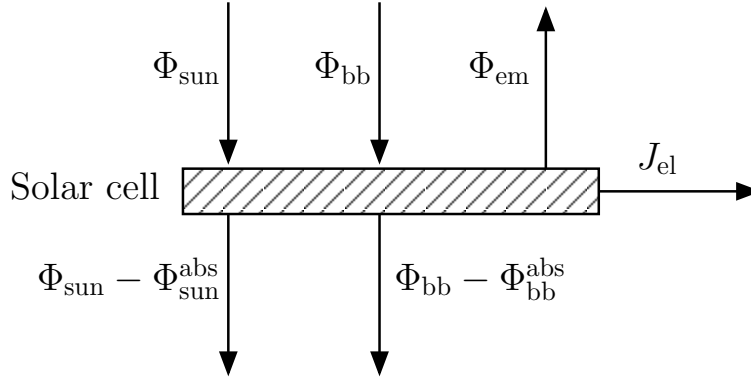


Fig. 2.2: Sketch of a solar cell as seen by Shockley and Queisser. The cell is a black box with complete carrier collection. Internal processes are not accounted for. Only the external radiation fluxes and the electrical current drawn from the cell are considered. From the incoming solar radiation Φ_{sun} and the ambient black body irradiation Φ_{bb} only the fluxes $\Phi_{\text{sun}}^{\text{abs}}$ and $\Phi_{\text{bb}}^{\text{abs}}$ are absorbed. The rest is transmitted (or rather: reflected, since the back side is perfectly reflected). The absorbed fluxes are balanced by the voltage-dependent emission flux Φ_{em} and the electrical current J_{el} .

2.3.1 Complete carrier collection

As it turns out, the absorptance spectrum $a(E)$ of the solar cell, where E is the photon energy, is the crucial material characteristic that determines the solar cell's radiative efficiency limit. In this section, I recapitulate the case of a solar cell with homogenous material parameters, in particular a homogeneous band gap energy E_g , which ideally results in a step like absorptance function. Appendix A presents the influence of lateral fluctuations of the band gap energy, which cause a broadening of the absorption spectrum, on the radiative efficiency limit. It also discusses the existence of an optimal absorptance spectrum that would result in an ultimate efficiency limit for a given irradiation spectrum.

Homogeneous band gap

The maximum power conversion efficiency of a solar cell with homogeneous band gap is given by the radiative recombination limit and depends only on the cell temperature, the spectral distribution of the solar irradiation, and on the band gap energy E_g of the semiconductor acting as the photovoltaic absorber material. This theoretical efficiency limit was initially presented by Shockley and Queisser [10] and consists of a very much

idealized thermodynamic approach that is based on the detailed balance between the radiation fluxes absorbed and emitted by the solar cell. Geometrical extensions as well as optical and electrical material parameters are not accounted for. The solar cell is regarded as a black box, and only external radiation fluxes and currents are balanced as sketched in Fig. 2.2.

The ideal solar cell is completely characterized by its absorptance $a(E)$ expressed by the Heavyside function

$$a(E) = \begin{cases} 1, & E \geq E_g \\ 0, & E < E_g, \end{cases} \quad (2.5)$$

where E is the photon energy.

From this starting point Shockley and Queisser based their derivation of the radiative efficiency limit on four basic assumptions:

- (i) All photons with energy larger than the band gap E_g are completely absorbed and generate one electron/hole pair each.
- (ii) Under short circuit conditions all photo-generated carriers are collected and contribute to the photocurrent J_{sc} .
- (iii) Spontaneous emission of photons by radiative recombination of electron/hole pairs is the only loss mechanism as required by the principle of detailed balance.
- (iv) All photons emitted by radiative recombination have the same chemical potential μ .

Hidden within these four assumptions are two important aspects. Assumption (i) implicitly requires virtually infinite thickness of the photovoltaic absorber and assumption (ii) and (iv) require virtually infinite mobility of the photogenerated minority carriers. Given the above assumptions, Shockley and Queisser now calculate the saturation current J_0 of the solar cell from the thermodynamic equilibrium in the dark and compute the short circuit current J_{sc} from the irradiating solar spectrum. They therewith arrive at the current/voltage characteristic of the solar cell from which they derive the conversion efficiency. In this section I recapitulate these calculations.

The fundamental starting point for the calculation of the SQ efficiency limit is the principle of detailed balance, which states that in thermodynamic equilibrium, every

process has to be in equilibrium with its reverse process. For a solar cell this means that in the dark, the radiation emitted from the surface of the cell has to balance the flux of black body radiation from the surroundings which is absorbed by the cell. As a consequence, the loss mechanism of radiative recombination which is the only feasible source of radiation in a solar cell and constitutes the reverse process of fundamental absorption cannot be circumvented.

In a black body the photon flux density $\phi_{\text{bb},\bar{n}}^{\text{d}\Omega}$ per energy interval dE and solid angle interval $d\Omega$ is given by the generalized Planck's law [14, 15]

$$\phi_{\text{bb},\bar{n}}^{\text{d}\Omega}(E, \mu) dE d\Omega = \frac{2\bar{n}^2}{h^3 c^2} \frac{E^2}{\exp\left(\frac{E-\mu}{k_{\text{B}}T}\right) - 1} dE d\Omega, \quad (2.6)$$

where μ is the chemical potential of the radiation, \bar{n} is the refraction index of the material, h is Planck's constant, c is the speed of light, k_{B} is Boltzmann's constant and T is the temperature of the cell and the surroundings. For the ambient black body radiation, it holds $\bar{n} = 1$ and $\mu = 0$.

The black body photon flux $\phi_{\text{bb}}(E)$ impinging on the solar cell per area element of the cell's surface is given by the integration of the irradiation density $\phi_{\text{bb},1}^{\text{d}\Omega}(E, 0)$ over $d\Omega = \sin(\theta) d\varphi d\theta$ and reads as

$$\begin{aligned} \phi_{\text{bb}}(E) dE &= \phi_{\text{bb},1}^{\text{d}\Omega}(E, 0) dE \int_0^{2\pi} d\varphi \int_0^{\frac{\pi}{2}} \cos(\theta) \sin(\theta) d\theta \\ &= \pi \phi_{\text{bb},1}^{\text{d}\Omega}(E, 0) dE. \end{aligned} \quad (2.7)$$

The factor $\cos(\theta)$ stems from the projection onto the plane surface of the solar cell. Both angles θ and φ are defined as sketched in Fig. B.1. Integrated over all photon energies E this yields the overall black body flux

$$\Phi_{\text{bb}} = \int_0^\infty \phi_{\text{bb}}(E) dE = \frac{4\pi (k_{\text{B}}T)^3}{h^3 c^2} \quad (2.8)$$

impinging on the cell's surface. The exact solution of the integral is obtained by using the Boltzmann approximation of Eq. (2.6) which neglects the 1 in the denominator.

If only the photons with energies larger than the band gap are considered, we obtain the photon flux

$$\Phi_{\text{bb}}^{\text{Eg}} = \int_{E_{\text{g}}}^\infty \phi_{\text{bb}}(E) dE = \frac{2\pi}{h^3 c^2} \exp\left(\frac{-E_{\text{g}}}{k_{\text{B}}T}\right) k_{\text{B}}T (E_{\text{g}}^2 + 2E_{\text{g}}k_{\text{B}}T + 2(k_{\text{B}}T)^2). \quad (2.9)$$

The black body photon flux absorbed by the solar cell is given by the integration of the irradiation density $\phi_{\text{bb},\bar{n}}^{\text{d}\Omega}(E, 0)$ over dE and $d\Omega = \sin(\theta) d\varphi d\theta$ and reads as¹

$$\begin{aligned}\Phi_{\text{bb}}^{\text{abs}} &= \int_0^\infty a(E) \phi_{\text{bb},\bar{n}}^{\text{d}\Omega}(E, 0) dE \int_0^{2\pi} d\varphi \int_0^{\theta_c} \cos(\theta) \sin(\theta) d\theta \\ &= \int_0^\infty a(E) \phi_{\text{bb}}(E) dE.\end{aligned}\quad (2.10)$$

Due to Snellius' law of refraction the half sphere outside of the cell will be mapped onto the cone with critical angle $\theta_c = \arcsin(1/\bar{n})$. Therefore, the interaction between cell and surroundings only affects radiation (inside the cell) within angles smaller than θ_c .² For the step function Eq. (2.5) we find $\Phi_{\text{bb}}^{\text{abs}} = \Phi_{\text{bb}}^{\text{Eg}}$.

With the equilibrium emission current $\Phi_{\text{em}}(V = 0)$ in the dark being equal to the absorbed black body radiation $\Phi_{\text{bb}}^{\text{Eg}}$ from the ambience we obtain from Eq. (2.10) the emission current under short-circuit conditions with $V = 0$. Next, we need to derive the current voltage dependence of the emission current. Whereas the chemical potential of the emitted photons is $\mu = 0$ in thermal equilibrium, it holds $\mu = E_{\text{Fn}} - E_{\text{Fp}} > 0$ if a voltage V is applied or if the cell is illuminated. Here, E_{Fn} and E_{Fp} are the quasi-Fermi levels for electrons and holes respectively. Under the assumption that the mobility μ_n of the minority carriers is large enough to guarantee that all carrier gradients will immediately be levelled out, μ is constant throughout the cell and equal to the applied voltage qV . This means that all photons emitted by radiative recombination have the same chemical potential $\mu = qV$ (assumption (iv)). Therewith and by using the Boltzmann approximation of Eq. (2.6) which is valid for $E - \mu \gg kT$, the emission current caused by radiative recombination is given by

$$\Phi_{\text{em}}(V) = \pi \int_0^\infty a(E) \phi_{\text{bb},1}^{\text{d}\Omega}(E, V) dE \approx \Phi_{\text{bb}}^{\text{Eg}} \exp\left(\frac{qV}{k_{\text{B}}T}\right). \quad (2.11)$$

Next, we consider the solar cell under illumination and compute the electrical current J_{sc} under short-circuit conditions. The solar irradiation impinges vertically on the solar cell surface with an integrated photon flux density

$$\Phi_{\text{sun}} = \int_0^\infty \phi_{\text{sun}}(E) dE, \quad (2.12)$$

¹Note that throughout this thesis I assume a perfectly reflecting back side which means that radiative interaction is limited to the front surface. Note also that all fluxes are denoted as particle flux densities per unit area ($\text{cm}^{-2} \text{s}^{-1}$)

²Note the equivalence of either integrating $\phi_{\text{bb},1}^{\text{d}\Omega}(E, 0)$ from $\theta = 0$ to $\pi/2$ outside the cell surface or integrating $\phi_{\text{bb},\bar{n}}^{\text{d}\Omega}(E, 0)$ from $\theta = 0$ to θ_c inside the cell.

where $\phi_{\text{sun}}(E)$ is the spectral density of the solar spectrum. In analogy to Eq. (2.9), I define the photon flux $\Phi_{\text{sun}}^{\text{Eg}}$ which includes all photons with an energy larger than the band gap.

For a step-function absorptance, all photons with energies $E \geq E_g$ are being absorbed and generate one electron/hole pair each regardless of any surplus energy (assumption (i)). The absorbed photon flux $\Phi_{\text{sun}}^{\text{abs}}$ is equal to $\Phi_{\text{sun}}^{\text{Eg}}$. From balancing incoming and outgoing photon fluxes and the electrical current under short-circuit conditions as depicted in Fig. 2.2, it holds for the electrical current $J_{\text{el}}(V = 0) = J_{\text{sc}} = \Phi_{\text{sun}}^{\text{Eg}} + \Phi_{\text{bb}}^{\text{Eg}} - \Phi_{\text{em}}(V = 0)$, i.e. $J_{\text{sc}} = \Phi_{\text{sun}}^{\text{Eg}}$. This means that under short-circuit conditions all excess carriers are completely collected and contribute to the current J_{sc} (assumption (ii)).

Balancing incoming and drawn off currents for $V \neq 0$ leads to the current/voltage characteristic

$$J_{\text{el}}(V) = \Phi_{\text{sun}}^{\text{Eg}} + \Phi_{\text{bb}}^{\text{Eg}} - \Phi_{\text{em}}(V) = \Phi_{\text{sun}}^{\text{Eg}} - \Phi_{\text{bb}}^{\text{Eg}} \left(\exp \left(\frac{qV}{k_{\text{B}}T} \right) - 1 \right), \quad (2.13)$$

with the short circuit current $J_{\text{sc}} = \Phi_{\text{sun}}^{\text{Eg}}$ and the saturation current $J_0 = \Phi_{\text{bb}}^{\text{Eg}}$ (cmp. Eq. (2.1)). Note again that all currents are denoted as particle currents and have to be multiplied with the elementary charge q to obtain electrical currents.

2.3.2 Incomplete carrier collection

When transport is non-ideal, the quantum efficiency no longer equals the absorptance. The short-circuit current is given by

$$J_{\text{sc}} = \int_0^\infty \text{EQE}(E) \phi_{\text{sun}}(E) dE. \quad (2.14)$$

As Rau shows in his disquisition on the reciprocity between photovoltaic quantum efficiency and electroluminescent emission of solar cells [16], the excess emission current caused by radiative recombination reads as

$$\Phi_{\text{em}}(V) - \Phi_{\text{bb}}^{\text{Eg}} = \int_0^\infty \text{EQE}(E) \phi_{\text{bb}}(E) dE \left\{ \exp \left(\frac{qV}{k_{\text{B}}T} \right) - 1 \right\}. \quad (2.15)$$

In analogy to Eq. (2.13), the short circuit and the emission current yield the current/voltage characteristic of the solar cell.

There exists no closed-form expression for the quantum efficiency EQE. Therefore, the next chapter derives a numerical computation scheme.

2.4 Classical diode theory

2.4.1 Incomplete carrier collection

Shockley's and Queisser's detailed balance considerations give the overall efficiency limit for any single band gap material in dependence of the semiconductor's band gap E_g . They do not take into account geometrical extensions and either incomplete absorption or incomplete carrier collection. A real solar cell is far from being perfect though. Therefore, it has to be treated differently. In this section, the cell is still ideal insofar as there are no parasitic Ohmic losses. I will consider an abrupt one-sided pn^+ -junction where I also neglect absorption and recombination in either emitter or space-charge region. Non-idealities are expressed by finite mobility μ_n of the minority carriers (in our case electrons), by the finite absorptance of the cell in terms of cell thickness d and absorption coefficient α and by non-radiative recombination mechanisms as expressed by the lifetime τ .

In contrast to the SQ efficiency limit the following classical derivation of the diode equation is based on charge carrier transport or, more precisely, diffusive minority carrier transport in the quasi-neutral base region of the absorber material. To describe the current/voltage characteristic of an abrupt one-sided pn -junction under low-level injection conditions with $n(x) \ll p(x) \approx N_A$, one has to solve the diffusion equation [17]

$$D_n \frac{d^2 n}{dx^2} - \frac{n - n_0}{\tau} = -G_{\text{sun}}(x) \quad (2.16)$$

for the minority carriers (electrons for p -type doped samples) in the quasi-neutral base of the device with the boundary conditions

$$n(x=0) = n_0 \exp\left(\frac{qV}{k_B T}\right) \quad (2.17)$$

at the edge of the space charge region ($x=0$) and

$$\left. \frac{dn}{dx} \right|_{x=d} = \frac{-S_n}{D_n} (n(x=d) - n_0) \quad (2.18)$$

at the back contact ($x=d$). Here, $D_n = (k_B T/q)\mu_n$ is the electron diffusion constant, τ is the electron lifetime and S_n is the electron recombination velocity at the back contact (which ideally equals zero). Also, $n_0 = n_i^2/N_A$ is the electron concentration in thermal equilibrium where n_i is the intrinsic carrier concentration and N_A is the doping density.

Carriers are generated by external excitation with the generation rate $G_{\text{sun}}(x)$ and recombine with the (low level injection) recombination rate $R = (n - n_0)/\tau$. Calculating the current $J_{\text{el}}(V) = D_n dn/dx$ at $x = 0$ yields the current/voltage characteristic

$$J_{\text{el}}(V) = J_{\text{sc}} - J_0 \left(\exp \left(\frac{qV}{k_B T} \right) - 1 \right) \quad (2.19)$$

where with $S_n = 0$, J_0 is given by

$$J_0 = \frac{D_n n_0}{L_n} \left(1 - \frac{2}{1 + \exp \left(\frac{2d}{L_n} \right)} \right) = \frac{D_n n_0}{L_n} \tanh \left(\frac{d}{L_n} \right). \quad (2.20)$$

Here, $L_n = \sqrt{D_n \tau}$ is the diffusion length of the minority carriers.

The short-circuit current J_{sc} depends on the generation profile $G_{\text{sun}}(x)$. For a thick cell with $d \gg 1/\alpha(E)$, where $\alpha(E)$ is the absorption coefficient, the easiest approach is [18]

$$G_{\text{sun}}(x, E) = \phi_{\text{sun}}(E) \alpha(E) \exp(-\alpha(E)x), \quad (2.21)$$

where $\phi_{\text{sun}}(E)$ is the incident photon flux. With $S_n = 0$ we obtain

$$\begin{aligned} J_{\text{sc}} &= \int_0^\infty \frac{\phi_{\text{sun}}(E) \alpha L_n}{1 - \alpha^2 L_n^2} \left\{ 1 - \alpha L_n + 2 \frac{\alpha L_n \exp(-\alpha d) - \exp \left(\frac{-d}{L_n} \right)}{\exp \left(\frac{d}{L_n} \right) + \exp \left(\frac{-d}{L_n} \right)} \right\} dE \\ &= \int_0^\infty \frac{\phi_{\text{sun}}(E) \alpha L_n}{1 - \alpha^2 L_n^2} \left\{ \tanh \left(\frac{d}{L_n} \right) - \alpha L_n + \frac{\alpha L_n \exp(-\alpha d)}{\cosh \left(\frac{d}{L_n} \right)} \right\} dE. \end{aligned} \quad (2.22)$$

2.4.2 Complete carrier collection

In the case of ideal transport with $\mu_n \rightarrow \infty$, the derivations of the previous section simplify significantly. Under short circuit conditions, all absorbed photons are collected and the short circuit current

$$J_{\text{sc}} = \int_0^\infty (1 - \exp(-\alpha d)) \phi_{\text{sun}}(E) dE = \int_0^\infty a(E) \phi_{\text{sun}}(E) dE = J_{\text{sc}}^{\text{SQ}} \quad (2.23)$$

is equal to the maximum achievable short circuit current $J_{\text{sc}}^{\text{SQ}}$.

For the non-radiative recombination current, the high mobility limit reads as

$$J_0^{\text{nr}} = \frac{n_0 d}{\tau_{\text{nr}}}. \quad (2.24)$$

If the non-radiative lifetime is comparable to the radiative lifetime then the overall recombination current is the sum of non-radiative and radiative recombination current according to $J_0 = J_0^{\text{nr}} + J_0^{\text{rad}}$, where J_0^{rad} is given by Eq. (2.9). Note that this simple summing up of the recombination currents is only applicable in the limit of complete carrier collection with $\mu_n \rightarrow \infty$. Otherwise, the spatially resolved recombination rates have to be added up, which is accomplished by adding up the inverse lifetimes. For the solution of the diffusion equation Eq. (2.16), this adding up of the inverse lifetimes does not lead to a simple linear superposition of the recombination currents, as can be verified by looking at Eq. (2.20).

And besides, at this point, microscopic detailed balance arguments come into play, which brings us to the elaborated model presented in the next chapter.

Chapter 3

Generalized efficiency limit

Abstract: This chapter presents a self-consistent model that combines charge carrier transport and detailed radiation balances to describe the efficiency of solar cells in the whole range of non-radiative and radiative recombination as well as complete and incomplete carrier collection. An extra generation term accounting for the absorption and reemission of photons emitted by radiative recombination (photon recycling) is incorporated into the diffusion equation, thereby fulfilling internal and external radiation balances. The chapter shows that if the minority carrier mobility drops below a critical mobility then the solar cell efficiency is reduced drastically even in the otherwise most ideal case. It presents an analytical approximation of the numerical model. After having discussed the hypothetical case of an energy-independent absorption coefficient, the model is extended to energy-dependent light absorption and applied to experimental absorption data of crystalline silicon, amorphous silicon, and Cu(In,Ga)Se_2 . While for crystalline silicon, transport is not a limiting factor, solar cells made of amorphous silicon or Cu(In,Ga)Se_2 need to utilize built-in electric fields or band gap grading to enhance carrier collection. Amorphous silicon comes close to having an inherent mobility problem even in the radiative recombination limit.

Based on the considerations presented in the previous chapter, this chapter develops a generalized model that combines the SQ theory with the classical diode theory by incorporating the detailed radiation balance of absorbed and emitted photons into a microscopic transport approach.

3.1 Radiative recombination and photon recycling

Understanding the interaction between photons and electrons inside a semiconductor begins with fundamental light absorption. A photon is absorbed by exciting a valence electron into the conduction band, thereby creating an electron/hole pair. After a certain time, this electron/hole pair will recombine again, thereby dispensing its surplus energy either in form of phonons to the crystal lattice (non-radiative recombination) or by emitting a photon (radiative recombination). Non-radiative recombination would lead to an increase in the cell temperature, were it not for the assumed perfect thermal coupling to the surroundings which act as an ideal heat sink. With such perfect thermal coupling, however, the surplus energy is simply transferred to the ambience in form of heat. It is irretrievably lost for the utilization of electrical energy.

In contrast, radiative recombination is not such a simple one-step mechanism. During the radiative recombination of an electron/hole pair, a photon is spontaneously emitted into an arbitrary direction. This photon is either emitted through the surface of the cell or it is reabsorbed along its path within the solar cell. In the latter case, it generates an additional electron/hole pair, which in turn can again recombine radiatively and emit another photon. The repeated absorption and emission of photons is called *photon recycling* (PR). As will be shown in this chapter, the photon recycling process supplies the missing link between the SQ theory and the classical diode theory. It is the basis for the internal and external radiation balances.

Furthermore, the additional generation rate caused by reabsorbed photons effectively decreases the loss of carriers caused by radiative recombination. Radiatively recombining carriers are only lost if they recombine close to the surface. Deep within the bulk material they are completely recycled and therefore not lost at all. As a consequence, the internal generation caused by photon recycling leads to an increase in cell efficiency when compared to the case without photon recycling.

After surveying the treatment of the photon recycling effect in the literature, quantifying the internal generation rate will be the main element in the model developed in section 3.3.

3.2 Photon recycling in the literature

The effect of photon recycling (PR) was first addressed by Dumke [19], Moss [20], and Landsberg [21] as early as 1957. Dumke was already aware of the fact that the PR would lead to an infinite radiative lifetime deep in the bulk. He also pointed out the relevance of photonic transport in addition to electron transport.

First experimental evidence of the PR effect was reported another 10 years later in the late 1960ies and early 1970ies. As was to be expected, the effect gained importance in direct semiconductors with low radiative and high non-radiative lifetimes such as GaAs that were used for optoelectronic devices. Carr [22] and later Carr and Kameda [23] discovered PR effects in luminescence measurements with GaAs samples and termed them 'self-excitation'. Hwang [24] found reabsorption of photons to influence the quantum efficiency of radiative recombination determined in photoluminescence experiments with heavily doped GaAs. Stern and Woodall [25] were the first to introduce the denotation 'photon recycling'. They found PR effects to reduce the threshold current of GaAs double-heterostructure lasers by roughly 20 %.

The first rigorous theoretical treatment was presented in 1977 by Kuriyama et al. [26] who used their theory to analyze quantum efficiencies and diffusion lengths in AlGaAs heterostructures. Whereas previously, small quantum efficiencies [27] and large surface recombination velocities [24] had led to a domination of non-radiative recombination which made the treatment of PR effects superfluous, the development of higher quality crystals now required the consideration of photon recycling. Analysis without the consideration of PR yielded obviously false internal quantum efficiencies and, thus, made a detailed theoretical treatment indispensable.

Despite being the first treatment of PR, the publication of Kuriyama et al. [26] still remains *the* basis for virtually all following publications. Additionally to providing the theoretical treatment to compute the internal generation rate caused by radiative interaction within the semiconductor, they also developed an iterative scheme to solve the integro-differential equation resulting from the formulation of the problem, which is still widely used amongst scholars working on the topic. Using the fundamental system of the homogeneous solution they compute the contribution of each reabsorption cycle from the previous carrier profile. The initial profile is obtained from the analytical solution without PR.

Almost simultaneously, Asbeck [28] derived a (numerical) expression for a modified radiative lifetime that includes reabsorption of photons. Mettler [29] modified Kuriyama's rather complex derivation with cylindrical coordinates, and developed the approach also used in this thesis.

Following publications extended the treatments to include, for instance, graded band gaps [30,31], transient effects [32–35], optical modulation [36], *pin* structures [37], and two-dimensional effects [38].

Various procedures have been proposed for the mathematical formulation of the problem. For perfect optical confinement, an infinite spatially periodic continuation of the problem allows for an anharmonic Fourier analysis [39]. Also, perturbational and variational methods have been developed [40–42]. However, these mathematically more sophisticated approaches suffer from their limited applicability arising from the dependence of the PR effect on device geometry, energy dependencies, and operating conditions.

Special emphasis was placed on analytical approximations that allowed for incorporating the PR effect as modified lifetime and diffusion constant into the classical diffusion equation [40, 43–50]. These approaches and either their usefulness or the potential conflicts with respect to the detailed balance principle will be discussed separately in section 3.7.1 in the context of developing analytical approximations for the solar cell efficiency.

Most of the above publications dealt with light emitting diodes and lasers and the role of photon recycling for the experimental determination of lifetimes and quantum efficiencies. The relevance of PR for solar cells was not investigated until 1991 when Parrott [51] and Durbin and Gray [52] presented simulations of solar cell efficiencies at the 22nd IEEE PVSEC conference. In a further publication [53], Durbin and Gray refined their numerical model. They investigated the influence of photon recycling on the efficiency of solar cells but restrained themselves to the practical cases with non-radiative recombination being the dominant recombination process. A similar focus was also chosen by Badescu and Landsberg [54], Yamamoto et al. [55], and Balenzategui and Martí [56].

Parrott [57] was the first to relate photon recycling and the detailed balance efficiency limit of Shockley and Queisser. However, while deriving his model for spatially dependent chemical potential of the emitted photons, all his computations are carried

out under the assumptions that the chemical potential is constant within one absorption length. Especially for low mobilities and for the relevant energy range close to the band gap, where the absorption coefficient is very small, this approximation is rather crude.

The objective of this thesis is to provide a detailed and, particularly important, self-consistent model that combines the diffusion equation with the detailed balance approach. Special emphasis is placed on finite carrier transport in the radiative efficiency limit and the interplay between photon recycling and the detailed balance principle. This approach differs from most other contributions in the literature insofar as the detailed radiation balances provide a relentless limit that imposes strict checks for the numerical accuracy of the computations. For instance, these radiation balance checks call for the self-consistent averaging of all generation rates, thereby warranting the conservation of particles¹. In the practical cases discussed in the vast variety of the literature, these strict conditions were not imposed. On the one hand this greatly simplified the equations entering in the numerical model but on the other hand deprived the model of an accuracy check that - with regard to the complexity of the equations - might prove utterly necessary to guarantee the accuracy of the obtained results.

3.3 Diffusion equation with reabsorption

This section tackles the task of incorporating the photon recycling effect into a microscopic transport approach. The starting point will be the classical diode theory, i.e. the minority carrier diffusion equation (2.16), which is valid under low-level injection conditions. The photon recycling leaves everything unchanged except for an additional generation term caused by reabsorbed photons.

For the mathematical treatment of the photon recycling effect, a one-dimensional description of electron transport is still sufficient but has to be complemented by the three-dimensional emission of photons by recombining electron/hole pairs. Photons emitted by radiative recombination which are reabsorbed cause an extra generation of carriers. The diffusion equation (2.16) is extended to

$$D_n \frac{d^2 n}{dx^2} + G_{\text{int}}(x) - \frac{n}{\tau_r} - \frac{n - n_0}{\tau_{\text{nr}}} = -G_{\text{sun}}(x) - G_{\text{bb}}(x), \quad (3.1)$$

¹In the literature, such averaging was only performed by Durbin and Gray [53].

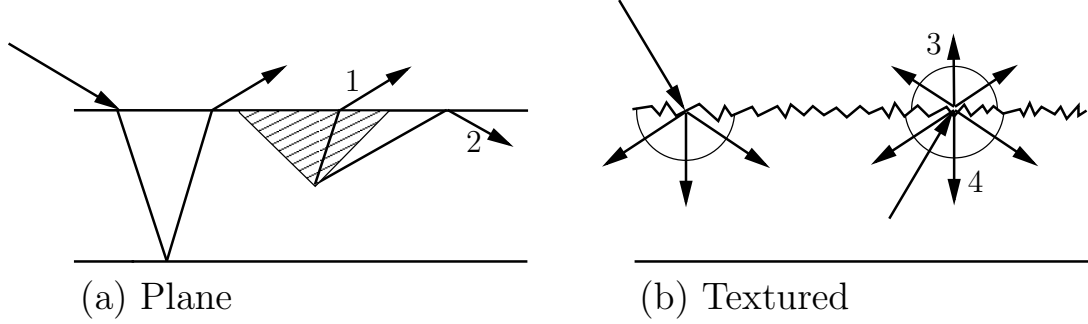


Fig. 3.1: In a solar cell with plane surface (a) all external rays impinging on the front surface are refracted towards the surface normal due to the higher refractive index \bar{n} inside the semiconductor. Internally emitted rays leave the cell if the emission angle is smaller than the critical angle $\theta_c = \arcsin(1/\bar{n})$ (ray 1). If the emission angle is larger than θ_c then the ray is internally reflected until it is completely absorbed within the solar cell (ray 2). In a cell with textured surface (b) an external ray is randomized upon transmitting the front surface. The same accounts for internally emitted rays. These internal rays are transmitted with the transmission probability t_{lamb} (rays 3) and reflected with the probability $1 - t_{\text{lamb}}$ (rays 4).

where recombination is split up into radiative recombination with the radiative lifetime τ_r and non-radiative recombination with the non-radiative lifetime τ_{nr} . The external generation consists of the equilibrium black body generation rate G_{bb} and the non-equilibrium solar generation rate G_{sun} . The extra internal generation is accounted for by adding the internal generation rate

$$G_{\text{int}}(x_g) = \int_{x_r=0}^{x_r=d} \delta G_{\text{int}}(x_g, x_r) = \text{const} \int_0^d f_r(x_g, x_r) n(x_r) dx_r \quad (3.2)$$

caused by radiative recombination throughout the sample. Here, $\delta G_{\text{int}}(x_g, x_r)$ denotes the generation rate at $x = x_g$ that is caused by radiatively recombining carriers in the incremental plain $x_r < x < x_r + \delta x_r$. As will be shown in appendix B, $\delta G_{\text{int}}(x_g, x_r)$ depends on the electron concentration at x_r and the optical interaction function $f_r(x_g, x_g)$. To obtain the overall internal generation rate at $x = x_g$ one has to integrate over all possible recombination events, that is over the whole thickness of the solar cell from $x_r = 0$ to $x_r = d$. For all terms that include light reflection at or light transmission through the front surface of the solar cell, the nature of the front surface has to be considered as well. As sketched in Fig. 3.1, I distinguish two cases, namely (a) a plane and (b) a textured front surface.

The detailed derivation of the model is provided in appendix B. The appendix starts

by reformulating the diffusion equation as a linear matrix equation based on linear operators. Then it gives expressions for the transport operator and the recombination operator. Subsequently, it derives an expression for the internal generation rate, starting with the direct radiative interaction between two locations in the cell, and followed by the inclusion of multiple reflections. Finally, it derives expressions for the external generation rates G_{bb} and G_{sun} caused by black body and solar irradiation respectively.

3.3.1 Parameter normalization

The major difference between the Shockley-Queisser detailed balance treatment and the considerations of the preceding section is, that non-ideal phenomena in terms of optical absorption and electrical transport can be analyzed with the latter approach. The analysis is not restricted to infinite mobility and complete absorption anymore as it had been in the SQ theory. Now the solar cell features the finite thickness d , the absorption coefficient α , the minority carrier mobility μ_n , the doping density N_A , and the non-radiative lifetime τ_{nr} .

In the following sections I investigate the influence of these device and material parameters on the saturation current J_0 and the short circuit current J_{sc} , and consequently on the power conversion efficiency η . To obtain J_{sc} , I solve the matrix equation obtained from the discretization of Eq. (3.3) performed in appendix B with illumination for the boundary conditions $V = 0$ at $x = 0$. Subsequently, I solve the matrix equation without illumination for $V = (k_B T/q) \ln(2)$ at $x = 0$ to obtain J_0 . From J_{sc} and J_0 I obtain the open-circuit voltage, the fill factor and the efficiency in dependence of μ_{norm} and E_g (cf. section 2.2).

In order to facilitate the analysis of the influence of the different parameters, I sum up several quantities in normalized parameters. To investigate the influence and mutual interplay of these parameters, it is convenient to introduce the normalized length $\xi = \alpha_0 x$, where $\alpha_0 = \alpha(E = E_g + k_B T)$ is the absorption coefficient at a photon energy $E_g + k_B T$. The electron concentration is normalized to $\nu = n/n_0$ with $n_0 = n_i^2/N_A$ being the equilibrium electron concentration that in turn depends on the intrinsic carrier concentration n_i and the doping density N_A . Additionally, I normalize the photon fluxes on the black body flux $\Phi_{\text{bb}}^{\text{Eg}}$ as defined in Eq. (2.9).

By dividing Eq. (3.1) by $\alpha_0 \Phi_{\text{bb}}^{\text{Eg}}$ one obtains the dimensionless equation

$$\mu_{\text{norm}} \frac{d^2 \nu}{d\xi^2} + \gamma_{\text{int}}(\xi) - \frac{\nu(\xi)(1 + \vartheta_r)}{\tau_{\text{norm}}^r} = -\gamma_{\text{sun}}(\xi) - \gamma_{\text{bb}}(\xi) - \frac{\vartheta_r}{\tau_{\text{norm}}^r} \quad (3.3)$$

with $\vartheta_r = \tau_r / \tau_{\text{nr}}$ and with the dimensionless rates $\gamma_i = G_i / (\alpha_0 \Phi_{\text{bb}}^{\text{Eg}})$. All dependencies on α_0 , μ_n and N_A are summed up in the normalized mobility

$$\mu_{\text{norm}} = \frac{\mu}{\mu_{\text{ref}}} \quad (3.4)$$

with the reference mobility

$$\mu_{\text{ref}} = \frac{q \Phi_{\text{bb}}^{\text{Eg}}}{k_B T \alpha_0 n_0} = \frac{q 2\pi N_A (E_g^2 + 2E_g k_B T + 2(k_B T)^2)}{h^3 c^2 N_C N_V \alpha_0}. \quad (3.5)$$

Here, I used $n_i^2 = N_C N_V \exp(-E_g / (k_B T))$ with N_C and N_V being the effective densities of states in the conduction and the valence band respectively. With τ_r given by Eq. (B.21), the normalized lifetime

$$\begin{aligned} \tau_{\text{norm}}^r &= \frac{\alpha_0 \Phi_{\text{bb}}^{\text{Eg}} \tau_r}{n_0} = \frac{\alpha_0 \Phi_{\text{bb}}^{\text{Eg}}}{R_0} \\ &= \frac{\alpha_0 2\pi \exp\left(\frac{-E_g}{k_B T}\right) k_B T (E_g^2 + 2E_g k_B T + 2(k_B T)^2)}{h^3 c^2 \int_{E_g}^{\infty} \alpha(E) 4\pi \phi_{\text{bb}, \bar{n}}^{\text{d}\Omega}(E, 0) dE} \end{aligned} \quad (3.6)$$

and the dimensionless rates γ_i only depend on the band gap E_g and on the functional dependence of the absorption coefficient $\alpha(E)$ on the energy E as listed in Tab. 3.2.

- For an energy-independent absorption coefficient $\alpha = \alpha_0$ for $E \geq E_g$ and $\alpha = 0$ for $E < E_g$ it holds $R_0 = 4\alpha_0 \bar{n}^2 \Phi_{\text{bb}}^{\text{Eg}}$ (cf. Eq. (2.9) and Eq. (B.19)) and therewith

$$\tau_{\text{norm}}^r(\text{const}) = \frac{1}{4\bar{n}^2}. \quad (3.7)$$

- With $\alpha(E) = \alpha_0 \sqrt{(E - E_g) / k_B T}$ for a direct semiconductor we obtain the Boltzmann approximation of the normalized lifetime

$$\tau_{\text{norm}}^r(\text{direct}) = \frac{4(E_g^2 + 2E_g k_B T + 2(k_B T)^2)}{\sqrt{\pi} \bar{n}^2 (4E_g^2 + 12E_g k_B T + 15(k_B T)^2)} \approx \frac{1}{\sqrt{\pi} \bar{n}^2} \quad (3.8)$$

- In an indirect semiconductor it holds $\alpha(E) = \alpha_0 (E - E_g)^2 / (k_B T)^2$ and therewith we obtain the normalized lifetime

$$\tau_{\text{norm}}^r(\text{indirect}) = \frac{E_g^2 + 2E_g k_B T + 2(k_B T)^2}{4\bar{n}^2 (E_g^2 + 6E_g k_B T + 12(k_B T)^2)} \approx \frac{1}{4\bar{n}^2} \quad (3.9)$$

The approximations in the previous equations (3.8) and (3.9) are valid as long the band gap E_g is larger than the thermal energy $k_B T$, which is the case for semiconductors commonly used for solar cells with $E_g > 1$ eV and $k_B T = 26$ meV at room temperature. In all three cases the generation rates γ_i are independent of α_0 as well. Thus, only the functional dependence of the absorption coefficient on the energy influences the normalized generation profiles.

For the electrical current

$$J_{\text{el}} = D_n \frac{dn}{dx} = \mu_{\text{norm}} \Phi_{\text{bb}}^{E_g} \frac{d\nu}{d\xi} \quad (3.10)$$

only the normalized mobility μ_{norm} is relevant and therefore also the efficiency only depends on the normalized lifetime and normalized mobility.

This result shows that in the ideal case where radiative recombination is the only loss mechanism, it is impossible to distinguish between the influence of the optical absorption in terms of α_0 and the influence of the minority carrier mobility μ_n for a given normalized thickness d/α_0 and given front and back side reflectivities. Only the product $\mu_n \alpha_0$ is relevant for the achievable efficiency. In the non-ideal case of non-radiative recombination however, electrical and optical effects can be separated. This will be described below in section 3.4.2. The repeated emission and reabsorption of photons causes an effective optical transport of charge carriers. The fact that only the product $\mu_n \alpha_0$ is important for the current-voltage characteristic of the device shows the virtual equivalence of optical and electrical carrier transport.

3.3.2 Free parameters

As a consequence of the normalization, the number of parameters is reduced and the only free parameters in the model are

- (i) the band gap energy E_g ,
- (ii) the normalized mobility $\mu_{\text{norm}} = \mu/\mu_{\text{ref}}$,
- (iii) the normalized thickness $\alpha_0 d$,
- (iv) the nature (textured or plane) of the front surface,
- (v) the lifetime ratio ϑ_r of radiative and non-radiative lifetime, and

Tab. 3.1: Standard parameters used for the computations of the reabsorption scheme.

E_g	\bar{n}	d	ϱ_f	ϱ_b	S_n	$\alpha(E)$	front surface
1 eV	3	$10/\alpha_0$	0	1	0	α_0	textured

- (vi) the energy-dependence of the absorption coefficient $\alpha(E)$ (constant, square root, parabolic).

All discussions are first performed for the theoretical case with constant absorption coefficient to emphasize fundamental dependencies. Afterwards, I discuss the cases of direct and indirect semiconductors. If not indicated otherwise, all computations use the parameters listed in Tab. 3.1. In fact, these parameters are also free parameters but they are not varied in this thesis. The thickness is chosen in a way that guarantees virtually complete absorption but still allows for a sufficiently accurate discretization (cf. appendix B.7). The reflection coefficients ϱ_f and ϱ_b and the back contact recombination velocity are part of the model but are assumed to be ideal throughout the whole chapter, since no new fundamental insights are expected that do not hold for the classical diode treatment as well.

3.4 Results with constant absorption coefficient

This section discusses the influence of the different parameters on the short circuit current J_{sc} and the saturation current J_0 for the case of constant absorption coefficient. I begin the analysis with the radiative efficiency limit, i.e. with radiative recombination being the only loss mechanism. For a sufficiently thick sample that guarantees virtually complete light absorption, I investigate the influence of normalized mobility and band gap energy. Subsequently, I analyze the impact of reduced sample thickness, combined with light trapping effects of a randomly textured front surface. Finally, I discuss the influence of non-radiative recombination.

The emphasis of this section lies in the descriptive presentation of the simulation results. The discussion of the results, analytical approximations, and explanations for the results are performed in the subsequent sections. Section 3.8 investigates the influence of energy-dependent absorption coefficient. All discussions before section 3.8 assume a constant $\alpha(E) = \alpha_0$ for $E > E_g$.

3.4.1 Radiative efficiency limit

In the SQ theory as described in section 2.3.1 the radiative efficiency limit of a solar cell depends only on the band gap energy E_g of the absorber material. The band gap energy defines the absorptance and consequently the number of absorbed photons from solar and black body irradiation, which in turn determine the short circuit current $J_{sc}^{SQ} = \Phi_{sun}^{Eg}$ and the saturation current $J_0^{SQ} = \Phi_{bb}^{Eg}$. Varying the band gap results in a varying spectral match to the two spectra and, thus, in a varying efficiency. Figure 3.2a displays the SQ efficiency limit for an AM1.5G spectrum [13] versus the band gap energy (stars). For a band gap $E_g = 1.15$ eV and $E_g = 1.35$ eV the efficiency reaches its maximum of approximately 33 %.

Figure 3.2a also displays the simulation results for a solar cell with radiative recombination as the only loss mechanism (assumption (iii) on page 11) but with finite mobility μ_{norm} . For very large μ_{norm} the efficiency is equivalent to the efficiency limit calculated by Shockley and Queisser. The large thickness $\alpha_0 d = 10$ guarantees complete light absorption (assumption (i)) and the large mobility guarantees complete collection of the generated carriers (assumption (ii)/(iv)). The photon recycling processes guarantee the fulfillment of the detailed internal and external radiation balances. Thus, all assumptions of the SQ theory are fulfilled, and with increasing mobility, the simulated efficiency converges towards the SQ efficiency. Upon decreasing the mobility μ_{norm} , the carrier collection is diminished, which leads to a reduction in the short circuit current and consequently a reduction in the efficiency.

As demonstrated in Fig. 3.2b, the influence of the mobility is completely independent of the band gap energy: The short circuit current $J_{sc}(E_g, \mu_{norm})$ normalized to the achievable maximum value $J_{sc}^{SQ}(E_g)$ for the respective band gap is constant for all band gap energies. Therefore, I restrict all following analyses to the band gap energy $E_g = 1$ eV.

Figure 3.3a demonstrates the influence of the mobility on the short circuit and the saturation current. The figure shows J_0 and J_{sc} normalized to $J_0^{SQ} = \Phi_{bb}^{Eg}$ and $J_{sc}^{SQ} = \Phi_{sun}^{Eg}$ versus the normalized mobility μ_{norm} . For sufficiently large mobilities the normalized currents approach unity i.e. the Shockley-Queisser limit. However, reducing the normalized mobility below a critical value μ_{crit} results in a sharp drop of the extracted currents. Section 3.6 derives an analytical expression for μ_{crit} .

Due to the spectral independence of the absorption coefficient $\alpha(E) = \alpha_0$ and the

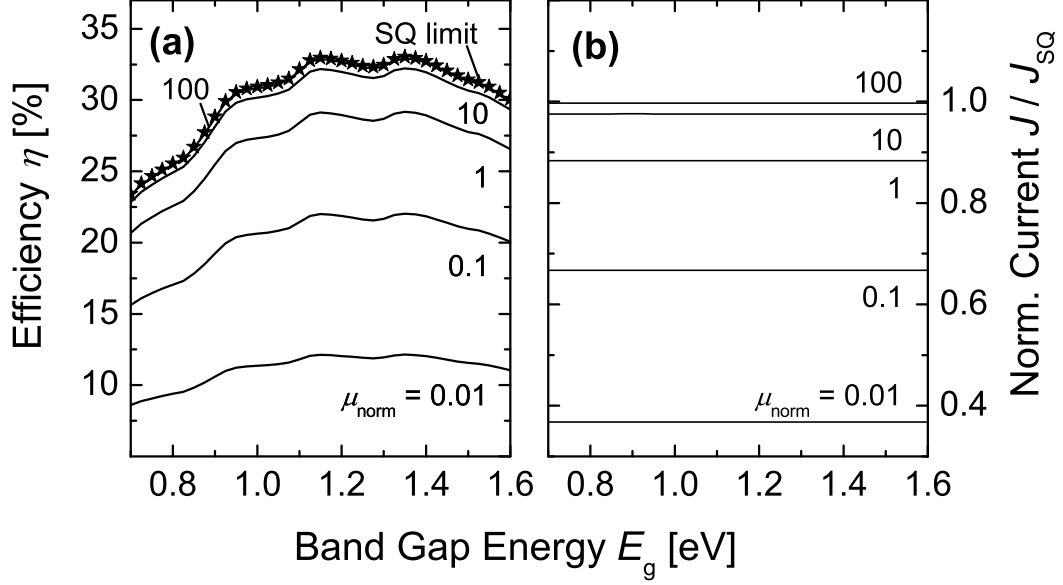


Fig. 3.2: a) Radiative efficiency (no non-radiative recombination) vs. band gap energy E_g . The absorption coefficient is $\alpha = \alpha_0$, the normalized thickness is $\alpha_0 d = 10$, and the front surface is textured. All parameters are listed in Tab. 3.1. For increasing mobility the efficiency approaches the Shockley Queisser limit (stars). For lower normalized mobilities however, the efficiency is reduced drastically, even though radiative recombination is the only loss mechanism. b) The efficiency loss is caused by reduced carrier collection manifested in a reduced short circuit current J_{sc} . The loss in $J_{\text{sc}}(E_g)$ when compared to the maximum value $J_{\text{sc}}^{\text{SQ}}(E_g)$ is completely independent of the band gap energy E_g .

textured front surface, the generation profiles caused by black body and solar irradiation are identical except for their magnitude. Therefore, J_0 and J_{sc} exhibit the same dependency on μ_{norm} and, thus, the open circuit voltage V_{oc} as depicted in Fig. 3.3b is completely independent of the normalized mobility. Consequently, the reduction of the efficiency with decreasing μ_{norm} is exclusively caused by the reduction of the short circuit current.

As Fig. 3.3a shows, J_{sc} and J_0 saturate (with increasing mobility) at lower levels when the sample thickness d is reduced. This effect stems from the reduced absorp-

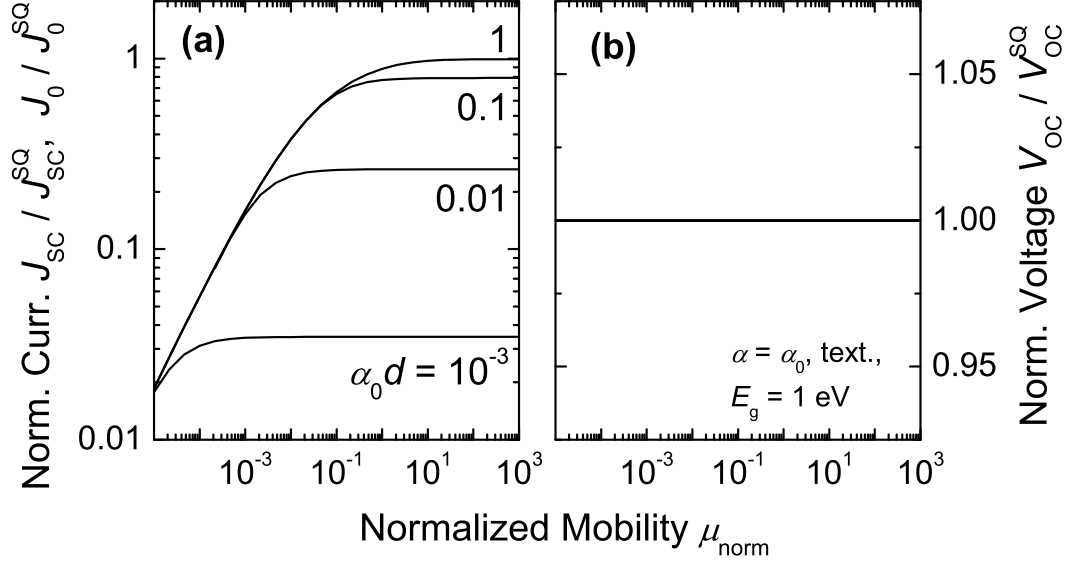


Fig. 3.3: Short circuit current J_{sc} and saturation current J_0 normalized to the maximum currents in the Shockley Queisser limit vs. the normalized mobility μ_{norm} (a). The currents approach their maximum value for sufficiently large mobility. With decreasing normalized mobility μ_{norm} , both, short circuit current and saturation current drop sharply once μ_{norm} falls below a critical mobility μ_{crit} . Due to the identical dependency of J_{sc} and J_0 on μ_{norm} , the open circuit voltage is for all thicknesses completely independent of the mobility (b). The absorption coefficient is $\alpha = \alpha_0$, the band gap is $E_g = 1$ eV, and the front surface is textured. All parameters are taken from Tab. 3.1

tance which in turn defines the maximum achievable current. Since the absorption coefficient is energy-independent, the absorptance is identical for solar and black body irradiation. Consequently, the normalized short circuit and saturation current are identical. Accordingly, the open circuit voltage is not only independent of the mobility but also independent of the sample thickness.

For low mobilities on the other hand, the absorptance has no influence on the currents. The diffusion length is much smaller than the absorption length and J_{sc} and J_0 are limited by transport rather than optics.

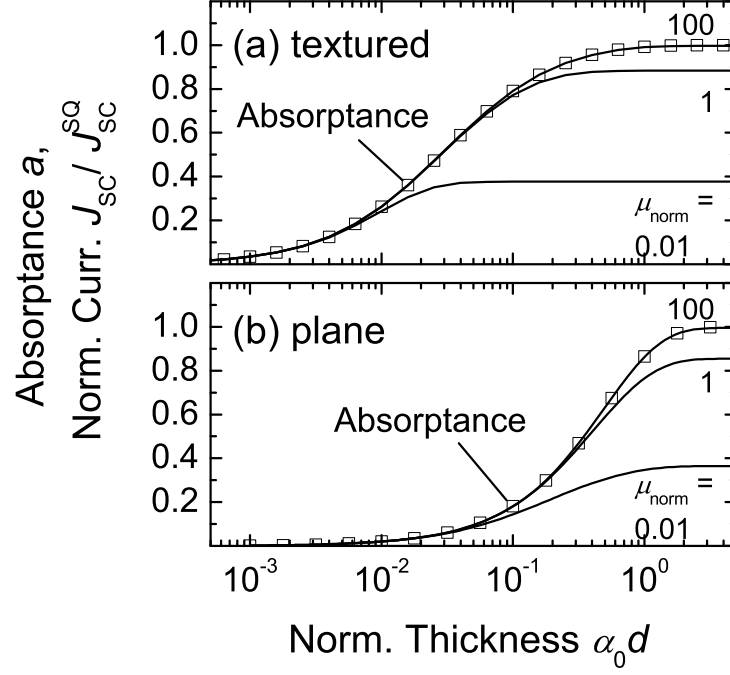


Fig. 3.4: Currents J_0 and J_{sc} normalized to the maximum values in the Shockley-Queisser limit vs cell thickness d for a textured (a) and plane (b) front surface. The absorption coefficient is $\alpha = \alpha_0$ and the band gap is $E_g = 1$ eV, all other parameters are listed in Tab. 3.1. For low d the currents are limited by the incomplete absorptance of the cell (open squares). For low mobilities μ_{norm} the current saturates at lower levels. This is because once the sample thickness is larger than the diffusion length, further increase of the thickness will not lead to increased carrier collection even though the absorptance might still be increased.

3.4.1.1 Light trapping

Figures 3.4a and b demonstrate the absorption losses due to decreasing sample thickness for a solar cell with either textured (a) or plane (b) front surface. The figures display the absorptance (squares) and the short circuit current (lines) vs. the normalized thickness $\alpha_0 d$.

Complete light absorption is only maintained as long as the sample is thicker than a critical thickness d_{crit} , below which the absorptance drops drastically. I define the

critical thickness as the thickness at which it holds $a(d_{\text{crit}}) = 0.5$. For thicknesses below d_{crit} the current is limited by incomplete light absorption and the mobility has no impact on the current. With increasing thickness and corresponding saturating absorptance the current is limited by the diffusion length if the mobility is too low.

In a solar cell with textured front surface the critical thickness is by roughly a factor of ten lower than in a solar cell with plane front surface. This effect is due to two reasons. Firstly, the incident light is diffracted and traverses the sample at an angle, thus experiencing a longer passage than light with normal incidence on a plane surface. Secondly, all rays are internally reflected at the front surface with the increased reflection coefficient $1 - t_{\text{amb}} = 1 - (1 - \varrho_f)/\bar{n}^2$, leading to efficient light trapping within the sample.

Note that in a solar cell with plane front surface, solar irradiation and black body irradiation cause slightly different generation profiles because of the different angular distribution of the impinging radiation. While the solar spectrum includes only rays with normal incidence, the black body spectrum impinges on the front surface from all directions and consequently, the rays within the sample cover all angles lower than the critical angle $\theta_c = \arcsin(1/\bar{n})$. Therefore, (i) the average path length is larger for black body irradiation than for solar irradiation and, thus, the absorptance is increased and (ii) carriers are generated closer to the front surface which leads to increased collection for low mobility. In total, the normalized saturation current is slightly larger than the normalized short circuit current. However, the effect is only very slight.

3.4.2 Non-radiative recombination

So far, radiative recombination was the only recombination mechanism considered in our investigation. But of course, besides finite mobility and absorption real solar cells also exhibit non-radiative recombination mechanisms such as Auger- or Shockley-Read-Hall recombination. All non-radiative recombination processes only affect excess carriers and can be expressed by a lifetime τ_{nr} . In the normalized differential equation Eq. (3.3), the non-radiative recombination rate $R_{\text{nr}} = (n - n_0)/\tau_{\text{nr}}$ is expressed as $\vartheta_r > 0$.

Naturally, non-radiative recombination processes reduce the resulting electron concentration. If τ_{nr} is much smaller than τ_r that is $\vartheta_r \gg 1$ then radiative recombination plays only a minor role and reabsorption can be neglected. In this case the conventional

diode treatment of section 2.4 is sufficient to describe the current/voltage characteristic of the device. For $\vartheta_r \ll 1$ non-radiative recombination can be neglected.

As in the ideal case with radiative recombination as the only recombination process, all dependencies on α_0 and μ_n are summed up in the normalized mobility μ_{norm} for all values of ϑ_r . However, this holds only for a given ratio ϑ_r of radiative and non-radiative recombination. Assuming that τ_{nr} is independent of α_0 then ϑ_r would of course depend on α_0 . For a given τ_{nr} , an increase of the absorption would reduce the radiative lifetime τ_r and thus also decrease ϑ_r . Therewith, the overall recombination will be reduced although the radiative recombination rate R_0 has been enlarged. This astonishing paradox stems from the reabsorption mechanism which recycles the emitted photons and therewith makes radiative recombination a far more desirable loss mechanism than non-radiative recombination. While the latter leads to an irreversible loss of all recombining charge carriers the former only induces a partial loss of carriers. Due to the competitive nature of all recombination processes, enlarging the radiative recombination rate implies an effective reduction of non-radiative recombination.

Figures 3.5a-d illustrate how the currents J_0 and J_{sc} , the open circuit voltage V_{oc} , and the efficiency η depend on the ratio ϑ_r of radiative and non-radiative recombination (solid lines). The quantities are displayed for the two normalized mobilities $\mu_{\text{norm}} = 1$ and $\mu_{\text{norm}} = 10^4$. With increasing non-radiative recombination (increasing ϑ_r) the recombination current J_0 increases as well (Fig. 3.5a). In contrast, the short circuit current in Fig. 3.5b decreases with increasing ϑ_r due to the decreasing diffusion length and the resulting reduced carrier collection. In both cases, a higher mobility increases the currents. For J_{sc} , only the diffusion length, i.e. the product of mobility and lifetime, is relevant, and, thus, the losses induced by decreasing lifetime can be compensated with high mobility (cmp. section 3.7). Therewith, almost complete carrier collection can be achieved even with miserable lifetimes.

Combined, J_0 and J_{sc} lead to a reduced V_{oc} with increasing ϑ_r (Fig. 3.5c). While the mobility has no influence on V_{oc} in the radiative limit for $\vartheta_r \rightarrow 0$, the open circuit voltage is slightly higher for lower mobilities when non-radiative recombination comes into play. However, the mobility by no means has the compensating effect it has on the short circuit current. For the open circuit voltage the crucial factor is definitely the lifetime. Since both, J_{sc} and V_{oc} , decrease with increasing ϑ_r , also the efficiency is decreased (Fig. 3.5d). For high mobilities, η is dominated by V_{oc} as long as the short

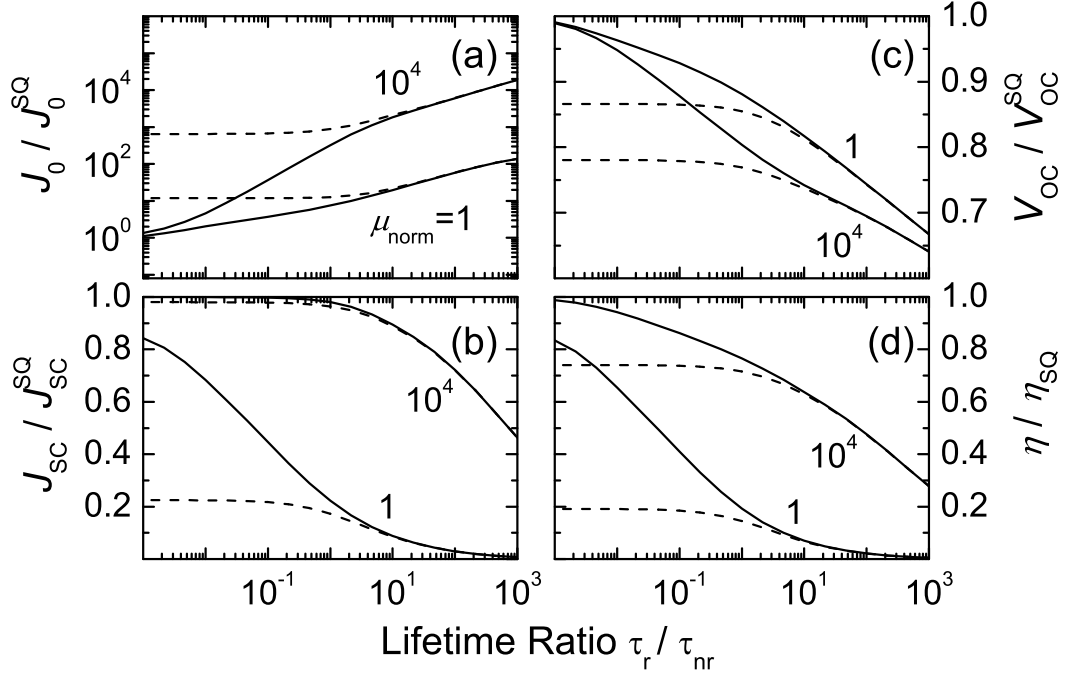


Fig. 3.5: Solar cell output parameters vs. the lifetime ratio ϑ_r of radiative and non-radiative lifetime for different normalized mobilities $\mu_{norm} = 1$ and $\mu_{norm} = 10^4$. Solid lines represent the numerical calculations including photon recycling (PR), dashed lines stand for the classical approach obtained by leaving out the PR term. The classical approach yields reasonable results only if the non-radiative lifetime is at least ten times smaller than the radiative lifetime, i.e. for $\vartheta_r > 10$. Whereas losses in the short circuit current J_{sc} for low lifetimes can be compensated by increasing the mobility (b), the open circuit voltage is almost exclusively dominated by the lifetime (c). For high mobilities, the efficiency is limited by V_{oc} , for low mobilities, J_{sc} is the limiting factor (d). The absorption coefficient is $\alpha = \alpha_0$, the normalized thickness is $\alpha_0 d = 10$, the band gap is $E_g = 1$ eV, and the front surface is textured. All parameters are listed in Tab. 3.1.

circuit current remains high. For low mobilities, however, the efficiency is dominated by the drastic losses in J_{sc} .

For comparison, the results from the classical diode theory are displayed as well (dashed lines). In this context, classical diode theory means leaving out the internal

generation rate γ_{int} in Eq. (3.3) that is caused by photon recycling. If recombination is dominated by non-radiative recombination, i.e. for $\vartheta_r > 10$, photon recycling is negligible and the classical diode theory is sufficiently accurate; the results with or without the inclusion of photon recycling converge.

With decreasing ϑ_r , radiative recombination and PR become much more important. The classical diode theory is not sufficient to describe the efficiency in the radiative limit. In the form chosen here, the classical theory predicts efficiencies that are far below the SQ limit. A detailed discussion will be given in section 3.7.

3.5 Photon recycling and detailed balance

This section analyzes the influence of the photon recycling (PR) on the spatial distribution of the electron concentration in the solar cell. It also discusses how the PR mechanism leads to the compliance of the internal and external radiation balances. Only with the inclusion of PR, the principle of detailed balance is warranted. All discussions are performed in the radiative recombination limit with $\tau_{\text{nr}} \gg \tau_r$ and assume a perfect back contact with the back surface recombination velocity $S_n = 0$.

3.5.1 Radiation balance in equilibrium

In thermodynamic equilibrium, all processes have to be in equilibrium with their reverse process. Therefore, photon and electron densities have to be constant throughout the cell. The electron concentration is given by the equilibrium value $n(x) = n_0$ and the radiative recombination rate equals the generation rate $R(x) = G(x) = R_0$.

This section analyzes how the reabsorption scheme developed in this chapter complies the internal and external radiation balances and leads to the required constant electron and photon distribution. For the numerical computation, the self-consistency of the model is particularly important in order to avoid a violation of the detailed balance principle

3.5.1.1 Internal radiation balance

Let us first consider a solar cell with a perfectly reflecting front and back side, i.e. without any radiative interaction with its surroundings. Let us further assume $\vartheta_r = 0$,

i.e. only radiative recombination. Then all right hand side excitation terms in Eq. (3.3) vanish. Let us now assume the equilibrium situation with $n(x)$ being constant. In the following, I analyze, what requirements this equilibrium situation poses for the internal generation rate γ_{int} and whether the approach developed above is capable of meeting those requirements.

For any given constant electron distribution, the curvature $d^2\nu/d\xi^2$ is zero. Thus, it follows from Eq. (3.3) without the external generation rates that the internal generation rate

$$\gamma_{\text{int}}(\xi) = \frac{\nu(\xi)}{\tau_{\text{norm}}^r} \quad (3.11)$$

equals the radiative recombination rate. According to Eq. (3.2) and with help of $R_0 = 4\alpha_0\bar{n}^2\Phi_{\text{bb}}^{\text{Eg}} = \alpha_0\Phi_{\text{bb}}^{\text{Eg}}/\tau_{\text{norm}}^r$ from Eq. (B.19) and Eq. (3.7) the internal generation rate reads as

$$\gamma_{\text{int}}(\xi) = \frac{1}{\alpha_0\Phi_{\text{bb}}^{\text{Eg}}} \int_0^{\alpha_0 d} \int_0^\infty r_0(E)\nu(\xi_r)f_r(E, \xi, \xi_r)dEd\xi_r, \quad (3.12)$$

where $f_r(\xi, \xi_r, E)$ is the radiative interaction function that describes the probability with which a photon emitted at ξ_r is reabsorbed at ξ .

For the sake of simplicity, let us restrict the following derivation to the case of energy independent absorption coefficient $\alpha(E) = \alpha_0$ for $E \geq E_g$. Then, the interaction function f_r becomes independent of the photon energy and the energy integral is given by Eq. (2.9). With help of $R_0 = 4\alpha_0\bar{n}^2\Phi_{\text{bb}}^{\text{Eg}} = \alpha_0\Phi_{\text{bb}}^{\text{Eg}}/\tau_{\text{norm}}^r$ we thus obtain

$$\begin{aligned} \gamma_{\text{int}}(\xi) &= \frac{1}{\alpha_0\Phi_{\text{bb}}^{\text{Eg}}} \int_0^{\alpha_0 d} \nu(\xi_r)f_r(\xi, \xi_r)d\xi_r \int_0^\infty r_0(E)dE \\ &= \frac{R_0}{\alpha_0\Phi_{\text{bb}}^{\text{Eg}}} \int_0^{\alpha_0 d} \nu(\xi_r)f_r(\xi, \xi_r)d\xi_r = \frac{1}{\tau_{\text{norm}}^r} \int_0^{\alpha_0 d} \nu(\xi_r)f_r(\xi, \xi_r)d\xi_r. \end{aligned} \quad (3.13)$$

Inserting this result into Eq. (3.11) and keeping in mind that $\nu(\xi)$ is constant yields the requirement

$$\int_0^{\alpha_0 d} f_r(\xi, \xi_r)d\xi_r = 1 \quad (3.14)$$

which needs to be fulfilled in order to satisfy the equilibrium condition of a constant electron distribution and to comply the condition of photon conservation.

Since both sides of the solar cell are ideal mirrors, no photons can leave the cell. The probability that a photon which is emitted at a certain location within the cell will be reabsorbed at some point within the cell is unity. Therewith, the condition Eq. (3.14) is intuitively fulfilled.

Another approach is to regard the perfectly reflecting surfaces as the infinite continuation of the solar cell (at least optically). Then, radiative interaction occurs only via direct paths of light and we obtain from Eq. (B.26)

$$f_r(\xi, \xi_r) = \frac{1}{2} \text{Ei}(|\xi - \xi_r|). \quad (3.15)$$

Since for the exponential integral $\text{Ei}(\xi)$ defined in Eq. (B.3) it holds

$$\frac{1}{2} \int_{-\infty}^{\infty} \text{Ei}(\xi) d\xi = 1, \quad (3.16)$$

the radiative interaction function f_r is indeed a normalized probability function and Eq. (3.14) is fulfilled.

Therewith, we arrive at the conclusion that the reabsorption scheme presented in this chapter leads to the compliance of internal radiation balances.

The requirement Eq. (3.14) is also extremely important for the accuracy of the discretization scheme utilized for the numerical computations as presented in appendix B. In our selfconsistent approach which averages recombination and generation over each interval, it is guaranteed that no photons are lost or unintendedly generated.

Except for Ref. [53], all other approaches in the literature neglect such averaging. While this might be justified for most applications, the averaging increases the precision of the computations substantially and is absolutely necessary to reproduce such results as the equilibrium situation discussed above.

In the discretization scheme used to solve the differential equation (3.3), the internal generation rate $\gamma_{\text{int}}(\xi) = \underline{PRn}(\xi)$ is expressed as a Matrix multiplication (cmp. section B.2.1). Now Eq. (3.14) implies that the sum of each row and each column in the matrix A representing the internal generation normalized to R_0 equals unity. Due to the perfect reflection at front and back side, a certain amount of photons emitted by recombination in a given interval δx_r generates exactly as many electrons throughout the cell.

So far we have only proven that any constant electron distribution is a solution to the differential equation Eq. (3.3). The result $\nu(\xi) = 1$ is only determined by the boundary condition at $\xi = 0$.

In fact, this argument leads us to a rather astonishing conclusion, namely, that the ideal diode discussed here is really no diode at all because there is no way an electric current can flow. For the special case discussed here with perfectly reflecting front and back side and only radiative recombination being allowed, no radiation can leave the cell and there will not be an electrical recombination current. The electron distribution will always be constant even with an applied voltage $V \neq 0$. There will be no carrier gradients and the arising electron concentration is $\nu(\xi) = \exp(qV/k_B T) = \text{const.}$

The situation changes for $\vartheta_r > 0$. Then, non-radiative recombination takes place for $V > 0$ and the equilibrium situation is only reached for $\nu(\xi) = 1$.

3.5.1.2 External radiation balance

Let us next consider a solar cell in the radiative recombination limit where the front side is not perfectly reflecting. Then, there will be radiative interaction between the cell and its ambience via the front surface. Recombination shall again be exclusively radiative.

In thermal equilibrium, the semiconductor now not only needs to be in equilibrium with itself but also with its surroundings. We have to consider the generation $\gamma_{\text{bb}}(\xi)$ caused by the ambient black body radiation as well. With the equilibrium electron concentration again being constant $\nu(\xi) = 1$ throughout the absorber, there exists an equilibrium of recombination and generation which, according to Eq. (3.3), reads as

$$\frac{1}{\tau_{\text{norm}}^r} = \gamma_{\text{bb}}(\xi) + \gamma_{\text{int}}(\xi). \quad (3.17)$$

In analogy to Eq. (3.14) and with $\tau_{\text{norm}}^r = 1/(4\bar{n}^2)$, we rewrite this equation and obtain the condition

$$\int_0^{\alpha_0 d} f_r(\xi, \xi_r) d\xi_r + \frac{1}{4\bar{n}^2} \gamma_{\text{bb}}(\xi) = 1, \quad (3.18)$$

which needs to be shown in the following.

Essentially, this equation states that all radiation losses through the front surface have to be balanced by the incident black body radiation. It therewith implicitly includes the external radiation balance.

By using γ_{int} from Eq. (B.28) and Eq. (B.27) and γ_{bb} from Eq. (B.38) for a plane front surface or γ_{int} from Eq. (B.36) and γ_{bb} from Eq. (B.41) for a textured surface,

the above condition can in principle be proven. Here, I restrict the analysis to a semi infinite solar cell with a plane front surface at $\xi = 0$. For angles smaller than the critical angle $\theta_c = \arcsin(1/\bar{n})$, the reflection coefficient is $\varrho_f = 0$.

The key to fulfilling the condition Eq.(3.18) lies in the connection between the exponential integral functions $\text{Ei}_1(z, \theta_c)$ and $\text{Ei}_2(z, \theta_c)$, which is given by

$$\text{Ei}_2(z, \theta_c) = \int_z^\infty \text{Ei}_1(\xi, \theta_c) d\xi \quad (3.19)$$

as shown in Eq. (B.6) in the appendix. As a result, all generation functions basically feature identical spatial dependencies.

Let us start with the internal radiative interaction f_r . For the case discussed here, $f_r(\xi, \xi_r)$ is limited to the direct interaction between ξ and ξ_r and one reflection at the front surface for angles $\theta > \theta_c$. According to Eq. (B.27) it holds

$$f_r(\xi, \xi_r) = \frac{1}{2}\text{Ei}(|\xi - \xi_r|) + \frac{1}{2}\text{Ei}\left(\frac{\xi + \xi_r}{\cos(\theta_c)}\right). \quad (3.20)$$

For the semi infinite sample with $d \rightarrow \infty$ we have to solve the integral $\int_0^\infty f_r(\xi, \xi_r) d\xi_r$. By splitting up the first integral and using the substitution $u = \pm(\xi - \xi_r)$ as well as $\int_0^\infty \text{Ei}(\xi) d\xi$ (cmp. Eq. (3.16)) we obtain

$$\begin{aligned} \int_0^\infty \frac{1}{2}\text{Ei}(|\xi - \xi_r|) d\xi_r &= \int_0^\xi \frac{1}{2}\text{Ei}(u) du + \int_0^\infty \frac{1}{2}\text{Ei}(u) du \\ &= 1 - \int_\xi^\infty \frac{1}{2}\text{Ei}(u) du = 1 - \frac{1}{2}\text{Ei}_2(\xi, 0). \end{aligned} \quad (3.21)$$

Accordingly, the second term in Eq. (3.20) yields the integral

$$\int_0^\infty \frac{1}{2}\text{Ei}\left(\frac{\xi + \xi_r}{\cos(\theta_c)}\right) d\xi_r = \frac{1}{2}\text{Ei}_2(\xi, \cos(\theta_c)). \quad (3.22)$$

Hence, it holds

$$\int_0^\infty f_r(\xi, \xi_r) d\xi_r = 1 - \frac{1}{2}\text{Ei}_2(\xi, 0) + \frac{1}{2}\text{Ei}_2(\xi, \cos(\theta_c)). \quad (3.23)$$

From Eq. (B.38) the black body generation rate is given as

$$\gamma_{\text{bb}}(\xi) = 2\bar{n}^2 \{\text{Ei}_2(\xi, 0) - \text{Ei}_2(\xi, \theta_c)\}. \quad (3.24)$$

Combining Eq. (3.23), and Eq. (3.24) then yields the condition Eq. (3.18).

We have thus shown that the thermal equilibrium holds outside the cell as well as within the cell and also across the front interface where the change in refractive index occurs.

3.5.2 Non-equilibrium concentration profile

Figures 3.6a-d demonstrate the impact of PR on the electron profile in the solar cell with and without illumination. The figures display the profiles $\nu(\xi) = n(\xi)/n_0$ versus the absorber depth $\xi = \alpha_0 x$ in the dark under applied voltage $V = (k_B T/q) \ln(2)$ (J_0 condition, (a), (b)) and under 1 sun illumination and short circuit (J_{sc} condition, (c), (d)). Recombination is purely radiative, all other parameters are listed in Tab. 3.1.

Profile in the dark

Let us first consider the dark case. The electron concentration at the front surface at $\xi = 0$ is given by the boundary condition $\nu(0) = 2$ (cmp. section 3.4). Without PR (i.e. by leaving out the internal generation rate γ_{int} in Eq. (3.3)), the electron concentration decreases exponentially towards the back contact. Due to the approach $R_r = n/\tau_r$ instead of $R_r = \Delta n/\tau_r$, $\nu(\xi)$ approaches zero deep in the absorber.

By including the internal generation rate in Eq. (3.3) and thereby accounting for the recycling of photons, the electron concentration is substantially increased throughout the sample. Therefore, also the absolute value of the gradient at $\xi = 0$ is reduced, which means that the recombination current according to Eq. (3.10) is always lower than in the classical approach (cf. Fig. 3.5a). The photon recycling ensures that $\nu(\xi)$ never drops below the equilibrium concentration $\nu = 1$, even deep in the absorber.

The PR effect is all the more pronounced the lower the normalized mobility. This is because the optical transport of photons from radiative recombination leads to increased carrier injection far away from the junction, which can be pictured as an increased 'effective diffusion length'. For low mobilities, i.e. low diffusion lengths $L_{norm} = \sqrt{\mu_{norm} \tau_{norm}^r}$ the role of optical transport in comparison to diffusive transport increases, and the impact of the PR on the electron profile is amplified.

Profile under illumination

Next, we consider the illuminated case (Fig. 3.6c, d). The illumination generates excess carriers. Due to the short circuit condition, it holds $\nu(0) = 1$. Again, the PR increases the electron concentration. Therewith, the gradient at $\xi = 0$ is enlarged, which leads to an enhanced short circuit current in comparison to the case without PR (cmp. Fig. 3.5b)

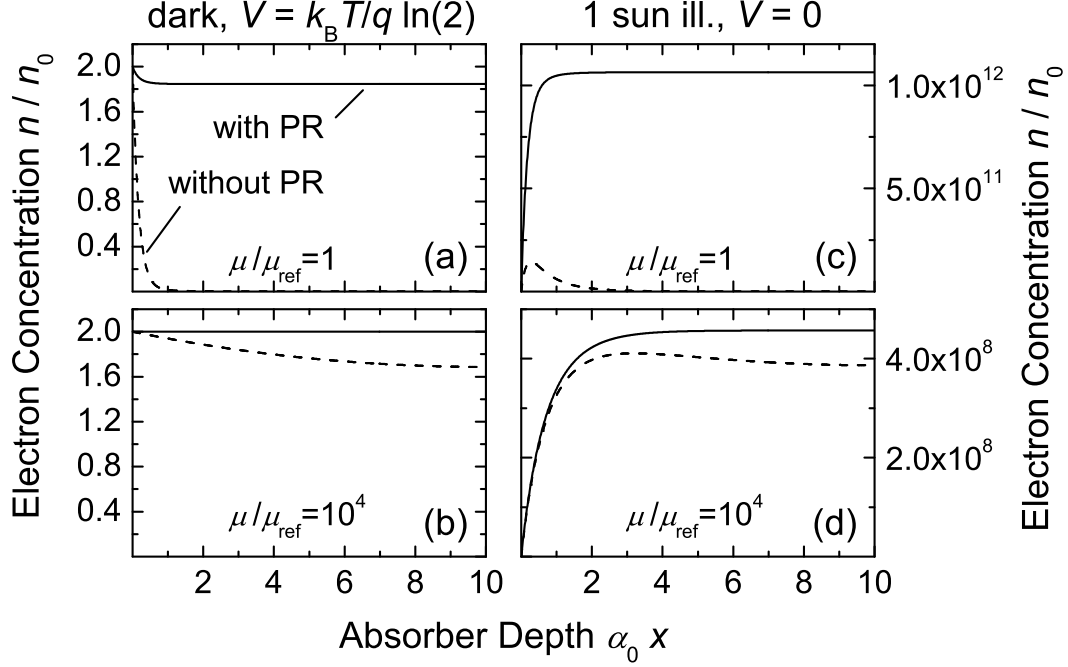


Fig. 3.6: Electron profiles with (solid lines) and without (dashed lines) PR in the dark under applied forward voltage (a, b) and under illumination without voltage (c, d). The absorption coefficient is $\alpha = \alpha_0$, the normalized thickness is $\alpha_0 d = 10$, the band gap is $E_g = 1 \text{ eV}$, and the front surface is textured. The parameters are listed in Tab. 3.1. Only radiative recombination is allowed ($\vartheta_r = 0$). The normalized mobilities are $\mu_{\text{norm}} = 1$ and $\mu_{\text{norm}} = 10^4$. The photon recycling significantly increases the electron concentration throughout the sample and therewith increases the efficiency. For lower mobilities the PR effect is more pronounced.

Interestingly, the electron concentration is a function which is monotonically increasing with the absorber depth ξ . This finding holds true independent of the thickness of the solar cell. At first glance, this result seems astonishing: Photons are only entering the cell from the front side, why should illumination then result in a higher electron concentration deep in the bulk?

To understand this apparent paradox, consider a thick solar cell in the dark with only radiative recombination, no recombination at the back contact and a perfectly reflecting back side. Upon switching on the light, carriers are generated primarily close to the front surface. There will be excess photons and electrons close to the front side

but deep in the bulk, electrons and photon concentrations still possess their equilibrium values. Therefore, there will be a net photon flux and a diffusive electron flux towards the bulk (in positive x -direction). Since neither photons nor electrons can be lost in the bulk, this net electron/photon flux into the bulk persists only until a steady state is reached. Such a steady state implies that at each point the photon flux into the bulk has to be balanced by an electron flux out of the bulk and vice versa. Under illumination (and $V < V_{oc}$), there will always be a net photon flux into the cell, the emitted photon flux cannot exceed the incident photon flux. Extending this reasoning to within the absorber implies that there cannot be a net photon flux out of the bulk (in negative x -direction) at any point. Therefore, there cannot be a steady state electron flux in positive x -direction. This means that there cannot be any negative gradients in the electron concentrations, i.e. that the electron concentration is a function which monotonically increases towards the back contact. In contrast, the electron profile obtained with the classical diode theory without PR does decrease towards the back contact and therewith violates the principle of detailed balance.

The number of electrons exiting the cell at the junction (at the front side) depends on the bias conditions of the solar cell which determine the electron concentration at $x = 0$. As long as $V < V_{oc}$, there will be an electron current flowing out of the cell. Under open circuit conditions, there is no net current flow and, thus, the gradient $dn(x)/dx$ at $x = 0$ vanishes. Therefore, the electron concentration under open circuit conditions will simply be constant $n(x) = n_0 \exp(qV_{oc}/(k_B T))$ throughout the absorber. With V_{oc} being independent of the mobility μ_{norm} as shown in Fig. 3.3, this means that under open circuit conditions also $n(x)$ is independent of μ_{norm} .²

3.5.3 Radiation balance in non-equilibrium

Sections 3.5.1.1 and 3.5.1.2 have shown how the photon recycling mechanism leads to a constant equilibrium concentration within the cell by guaranteeing the internal and external detailed balance requirements. We have included the incoming black body radiation in form of the generation rate γ_{bb} . However, we have hitherto not yet scrutinized the other direction of external radiative interaction, namely the emission

²Note however that these considerations hold only in the radiative recombination limit and for a perfect back side. As soon as non-radiative recombination is introduced carriers can be lost in the bulk as well and the electron distribution is not monotonically increasing any more.

of radiation.

This section takes a closer look at the emitted radiation, first deriving an expression how to compute the emission current for a given voltage from the electron profile and then discussing the relation between radiative recombination current and emitted radiation.

3.5.3.1 Reciprocity of emission and absorption

In principle, a complete derivation of the emitted radiation that is in line with the derivations for the internal and external generation rates in section 3.3 would include direct and reflected rays of light and would also include the cases of plane and textured front surfaces. However, I will refrain from performing all derivations here. Instead, I restrict the analysis to direct emission of radiation through a plane surface for an energy-independent absorption coefficient $\alpha(E) = \alpha_0$ for $E \geq E_g$. From the obtained result I exemplarily show the reciprocity between emitted radiation and the absorption of black body radiation thereby providing an easy way to calculating the emission current if the black body generation rate $\gamma_{bb}(\xi)$ and the electron concentration $\nu(\xi)$ are known.

In analogy to Eq. (B.25) the photon flux directly emitted through the (plane) front surface at $x = 0$ from recombination within the infinitesimal plane $\delta x =$ at x reads as

$$\delta\Phi_{em}(x) = \int_0^\infty \int_0^{2\pi} d\varphi \int_0^{\theta_c} \frac{r_0}{4\pi} \nu(x) (1 - \varrho_f) \exp\left(\frac{-\alpha x}{\cos(\theta)}\right) \cos(\theta) \frac{\delta x}{\cos(\theta)} \sin(\theta) d\theta dE. \quad (3.25)$$

Note that $r_0/(4\pi)\nu(x)\delta x/\cos(\theta)$ is the emitted photon flux per solid angle interval and $(1 - \varrho_f)\exp(-\alpha x/\cos(\theta))\cos(\theta)$, where ϱ_f is the reflection coefficient of the front surface, denotes the emission probability through the front surface. In this last term, the factor $\cos(\theta)$ stems from the projection onto the front surface (cmp. Eq. (2.7)), which is needed because the areal photon flux density Φ_{em} of the emitted radiation refers to a unit front surface area.

Using Eq. (B.4) and keeping in mind that $\alpha = \alpha_0$ is constant we obtain

$$\delta\Phi_{em}(x) = \frac{R_0}{2} \nu(x) (1 - \varrho_f) \{ \text{Ei}_2(\alpha x, 0) - \text{Ei}_2(\alpha x, \theta_c) \} \delta x. \quad (3.26)$$

With $R_0 = \int_0^\infty r_0(E) dE = 4\alpha_0 \bar{n}^2 \Phi_{bb}^{Eg}$ from Eq. (B.19) and Eq. (2.9) this yields the

normalized expression

$$\frac{\delta\Phi_{\text{em}}(\xi)}{\Phi_{\text{bb}}^{\text{Eg}}} = 2\bar{n}^2\nu(\xi) \{ \text{Ei}_2(\xi, 0) - \text{Ei}_2(\xi, \theta_c) \} \delta\xi. \quad (3.27)$$

Comparison with the direct black body generation rate $\gamma_{\text{bb}}(\xi)$ as given in Eq. (3.24) finally brings us to the reciprocity relation

$$\frac{\delta\Phi_{\text{em}}(\xi)}{\Phi_{\text{bb}}^{\text{Eg}}} = \gamma_{\text{bb}}(\xi)\nu(\xi)\delta\xi. \quad (3.28)$$

This relation is not only valid for direct rays as shown here, but also for multiple reflections. It stems from the fundamental theorem of the reversibility of the direction of light. In our case this means that the probability of absorbing a photon impinging on the surface from a certain direction at the location ξ is identical to the probability of emitting a photon generated by recombination at ξ into the same direction.

The total flux of emitted photons is given by the integral

$$\frac{\Phi_{\text{em}}(\xi)}{\Phi_{\text{bb}}^{\text{Eg}}} = \int_0^{\alpha_0 d} \gamma_{\text{bb}}(\xi)\nu(\xi)\delta\xi. \quad (3.29)$$

3.5.3.2 Emission flux and recombination current

In this section I discuss the relation between emitted radiation and the recombination current. In thermodynamic equilibrium, the emitted photon flux $\Phi_{\text{em}}(V = 0)$ is equal to the part of the black body radiation that is absorbed by the solar cell. This follows directly from Eq. (3.29). In equilibrium, the electron concentration is $\nu(\xi) = 1$ throughout the whole solar cell (see section 3.5.1). Then, the overall emitted radiation is simply determined by the absorptance a of the sample and reads as

$$\frac{\Phi_{\text{em}}(V = 0)}{\Phi_{\text{bb}}^{\text{Eg}}} = \int_0^{\alpha_0 d} \gamma_{\text{bb}}(\xi)\delta\xi = a(\alpha_0 d). \quad (3.30)$$

Assuming a thick solar cell with $a(d) = 1$ for $E \geq E_g$ it holds $\Phi_{\text{em}}(V = 0) = \Phi_{\text{bb}}^{\text{Eg}}$.

Let us now take a look at the voltage dependence of the emission current. Shockley and Queisser simply assumed (cf. Eq. (2.11)) the exponential voltage dependence

$$\Phi_{\text{em}}(V) = \Phi_{\text{bb}}^{\text{Eg}} \exp\left(\frac{qV}{k_B T}\right). \quad (3.31)$$

They have also tacitly equated the saturation current J_0 with the emission flux $\Phi_{\text{em}}(V = 0) = \Phi_{\text{bb}}^{\text{Eg}}$. But this assumption would imply that in the radiative recombination limit

all diodes with the same band gap E_g would exhibit the same current/voltage characteristic in the dark regardless of their minority carrier mobility μ_n . As shown in Fig. 3.3 this is obviously not the case. But when the saturation current J_0 depends on the mobility how does this affect the emission flux without violating the equilibrium condition $\Phi_{\text{em}}(V=0) = \Phi_{\text{bb}}^{\text{Eg}}$? Furthermore, this equilibrium condition also has to hold in the case of additional non-radiative recombination.

Let us consider a diode in the dark to which we apply a certain voltage V which leads to the electrical recombination current $J_{\text{rec}} = J_{\text{rec}}^{\text{rad}} + J_{\text{rec}}^{\text{nr}}$ consisting of the radiative part $J_{\text{rec}}^{\text{rad}}$ and the non-radiative part $J_{\text{rec}}^{\text{nr}}$. To obtain the relation between emitted photon flux and injected electron current we balance all fluxes being injected or extracted from the cell. Balancing the recombination current with the absorbed black body photon current $\Phi_{\text{bb}}^{\text{abs}} = \Phi_{\text{bb}}^{\text{Eg}}$ and the emitted photon flux Φ_{em} leads to $J_{\text{el}}(V) = J_{\text{rec}}^{\text{rad}}(V) + J_{\text{rec}}^{\text{nr}}(V) = \Phi_{\text{bb}}^{\text{Eg}} - \Phi_{\text{em}}(V)$ ³.

Let us first assume completely immobile carriers, i.e. $\mu_{\text{norm}} = 0$. Then it is not possible to inject or extract carriers. In that case, there will not be an electric current, no matter how high the voltage is increased. Therefore, the emitted photon flux $\Phi_{\text{em}}(V) = \Phi_{\text{bb}}^{\text{Eg}}$ is independent of the applied voltage and equal to the flux of incoming black body radiation. Except for a voltage dependent delta peak at $\xi = 0$ caused by the boundary condition Eq. (2.17) the electron distribution is constant with $\nu(\xi) = 1$.

In the other extreme case with $\mu_{\text{norm}} \rightarrow \infty$ the electron distribution is also constant but voltage-dependent with $\nu(\xi) = \exp(qV/(k_B T))$. This electron distribution is associated with the highest possible splitting of the quasi-Fermi levels, i.e. the highest chemical potential of the emitted photons $\mu(\xi) = E_{\text{Fn}}(\xi) - E_{\text{Fp}}(\xi) = V$. For a given voltage and lifetime this implies that recombination and emission current are maximized for $\mu_{\text{norm}} \rightarrow \infty$.

In general, the saturation current $J_0 = J_0^{\text{rad}}(\mu_{\text{norm}}, \vartheta_r) + J_0^{\text{nr}}(\mu_{\text{norm}}, \vartheta_r)$, where J_0^{rad} is the radiative part and J_0^{nr} is the non-radiative part, is a function of the normalized mobility μ_{norm} and the ratio ϑ_r of radiative and non-radiative lifetime. Then the recombination current obeys the diode characteristic

$$J_{\text{rec}}(V) = -J_0(\mu_{\text{norm}}, \vartheta_r) \left(\exp\left(\frac{qV}{k_B T}\right) - 1 \right) \quad (3.32)$$

³Throughout this chapter I follow the convention that recombination currents are negative and photo currents J_{sc} are positive.

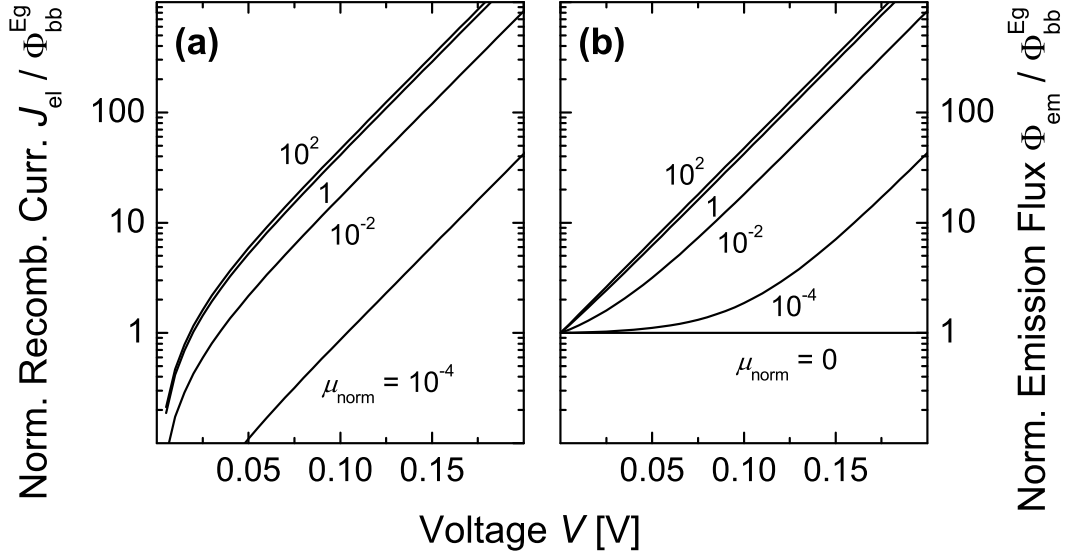


Fig. 3.7: Normalized recombination current (a) and emission flux (b) in the radiative recombination limit versus applied voltage V . The absorption coefficient is $\alpha = \alpha_0$, the normalized thickness is $\alpha_0 d = 10$, the band gap is $E_g = 1 \text{ eV}$, and the front surface is textured. All parameters are listed in Tab. 3.1. The saturation current J_0 increases with increasing normalized mobility μ_{norm} until it reaches the Shockley-Queisser limit $J_0^{\text{rad}} = J_0^{\text{SQ}} = \Phi_{\text{bb}}^{\text{Eg}}$ (a). The emission flux (b) consists of a superposition of a constant part $\Phi_{\text{bb}}^{\text{Eg}}$ plus an exponentially voltage-dependent part. In compliance with the detailed balance principle it holds $\Phi_{\text{em}}(V = 0) = \Phi_{\text{bb}}^{\text{Eg}}$ for all mobilities.

With $\Phi_{\text{em}}(V) = \Phi_{\text{bb}}^{\text{Eg}} - J_{\text{rec}}^{\text{rad}}(V) - J_{\text{rec}}^{\text{nr}}(V)$ we obtain the emission

$$\Phi_{\text{em}}(V) = (J_0^{\text{rad}}(\mu_{\text{norm}}, \vartheta_r) + J_0^{\text{nr}}(\mu_{\text{norm}}, \vartheta_r)) \left(\exp\left(\frac{qV}{k_B T}\right) - 1 \right) + \Phi_{\text{bb}}^{\text{Eg}}. \quad (3.33)$$

Figures 3.7a and b display the normalized recombination current $J_{\text{el}}(V)/\Phi_{\text{bb}}^{\text{Eg}}$ and the emission current $\Phi_{\text{em}}(V)/\Phi_{\text{bb}}^{\text{Eg}}$ versus the applied voltage in the radiative recombination limit with $\vartheta_r = 0$ for a textured cell (parameters see Tab. 3.1). The figures illustrate how the electrical recombination current and the emitted radiation are affected by the mobility μ_{norm} . For $V = 0$ the emission is always $\Phi_{\text{em}}(V = 0) = \Phi_{\text{bb}}^{\text{Eg}}$. While for $\mu_{\text{norm}} = 0$ it holds $J_{\text{rec}} = 0$ and $\Phi_{\text{em}} = \Phi_{\text{bb}}^{\text{Eg}}$, emission and recombination current

increase with increasing mobility until they approach the Shockley-Queisser limit $\Phi_{\text{em}} = \Phi_{\text{bb}}^{\text{Eg}} \exp(qV/(k_{\text{B}}T))$ where it holds $J_0 = J_0^{\text{rad}} = \Phi_{\text{em}}(V = 0) = \Phi_{\text{bb}}^{\text{Eg}}$. For sufficiently high voltages, the equilibrium fraction $\Phi_{\text{bb}}^{\text{Eg}}$ of the emission flux becomes negligible and emission flux and recombination current are equal.

3.5.4 Reciprocity between solar cell and light emitting diode

The radiative efficiency limit of a solar cell is based on the radiative interaction between the solar cell and its surroundings. While light emission is the reason for the upper limit of solar cells, it is also utilized in light emitting diodes (LEDs). Such LEDs are reciprocal devices to solar cells. Whereas the former convert electrical energy into optical energy, the latter convert optical energy into electrical energy.

However, the reciprocity between solar cells and LEDs does not automatically imply that both devices have the same material requirements in terms of lifetime and mobility. This section analyzes the relationship between solar cell and LED performance and points out the different material criteria to obtain high performance device.

Whereas the performance of a solar cell is measured by its power conversion efficiency, the performance of a light emitting diode is mostly not quantified in energy terms but in terms of the (external) quantum efficiency

$$\text{EQE}_{\text{LED}} = \frac{\Phi_{\text{em}}(V) - \Phi_{\text{bb}}^{\text{Eg}}}{J_{\text{el}}(V)}. \quad (3.34)$$

that states which part of the electrical current J_{el} is converted into the excess photon flux $\Phi_{\text{em}} - \Phi_{\text{bb}}^{\text{Eg}}$.

On page 58 in section 3.7, we will see that the quantum efficiency of a solar cell is linked to the emission flux (cmp. Eq. (3.55)). In Ref. [16], Rau shows that the LED quantum efficiency in turn is coupled to the open circuit voltage of a solar cell.

Under the assumption that radiative and non-radiative recombination current obey the same dependency on the applied voltage we rewrite Eq. (3.34) at $V = k_{\text{B}}T/q \ln(2)$ to obtain

$$\begin{aligned} \text{EQE}_{\text{LED}} &= \frac{J_0^{\text{rad}}}{J_0^{\text{rad}} + J_0^{\text{nr}}} = \frac{J_{\text{sc}}}{J_0^{\text{rad}} + J_0^{\text{nr}}} \times \frac{J_0^{\text{rad}}}{J_{\text{sc}}} \\ &= \exp\left(\frac{qV_{\text{oc}}}{k_{\text{B}}T}\right) \exp\left(\frac{-qV_{\text{oc}}^{\text{rad}}}{k_{\text{B}}T}\right) = \exp\left(\frac{q}{k_{\text{B}}T} (V_{\text{oc}} - V_{\text{oc}}^{\text{rad}})\right), \end{aligned} \quad (3.35)$$

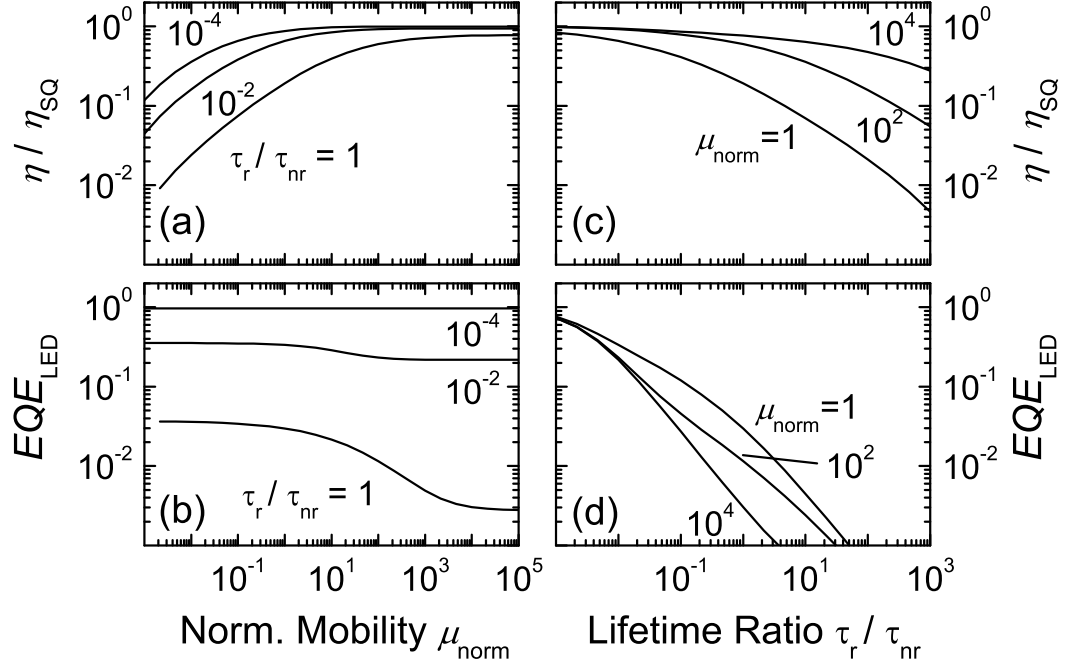


Fig. 3.8: Solar cell efficiency η/η_{SQ} (a, c) and LED quantum efficiency EQE_{LED} (b, d) versus the normalized mobility μ_{norm} (a, b) and the lifetime ratio τ_r of radiative and non-radiative lifetime (c, d). Whereas the decrease of the power conversion efficiency η caused by non-radiative recombination can be compensated by a sufficiently high mobility μ_{norm} , the quantum efficiency EQE_{LED} depends almost exclusively on the non-radiative carrier lifetime and is hardly influenced by the mobility. The absorption coefficient is $\alpha = \alpha_0$, the normalized thickness is $\alpha_0 d = 10$, the band gap is $E_g = 1$ eV, and the front surface is textured. All parameters are identical to the parameters used in Fig. 3.5.

where V_{oc}^{rad} is the open circuit voltage that would be achieved if the device were dominated by radiative recombination only. In a first order approximation, V_{oc}^{rad} is equal to V_{oc}^{SQ} . The relation Eq. (3.35) demonstrates that the LED quantum efficiency EQE_{LED} , i.e. the quality of an LED is coupled directly to the open circuit voltage of the device when acting as a solar cell. Therefore, the crucial material parameter to obtain a good quantum efficiency EQE_{LED} is - just as for the open circuit voltage V_{oc} - the lifetime ratio τ_r/τ_{nr} .

Figures 3.8a-d display the normalized solar cell efficiency η/η_{SQ} (a, c) and the LED quantum efficiency EQE_{LED} (b, d) vs. the normalized mobility μ_{norm} (a, b) and the lifetime ratio $\tau_{\text{r}}/\tau_{\text{nr}}$ (c, d). The figures clearly underline that the carrier mobility has only minor effects on the LED quantum efficiency. For a light emitting diode the relevant parameter is the carrier lifetime or more precisely the ratio ϑ_{r} of radiative and non-radiative lifetime. Comparison with Fig. 3.5c on page 34 points out the analogy of LED quantum efficiency and open circuit voltage. Both quantities are almost exclusively governed by the carrier lifetime.

These considerations show that the material requirements to obtain a good light emitting diode are not necessarily equivalent to the requirements necessary to obtain a good solar cell. Whereas for the LED a high lifetime is essential, the solar cell additionally needs a high carrier mobility (cf. section 3.6). In a solar cell it is not enough to prevent non-radiative recombination. One also has to ensure the transport of photo-generated minority carriers out of the cell.

3.6 Critical mobility

In section 3.4.1 we have seen that even in the radiative efficiency limit the power conversion efficiency strongly depends on carrier transport and drops sharply once the normalized carrier mobility μ_{norm} drops below a critical value μ_{crit} . This section derives an expression for this critical mobility. The critical mobility provides a means to assess the suitability of a material with respect to photovoltaic energy conversion. Moreover, it gives an estimate, whether the upper efficiency limit of a photovoltaic absorber material needs to be computed numerically (which is the case for $\mu < \mu_{\text{crit}}$) or whether the limit is given by the SQ limit corresponding to the material's band gap (for $\mu > \mu_{\text{crit}}$).

This section is structured in the following manner: I derive expressions for the radiative recombination current in the high mobility limit and in the low mobility limit. Then I define the critical mobility as the intersect between the resulting two limiting asymptotes. For very high mobilities on the one hand, the maximum radiative recombination current $J_0^{\text{rad}}(\mu_{\text{norm}} \rightarrow \infty)$ is given by the absorptance of the solar cell. For very low mobilities on the other hand, certain simplifications can be made that allow for an analytical solution of the integro-differential equation Eq. (3.3).

3.6.1 High mobility limit - absorptance

The maximal short circuit current that can be extracted from a solar cell for sufficiently high carrier mobility is given by the number of absorbed photons. The same holds true for the radiative recombination current with respect to the ambient black body irradiation. This section derives an expression for the absorptance $a(d)$ of a solar cell with energy-independent absorption coefficient $\alpha(E) = \alpha_0$ for $E \geq E_g$ and thickness d . Then the average absorptance is identical for solar and black body irradiation and for $\mu_{\text{norm}} \rightarrow \infty$ it holds $J_0^{\text{rad}}/\Phi_{\text{bb}}^{\text{Eg}} = J_{\text{sc}}/J_{\text{sc}}^{\text{SQ}} = a(d)$.⁴

3.6.1.1 Textured front surface

Let us consider the photon fluxes at the cell's front surface in Fig.B.3. Since the textured surface leads to a complete randomization, the angle at which the incident irradiation impinges on the cell becomes irrelevant and, thus, the absorptance is identical for solar and black body irradiation.⁵ With $\varrho_b = 1$, there is no light transmission through the sample and the absorptance $a(d)$ is simply determined by the total reflectance of the cell according to

$$a(d) = 1 - \varrho_f - \frac{t_{\text{lamb}} \Phi_{\text{ref}}^{\text{lamb}}}{\Phi_{\text{bb}}^{\text{Eg}} + \Phi_{\text{sun}}^{\text{Eg}}} = 1 - \varrho_f - \frac{t_{\text{lamb}} t_{\text{cell}} \Phi_{\text{em}}^{\text{lamb}}}{\Phi_{\text{bb}}^{\text{Eg}} + \Phi_{\text{sun}}^{\text{Eg}}}, \quad (3.36)$$

where I used $\Phi_{\text{ref}}^{\text{lamb}} = t_{\text{cell}} \Phi_{\text{em}}^{\text{lamb}}$. With help of $t_{\text{lamb}} = (1 - \varrho_f)/\bar{n}^2$ from Eq. (B.30) and $\Phi_{\text{em}}^{\text{lamb}}$ from Eq. (B.40) plus Eq. (B.42) this yields

$$a(d) = \frac{(1 - \varrho_f)(1 - t_{\text{cell}})}{1 - t_{\text{cell}} + \frac{(1 - \varrho_f)}{\bar{n}^2} t_{\text{cell}}} = \frac{(1 - \varrho_f)(1/t_{\text{cell}} - 1)\bar{n}^2}{(1/t_{\text{cell}} - 1)\bar{n}^2 + 1 - \varrho_f}. \quad (3.37)$$

Figure 3.9b depicts the term $1/t_{\text{cell}} - 1$ with the transmission probability $t_{\text{cell}} = 2\text{Ei}_3(2\alpha_0 d, 0)$ according to Eq. (B.31) vs. the cell thickness $\alpha_0 d$. For $\alpha_0 d < 0.1$, this expression can be approximated linearly by $1/t_{\text{cell}} - 1 \approx 4\alpha_0 d$. For larger thicknesses $\alpha_0 d > 0.1$, the expression $1/t_{\text{cell}} - 1$ cancels out in Eq. (3.37). Therefore, the given approximation holds for all thicknesses and we obtain the simplified relation

$$a(d) \approx \frac{(1 - \varrho_f) 4\alpha_0 d \bar{n}^2}{4\alpha_0 d \bar{n}^2 + (1 - \varrho_f)} = \frac{(1 - \varrho_f) d}{d + d_{\text{crit}}}. \quad (3.38)$$

⁴Due to the different angular distributions of the two spectra, this is not entirely true for a cell with a plane front surface

⁵This holds only at a given energy when the absorption coefficient is energy-dependent.

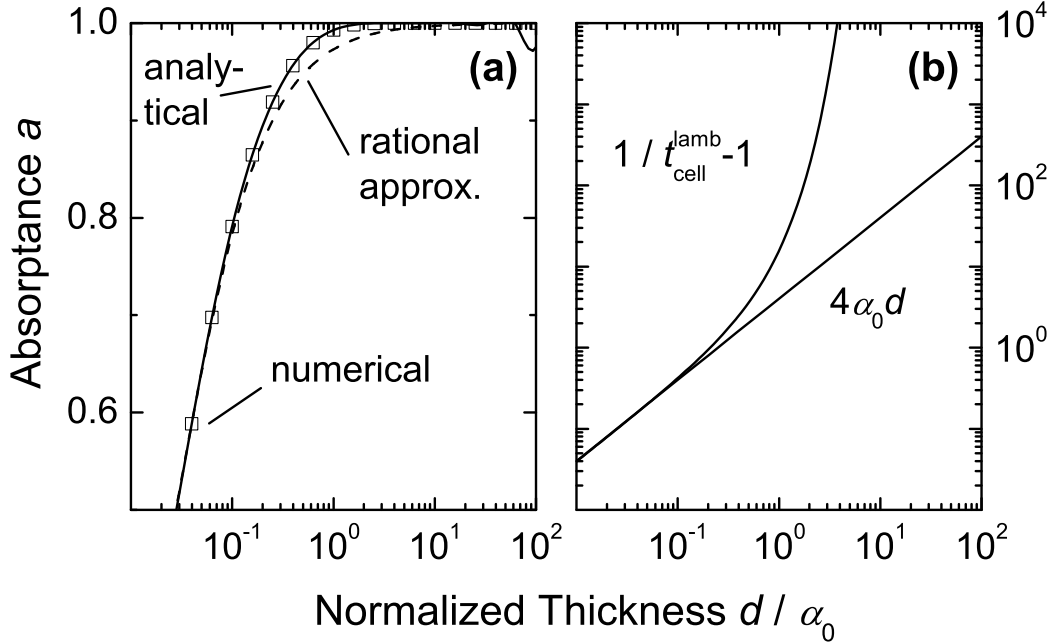


Fig. 3.9: a) Absorptance vs. cell thickness for a textured solar cell with energy-independent absorption coefficient. The band gap is $E_g = 1$ eV, all other parameters are listed in Tab. 3.1. The numerical results (open squares) are identical to the exact solution Eq. (3.37) (solid line) which is approximated by the rational function Eq. (3.38) (dashed line). b) Functions underlying the approximation in a). Below a thickness $\alpha_0 d \approx 0.1$ both functions $1/t_{\text{cell}} - 1$ and $4\alpha_0 d$ are identical.

This expression is identical to the one derived in Ref. [14]. Here, the critical thickness

$$d_{\text{crit}} = \frac{(1 - \varrho_f)}{4\alpha_0 \bar{n}^2} \quad (3.39)$$

is defined as the thickness at which it holds $a(d) = 0.5(1 - \varrho_f)$.

Figure 3.9a depicts the absorptance vs. the sample thickness for the constant absorption coefficient $\alpha = \alpha_0$ and $\varrho_f = 0$. The absorptance is unity for large sample thicknesses but drops sharply for $d < d_{\text{crit}}$.

3.6.1.2 Plane front surface

For a plane front surface the absorptance differs slightly for solar irradiation with normal incidence and black body irradiation with spherical incidence. For normal incidence and with $\varrho_b = 1$ the absorptance reads as

$$a(d) = (1 - \varrho_f) \frac{1 - \exp(-2\alpha_0 d)}{1 - \varrho_f \exp(-2\alpha_0 d)}, \quad (3.40)$$

where ϱ_f is the reflection coefficient of the front surface. From $a(d_{\text{crit}}) = 0.5(1 - \varrho_f)$ we obtain the critical thickness

$$d_{\text{crit}} = \frac{\ln(2 - \varrho_f)}{2\alpha_0}. \quad (3.41)$$

Figure 3.10 compares the absorptance of a solar cell with textured front surface and plane front surface. There is no direct reflection at the front surface, i.e. it holds $\varrho_f = 0$. All other parameters are listed in Tab. 3.1. Numerical simulation results are depicted as solid squares for the textured and open squares for the plane front surface. Also displayed are the analytical expressions Eq. (3.38) (solid line) and Eq. (3.40) (dashed line).

By texturing the front surface, the critical thickness below which incomplete absorption occurs is more than ten times lower than in a sample with plane surface. This effect stems from two causes. Firstly, the incident light is diffracted and traverses the sample at an angle, thus experiencing a longer passage than light with normal incidence on a plane surface. Secondly, rays are internally reflected at the front surface with the increased internal reflection coefficient $1 - t_{\text{lamb}} = 1 - (1 - \varrho_f)/\bar{n}^2$. Especially for $\varrho_f = 0$ light rays with normal incidence only traverse the cell twice in cells with plane front surface. In a textured cell, however, the reflection at the front surface with $1 - t_{\text{lamb}} = 1 - 1/\bar{n}^2 = 0.88$ (for $\bar{n} = 3$) leads to efficient light trapping within the sample.

3.6.2 Low mobility limit

In this section I analyze the radiative recombination current in the limit $\mu_{\text{norm}} \rightarrow 0$. I begin with a recapitulation of the non-radiative recombination current from the classical diode theory to emphasize the analogies between non-radiative and radiative recombination.

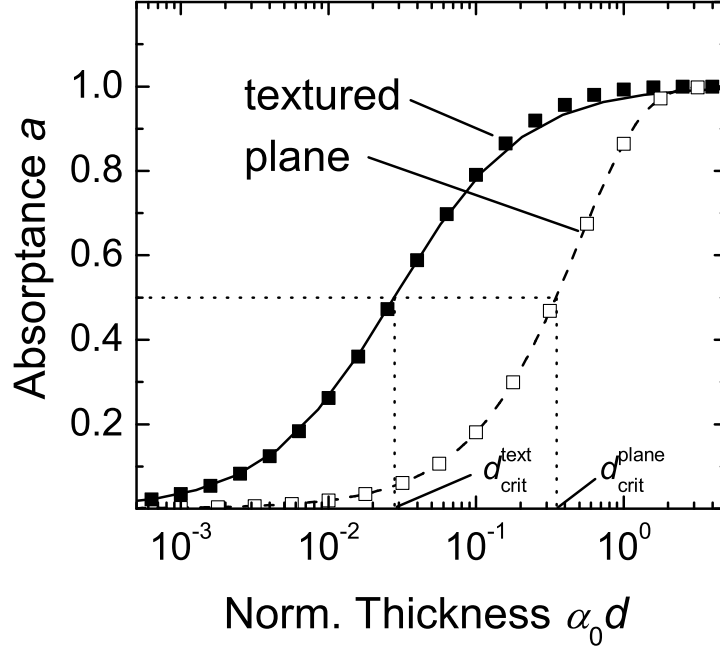


Fig. 3.10: Absorbance of a solar cell with textured (solid squares, solid line) and plane front surface (open squares, dashed line). The absorption coefficient is $\alpha = \alpha_0$ and the band gap is $E_g = 1$ eV. The reflection coefficient is $\varrho_f = 0$, all other parameters are listed in Tab. 3.1. Squares represent numerical simulation results and lines are the analytical expressions Eq.(3.38) (solid line) and Eq.(3.40) (dashed line). The fact that the critical thickness at which it holds $a(d_{\text{crit}}) = 0.5$ is more than ten times larger for a plane than for a textured front surface underlines the importance of Lambertian light trapping for thin solar cells.

3.6.2.1 Non-radiative recombination

For a real solar cell far from the radiative efficiency limit, the non-radiative recombination current is given by Eq.(2.20). Normalized, this equation turns into

$$\frac{J_0^{\text{nr}}}{\Phi_{\text{bb}}^{\text{Eg}}} = \sqrt{\frac{\mu_{\text{norm}}}{\tau_{\text{norm}}^{\text{nr}}}} \tanh\left(\frac{\alpha_0 d}{\sqrt{\mu_{\text{norm}} \tau_{\text{norm}}^{\text{nr}}}}\right), \quad (3.42)$$

where the normalized mobility and non-radiative lifetime are given by $\mu_{\text{norm}} = k_B T \alpha_0 n_0 \mu_n / (q \Phi_{\text{bb}}^{\text{Eg}})$ (cmp. Eq.(3.4) and Eq.(3.5)) and $\tau_{\text{norm}}^{\text{nr}} = \alpha_0 \Phi_{\text{bb}}^{\text{Eg}} \tau_{\text{nr}} / n_0$ (cmp. Eq.(3.6)). To analyze the influence of the carrier mobility μ_{norm} , we shall consider the limiting

cases $\mu_{\text{norm}} \rightarrow \infty$ and $\mu_{\text{norm}} \rightarrow 0$. For $\mu_{\text{norm}} \rightarrow \infty$ and with help of $\tanh(x) \approx x$ for $|x| \rightarrow 0$, Eq. (3.42) turns into

$$\lim_{\mu_{\text{norm}} \rightarrow \infty} \frac{J_0^{\text{nr}}}{\Phi_{\text{bb}}^{\text{Eg}}} = \sqrt{\frac{\mu_{\text{norm}}}{\tau_{\text{norm}}^{\text{nr}}}} \frac{\alpha_0 d}{\sqrt{\mu_{\text{norm}} \tau_{\text{norm}}^{\text{nr}}}} = \frac{\alpha_0 d}{\tau_{\text{norm}}^{\text{nr}}}. \quad (3.43)$$

For $\mu_{\text{norm}} \rightarrow 0$ and with help of $\tanh(x) \rightarrow 1$ for $x \rightarrow \infty$ it holds

$$\lim_{\mu_{\text{norm}} \rightarrow 0} \frac{J_0^{\text{nr}}}{\Phi_{\text{bb}}^{\text{Eg}}} = \sqrt{\frac{\mu_{\text{norm}}}{\tau_{\text{norm}}^{\text{nr}}}}. \quad (3.44)$$

3.6.2.2 Radiative recombination

As mentioned in section 3.6.1, the maximum radiative saturation current, which is reached for $\mu_{\text{norm}} \rightarrow \infty$, is given by the absorptance. In the following, I derive an expression for the limit $\mu_{\text{norm}} \rightarrow 0$. For the sake of simplicity, I restrict the derivation to the case of an energy-independent absorption coefficient $\alpha(E) = \alpha_0$ for $E \geq E_g$.

To obtain the radiative saturation current, we have to solve the integro differential equation (3.3) in the dark with the boundary condition $\nu(\xi = 0) = 2$. For short diffusion lengths, the electron distribution will decay towards $\nu(\xi) = 1$ deep in the bulk. If the diffusion length, i.e. if the normalized mobility is small enough the decay is so steep that we can approximate $\nu(\xi_r)$ in the internal generation rate by $\nu(\xi) \approx 1$.

With this approximation the internal generation rate from Eq. (3.13) reads as

$$\gamma_{\text{int}}(\xi) = \frac{1}{\tau_{\text{norm}}^{\text{r}}} \int_0^{\alpha_0 d} \nu(\xi) f_{\text{r}}(\xi, \xi_r) d\xi_r \approx \frac{1}{\tau_{\text{norm}}^{\text{r}}} \int_0^{\alpha_0 d} f_{\text{r}}(\xi, \xi_r) d\xi_r. \quad (3.45)$$

The integral of the radiative interaction function $f_{\text{r}}(\xi, \xi_r)$ is obtained from the equilibrium situation as described in section 3.5.1.2. In thermodynamic equilibrium it holds $\nu(\xi) = 1$ for all ξ (the applied voltage is $V = 0$). Then the integro-differential equation Eq. (3.3) simplifies to Eq. (3.17) and we obtain Eq. (3.18), which slightly rearranged reads as

$$\gamma_{\text{int}}(\xi) = \frac{1}{\tau_{\text{norm}}^{\text{r}}} \int_0^{\alpha_0 d} f_{\text{r}}(\xi, \xi_r) d\xi_r = -\gamma_{\text{bb}}(\xi) + \frac{1}{\tau_{\text{norm}}^{\text{r}}}. \quad (3.46)$$

Therewith, we obtain the low mobility limit of the integro-differential equation Eq. (3.3) in the dark with applied voltage $V = (k_{\text{B}}T/q)\ln(2)$ (boundary condition

$\nu(\xi = 0) = 2$) as the ordinary differential equation

$$\mu_{\text{norm}} \frac{d^2 \nu}{d\xi^2} - \frac{\nu}{\tau_{\text{norm}}^r} = -\gamma_{\text{bb}}(\xi) - \gamma_{\text{int}}(\xi) \approx -\frac{1}{\tau_{\text{norm}}^r}. \quad (3.47)$$

Using $\delta\nu = \nu - 1$, this becomes the simple homogeneous differential equation

$$\mu_{\text{norm}} \frac{d^2 \delta\nu}{d\xi^2} - \frac{\delta\nu}{\tau_{\text{norm}}^r} = 0, \quad (3.48)$$

which together with the boundary conditions $\delta\nu(\xi = 0) = 1$ and $d\delta\nu/d\xi|_{\xi=\alpha_0 d} = 0$ leads to

$$\lim_{\mu_{\text{norm}} \rightarrow 0} \frac{J_0^{\text{rad}}}{\Phi_{\text{bb}}^{\text{Eg}}} = \sqrt{\frac{\mu_{\text{norm}}}{\tau_{\text{norm}}^r}} \tanh\left(\frac{\alpha_0 d}{\sqrt{\mu_{\text{norm}} \tau_{\text{norm}}^r}}\right). \quad (3.49)$$

This result is identical to the non-radiative recombination current Eq. (3.42) with only the lifetime replaced by the radiative lifetime $\tau_{\text{norm}}^r = 1/(4\bar{n}^2)$. Keeping in mind that this result is only valid in the low mobility limit, we simplify further to obtain

$$\lim_{\mu_{\text{norm}} \rightarrow 0} \frac{J_0^{\text{rad}}}{\Phi_{\text{bb}}^{\text{Eg}}} = \sqrt{\frac{\mu_{\text{norm}}}{\tau_{\text{norm}}^r}} = 2\bar{n}\sqrt{\mu_{\text{norm}}}. \quad (3.50)$$

3.6.3 Critical mobility in the radiative recombination limit

The previous two sections have provided analytical expressions for the radiative recombination current in the high and in the low mobility limit. Since in the radiative recombination limit the short circuit current and the saturation current normalized to their respective maximum values are identical (cf. section 3.4.1), these expressions hold for the short circuit current as well.

Figure 3.11a displays the normalized short circuit current versus the normalized mobility for a cell with textured front surface. The intersect of the low mobility limit $J_{\text{sc}}/J_{\text{sc}}^{\text{SQ}} \rightarrow 2\bar{n}\sqrt{\mu_{\text{norm}}} = 2\bar{n}\sqrt{\mu_{\text{n}}/\mu_{\text{ref}}}$ and the high mobility limit $J_{\text{sc}}/J_{\text{sc}}^{\text{SQ}} \rightarrow a(d)$ defines the critical mobility

$$\mu_{\text{crit}}^{\text{rad}} = \frac{\mu_{\text{ref}}}{4\bar{n}^2} a^2(d) = \frac{q\Phi_{\text{bb}}^{\text{Eg}} N_{\text{A}}}{4\bar{n}^2 k_{\text{B}} T \alpha_0 n_{\text{i}}^2} a^2(d). \quad (3.51)$$

If the minority carrier mobility drops below the critical mobility μ_{crit} the short circuit current and therewith the efficiency drops drastically. Materials with lower mobility

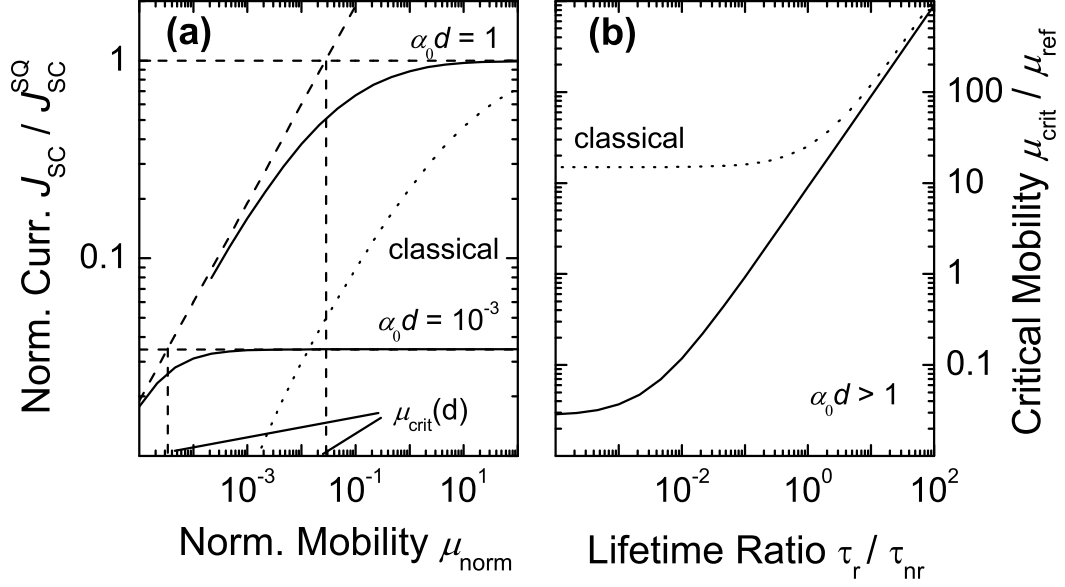


Fig. 3.11: a) Normalized short circuit current in the radiative recombination limit vs. normalized mobility for different absorber thicknesses $\alpha_0 d = 10^{-3}$ and $\alpha_0 d = 1$. The intersect of low mobility limit and high mobility limit, i.e. absorptance, defines the critical mobility μ_{crit} . b) Critical mobility vs. lifetime ratio τ_r for thick solar cells with $\alpha_0 d > 1$, for which the critical mobility is given by Eq. (3.53). For comparison, Fig. a) also displays the normalized short circuit current calculated with the classical diode theory (dotted line, cf. section 3.4.2). As Fig. b) shows, the radiative critical mobility obtained from the classical solution is by a factor of 550 too large. The absorption coefficient is $\alpha = \alpha_0$, the band gap is $E_g = 1$ eV, and the front surface is textured. All parameters are taken from Tab. 3.1.

than the critical mobility μ_{crit}^{rad} in the radiative limit are not suited as photovoltaic absorber material without current-enhancing device features such as built-in electric fields.

For comparison, Fig. 3.11a also displays the short circuit current that would be obtained from a computation based on the classical diode theory, i.e. based on the solution of Eq. (3.1) without the internal generation rate G_{int} . Figure 3.11b clearly conveys the impact of the photon recycling in the radiative limit. The radiative critical

mobility in the classical case is 550 times larger than $\mu_{\text{crit}}^{\text{rad}}$ from Eq. (3.51).

3.6.4 Critical mobility for non-radiative recombination

Section 3.7.3 will derive the low mobility limit for the general case. From this limit as expressed by Eq. (3.61), we derive the general critical mobility

$$\mu_{\text{crit}} = \frac{\mu_{\text{ref}}}{\tau_{\text{norm}}} \left(\frac{a(d)J_{\text{sc}}^{\text{SQ}}/k_{\alpha}}{F_0 + F_{\text{r}}\exp(-2k_{\alpha}\alpha_0 d)} \right)^2. \quad (3.52)$$

The normalized lifetime τ_{norm} and the parameters F_0 , F_{r} , and k_{α} are defined by the modified lifetime model in section 3.7.3. With increasing non-radiative recombination, i.e. with decreasing τ_{norm} , the critical mobility is increased linearly. A lower lifetime has to be compensated by a higher mobility in order to maintain sufficient carrier collection. While in the classical limit, only the diffusion length, i.e. the product of lifetime and mobility, determines the short circuit current, the situation changes when coming closer to the radiative limit, where J_{sc} is proportional to the ratio $\sqrt{\mu_{\text{norm}}/\tau_{\text{norm}}^{\text{r}}}$. This shift will be discussed during the analytical approximation in the next section.

For thick solar cells with $\alpha_0 d > 1$ reflections at the back side can be neglected. It follows $a = 1$, $F_0 = J_{\text{sc}}^{\text{SQ}}$, $F_{\text{r}} = 0$, and $k_{\alpha} = 2$ (for a Lambertian front surface). Therewith, Eq. (3.52) simplifies to

$$\mu_{\text{crit}} = \mu_{\text{ref}} \left(\frac{1}{4\bar{n}^2} + \bar{n}^2\vartheta_{\text{r}} \right) = \mu_{\text{crit}}^{\text{rad}} + \mu_{\text{ref}}\bar{n}^2\vartheta_{\text{r}}. \quad (3.53)$$

This dependence of the critical mobility on the ratio ϑ_{r} of radiative and non-radiative lifetime is illustrated in Fig. 3.11b. The critical mobility approaches its radiative limit $\mu_{\text{crit}}^{\text{rad}}$ for $\vartheta_{\text{r}} \leq 10^{-3}$. For increasing non-radiative recombination, where the diffusion length, i. e. the product of lifetime and mobility, is the crucial factor for the collection of carriers, μ_{crit} is proportional to ϑ_{r} .

3.7 Analytical approximation

The objective of this section is to provide an analytical approach that is capable of computing the efficiency of solar cells over the whole lifetime range. As the previous sections have shown, the rigorous treatment of the photon recycling leads to a rather complicated model that can only be solved numerically. For a simpler applicability and

also to understand the fundamental consequences of the PR, it would be desirable to have a simple analytical model that approximates the numerical results. Moreover, such a model can also serve as a test to verify the validity of the numerical computations.

Let me proleptically anticipate the results: To my knowledge, there is no consistent classical approach that is capable of correctly reproducing the dependence of both, short circuit current and saturation current on the mobility in the radiative recombination limit. The reason for this lies in an inherent contradiction:

As we have seen in section 3.4.1, J_0 and J_{sc} feature an identical dependence on the mobility in the radiative recombination limit. This is because the radiative recombination current J_0^{rad} is linked to the emission flux Φ_{em} at $V = (k_B T/q) \ln(2)$ via the flux balance $J_0^{\text{rad}} = \Phi_{\text{em}} - \Phi_{\text{bb}}^{\text{Eg}}$ and the emission flux in turn is linked to the short circuit current via a reciprocity relation [16].

The short circuit current can be written as

$$J_{sc} = \text{EQE} \Phi_{\text{sun}}^{\text{Eg}}, \quad (3.54)$$

where EQE is the external quantum efficiency, i.e. the percentage of the impinging photons that contributes to the short circuit current.⁶

From the reciprocity theorem derived by Rau [16] it follows for the excess emission flux

$$\Phi_{\text{em}} - \Phi_{\text{bb}}^{\text{Eg}} = J_0^{\text{rad}} = \text{EQE} \Phi_{\text{bb}}^{\text{Eg}}. \quad (3.55)$$

Since these two equations are valid for all mobilities, it is obvious that J_{sc} and J_0^{rad} have to obey the same dependence on the mobility.

The situation changes when non-radiative recombination becomes dominant. Then, $J_0 = J_0^{\text{rad}} + J_0^{\text{nr}}$ is no longer linked directly to the emission current, but depends also on non-radiative recombination.

To illustrate the resulting dependence on the mobility, let us look at the low mobility limit: The saturation current is given by

$$J_0 / \Phi_{\text{bb}}^{\text{Eg}} = \sqrt{\mu_{\text{norm}} / \tau_{\text{norm}}} \quad (3.56)$$

(cmp. Eq. (3.44)), but as will be shown below, the low mobility limit of the short circuit current is given by

$$J_{sc} / J_{sc}^{\text{SQ}} = \sqrt{\mu_{\text{norm}} \tau_{\text{norm}}} \quad (3.57)$$

⁶For a constant absorption coefficient $\alpha(E) = \alpha_0$, EQE(E) is constant for all energies $E \geq E_g$.

(cmp. Eq. (3.61)).

These reciprocity considerations for the low mobility limit underline the impossibility to reproduce all effects of the photon recycling with one consistent model that is based on the classical approach. Therefore, in the next sections I present two separate models to compute J_0 and J_{sc} .

Before doing so, I review the attempts to introduce analytical approximations of the photon recycling effect in the literature. Then I introduce a two-layer model that captures the fundamental effect of the PR, namely that deep in the volume of the solar cell, there is no limitation induced by radiative recombination because all photons are recycled. This model provides a surprisingly accurate approximation for the saturation current. However, as pointed out above, the short circuit current is not reproduced by this model as accurately as desired. Therefore, I derive the short circuit current from a phenomenological extension of the classical diode theory. Subsequently, I discuss the quality of the approximations.

3.7.1 Analytical approximations in the literature

From the very discovery of the photon recycling effect, there have been several suggestions for analytical approximations of the relatively complex formulation of the problem. Probably the most well-known ansatz consists of the lifetime enhancement factor introduced by Asbeck in 1977 [28]. Asbeck calculates the fraction $F_e(d, \bar{n})$ of the emitted photons that are reabsorbed in the solar cell. Neglecting carrier diffusion he assumes that in steady state, i.e. under open circuit conditions, the minority carrier concentration is constant throughout the sample. The lifetime is then given by

$$\frac{1}{\tau_{\text{eff}}} = \frac{1}{\tau_{\text{nr}}} + \frac{1 - F_e(d, \bar{n})}{\tau_r}. \quad (3.58)$$

This implies that of all photons from radiative recombination only the fraction $1 - F_e(d, \bar{n})$ which is emitted from the cell contributes to the limitation of the lifetime. Therefore, the radiative lifetime is effectively enhanced by the lifetime multiplication factor $1/(1 - F_e)$.

This approach has found ample use to describe the lifetimes and internal quantum efficiencies extracted from photoluminescence measurements [58–63]. For these steady state measurements, it is well suited. However, it is questionable, what the obtained lifetimes tell us about the photovoltaic performance of the devices. Obviously, the

lifetime can be applied to the open circuit case to compute the open circuit voltage V_{oc} . However, it is not suited to describe the non-steady-state case including the diffusion of carriers as has been attempted by Kerr et al. [64].

For the non-steady-state situation, besides carrier recombination, one needs to consider carrier transport. Dumke pointed out the influence of photon recycling on the diffusion constant already in 1957 [19]. He derived a diffusion constant

$$D_{\text{eff}} = D_n + \frac{1}{3\tau_r\alpha^2}. \quad (3.59)$$

Similar or slightly modified expressions have also been found by other authors who approximated the PR term in the diffusion equation by using Taylor expansions or by using other methods such as variational or perturbational methods [39–41, 44, 46, 48, 65]. However, Eq. (3.59) is only valid under certain conditions, for instance, $\alpha L_n > 1$.

These more sophisticated approaches tried to convert the integro-differential Eq. (3.1) with PR into a quasi-classical diffusion equation with modified lifetimes and diffusion constants. As it turns out, such a quasi-classical diffusion equation can indeed be derived. Both, lifetime and diffusion constant are, however, functions of the applied bias voltage V and of the spatial coordinate x [46, 49, 50, 53, 57].

Therewith, the derived quasi-classical diffusion equation can not be solved analytically. Just as the initial integro-differential equation 3.1, a numerical scheme is required for the solution of the problem.

Rossin and Sidorov [45, 66] proposed an analytical solution for the transport equation under short circuit conditions, but had to use multiple assumptions that restrict the applicability of the approximation to only a handful of special cases.

Von Roos [47] addressed the influence of photon recycling on the saturation current. While he derived a relatively simple expression, his approach suffers from not accounting for the external detailed balance principle. Therefore, his approach obviously yields erroneous results when coming close to the radiative recombination limit, i.e. when PR effects start to matter in the first place.

Summing up, there are no analytical models available that are capable of computing the current/voltage characteristics of solar cells in the complete lifetime and mobility range. The following sections try to fill this gap.

3.7.2 Two-layer model

The two-layer model is based on the following considerations: Deep in the bulk of the solar cell, all photons emitted from radiatively recombining electron/hole-pairs are reabsorbed. Therefore, there exists no such thing as a loss mechanism inflicted by radiative recombination. The radiative lifetime is infinity.

Close, i.e. within one absorption length to the front surface, however, internally emitted photons can actually leave the cell via external emission through the front surface. These emitted photons are irretrievably lost to the system.

The idea of the two-layer model is to approximate the exponential emission characteristic by a discrete approach. I divide the absorber into two regions as illustrated in Fig. 3.12. In region 1 close to the front surface, all radiatively recombining electrons are assumed to be lost to the system, photon recycling does not exist (0 % PR). In region 2 in the bulk, all photons are completely recycled thereby completely compensating radiative recombination (100 % PR). In terms of the radiative lifetime this implies the 'standard' radiative lifetime $\tau_{\text{norm}}^r = 1/(4\bar{n}^2)$ in region 1 and an infinite radiative lifetime in region 2.

With these assumptions, I arrive at a classical treatment that solves the diffusion equation in both layers and in conjunction with the boundary conditions at the interface between the two regions leads to an analytical solution for the electron concentration and the resulting electrical current. The mathematical derivation of the two-layer model is given in appendix C.

As will be shown in section 3.7.4, the saturation current computed with the current two-layer approach is a surprisingly accurate approximation of the numerical results from the 'exact' PR treatment. However, as it turns out, the approximation of the short circuit current lacks the desired accuracy. Therefore, I will introduce a phenomenological approach in section 3.7.3 that yields an approximation of the short circuit current from a modified classical approach with a rather simple substitution of the radiative lifetime.

3.7.3 Modified-lifetime model

The goal of this section is to provide an approximation of the photon recycling effect on the short circuit current by slightly modifying the classical approach without PR. This

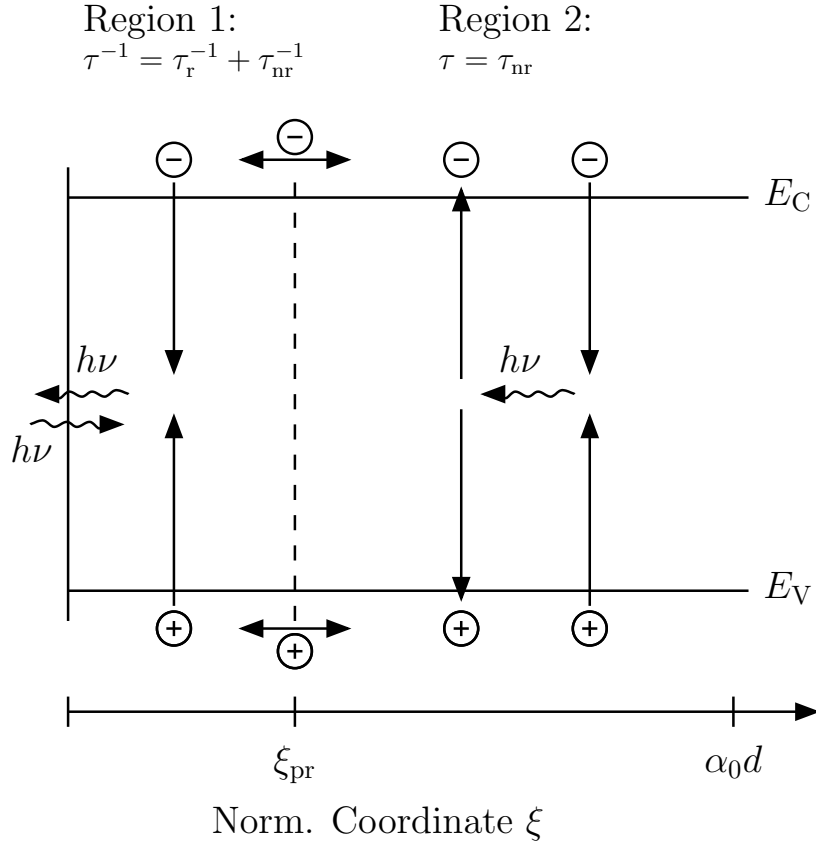


Fig. 3.12: Two-layer model of the solar cell. The solar cell is divided into a top layer (region 1) and a bottom layer. In region 1 with $0 \leq \xi \leq \xi_{pr}$, there is no photon recycling at all, all photons emitted by radiative recombination leave the cell through the front surface, it holds $\tau^{-1} = \tau_r^{-1} + \tau_{nr}^{-1}$. In region 2 with $\xi_{pr} \leq \xi \leq \alpha_0 d$, all photons emitted by radiative recombination are completely recycled, it holds $\tau = \tau_{nr}$.

approach will not reproduce the saturation current correctly, let alone fulfill detailed balance requirements. It is, however, capable of reproducing the short circuit current more precisely than the two-layer approximation. The idea of this approach is to analyze the effect of the PR on J_{sc} in the radiative limit and then modify the classical approach in such a way that the same radiative limit is obtained.

In the high mobility limit, all generated excess carriers are collected and both, PR treatment as well as classical diode treatment result in the same limit of unity for the short circuit current J_{sc} normalized to the maximum current J_{sc}^{SQ} .

From section 3.6.2 we know that in the radiative limit the low mobility limit of short circuit and radiative saturation current is given by $\sqrt{\mu_{norm}/\tau_{norm}^r} = 2\bar{n}\sqrt{\mu_{norm}}$ (cf. Eq. (3.50)). In the following, I recapitulate the low mobility limit predicted by

the classical diode theory and subsequently present a modification of the lifetime that ensures the accordance with the radiative limit.

The classical one-layer treatment as presented in section 2.4 with g_{sun} according to Eq. (C.2) results in the same differential equation as Eq. (C.3) extended over the whole absorber thickness. The short circuit current then reads as

$$\frac{J_{\text{sc}}}{J_{\text{sc}}^{\text{SQ}}} = \frac{k_{\alpha}^2 L_{\text{norm}}^2}{1 - k_{\alpha}^2 L_{\text{norm}}^2} \left\{ \frac{F_0}{J_{\text{sc}}^{\text{SQ}}} \left(-1 + \frac{\tanh\left(\frac{\alpha_0 d}{L_{\text{norm}}}\right)}{k_{\alpha} L_{\text{norm}}} + \frac{\exp(-k_{\alpha} \alpha_0 d)}{\cosh\left(\frac{\alpha_0 d}{L_{\text{norm}}}\right)} \right) + \frac{F_r}{J_{\text{sc}}^{\text{SQ}}} \exp(-2k_{\alpha} \alpha_0 d) \left(-1 + \frac{\tanh\left(\frac{\alpha_0 d}{L_{\text{norm}}}\right)}{k_{\alpha} L_{\text{norm}}} - \frac{\exp(k_{\alpha} \alpha_0 d)}{\cosh\left(\frac{\alpha_0 d}{L_{\text{norm}}}\right)} \right) \right\}. \quad (3.60)$$

For $\mu_{\text{norm}} \rightarrow 0$ it holds

$$\lim_{\mu_{\text{norm}} \rightarrow 0} \frac{J_{\text{sc}}}{J_{\text{sc}}^{\text{SQ}}} = k_{\alpha} L_{\text{norm}} \frac{F_0 + F_r \exp(-2k_{\alpha} \alpha_0 d)}{J_{\text{sc}}^{\text{SQ}}}. \quad (3.61)$$

With $L_{\text{norm}} = \sqrt{\mu_{\text{norm}} \tau_{\text{norm}}}$ it is clear that in the radiative limit the low mobility limit Eq. (3.61) is not identical to the low mobility limit $\sqrt{\mu_{\text{norm}} / \tau_{\text{norm}}^r}$. However, we can force such an agreement by modifying the radiative lifetime in Eq. (3.61) such that $L_{\text{norm}} = \sqrt{\mu_{\text{norm}} \tau_{\text{norm}}^{\text{r,mod}}}$. Equating Eq. (3.61) with $\sqrt{\mu_{\text{norm}} / \tau_{\text{norm}}^r} = 2\bar{n} \sqrt{\mu_{\text{norm}}}$ in the radiative limit $\tau_{\text{nr}} \rightarrow \infty$ yields the modified radiative lifetime

$$\tau_{\text{norm}}^{\text{r,mod}} = 4\bar{n}^2 \left(\frac{J_{\text{sc}}^{\text{SQ}} / k_{\alpha}}{F_0 + F_r \exp(-2k_{\alpha} \alpha_0 d)} \right)^2 = \frac{1}{\tau_{\text{norm}}^r} \left(\frac{J_{\text{sc}}^{\text{SQ}} / k_{\alpha}}{F_0 + F_r \exp(-2k_{\alpha} \alpha_0 d)} \right)^2. \quad (3.62)$$

For a thick solar cell with $\alpha_0 d \gg 1$ it holds $F_r \approx 0$, and $F_0 \approx J_{\text{sc}}^{\text{SQ}}$. Due to the refraction of light at the textured front surface, we obtain $k_{\alpha} = 2$ for a textured solar cell and $k_{\alpha} = 1$ for a plane solar cell. Therewith, the modified lifetime becomes $\tau_{\text{norm}}^{\text{r,mod}} \approx 1/(4\tau_{\text{norm}}^r) = \bar{n}^2$ for a textured cell and $\tau_{\text{norm}}^{\text{r,mod}} \approx 1/\tau_{\text{norm}}^r = 4\bar{n}^2$ for a plane solar cell. This means that the modified radiative lifetime is increased by an enhancement factor of $4\bar{n}^4 \approx 320$ or $16\bar{n}^4 \approx 1300$ when compared to the radiative lifetime τ_{norm}^r .

The total normalized lifetime of the modified approach is then given by

$$\frac{1}{\tau_{\text{norm}}^{\text{mod}}} = \frac{1}{\tau_{\text{norm}}^{\text{nr}}} + \frac{1}{\tau_{\text{norm}}^{\text{r,mod}}}. \quad (3.63)$$

3.7.3.1 Critical diffusion length

The purpose of this section is to interpret the critical mobility in terms of a critical diffusion length. For the classical situation and assuming $\alpha_0 d \gg 1$, Eq. (3.61) yields

the critical diffusion length

$$L_{\text{crit}} := \sqrt{\frac{k_B T}{q}} \mu_{\text{crit}} \tau_n = \frac{L_{\alpha 0}}{k_\alpha} \quad (3.64)$$

from the intersect $k_\alpha L_{\text{norm}} = 1$.

While the low mobility limit in the classical case is proportional to the diffusion length $L_n = \sqrt{k_B T / q \mu_n \tau_n}$, the low mobility limit in the radiative case is given by Eq. (3.50) and reads as

$$\lim_{\mu_{\text{norm}} \rightarrow 0} \frac{J_{\text{sc}}}{\Phi_{\text{bb}}^{\text{Eg}}} = \sqrt{\frac{\mu_{\text{norm}}}{\tau_{\text{norm}}^r}} = \frac{n_0}{\Phi_{\text{bb}}^{\text{Eg}}} \sqrt{\frac{k_B T \mu_n}{q \tau_r}}. \quad (3.65)$$

As pointed out above, this inverse dependency on τ_r at first glance disqualifies the attempt to define a critical diffusion length in the radiative limit. However, since the radiative lifetime is a given material parameter and in the case of constant absorption coefficient reads as

$$\tau_r = \frac{n_i^2}{4\alpha_0 N_A \bar{n}^2 \Phi_{\text{bb}}^{\text{Eg}}} \quad (3.66)$$

we can easily transform τ_r into $1/\tau_r$ to obtain the low mobility limit as a modified version of Eq. (3.65)

$$\lim_{\mu_{\text{norm}} \rightarrow 0} \frac{J_{\text{sc}}}{\Phi_{\text{bb}}^{\text{Eg}}} = 4\alpha_0 \bar{n}^2 \sqrt{\frac{k_B T \mu_n \tau_r}{q}}. \quad (3.67)$$

Therewith, the critical diffusion length in the radiative limit is given by

$$L_{\text{crit}}^{\text{rad}} := \sqrt{\frac{k_B T \mu_{\text{crit}}^{\text{rad}} \tau_r}{q}} = \frac{L_{\alpha 0}}{4\bar{n}^2}. \quad (3.68)$$

Comparison with Eq. (3.64) shows that the impact of PR in the radiative recombination limit is comparable to the effect of a light trapping scheme in the non-radiative situation with path length enhancement factor $k_\alpha = 4\bar{n}^2$.

3.7.4 Evaluation of the approximation

This section analyzes the accuracy of the approximations introduced in the previous two sections. Starting the discussion with the electron profiles in the radiative limit, I will then turn to the comparison of simulated and approximated solar cell output parameters J_0 , J_{sc} , V_{oc} and η .

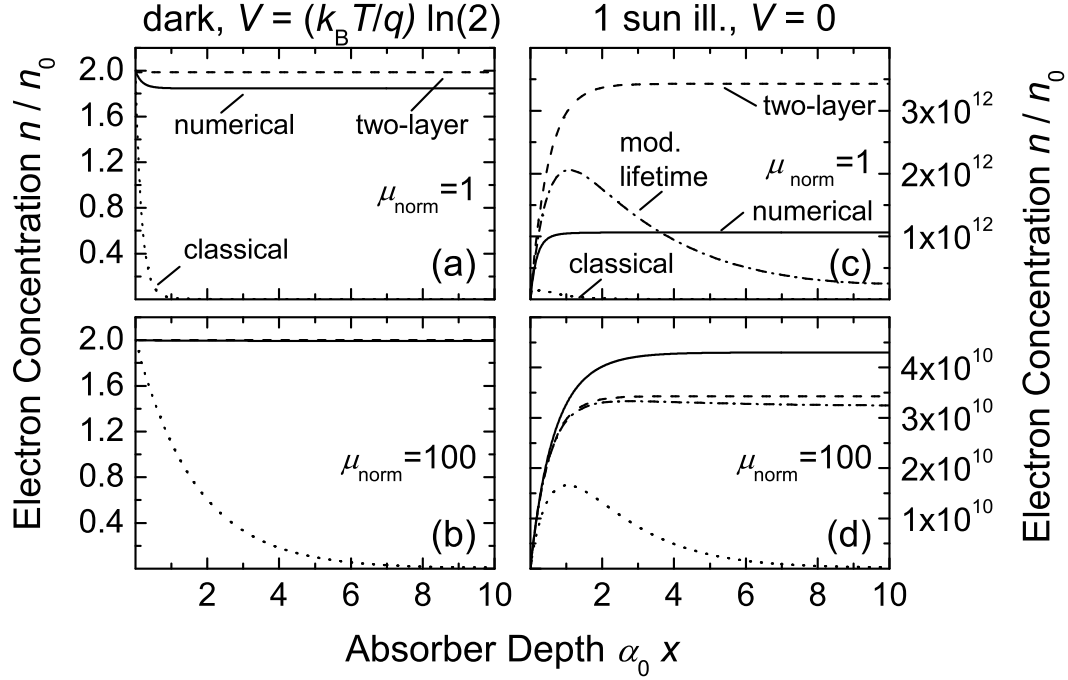


Fig. 3.13: Electron profiles in the radiative recombination limit with $\vartheta_r = 0$ for different mobilities $\mu_{\text{norm}} = 1$ and 100 . Solid lines represent numerical simulations, dashed lines stand for the results from the two-layer model, dotted lines are the classical approach as introduced in section 3.5.2, and dashed-dotted lines in Figs. c and d represent the results from the classical approach with modified radiative lifetime. The absorption coefficient is $\alpha = \alpha_0$, the normalized thickness is $\alpha_0 d = 10$, the band gap is $E_g = 1 \text{ eV}$, and the front surface is textured. All parameters are listed in Tab. 3.1. While the two-layer model correctly captures the slope of the electron profile in the dark at $\xi = 0$ (J_0), it does not reproduce the profile in the bulk very accurately for low mobilities (a). Therefore, it does not accurately reproduce the short circuit current J_{sc} , and the modified classical model provides a much more accurate approximation of the slope at $\xi = 0$ under illumination (c).

3.7.4.1 Electron profile

Figures 3.13a-d display the electron profiles in the radiative recombination limit versus the absorber depth. The thickness of the cell is $\alpha_0 d = 10$, all other parameters are listed in Tab. 3.1. Figures a and b depict the profile in the dark for $\nu(\xi = 0) = 2$, i.e. $V = (k_B T/q) \ln(2)$, which corresponds to an electrical current $J_{\text{el}} = -J_0^{\text{rad}}$. Figures c

and d depict the profile under illumination and short circuit conditions with $\nu(\xi = 0) = 1$, which yields the short circuit current J_{sc} . Both cases are displayed for a normalized mobility $\mu_{\text{norm}} = 1$ (a and c) and $\mu_{\text{norm}} = 100$ (b and d).

In all figures, solid lines represent the results from the numerical simulations, dashed lines are the profiles from the two-layer model, and in the illuminated case, dashed-dotted lines stand for the profile computed with the modified radiative lifetime. For comparison, the profiles computed with the classical approach are displayed as well (dotted lines). These results are obtained numerically by simply leaving out the internal generation term in Eq. (3.3) as described in section 3.4.2.

Let us first discuss the dark profiles in Fig. 3.13 with $\mu_{\text{norm}} = 1$. The short diffusion length leads to a steep exponential decay towards $\delta\nu = 0$ in the classical profile. In contrast, photon recycling leads to an increased electron density which is constant almost throughout the absorber depth.

This feature is correctly captured by the two-layer model. However, the exact level of the electron density is not necessarily reproduced accurately. Without external irradiation, i.e. $G = H = 0$, it follows $E = 0$ from Eq. (C.26). Therefore, the electron profile from Eq. (C.8) with $L_{\text{norm}}^{\text{nr}} \rightarrow \infty$ is constant

$$\delta\nu_2 = F = -\tanh\left(\frac{\xi_{\text{pr}}}{L_{\text{norm}}}\right) \sinh\left(\frac{\xi_{\text{pr}}}{L_{\text{norm}}}\right) + \cosh\left(\frac{\xi_{\text{pr}}}{L_{\text{norm}}}\right) \quad (3.69)$$

for $\xi \geq \xi_{\text{pr}}$. For a thick cell with absorptance $a = 1$ it holds $\xi_{\text{pr}} = \tau_{\text{norm}}^{\text{r}} = 0.028$ which yields $\nu_2 = 1.99$ for $\mu_{\text{norm}} = 1$. As can be seen in Fig. 3.13a, this level is higher than the level of $\nu_2 = 1.84$ obtained from the numerical simulations. The two-layer model is only capable of reproducing the complete profile in the high mobility limit depicted in Fig. 3.13b.

However, for the saturation current, only the initial slope $d\nu/d\xi$ at $\xi = 0$ is of interest. In the low mobility limit, the numerical approach with PR, the two-layer model, and the classical approach without PR result in the same dependence $\sqrt{\mu_{\text{norm}}\tau_{\text{norm}}^{\text{r}}}$. And since the thickness ξ_{pr} has been chosen appropriately the radiative recombination current $J_0^{\text{rad}} = a$ in the high mobility limit is rendered correctly by definition of the model. This means that in both limits, the initial slope $d\nu/d\xi$ at $\xi = 0$ is reproduced correctly by the two-layer model. Abberations can occur only in the intermediate mobility range.

Whereas the saturation current J_0 depends only on the slope at $\xi = 0$, the short

circuit current is related to the integral of the electron profile in the dark. The probability that an electron generated at a position ξ contributes to the short circuit current is given by the collection efficiency $f_C(\xi)$. Then, the total short circuit current reads as

$$J_{\text{sc}} = \int_0^{\alpha_0 d} G_{\text{sun}}(\xi) f_C(\xi) d\xi. \quad (3.70)$$

From a reciprocity relation derived by Donolato [67] the collection efficiency is linked to the electron profile in the dark according to

$$f_C(\xi) = \frac{\delta\nu(\xi)}{\exp\left(\frac{qV}{k_B T}\right) - 1}. \quad (3.71)$$

Therefore, the short circuit current is related to the spatial integral over the electron profile in the dark. From the inaccuracy of the electron profile it is thus clear that the two-layer model does not reproduce the short circuit current correctly for low mobilities.

Let us now turn to the profiles under illumination. Here, only the initial slope at $\xi = 0$ is important for the computation of the short circuit current. Figures 3.13c and d illustrate again the difference between the correct profile with photon recycling (solid lines) and the profile obtained with the classical treatment (dotted lines). As has been discussed in section 3.5.2, the PR prevents a decrease of the profile towards the back contact in the radiative limit. Again, this feature is correctly captured by the two-layer model. But again, a different level deep in the bulk is predicted.

In contrast to the two-layer model, the modified classical model with the increased radiative lifetime $\tau_{\text{norm}}^{\text{r,mod}}$ from Eq. (3.62) does not reproduce the qualitative features of the correct profile with photon recycling. The profile of the modified classical approach (dashed-dotted lines) decreases towards the back contact as does the profile from the classical approach (dotted lines). However, the modified classical approach is designed in such a way that the low mobility limit for the short circuit current is identical to the theoretical limit $2\bar{n}\sqrt{\mu_{\text{norm}}}$. Therefore, the slope of the electron profile at $\xi = 0$ in Fig. 3.13c is almost identical to the slope obtained from the numerical simulation.

As pointed out at the beginning of this section, a consistent quasi-classical analytical model that is able to reproduce both, J_0^{rad} and J_{sc} correctly, does not exist because of the inherent discrepancy with respect to the low mobility limits of J_0^{rad} and J_{sc} (cf.

p. 58). Therefore, I use the two-layer model to compute J_0 and the modified-lifetime model to compute J_{sc} . The combination of the two models thus yields a fairly accurate approximation of the numerical results which allows us to analytically calculate the efficiency of pn -junction solar cells in the whole thickness, mobility and lifetime range. The results of these computations are presented in the next section.

3.7.4.2 Photovoltaic output parameters

Figures 3.14a-d and 3.15a-d demonstrate the accuracy of the analytical approximations for a solar cell with textured front surface, a constant absorption coefficient $\alpha = \alpha_0$ and a cell thickness $\alpha_0 d = 0.1$ and 10. All other parameters are listed in Tab. 3.1.

The figures display the normalized saturation current J_0/Φ_{bb}^{Eg} (a), the normalized short circuit current J_{sc}/J_{sc}^{SQ} (b), the open circuit voltage V_{oc} (c), and the efficiency η (d) versus the normalized mobility μ_{norm} for different ratios $\vartheta_r = 10^{-2}, 1$ and 100 of radiative and non-radiative lifetime. Open squares represent the numerical results, solid lines are the approximated results where both, J_0 and J_{sc} are computed with the two-layer model, and dashed lines stand for the results obtained from combining the saturation current J_0 from the two-layer model with the short circuit current J_{sc} from the modified-lifetime model. Note in Fig. 3.15 that at low mobilities the numerical results are prone to be flawed with discretization errors when the diffusion length is smaller than the discretization interval d/N (see p. 173 in appendix B.7).

The two-layer model is well suited to describe the saturation current in the complete lifetime and mobility range. The model is constructed in such a way that in the radiative recombination limit the high mobility limit of J_0 converges towards the absorptance of the sample. The low mobility converges towards $\sqrt{\mu_{norm}/\tau_{norm}^r}$ and therewith also meets the requirements. Only in an intermediate range around the critical mobility μ_{crit}^{norm} does the approximation differ from the numerical results. The difference is more pronounced in solar cells with a thickness larger than the absorption length (Fig. 3.15a), where PR is more important than in solar cells with a thickness $\alpha_0 d < 1$ (Fig. 3.14a).

The two-layer model also yields a correct approximation of the short circuit current for $\vartheta_r > 1$ as depicted in Fig. 3.14b and Fig. 3.15b (solid lines). The differences to the numerical results (squares) stem from the errors in the approximation of the generation profile, since the profile of a cell with textured surface can not completely be reproduced

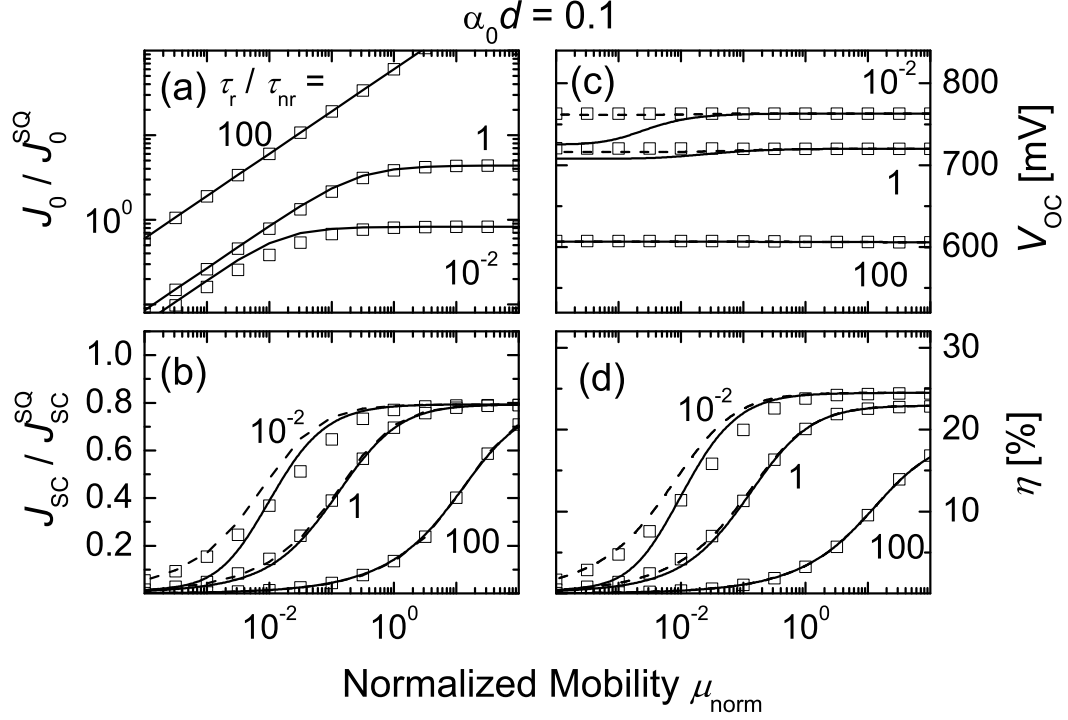


Fig. 3.14: Photovoltaic output parameters versus the normalized mobility μ_{norm} . The absorption coefficient is $\alpha = \alpha_0$, the normalized thickness is $\alpha_0 d = 0.1$, the band gap is $E_g = 1$ eV, and the front surface is textured. All parameters are listed in Tab. 3.1. Open squares are the numerical results, solid lines are the results from the two-layer model, and dashed lines are the results from combining the saturation current from the two-layer model with the short circuit current from the modified-lifetime model. While the two-layer model provides a good approximation of the saturation current, it is not suited to describe the short circuit current accurately. In combination with the modified-lifetime model however, it presents a fairly accurate analytical model to compute the efficiency of pn -junction solar cells in the whole lifetime and mobility range. (Note that the modified-lifetime model (dashed lines) is only included in figures b-d.)

by two exponential functions.

However, the approximation of J_{sc} in the radiative recombination limit with $\vartheta_r \rightarrow 0$ is rather crude. In particular, the low mobility limit for the short circuit current is given by the radiative diffusion length $L_{\text{norm}} = \sqrt{\mu_{\text{norm}} \tau_{\text{norm}}^r}$ (corrected by the optical

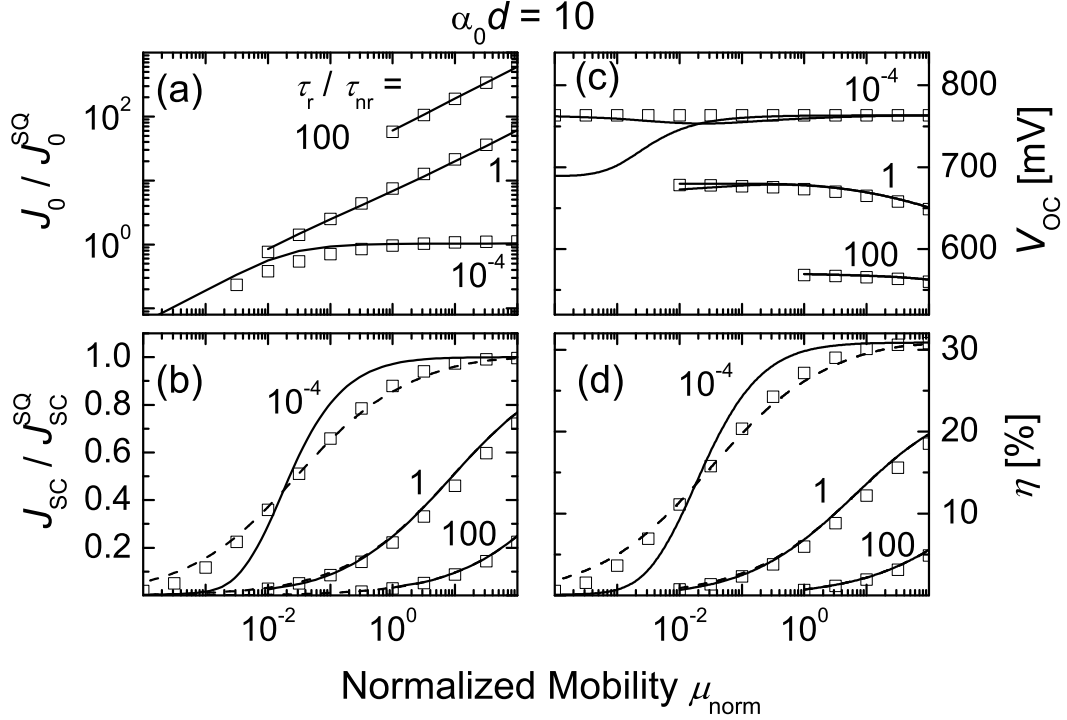


Fig. 3.15: Photovoltaic output parameters versus the normalized mobility μ_{norm} . The absorption coefficient is $\alpha = \alpha_0$, the normalized thickness is $\alpha_0 d = 10$, the band gap is $E_g = 1\text{ eV}$, and the front surface is textured. All parameters except for the thickness are identical to the parameters in Fig. 3.14. Open squares are the numerical results, solid lines are the results from the two-layer model, and dashed lines are the results from combining the saturation current from the two-layer model with the short circuit current from the modified-lifetime model. For low mobilities, discretization errors lead to flawed numerical results, which are therefore not displayed here.

term in Eq. (3.61)). It is therewith by roughly a factor of $4\bar{n}^2$ smaller than the limit $\sqrt{\mu_{\text{norm}}/\tau_{\text{norm}}^r}$.

The modified-lifetime model is not based on physical reasons but it is constructed to reproduce the radiative low mobility limit of the short circuit current correctly. As Fig. 3.14b and Fig. 3.15b demonstrate (dashed lines), the model yields a surprisingly accurate approximation of the numerical results. Only in an intermediate range around the critical mobility does the approximation depart from the numerical results.

In the next step we combine the saturation current from the two-layer model with the short circuit current from the modified-lifetime model to obtain the open circuit voltage and the efficiency (dashed lines). For comparison, the results where both currents are taken from the two-layer model are displayed as well (solid lines). For low mobilities the underestimated short circuit current leads here to a large error in the open circuit voltage which for all lifetime ratios $\vartheta_r < 1$ converges towards the voltage corresponding to $\vartheta_r = 1$.

The combined model provides a simple tool to compute the efficiency of *pn*-junction solar cells for all thicknesses and different kinds of front surfaces. It is capable of predicting the efficiency with an error of typically less than 0.5 % (absolute). The error is largest for the radiative recombination limit in the mobility range approximately two decades below the critical mobility $\mu_{\text{crit}}^{\text{norm}}$. In this range, the error can be as large as 3.5 % (absolute).

The model replaces the exact but very complicated numerical model with a simple analytical approach. It is here only presented for the case with constant absorption coefficient but can be extended to energy-dependent absorption coefficients (see section 3.9.1).

3.8 Energy-dependent absorption coefficient

So far, all simulations have been performed for the hypothetical case with constant absorption coefficient. This section analyzes the influence of energy-dependent absorption coefficient $\alpha(E)$. With respect to the spectral dependence of $\alpha(E)$ on the photon energy E I distinguish the three different cases listed in Tab. 3.2: (i) The hypothetical case of constant absorption above the band gap energy, (ii) direct semiconductors where the absorption of photons occurs via direct transitions without a change in momentum and which therefore exhibit a square-root dependence of the absorption coefficient on the energy [68, p. 36], and (iii) indirect semiconductors, where phonons are needed for momentum conservation during light absorption and which therefore exhibit a parabolic dependence [68, p. 38].

The parameter α_0 in Tab. 3.2 is the absorption coefficient at the photon energy $E = E_g + k_B T$ for all three cases. Note that the choice of $E_g + k_B T$ as this crossover energy is somewhat arbitrary. To compare the three cases, we assume identical α_0

Tab. 3.2: Spectral dependence of the absorption coefficient. At $E = E_g + k_B T$, all types feature the absorption coefficient $\alpha(E_g + k_B T) = \alpha_0$.

Type	$\alpha(E)$
constant	α_0
direct	$\alpha_0 \sqrt{\frac{E - E_g}{k_B T}}$
indirect	$\alpha_0 \left(\frac{E - E_g}{k_B T} \right)^2$

for all. In reality, though, indirect semiconductors possess much lower absorption coefficients than direct semiconductors, which leads to a crossover energy more in the proximity of $E_g + 1 \text{ eV}$. However, such an approach would imply that for a given sample thickness d the average absorptance in an indirect semiconductor would be much smaller than in a direct semiconductor, which in turn would distort the comparability of the currents. Therefore, I chose to stick with the crossover energy $E_g + k_B T$ close to the band gap energy.

Figures 3.16a-i demonstrate the influence of the spectral dependence of the absorption coefficient on the currents J_{sc} and J_0 , the open circuit voltage V_{oc} , and the efficiency η . All quantities are again normalized to their respective maximum values in the SQ limit. In analogy to the representation in Fig. 3.4, all quantities are displayed vs. the thickness $\alpha_0 d$ of the solar cell. The front surface is textured.

Constant absorption The energy independent light absorption leads to identical generation profiles for solar and black body irradiation. Therefore, the external quantum efficiency $\text{EQE}(E)$ is independent of the photon energy, and Rau's reciprocity relation [16] which relates the EQE to the radiative recombination current as elucidated in section 3.7 on page 58, holds not only for the spectral quantity $\text{EQE}(E)$ but also for the integrated spectrum. In consequence, the normalized currents $J_{sc}/J_{sc}^{\text{SQ}}$ and J_0/J_0^{SQ} are identical (Fig. 3.16a). As in Fig. 3.4a, the currents approach the absorptance a of the sample for sufficiently large mobilities. For lower mobilities, however, the currents are limited by insufficient transport.

Since the ratios $J_{sc}/J_{sc}^{\text{SQ}}$ and J_0/J_0^{SQ} are independent of the absorber thickness, it always holds $J_{sc}/J_0 = J_{sc}^{\text{SQ}}/J_0^{\text{SQ}}$ and, therefore, the open circuit voltage is always $V_{oc} = V_{oc}^{\text{SQ}}$ (Fig. 3.16d). Accordingly, the efficiency is exclusively determined by the

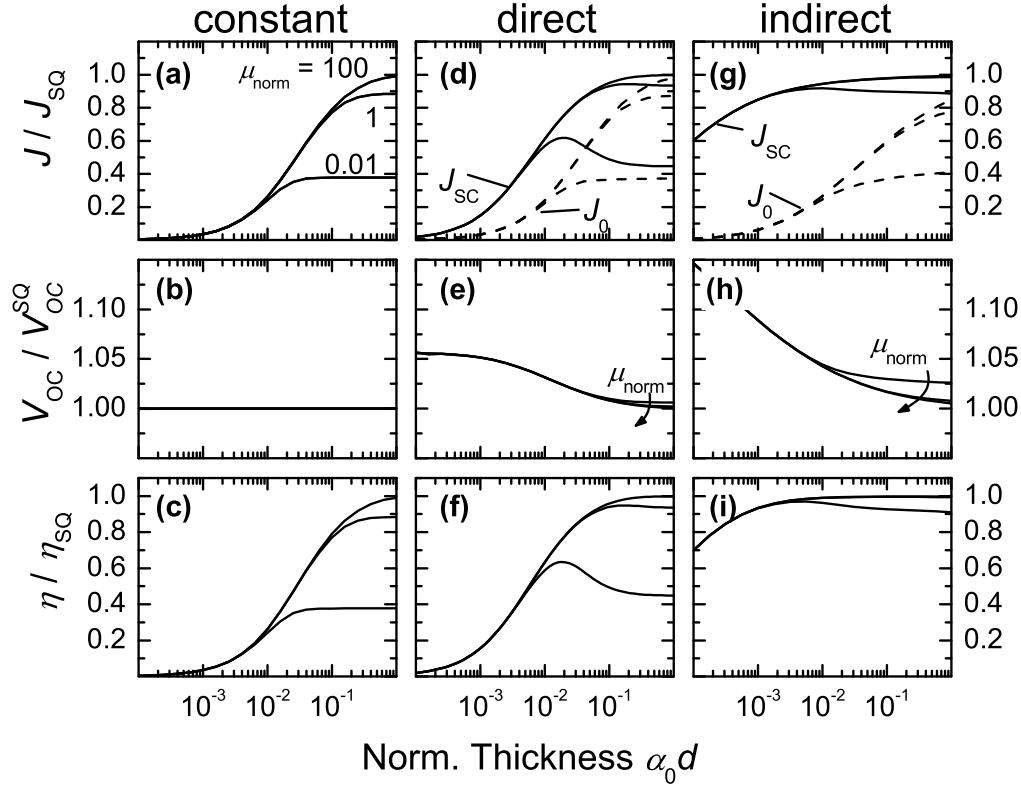


Fig. 3.16: Currents J_{sc} and J_0 in the radiative recombination limit with $\vartheta_r = 0$ normalized to the maximum values in the Shockley-Queisser limit vs cell thickness d for a textured front surface (a, d, g). The band gap is $E_g = 1$ eV and the front surface is textured. I distinguish between constant absorption above the band gap (a-c), a direct semiconductor (d-f), and an indirect semiconductor (g-i). The spectral dependence of the absorption coefficient $\alpha(E)$ in comparison to the spectrum of the incident light leads to different spatial generation profiles for solar and black body irradiation and, therefore, to differences between J_{sc} and J_0 . Figures b, e, and h display the resulting normalized open circuit voltage V_{oc}/V_{oc}^{SQ} . With the normalized short circuit current being larger than the normalized saturation current for small thicknesses, the open circuit voltage exceeds the SQ limit V_{oc}^{SQ} (e, h). The efficiency η/η_{SQ} displayed in Figs. c, f, and i is mainly dominated by the short circuit current. Apart from the absorption coefficient, all parameters are listed in Tab. 3.1.

loss in the short circuit current (Fig. 3.16b).

Direct absorption Due to the spectral dependence of the absorption coefficient, the solar spectrum and the 300 K black body spectrum cause different generation profiles. Consequently, the absorptance $a(E, d)$ is energy-dependent, and the average absorptance as defined in appendix B.7 is different for the two spectra. Therefore, the reciprocity relation is restricted to the spectral quantities, and J_{sc}/J_{sc}^{SQ} is not identical to J_o/J_o^{SQ} anymore.

Since the spectral density of the solar spectrum is larger for higher photon energies when compared to the density of the black body spectrum, the average absorption coefficient is also larger for the solar spectrum. This means that for small absorber thicknesses the average absorptance a_{sun} of the solar spectrum exceeds the average absorptance a_{bb} of the black body spectrum, and, therefore, J_{sc}/J_{sc}^{SQ} in Fig. 3.16d is larger than J_o/J_o^{SQ} .

Consequently - and at first glance astonishingly - the open circuit voltage V_{oc} in Fig. 3.16e exceeds the open circuit voltage V_{oc}^{SQ} for low thicknesses. The efficiency in Fig. 3.16f, however, does not exceed the SQ efficiency η_{SQ} because with decreasing thickness the absorption losses that result in a reduction of J_{sc} more than counterbalance the increase in V_{oc} .

The detailed discussion in section 3.8.1 reveals that such efficiency enhancement above the SQ limit is indeed possible, but only for small band gap energies. Effectively, the variation of the spectral dependence of the absorption coefficient can be regarded as an increase of the band gap energy. In particular, the indirect semiconductor with the parabolic dependence of α exhibits hardly any absorption below $E_g + k_B T$ when the sample is thin enough.

Indirect absorption The reasoning given for the direct semiconductor holds for indirect semiconductors as well. The difference between J_{sc} and J_o in Fig. 3.16g is even more pronounced. For energies $E < E_g + k_B T$ the absorption coefficient is much smaller than α_0 which implies a reduced a_{bb} . For $E > E_g + k_B T$ on the other hand, α is much larger than α_0 which results in an amplified a_{sun} . Note again that the choice of $E_g + k_B T$ as a crossover point is somewhat arbitrary and does not reflect crossover points of real semiconductor materials.

Note that with respect to the shift of the critical thickness towards smaller thicknesses, the opposite holds true for the saturation current J_0 because the black body spectrum possesses its maximum at an energy much below the band gap $E_g = 1\text{ eV}$ and only the exponentially decreasing Boltzmann tail of the spectrum is relevant for the saturation current. Therefore, the relevant energy regime for J_0 lies between E_g and $E_g + k_B T$, where direct and indirect semiconductors have an absorption coefficient below α_0 .

3.8.1 Thickness-dependent current enhancement

Figure 3.16d shows that for a certain cell thickness d the short circuit current J_{sc} features a maximum. This section takes a closer look at this phenomenon and explains the underlying mechanism. As will be discussed in the following, this mechanism involves the relationship between photon absorption and emission and carrier collection. In principle, there are two questions arising from the observations in Fig. 3.16d that need to be answered: (i) Why does the short circuit current only feature a maximum for low mobilities and (ii) Why does this maximum not occur for energy-independent absorption coefficient?

3.8.1.1 High mobility

Let us first consider the high mobility limit of the short circuit current, which is given by the absorptance. In this context, high mobility limit means that the minority carrier diffusion length is larger than the average absorption length of the photon flux impinging on the cell, i.e. that all generated carriers contribute to the short circuit current.

As pointed out in section 3.6.1, the absorptance increases monotonically with increasing sample thickness. Even though the generation rate close to the front surface decreases with increasing thickness when the influence of multiple reflections recedes, the overall absorptance given by the integrated generation rate over the cell thickness always increases with increasing thickness. Consequently, for high mobilities the short circuit current increases monotonically with increasing thickness as well and does not show a maximum over the cell thickness.

3.8.1.2 Low mobility

The case is different for lower mobilities. If the collection length (i.e. the diffusion length) of the photo-generated carriers is smaller than the absorption length then not all generated carriers can contribute to the short circuit current. Carriers that are generated deep in the bulk are not collected and thus recombine.

In the radiative recombination limit, a carrier that is absorbed but not collected can only be emitted by the cell. We thus have to consider the relation between absorption and emission length. To do so, we have to differentiate between energy-independent and energy-dependent absorption coefficient.

Constant absorption coefficient In the case of constant absorption coefficient as depicted in Fig. 3.16a, the emission length is identical to the absorption length. Let us now consider the influence of the cell thickness on the carrier collection in the low mobility limit. As long as the thickness is smaller than the diffusion length, all generated carriers are collected and the short circuit current is identical to the absorptance. With increasing thickness, however, not all generated carriers are collected anymore and the current is lower than the absorptance. Once the thickness exceeds the absorption length, J_{sc}/J_{sc}^{SQ} saturates. The saturation level is below unity and is determined by the collection length, i.e. the carrier mobility.

Energy-dependent absorption coefficient Let us now turn to energy-dependent light absorption. Consider the low mobility limit of the short circuit current as depicted in Fig. 3.16d. In the following, I will illustrate, why the current features a maximum over the sample thickness.

As long as the thickness is smaller than the diffusion length, the short circuit current is again equal to the absorptance. It keeps increasing with a lower slope than the absorptance until the thickness is identical to the average absorption length $L_{\alpha, \text{norm}} = \alpha_0/(5\alpha_0) = 0.2$ (cf. Tab. B.2 on page 172) for the solar irradiation. Any further increase of the thickness, however, leads to increased emission of internally reabsorbed carriers, while the absorptance of solar radiation essentially remains unaffected. Therefore, the current decreases until the thickness is equal to the emission length $L_{\text{em, norm}} = \alpha_0/\alpha_0 = 1$, which is identical to the absorption length of the black body spectrum. For thicknesses larger than the emission length, the current saturates

at a slightly higher level than in Fig. 3.16a because of the higher average absorption coefficient for the solar irradiation.

Summing up, the discrepancy between absorption and emission length leads to the maximum of the short circuit current over the cell thickness. In a range $L_{\alpha, \text{norm}} < \alpha_0 d < L_{\text{em}, \text{norm}}$ any increase of the thickness leads to emission losses which are larger than the gain in absorptance and therefore to a decreasing current. Since for the black body spectrum the absorption length is equal to the emission length, this effect can not be seen in the saturation current, which therefore increases monotonically with the cell thickness.

3.8.2 Thickness-dependent efficiency enhancement

In the last section we have seen that the discrepancy between the absorptance of solar and black body irradiation leads to a maximum in the short circuit current for low mobilities. This discrepancy, which in a certain thickness range leads to $J_{\text{sc}}(d)/J_{\text{sc}}^{\text{SQ}} > J_0(d)/J_0^{\text{SQ}}$ for all mobilities, is also responsible for the enhancement of the open circuit voltage $V_{\text{oc}}(d)$ above $V_{\text{oc}}^{\text{SQ}}$ as depicted in Fig. 3.16e and h.

From a thermodynamic point of view, the reduced radiative recombination current in comparison to the short circuit current can lead to a reduced entropy production per absorbed photon [69], which results in higher open circuit voltages. Unfortunately, the voltage enhancement occurs in a thickness range, where the cell is so thin that the short circuit current $J_{\text{sc}}/J_{\text{sc}}^{\text{SQ}}$ is significantly lower than unity. Therefore, the efficiency as the product of J_{sc} and V_{oc} does not exceed the Shockley-Queisser limit.

This situation changes, when the band gap energy of the solar cell is reduced. Figure 3.17 demonstrates that for a cell with $E_g = 0.5 \text{ eV}$, the maximum radiative efficiency, i.e. the high mobility limit with $\mu_{\text{norm}} = 10^4$, can indeed exceed the SQ limit for this particular band gap. The figure depicts the normalized efficiency versus the cell thickness for a semiconductor with constant absorption coefficient (const), a direct semiconductor (dir), and an indirect semiconductor (ind). Both, the direct and the indirect semiconductor feature a thickness regime, where the normalized efficiency is larger than unity. Especially the absorptance spectrum of the indirect semiconductor as depicted in Fig. 3.17 leads to the efficiency enhancement of almost 15 % (relative) for a thin cell with thickness $\alpha_0 d \approx 3 \times 10^{-4}$. These considerations have also been carried out in a similar form by Araújo and Martí [70]. They have shown that even with the

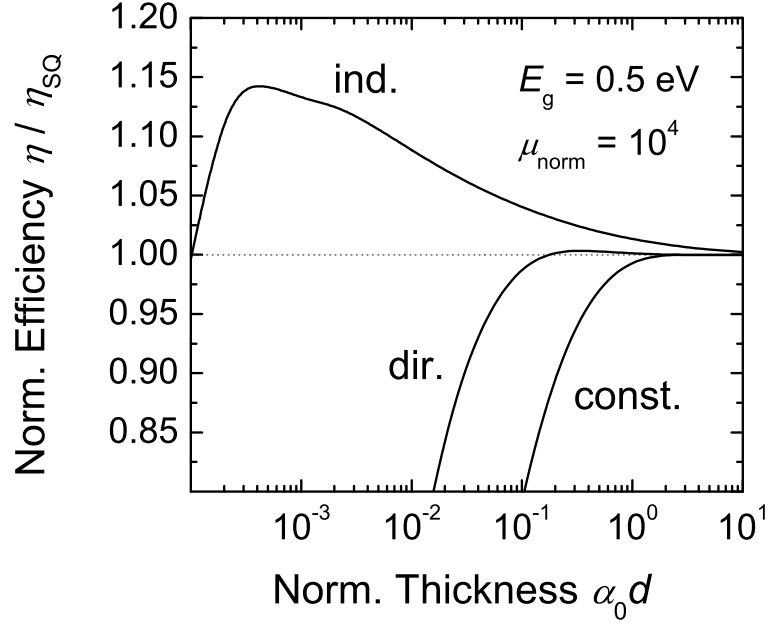


Fig. 3.17: Normalized radiative efficiency versus cell thickness $\alpha_0 d$ for a semiconductor with constant absorption above the band gap energy (const), a direct semiconductor (dir), and an indirect semiconductor (ind). The band gap is $E_g = 0.5$ eV, the mobility is $\mu_{\text{norm}} = 10^4$, and the front surface is textured. All other parameters are listed in Tab. 3.1. Due to the higher absorptance of the solar irradiation compared to the black body irradiation, the efficiency $\eta(E_g)$ exceeds the SQ efficiency $\eta_{\text{SQ}}(E_g)$ for the direct semiconductor and even more so for the indirect semiconductor.

band gap of silicon, a maximum radiative efficiency is obtained for the (rather large) optimal thickness $d \approx 1$ mm.

The reason for this rather astonishing phenomenon lies in the fact that the energy-dependent absorption coefficient of the solar cell translates into an energy-dependent absorptance if the sample is thin enough. When the sample is thick enough, the absorptance is unity for all energies larger than E_g . This means that the absorptance can be expressed by a step function as described in Eq. (2.5). Reducing the cell thickness results in a reduction of the absorptance at energies, where the absorption coefficient is low, i.e. at energies close to the band gap energy. This means that the absorp-

tance for thin cells can again be approximated with a step function, but one that is shifted towards higher energies. Consequently, the thickness reduction can effectively be described as an increase of the band gap E_g . This increase of the band gap in turn implies a higher maximum efficiency $\eta_{\text{SQ}}(E_g)$ if the band gap is below the band gap $E_g \approx 1.1 \text{ eV}$ that corresponds to the global maximum efficiency $\eta_{\text{SQ}} \approx 33 \%$. For band gaps larger $E_g = 1.4 \text{ eV}$, which corresponds to the second global maximum, there is no such efficiency enhancement for thin cells. This is because increasing the effective band gap would only result in lower efficiencies (cmp. Fig. 3.2).

3.8.3 Maximum open circuit voltage

The previous section 3.8.2 has shown that it is possible to exceed the SQ efficiency limit of a solar cell with given band gap if the band gap is small enough. Due to energy-dependent light absorption, the thickness of the cell can be tuned in such a way that almost the entire solar irradiation above the band gap is absorbed while the black body irradiation, which occurs predominately at lower photon energies, is only partly absorbed. Therewith, the open circuit voltage is increased above its SQ limit. If this increase is not compensated entirely by the loss in J_{sc} due to incomplete absorption, the efficiency is also increased above its SQ limit $\eta_{\text{SQ}}(E_g)$.

This result brings up two questions: (i) What is the maximum open circuit voltage for a given band gap energy and (ii) Is it possible to exceed even the global maximum $\eta_{\text{SQ}} \approx 33 \%$, or in other words: Is there an optimal absorptance spectrum that is superior to the step function absorptance assumed by Shockley and Queisser?

The latter question has already been answered in section A.2, which proves that the global SQ limit of 33% , which is obtained with a step-like absorptance function, is indeed the ultimate maximum efficiency that can be obtained with a single junction solar cell. A similar proof has also been derived by Araújo and Martí Ref. [70]. This section discusses the first question of the maximum open circuit voltage obtainable with a single junction solar cell with a given band gap energy.

It is often assumed that the maximum open circuit voltage in the SQ limit is given by the band gap energy E_g . Indeed, Shockley and Queisser introduced a so-called ultimate efficiency in their publication [10] that is obtained when $V_{\text{oc}} = E_g$ is assumed. However, the detailed balance limit itself does not include an inherent restriction to the open circuit voltage. The open circuit voltage is exclusively determined by the ratio of

short circuit current and saturation current, i.e. by $V_{oc} = (k_B T/q) \ln(J_{sc}/J_0 + 1)$. The currents in turn are entirely determined by the solar and the black body spectrum and the absorptance $a(E)$.

In a strict sense, it is a mere coincidence that $V_{oc}^{SQ}(E_g)$ is smaller than the band gap. In fact, the SQ theory would predict $V_{oc} > E_g$ for highly concentrated sunlight with concentration factors exceeding 30000.

However, the SQ theory only accounts for the spontaneous radiative recombination of electron and holes. If the voltage exceeds the band gap, then the quasi Fermi levels will be located in the conduction and valence band, which would result in stimulated emission. Due to this additional recombination the maximum open circuit voltage of a single pn -junction solar cell is indeed given by the band gap energy E_g .

3.9 Maximum efficiencies of real materials

So far, most of the discussions have focused on the hypothetical case of constant absorption coefficient to facilitate the understanding of the fundamental mechanisms involved and to allow for relatively simple analytical expressions. As helpful as these analyses proved for the theoretical construction of the model features, they fail to provide any practical information.

This section analyzes the critical mobility and the efficiency limits for the three semiconducting materials crystalline silicon (c-Si), hydrogenated amorphous silicon (a-Si:H), and $\text{Cu}(\text{In}_{1-x}\text{Ga}_x)\text{Se}_2$ with $x = 0.26$ (CIGS). Admittedly though, it needs to be mentioned that the simulations conducted here only describe the efficiencies of idealized pn -junction solar cells without, for instance, optical losses or recombination in the space charge region, in the emitter or at the back contact. On the other hand, carrier generation and collection in the space charge region are neglected as well. While the model quite reasonably describes crystalline silicon solar cells, it is hardly suited to simulate actual devices made of amorphous silicon or CIGS.

The parameters used for the simulations are listed in Tab. 3.3. The cell thicknesses are chosen as typical values but also large enough to guarantee virtually complete absorption of the solar spectrum. All solar cells are assumed to be pn -junction solar cells with a zero reflectance textured front surface, and no recombination at the back contact. The absorption coefficients are taken from Ref. [12] in the case of crystalline silicon

Tab. 3.3: Parameters used for the computation of the critical mobility of crystalline silicon (c-Si), hydrogenated amorphous silicon (a-Si:H), and Cu(In_{1-x}Ga_x)Se₂ (CIGS, $x = 0.26$).

	E_g [eV]	\bar{n}	α_0 (Type) [cm ⁻¹]	n_i [cm ⁻³]	d [μm]	Ref.
c-Si	1.124	3.6	3.3 (indirect)	1.04×10^{10}	200	[12, 17]
a-Si:H	1.75	4	180 (indirect)	1×10^6	1	[5, 71]
CIGS	1.17	3.1	11000 (direct)	3×10^8	2	[72]

or from measured data and are displayed in Fig. 3.18. Table 3.3 lists the absorption coefficients at an energy $E_g + k_B T$ and the type of the semiconductor. In contrast to the theoretical types listed in Tab. 3.2, the measured data also include sub band gap tail-like absorption and at higher energies aberrations of the strict theoretical square-root or parabolic dependencies on the energy.

Figures 3.19a-d, 3.20a-d, and 3.21a-d display the results of the simulations, i.e., the saturation current J_0 (a), the short circuit current J_{sc} (b), the open circuit voltage V_{oc} (c), and the efficiency η (d), versus the non-radiative lifetime τ_{nr} for different mobilities (open symbols). The chosen mobilities vary between the materials and are chosen in such a way that measured values fall in the displayed range. The mobilities are $\mu_n = 24, 240, \text{ and } 2400 \text{ cm}^2(\text{Vs})^{-1}$ for c-Si, $\mu_n = 0.34, 3.4, \text{ and } 34 \text{ cm}^2(\text{Vs})^{-1}$ for a-Si:H, and $\mu_n = 0.15, 1.5, \text{ and } 150 \text{ cm}^2(\text{Vs})^{-1}$ for CIGS.⁷

For the transformation of the normalized mobility μ_{norm} and the normalized lifetimes τ_{norm}^r and τ_{norm}^{nr} into the unit-bearing quantities μ_n , τ_r , and τ_{nr} , one requires the doping concentration N_A . I assume $N_A = 5 \times 10^{16} \text{ cm}^{-3}$ which is a typical value for silicon solar cells. However, as section 3.10 shows, the doping concentration must not be chosen too low in order not to violate the low-level injection assumptions, in particular in the radiative recombination limit.

Section 3.9.3 discusses the results of the simulation. Before doing so, however, the next section applies the analytical model of section 3.7 to the analyzed materials.

⁷The unconventional values result from the de-normalization of the normalized mobilities. Note that for CIGS, the chosen range is by a factor of 10 larger than for the other two cases because of the uncertainty connected with measured values.

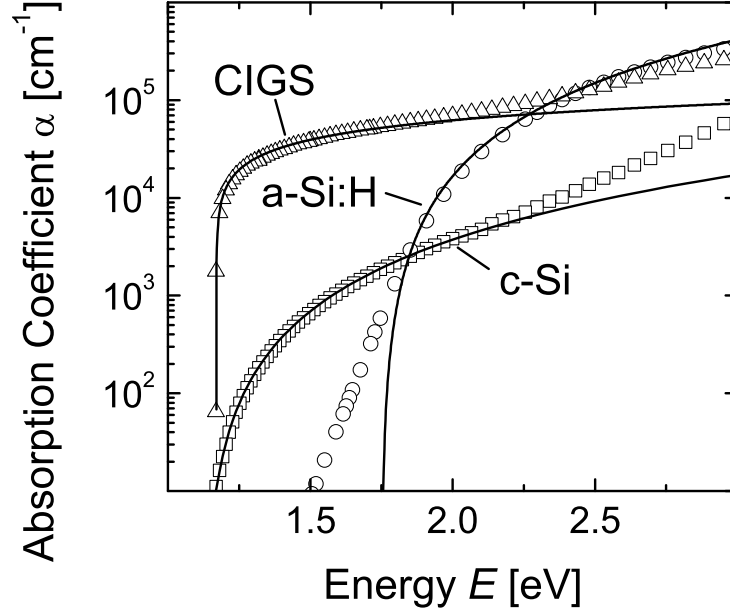


Fig. 3.18: Experimental absorption coefficients of crystalline silicon (c-Si, squares), hydrogenated amorphous silicon (a-Si:H, circles), and $\text{Cu}(\text{In}_{1-x}\text{Ga}_x)\text{Se}_2$ (CIGS, triangles) with $x = 0.26$ versus the photon energy. The measured data are fit with either a square-root function for the direct semiconductor CIGS or a parabolic function in the case of crystalline and amorphous silicon (lines). Table 3.3 lists the fit parameters. Amorphous silicon exhibits a significant sub band gap absorption in band tail states. In the chosen spectrum of CIGS the band tails are much less pronounced. In crystalline silicon and CIGS, the absorption coefficient shows a sharp increase at photon energies above 2 eV that cannot be explained with the simple parabolic or square-root dependence.

3.9.1 Analytical approximation

This section discusses the applicability of the analytical model derived in section 3.7 to the three materials under investigation and introduces necessary modifications. The model with constant absorption in section 3.7 was based on the analysis of the low mobility limits of saturation and short circuit current. Hence, the main question that needs to be answered is, what influence the energy-dependent absorption coefficient has on those low-mobility limits.

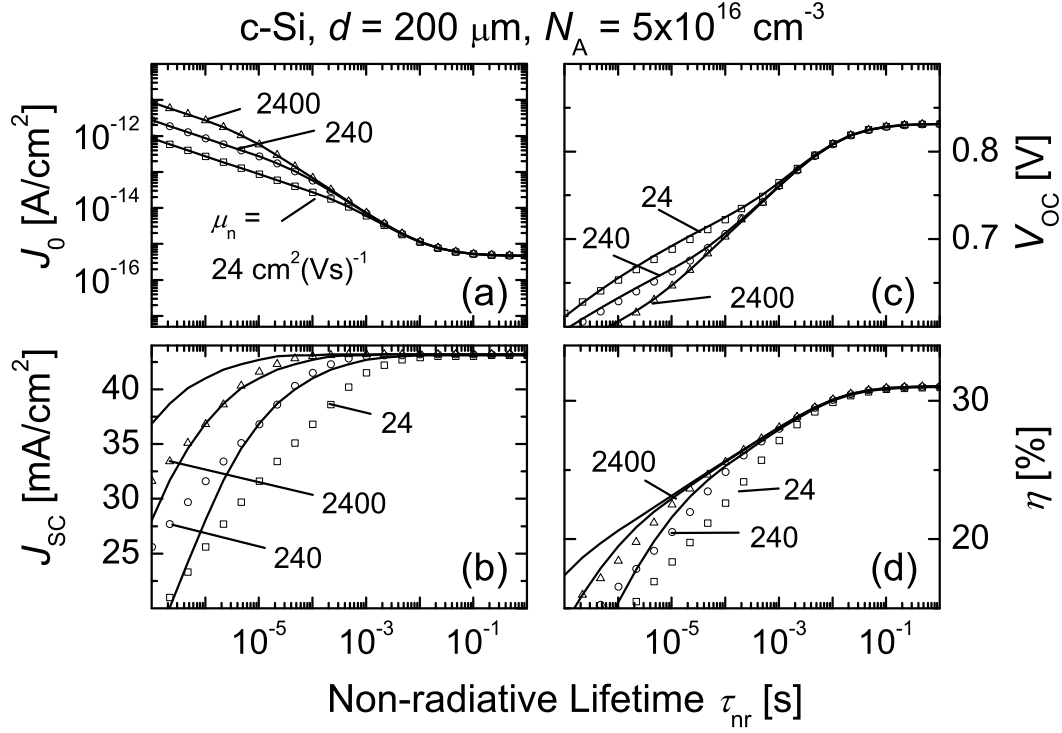


Fig. 3.19: Simulation results of a crystalline silicon pn -junction solar cell (open symbols): Saturation current J_0 (a), short circuit current J_{sc} (b), open circuit voltage V_{oc} (c), and efficiency η (d) versus the non-radiative lifetime τ_{nr} . The thickness of the solar cell is $d = 200 \mu\text{m}$ and the doping density is $N_A = 5 \times 10^{16} \text{ cm}^{-3}$. The minority carrier mobility is assumed as $\mu_n = 24, 240$, and $2400 \text{ cm}^2(\text{Vs})^{-1}$.

3.9.1.1 Saturation current

The low mobility limit of J_0^{rad} can still be obtained in the simple fashion of section 3.6.2, where the generation rates need to be augmented by integrating over the photon energy. Interestingly, the relation $\lim_{\mu_{\text{norm}} \rightarrow \infty} J_0^{\text{rad}} / \Phi_{\text{bb}}^{\text{Eg}} = \sqrt{\mu_{\text{norm}} / \tau_{\text{norm}}^{\text{r}}}$ is only valid for the integrated spectrum, but not for the spectral radiative saturation current $j_0^{\text{rad}}(E)$ that is obtained under monochromatic excitation with the black body intensity $\phi_{\text{bb}}(E)$. This is because even with monochromatic generation rate $g_{\text{bb}}(E)$, the internal generation still includes the complete integral $G_{\text{int}} = \int_0^\infty g_{\text{int}}(E) dE$. The thermodynamic equilibrium as expressed in Eq. (3.46) requires illumination with the integrated black

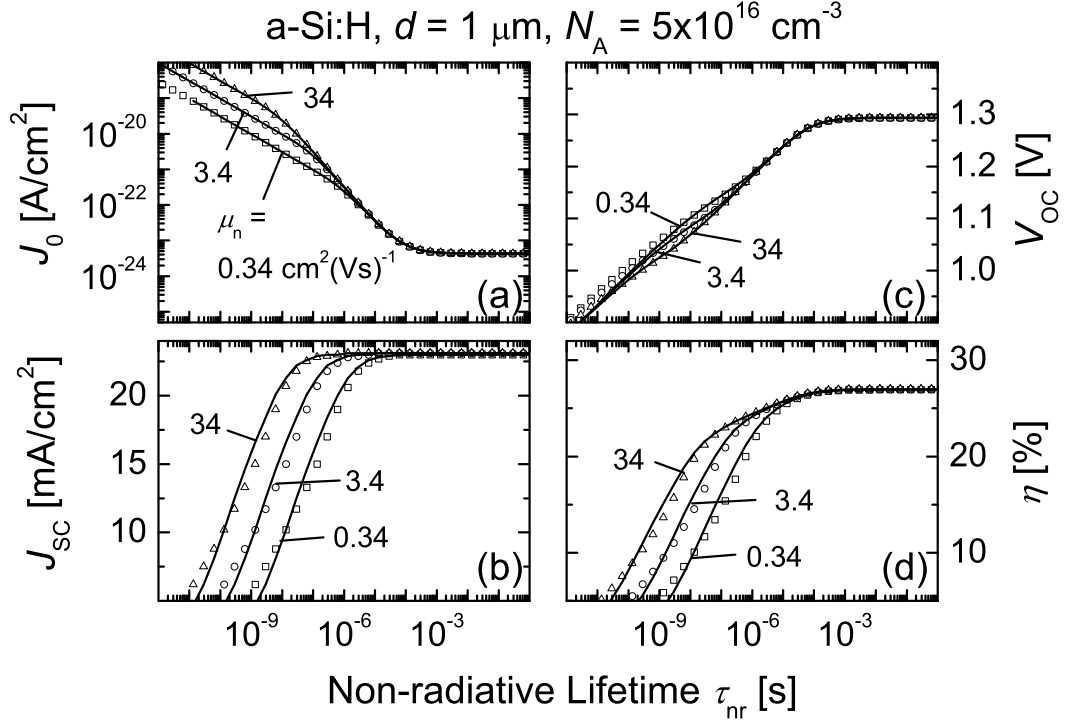


Fig. 3.20: Simulation results of an amorphous silicon pn -junction solar cell (open symbols): Saturation current J_0 (a), short circuit current J_{sc} (b), open circuit voltage V_{oc} (c), and efficiency η (d) versus the non-radiative lifetime τ_{nr} . The thickness of the solar cell is $d = 1 \mu\text{m}$ and the doping density is $N_A = 5 \times 10^{16} \text{ cm}^{-3}$. The minority carrier mobility is assumed as $\mu_n = 0.34, 3.4, \text{ and } 34 \text{ cm}^2(\text{Vs})^{-1}$.

body spectrum, which implies that the approximation performed in Eq. (3.47) is only valid for the integrated spectrum.

The high mobility limit is also still given by the integrated absorbed black body spectrum Φ_{bb}^{abs} as listed in Tab 3.4. To define the thickness ξ_{pr} of layer 1 in the two layer model, we need the absorptance $a = \Phi_{bb}^{\text{abs}} / \Phi_{bb}^{\text{Eg}}$. Then we can apply the two-layer model from section 3.7.2 without any other modifications.

Figures 3.19a, 3.20a, and 3.21a display the analytical saturation currents computed with the two-layer model as solid lines. The figures demonstrate the excellent agreement of the analytical model and the numerical simulations.

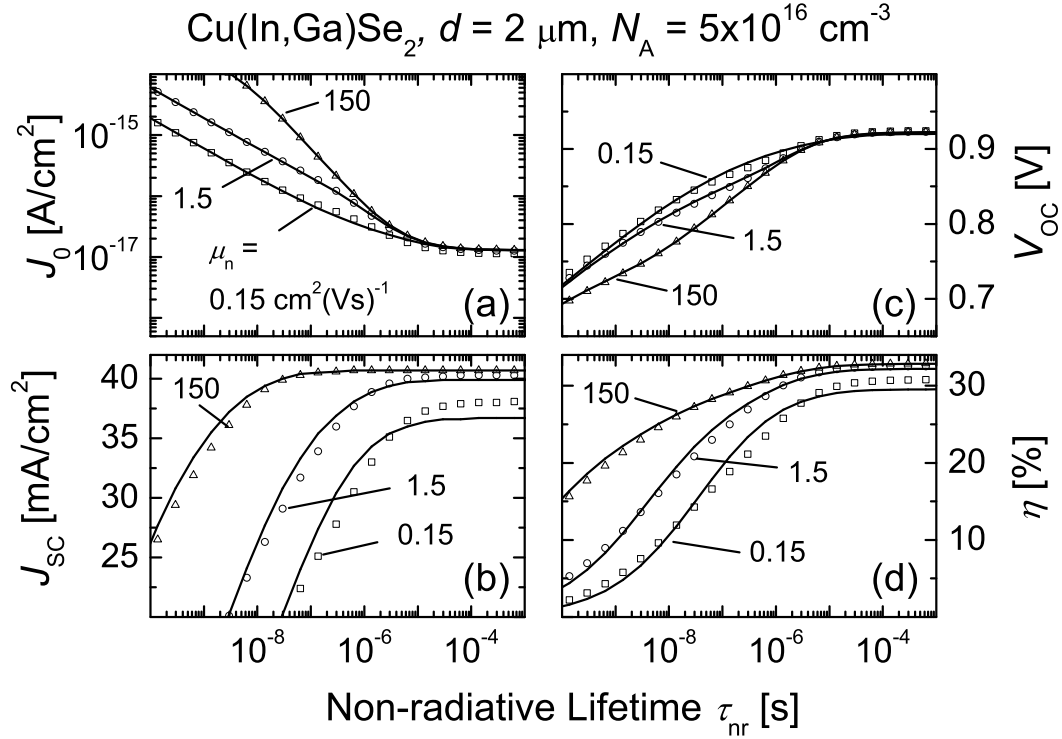


Fig. 3.21: Simulation results of a Cu(In,Ga)Se_2 pn -junction solar cell (open symbols): Saturation current J_0 (a), short circuit current J_{sc} (b), open circuit voltage V_{oc} (c), and efficiency η (d) versus the non-radiative lifetime τ_{nr} . The thickness of the solar cell is $d = 2 \mu\text{m}$ and the doping density is $N_A = 5 \times 10^{16} \text{ cm}^{-3}$. The minority carrier mobility is assumed as $\mu_n = 0.15, 1.5$, and $150 \text{ cm}^2 (\text{Vs})^{-1}$.

3.9.1.2 Short circuit current

The derivation of the modified-lifetime model for the determination of the short circuit current in section 3.7.3 was based on the reciprocity between the short circuit current and the radiative recombination current. This section discusses the influence of the energy-dependent absorption coefficient on the reciprocity relation.

Let us first have a look at the relationship between short circuit current and radiative saturation current in the radiative recombination limit if the absorption coefficient is energy-dependent. In section 3.6.2 we have seen that the low mobility limit of short circuit and saturation current is identical if the absorption coefficient is energy-

independent. In the following, I explain, why this relation does not hold for energy-dependent light absorption, and what consequences this fact implies for the modified lifetime model.

For energy-dependent light absorption, the reciprocity theorem Eq. (3.55) is still valid, but now has to be considered separately for each individual photon energy E according to

$$\text{EQE}(E) = \frac{j_{\text{sc}}(E)}{\phi_{\text{sun}}(E)} = \frac{j_0^{\text{rad}}(E)}{\phi_{\text{bb}}(E)}. \quad (3.72)$$

Here, the spectral currents refer to the short circuit current $j_{\text{sc}}(E)$ and saturation current $j_0(E)$ that are obtained under monochromatic illumination at the energy E with intensity $\phi_{\text{sun}}(E)$ or $\phi_{\text{bb}}(E)$ ⁸. The total currents J_{sc} and J_0^{rad} are then obtained by integrating the quantum efficiency $\text{EQE}(E)$ weighted with the corresponding photon flux $\phi_{\text{sun}}(E)$ or $\phi_{\text{bb}}(E)$ over all energies E . Therewith, we arrive at

$$\frac{J_{\text{sc}}}{\Phi_{\text{sun}}} = \frac{\int_0^\infty \text{EQE}(E) \phi_{\text{sun}}(E) dE}{\int_0^\infty \phi_{\text{sun}}(E) dE} \neq \frac{\int_0^\infty \text{EQE}(E) \phi_{\text{bb}}(E) dE}{\int_0^\infty \phi_{\text{bb}}(E) dE} = \frac{J_0^{\text{rad}}}{\Phi_{\text{bb}}}. \quad (3.73)$$

Only if the EQE were energy-independent, would the reciprocity relation hold for the integrated currents as well. For high mobilities, all photo-generated carriers are collected and the quantum efficiency $\text{EQE}(E)$ equals the absorptance $a(E)$. If the sample is sufficiently thick and subbandgap absorption is neglected, then $a(E) = 1$ for energies $E \geq E_g$. This case is equivalent to the monochromatic case. For the general case with energy-dependent absorptance $a(E)$ and/or lower mobilities, however, the reciprocity holds only for the spectral quantities $j_{\text{sc}}(E)$ and $j_0(E)$. But unfortunately, this spectral reciprocity does not help, since - as section 3.9.1.1 has shown - there is no simple analytical expression for the low mobility limit of $j_0^{\text{rad}}(E)$.

In the case of low mobilities, carrier collection is limited and the quantum efficiency $\text{EQE}(E)$ is smaller than the absorptance $a(E)$, i.e. even more energy-dependent. Therefore, and because they are weighted with the different spectra $\phi_{\text{sun}}(E)$ and $\phi_{\text{bb}}(E)$, the integrated short circuit current J_{sc} and the integrated saturation current J_0^{rad} feature different low mobility limits.

⁸Note that the reciprocity relation has to consider the angular distribution of solar and black body radiation as well. Therefore, Eq. (3.72) holds only for solar cells with a Lambertian texture that ensures complete directional randomization of the incident light rays.

In sections 3.6.2 and 3.6.3, we have used the equivalence of the low mobility limit of J_{sc} and J_0^{rad} to derive an expression for the critical mobility and later for the modified lifetime $\tau_{\text{norm}}^{\text{mod}}$ from Eq. (3.63). This path is now blocked. For the short circuit current, no simple low mobility limit is available. However, an analytical approximation for J_{sc} can be derived from fitting the results of the numerical simulations with help of the modified lifetime model.

From the simulation results one finds that the low mobility limit of the short circuit current is still proportional to the square-root $\sqrt{\mu_{\text{norm}}}$ according to $J_{sc}/\Phi_{\text{sun}}^{\text{abs}} = c_{\mu}(\vartheta_r)\sqrt{\mu_{\text{norm}}}$, where the proportionality constant $c_{\mu}(\vartheta_r)$ depends on the ratio ϑ_r of radiative and non-radiative lifetime.

Even though being aware of the crudeness of the approximation, I assume that not only under monochromatic illumination with excitation flux $\phi_{\text{sun}}(E)$, but also under illumination with the integrated spectrum Φ_{sun} , the short circuit current can be described with the modified lifetime model resulting in Eq. (3.60). If the cell is thick enough, so that virtually all photons are absorbed during the first transition through the cell, then it holds $F_0 = \Phi_{\text{sun}}^{\text{abs}}$ (see Tab. 3.4) and $F_r = 0$, and Eq. (3.60) simplifies to

$$\frac{J_{sc}}{\Phi_{\text{sun}}^{\text{abs}}} = \frac{k_{\alpha}^2 L_{\text{norm}}^2}{1 - k_{\alpha}^2 L_{\text{norm}}^2} \left(-1 + \frac{\tanh\left(\frac{\alpha_0 d}{L_{\text{norm}}}\right)}{k_{\alpha} L_{\text{norm}}} + \frac{\exp(-k_{\alpha} \alpha_0 d)}{\cosh\left(\frac{\alpha_0 d}{L_{\text{norm}}}\right)} \right). \quad (3.74)$$

Here, the quantity $k_{\alpha} = k_{\text{lam}} \alpha_{\text{sun}} / \alpha_0$ comprises the average absorption coefficient α_{sun} as well as the factor $k_{\text{lam}} = 1$ for plane front surfaces or $k_{\text{lam}} = 2$ for textured surfaces which accounts for the diffraction of light at the textured front surface (with an angle of 60°). As in section 3.7.3, the normalized diffusion length reads as $L_{\text{norm}} = \sqrt{\mu_{\text{norm}} \tau_{\text{norm}}^{\text{mod}}}$, where $\tau_{\text{norm}}^{\text{mod}}$ is the modified lifetime. The modified lifetime is given by $1/\tau_{\text{norm}}^{\text{mod}} = 1/\tau_{\text{norm}}^{\text{nr}} + 1/\tau_{\text{norm}}^{\text{r,mod}}$ according to Eq. (3.63). However, $\tau_{\text{norm}}^{\text{r,mod}}$ is no longer given by Eq. (3.62) because the low mobility limit of J_{sc} and J_0 are not identical. Therefore, we have to extract $\tau_{\text{norm}}^{\text{r,mod}}$ from fitting the numerical results.

To obtain the two unknown quantities k_{α} and $\tau_{\text{norm}}^{\text{r,mod}}$, I proceed as follows: First I fit Eq. (3.74) to the numerical data for $\vartheta_r \gg 1$, where $\tau_{\text{norm}}^{\text{mod}} = \tau_{\text{norm}}^{\text{nr}}$, to obtain k_{α} . Then I extract the modified radiative lifetime $\tau_{\text{norm}}^{\text{r,mod}}$. In analogy to Eq. (3.62), I define $\tau_{\text{norm}}^{\text{r,mod}} = 1/(c_r \tau_{\text{norm}}^{\text{r}})$ and use the radiative lifetime multiplication factor c_r as a fit parameter, which I extract from fitting Eq. (3.74) to the numerical data for $\vartheta_r = 0$. Table 3.4 displays the fit parameters for crystalline silicon, amorphous silicon, and

Tab. 3.4: Parameters obtained from the numerical computation of the critical mobility of crystalline silicon (c-Si), hydrogenated amorphous silicon (a-Si:H), and Cu(In_{1-x}Ga_x)Se₂ (CIGS, $x = 0.26$). The doping density used to compute the radiative lifetimes is ($N_A = 5 \times 10^{16} \text{ cm}^{-3}$).

	$\Phi_{\text{bb}}^{\text{Eg}}/\Phi_{\text{bb}}^{\text{abs}}$ [cm ⁻² s ⁻¹]	$q\Phi_{\text{sun}}^{\text{Eg}}/q\Phi_{\text{sun}}^{\text{abs}}$ [mA cm ⁻²]	τ_r [s]	k_α	c_r	L_{crit} [nm]
c-Si	446/2871	42.7/43.2	4.7×10^{-3}	710	64757	4268
a-Si:H	$6.2/2.7 \times 10^{-5}$	20.76/23.1	6.2×10^{-5}	404	2.7×10^9	138
CIGS	81.4/80.4	40.75/40.7	6.4×10^{-8}	8.36	29.5	109

CIGS.

Figures 3.19b, 3.20b, and 3.21b display the analytical short circuit currents computed with the modified lifetime model as solid lines. The figures show that the modified lifetime approach is capable of capturing the general trends of the short circuit current. However, it is obvious that the approach is too crude to precisely reproduce the numerical simulations. The aberrations between analytical and numerical results are particularly severe in the case of crystalline silicon.

Due to the misfits in the short circuit current, also the analytical results for the open circuit voltage and the efficiency as displayed in Figs. 3.19c,d 3.20c,d, and 3.21c,d deviate from the numerical results. While V_{oc} is hardly influenced because the dependence on J_{sc} is only logarithmic, the efficiency exhibits severe aberrations between analytical and numerical results. For more precise results, one would have to obtain energy-dependent $k_\alpha(E)$ and $c_r(E)$. However, this would significantly complicate the procedure. Moreover, the low mobility limit would also consist of an integral over the energy.

As Figs. 3.19b, 3.20b, and 3.21b demonstrate, the analytically computed short circuit currents intersect the numerically obtained currents when the current is roughly half of the maximum attainable value. This is because the fitting routine to determine the parameter k_α is designed accordingly. Therewith, we are able to give a quite accurate approximation for the critical mobility of the three materials under investigation.

3.9.2 Critical mobility

This section derives a closed-form expression for the critical mobility $\mu_{\text{crit}}(\tau_{\text{nr}})$ of crystalline and amorphous silicon and CIGS from the analytical modified lifetime model developed in the previous section.

The low mobility limit of Eq. (3.74) yields

$$\lim_{\mu_{\text{norm}} \rightarrow 0} \frac{J_{\text{sc}}}{J_{\text{sc}}^{\text{SQ}}} = k_{\alpha} L_{\text{norm}} = k_{\alpha} \sqrt{\mu_{\text{norm}} \tau_{\text{norm}}^{\text{mod}}}. \quad (3.75)$$

Equating Eq. (3.75) at $\mu_{\text{norm}} = \mu_{\text{crit}}$ with the absorptance $a_{\text{sun}}(d)$ (which is unity if the cell is thick enough) for the solar spectrum yields the critical mobility

$$\mu_{\text{crit}}(\vartheta_{\text{r}}) = \frac{a_{\text{sun}}^2(d)}{k_{\alpha}^2 \tau_{\text{norm}}^{\text{mod}}(\vartheta_{\text{r}})} \mu_{\text{ref}} \quad (3.76)$$

in dependence of ϑ_{r} , i.e., the non-radiative lifetime.

With k_{α} and c_{r} obtained from the fits and $a_{\text{sun}}(d) \approx 1$, we compute the critical mobility in dependence of the non-radiative lifetime as

$$\begin{aligned} \mu_{\text{crit}}(\tau_{\text{nr}}) &= \frac{\mu_{\text{ref}}}{k_{\alpha}^2} \left(\frac{1}{\tau_{\text{norm}}^{\text{nr}}} + c_{\text{r}} \tau_{\text{norm}}^{\text{r}} \right) \\ &= \frac{q}{k_{\text{B}} T k_{\alpha}^2 \alpha_0^2 \tau_{\text{nr}}} + \mu_{\text{crit}}^{\text{rad}}, \end{aligned} \quad (3.77)$$

where the critical mobility in the radiative limit is given by

$$\mu_{\text{crit}}^{\text{rad}} = \frac{q \Phi_{\text{bb}}^{\text{Eg}} N_{\text{A}} c_{\text{r}} \tau_{\text{norm}}^{\text{r}}}{k_{\text{B}} T k_{\alpha}^2 \alpha_0^2 n_{\text{i}}^2} = \frac{q}{k_{\text{B}} T} \left(\frac{\Phi_{\text{bb}}^{\text{Eg}} N_{\text{A}}}{k_{\alpha} n_{\text{i}}^2} \right)^2 c_{\text{r}} \tau_{\text{r}}. \quad (3.78)$$

Figures 3.22a-c display the dependency of the critical mobility of c-Si, a-Si:H, and CIGS on the non-radiative lifetime. From inserting the critical mobility in Eq. (3.74), one finds that $J_{\text{sc}}(\mu_{\text{n}} = \mu_{\text{crit}})/\Phi_{\text{sun}}^{\text{abs}} = 0.5$. Therefore, I extract the critical mobility from the numerical simulation as the mobility where the short circuit current has reached 50 % of its maximum value. These values are depicted as solid symbols in Figs. 3.22a-c. As a comparison, the figures also display the mobility, where the current has reached 90 % of its maximum value (open symbols). Depending on the steepness of the absorption spectrum, the mobility needed to achieve 90 % of the current is by a factor of 400 for c-Si, 70 for a-Si:H, and 40 for CIGS larger than the critical mobility μ_{crit} needed to obtain 50 % of the current. This factor is independent of the non-radiative lifetime τ_{nr} .

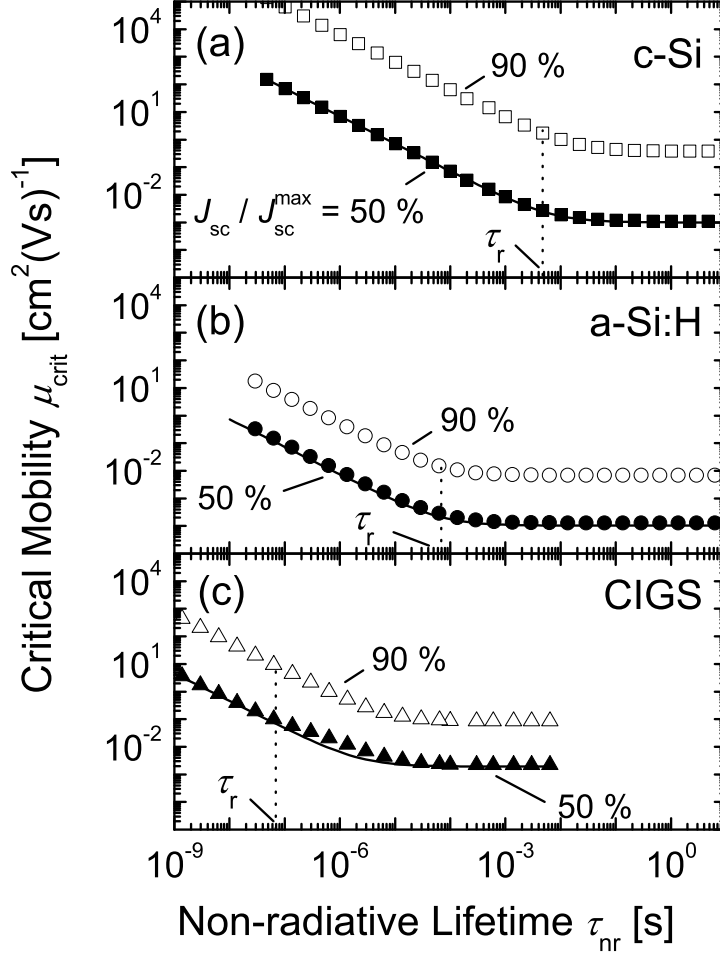


Fig. 3.22: Critical mobility for crystalline silicon (c-Si), hydrogenated amorphous silicon (a-Si:H), and Cu(In,Ga)Se₂ (CIGS, with $x = 0.26$) versus non-radiative lifetime. The critical mobility is inversely proportional to the non-radiative lifetime and saturates once the non-radiative lifetime is much larger than the radiative lifetime τ_r of the respective material. At a doping level $N_A = 5 \times 10^{16} \text{ cm}^{-3}$, it holds $\tau_r = 4.7 \times 10^{-3} \text{ s}$ for c-Si, $\tau_r = 6.2 \times 10^{-5} \text{ s}$ for a-Si:H, and $\tau_r = 6.4 \times 10^{-8} \text{ s}$ for CIGS. The saturation level depends linearly on the doping concentration.

The analytically obtained critical mobilities according to Eq. (3.77) are included in the figures as well (solid lines). Even though the modified lifetime model does not

render the current correctly in the whole mobility and lifetime range, the analytical approximations for the critical mobility are excellent.

From the integrated absorption spectra, one obtains the radiative lifetimes $\tau_r = n_i^2/(N_A R_0)$ with R_0 according to Eq. (B.19). The radiative lifetimes τ_r for the different materials are listed in Tab. 3.4 for a doping density $N_A = 5 \times 10^{16} \text{ cm}^{-3}$. For crystalline silicon, it holds $\tau_r = 4.7 \times 10^{-3} \text{ s}$. This value translates into the radiative recombination constant $B = R_0/n_i^2 = 4.25 \times 10^{-15} \text{ cm}^3 \text{ s}^{-1}$, which corresponds well to the values reported in Ref. [73]. The radiative lifetime in amorphous silicon is $\tau_r = 6.2 \times 10^{-5} \text{ s}$ which strongly depends on the bandtails of the utilized absorption spectrum. The associated radiative recombination coefficient $B = 3.2 \times 10^{-13} \text{ cm}^3 \text{ s}^{-1}$. For CIGS, one obtains $\tau_r = 6.4 \times 10^{-8} \text{ s}$ and $B = 3.1 \times 10^{-10} \text{ cm}^3 \text{ s}^{-1}$ which is comparable to the value of $B = 7 \times 10^{-9} \text{ cm}^3 \text{ s}^{-1}$ published in Ref. [74]

In analogy to the critical mobility with constant absorption coefficient depicted in Fig. 3.11b, μ_{crit} decreases with increasing carrier lifetime and saturates once the radiative recombination limit is reached. For very low non-radiative lifetimes $\tau_{\text{nr}} \ll \tau_r$, μ_{crit} is proportional to $1/\tau_{\text{nr}}$, i.e., the product of μ_{crit} and τ_{nr} is constant. Therefore, the critical mobility translates into a critical diffusion length

$$L_{\text{crit}} = \sqrt{\frac{k_B T \mu_{\text{crit}} \tau_{\text{nr}}}{q}} = \frac{1}{k_\alpha \alpha_0} = L_\alpha, \quad (3.79)$$

which is identical to the average absorption length L_α of the solar spectrum.

Amorphous silicon and CIGS both feature very similar absorption lengths, and, consequently, similar critical diffusion lengths. Crystalline silicon with the larger absorption length has a much larger critical diffusion length. The critical diffusion lengths are listed in Tab. 3.4.

3.9.3 Discussion

This section compares and discusses the photovoltaic performance of the three materials c-Si, a-Si:H, and CIGS as presented in Figs. 3.19a-d 3.20a-d, and 3.21a-d.

Crystalline silicon

Mono-crystalline silicon has a very high electron mobility $\mu_n = 1240 \text{ cm}^2 (\text{Vs})^{-1}$ [17]. With passivated surfaces, at a doping density $N_A = 5 \times 10^{16} \text{ cm}^{-3}$, lifetimes of several

hundreds of microseconds are attainable, (see for example Ref. [75]). Therefore, at such lifetimes, insufficient transport is not an issue. All photo-generated charge carriers are completely collected and the short circuit current has already reached its maximum value. The diffusion lengths are in the range of several hundreds of microns [18], thus by far surpassing the critical diffusion length $L_{\text{crit}} = 4.3 \mu\text{m}$ (cmp. Tab. 3.4). Figure 3.23a depicts the short circuit current of a crystalline silicon solar cell with textured front surface versus the cell thickness. Short circuit currents above $J_{\text{sc}} = 40 \text{ mA cm}^{-2}$ are already achievable with a thickness of $d = 20 \mu\text{m}$. For non-radiative lifetimes $\tau_{\text{nr}} \geq 10 \mu\text{s}$, the current is almost independent of the lifetime. Insufficient carrier collection is only an issue in poly-crystalline silicon solar cells with lifetimes below $\tau = 10 \mu\text{s}$.

High efficiency silicon solar cells are limited by the open circuit voltage. The physical limit is reached when Auger recombination dominates the lifetime. At a doping concentration $N_{\text{A}} = 5 \times 10^{16} \text{ cm}^{-3}$ the Auger lifetime is $\tau_{\text{nr}} = 466 \mu\text{s}$ [76]. Figure 3.23b displays the thickness-dependence of the open circuit voltage for different lifetimes (solid lines). In the Auger limit, the maximum open circuit voltage at a thickness $d = 200 \mu\text{m}$ is $V_{\text{oc}} \approx 750 \text{ mV}$ (cmp. Ref. [77]). This limit is enhanced by another 50 mV by thinning down the solar cell to a thickness of $20 \mu\text{m}$. Existing record solar cells feature open circuit voltages below 710 mV [78]. To achieve higher voltages, thinner solar cells with perfect surface passivation are necessary. Another way to improve the voltage is the usage of *n*-type silicon which is less prone to Shockley-Read-Hall recombination [79].

As Fig. 3.23c demonstrates, the converse thickness-dependence of J_{sc} and V_{oc} leads to an efficiency maximum at $d \approx 20 \mu\text{m}$, which underlines the great potential for reducing the consumption of expensive silicon.

For comparison, Figs. 3.23a-c also include the numerical results without PR (dashed lines). The simulations unveil that the elaborate computations with PR are only necessary for (unrealistically high) non-radiative lifetimes $\tau_{\text{nr}} > 1 \text{ ms}$ and can be readily neglected in physically relevant cases.

Amorphous silicon

Existing amorphous silicon solar cells suffer from very low short circuit currents of $J_{\text{sc}} \leq 17.5 \text{ mA cm}^{-2}$ [80], even though *pin* structures are used to enhance carrier collection. Electron mobilities in intrinsic a-Si:H are in the range of $\mu_{\text{n}} = 1 - 5 \text{ cm}^2 (\text{Vs})^{-1}$ (see

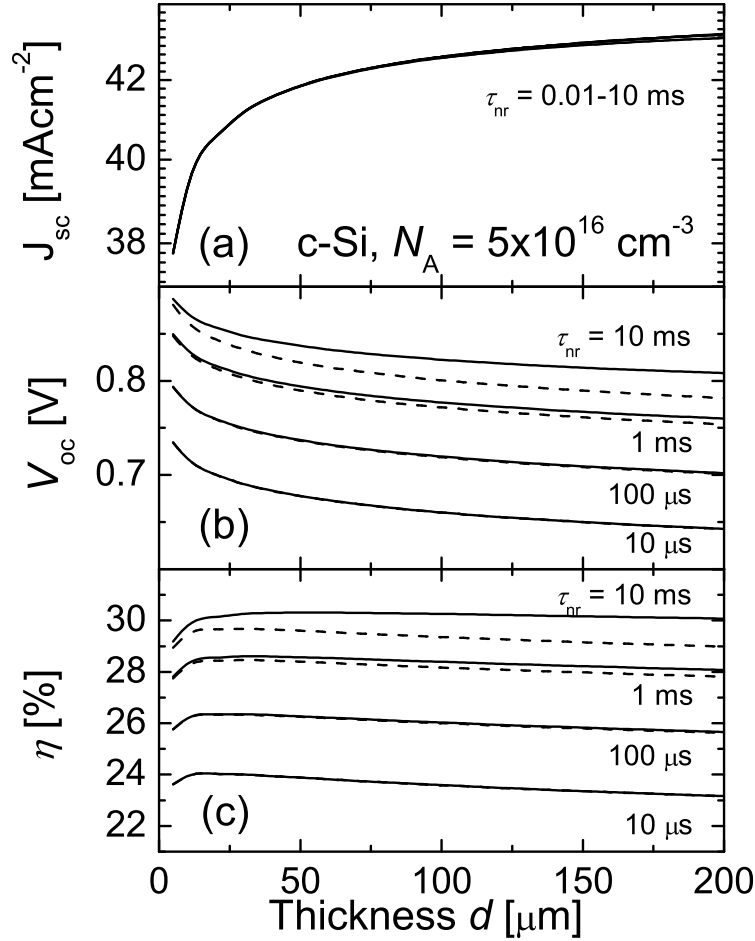


Fig. 3.23: Short circuit current J_{sc} (a), open circuit voltage V_{oc} (b), and efficiency η of a crystalline silicon solar cell versus the cell thickness d for different non-radiative lifetimes τ_{nr} from $\tau_{nr} = 10 \mu\text{s}$ to $\tau_{nr} = 10 \text{ ms}$. The doping concentration is $N_A = 5 \times 10^{16} \text{ cm}^{-3}$, the front surface is textured and all other parameters are identical to the parameters used in Fig. 3.19. Solid lines are the results including PR and dashed lines are the results without PR. While J_{sc} increases with increasing thickness, V_{oc} decreases because of increasing non-radiative bulk recombination. Therefore, the efficiency features a maximum at $d \approx 20 \mu\text{m}$.

for example Refs. [81, 82]). With the critical mobility $\mu_{crit}^{rad} = 8.5 \times 10^{-3} \text{ cm}^2 (\text{Vs})^{-1}$, which allows to collect 90 % of the current, these mobilities would be high enough to

guarantee complete carrier collection in the radiative recombination limit if the device were only limited by electron transport.

However, when looking at hole mobilities, one finds such low values that holes might limit carrier collection even when holes are majority carriers. For hole mobilities we have to distinguish between the band mobility μ_p^{band} that accounts for a mobile hole above the mobility edge and the effective drift mobility μ_p^{eff} that takes into account trapping of the carriers in the valence band tails during their transport to the electrical terminal [83]. The band mobility is $\mu_p^{\text{band}} = 0.3 \text{ cm}^2 (\text{Vs})^{-1}$ [83] or even much larger [84]. However, this quantity is irrelevant for the practical working conditions of the device. Values for the relevant drift mobility μ_p^{eff} range between few times $10^{-4} \text{ cm}^2 (\text{Vs})^{-1}$ and few times $10^{-2} \text{ cm}^2 (\text{Vs})^{-1}$ [83, 84]. When considering a *pin* model that is based on non-radiative recombination Schiff found a critical mobility of about $1 \text{ cm}^2 (\text{Vs})^{-1}$ which by far exceeds the measured values for μ_p^{eff} [5, 83], and therefore proposed the term 'low-mobility solar cells' [5]. As the current considerations show, only the best of the measured values are above the critical value $\mu_{\text{crit}}^{\text{rad}} = 8.5 \times 10^{-3} \text{ cm}^2 (\text{Vs})^{-1}$ that allows to collect 90 % of the available short circuit current density (cf. Fig. 3.22b). Therefore, a-Si:H is a photovoltaic material which comes close to having an inherent mobility problem.

Cu(In,Ga)Se₂

Solar cell absorbers made from Cu(In,Ga)Se₂ (CIGS) exhibit mobilities in the range of $1 - 20 \text{ cm}^2 (\text{Vs})^{-1}$ [85].⁹ Therewith, in the radiative recombination limit, CIGS is not being limited by insufficient carrier collection. The critical mobility to achieve 90 % of the maximal short circuit current in the radiative recombination limit is $\mu_{\text{crit}}^{\text{rad}} = 0.08 \text{ cm}^2 (\text{Vs})^{-1}$.

Whether existing devices are limited by insufficient carrier collection depends on the lifetime. Due to the extremely low radiative lifetime $\tau_r = 64 \text{ ns}$, the material is very tolerant towards non-radiative recombination. Although reported lifetimes are in the low ns range [74, 87], measured diffusion lengths are in the range of $0.5 - 1.5 \mu\text{m}$ [6]

⁹The values reported in Ref. [85] are majority carrier (hole) mobilities. However, the determination of the minority carrier mobilities is rather difficult. Therefore, I use the hole mobilities as a rough estimate for the electron mobilities. In fact, since electrons mostly possess a higher mobility than holes, the values should be regarded as lower limits. An overview is given in Ref. [86]

and thus exceed the critical diffusion length $L_{\text{crit}} = 109 \text{ nm}$. Consequently, insufficient carrier collection is not a problem (for a review of the topic see Ref. [86]).

Moreover, carrier collection is enhanced by collection in the space charge region and by band gap grading [88]. The grading also leads to an effective passivation of the interface to the back contact.

In total, CIGS solar cells are limited by their open circuit voltage rather than by carrier collection [89]. In order to reach higher efficiencies, higher minority carrier lifetimes are the top priority.

3.10 Limitations to the model

Restricting the computation of solar cell efficiencies to a mere minority carrier problem relies on the assumption that the majority carrier concentration is much larger than the minority carrier concentration throughout the solar cell. This situation is termed 'low-level injection'.

The maximum minority carrier concentration is achieved in the radiative recombination limit under open circuit conditions. This is because (i) any additional recombination and (ii) the extraction of carriers under non-open circuit conditions both result in reduced carrier concentrations.

If we neglect thickness-dependent voltage enhancement then for given illumination conditions, the maximum open circuit voltage in the radiative recombination limit is given by the Shockley-Queisser limit $V_{\text{oc}} = V_{\text{oc}}^{\text{SQ}}$. In a p -type semiconductor the majority carrier (hole) concentration is equal to the doping concentration N_{A} . Therewith, it holds for the maximum minority carrier (electron) concentration

$$n^{\text{max}} = \frac{n_{\text{i}}^2}{N_{\text{A}}} \exp\left(\frac{qV_{\text{oc}}^{\text{SQ}}}{k_{\text{B}}T}\right). \quad (3.80)$$

Therefore, the minimum doping concentration necessary to fulfill the low-level injection condition $n^{\text{max}} < N_{\text{A}}$ reads as

$$N_{\text{A}}^{\text{min}} = n_{\text{i}} \exp\left(\frac{qV_{\text{oc}}^{\text{SQ}}}{2k_{\text{B}}T}\right). \quad (3.81)$$

For the above materials, the minimum doping concentrations are $N_{\text{A}}^{\text{min}} = 2.5 \times 10^{17} \text{ cm}^{-3}$ for crystalline silicon, $N_{\text{A}}^{\text{min}} = 2 \times 10^{18} \text{ cm}^{-3}$ for amorphous silicon, and

$N_A^{\min} = 1.6 \times 10^{16} \text{ cm}^{-3}$ for CIGS. Therefore, it is obvious that the doping concentration $N_A = 5 \times 10^{16} \text{ cm}^{-3}$ is too low for crystalline and amorphous silicon once the open circuit voltage approaches the SQ limit. In other words, the computations presented in Figs. 3.19-3.21 are only valid below a voltage $V_{oc}^{\max} = (2k_B T/q) \ln(N_A/n_i)$. For $N_A = 5 \times 10^{16} \text{ cm}^{-3}$, it holds $V_{oc}^{\max} = 0.797 \text{ V}$ for c-Si, $V_{oc}^{\max} = 1.28 \text{ V}$ for a-Si:H, and $V_{oc}^{\max} = 0.98 \text{ V}$ for CIGS.

In that case the problem cannot be treated as a mere minority carrier problem any more. Instead, it requires the simultaneous solution of the generalized drift-diffusion equations for electrons and holes including the photon recycling integrals. At that point, the problem is not linear anymore and the system of equations needs to be solved iteratively. This task, however, will be addressed in a later publication [90] which also encompasses the coverage of *pin* structures.

3.11 Conclusion

This chapter has pointed out the importance of carrier transport for the efficiency of solar cells. Even in the radiative recombination limit the efficiency is reduced drastically once the minority carrier mobility drops below a critical mobility.

In crystalline silicon solar cells, insufficient transport is neither a problem in the radiative limit nor in existing devices. In CIGS, mobilities are at most two orders of magnitude above the critical mobility in the radiative recombination limit. Complete carrier collection is maintained only as long as non-radiative lifetimes are only one or two orders of magnitude below the radiative lifetime. In amorphous silicon, however, drift mobilities of holes are in the range of the critical mobility even in the radiative limit and, therefore, a-Si:H must be considered as having an inherent mobility problem.

While existing solar cells made of crystalline silicon rely almost exclusively on diffusive carrier collection, solar cells made of amorphous silicon utilize *pin* structures to enhance carrier collection and overcome mobility problems (see for example Ref. [5]). In CIGS solar cells, band gap gradings play an analogous role [91].

However, such collection enhancement by means of built-in (quasi-)electric fields is not possible in excitonic solar cells that rely on the diffusive transport of coupled (and therefore neutral) electron/hole pairs (excitons) [92,93]. This explains, why organic or dye-sensitized solar cells as examples of excitonic solar cells suffer from extremely low

short circuit currents although they feature excellent absorptance and lifetimes (for reviews see Refs. [8, 94, 95]). While organic materials are well-suited for light-emitting diodes where transport is not such a big issue [96], their utilization as photovoltaic absorber materials is hampered by the limited diffusive transport of low-mobility excitons.¹⁰ In such devices, insufficient transport not only poses a problem for existing devices but also most probably limits the maximum attainable efficiency in the radiative recombination limit. It is in excitonic solar cells, where the considerations presented in this chapter unfold their real importance.

¹⁰Since doping is irrelevant in excitonic solar cells, the model will not be limited by such strict restrictions as imposed on *pn*-junction solar cells, either.

Chapter 4

Band gap fluctuations

Abstract: This chapter investigates the influence of lateral fluctuations of the fundamental band gap on the global light absorptance and emission spectra of spatially inhomogeneous semiconductors. A model that assumes a Gaussian distribution for the local band gaps yields closed-form expressions for the spectral absorptance and emission. Band gap fluctuations broaden the absorption edge of the fundamental band gap as well as the associated emission peak. The spectral position of the photoluminescence emission peak depends on the length-scale of the fluctuations in relation to the characteristic charge carrier transport length. The model is applied to experimental results from $\text{Cu}(\text{In}_{1-x}\text{Ga}_x)\text{Se}_2$ thin films. The films feature band gap fluctuations with standard deviations between 15 meV and 65 meV which would lead to losses in the open circuit voltage of solar cells made from these films in the range of 5 to 80 mV. The fact that the pure ternary compounds CuInSe_2 and CuGaSe_2 exhibit smaller standard deviations than their quaternary alloys indicates alloy disorder as one possible source of band gap inhomogeneities. The length-scale of the observed fluctuations turns out to be much smaller than the minority carrier diffusion length. Hence, the fluctuations occur on a length-scale below 100 nm.

The previous chapter has analyzed the influence of finite carrier mobility on the radiative efficiency limit of *pn*-junction solar cells. The approach was based on the analysis of the radiative interaction within the solar cell as well as between the solar cell and its ambience. Such radiative interaction consists of (i) light absorption and (ii) light emission.

The absorption of light at a given photon energy E only depends on optical material

properties, i.e. the complex refractive index. Primarily important is the imaginary part expressed as the absorption coefficient $\alpha(E)$, which is a function of the band gap energy E_g of the photovoltaic absorber material (cmp. Tab. 3.2). The emission of light on the other hand does not only depend on optical properties but also on local charge carrier concentrations, i.e. the chemical potential μ .

In the last chapter, the solar cell featured completely homogeneous material properties throughout the entire device. Low minority carrier (electron) mobilities, however, caused non-constant carrier profiles in the direction of current transport, i.e. a vertical spatial variation of the chemical potential over the depth of the solar cell. Therewith, light emission (and consequently, the radiative power conversion efficiency) turned out to depend on the carrier mobility.

This chapter puts a different aspect of the problem into the center of attention, namely material inhomogeneities in form of lateral fluctuations of the band gap energy, as they occur, for instance, in polycrystalline compound semiconductors.

In a manner of speaking, this problem is complementary to the low mobility problem of the previous chapter, where the device had a homogeneous band gap but featured vertical spatial variations of the chemical potential. Now, in contrast, the carrier mobility is assumed to be sufficiently large to guarantee a constant chemical potential throughout the absorber depth. Laterally, however, the band gap fluctuations under certain conditions induce lateral variations of the chemical potential as well.

As will be shown below, the lateral band gap inhomogeneities influence the absorptance and emission spectrum of the semiconductor acting as photovoltaic absorber material. The emission spectrum additionally depends on the lateral variations of the chemical potential. Anticipating the results of the following analysis, the extent to which band gap fluctuations lead to fluctuations of the chemical potential depends on the length-scale of the band gap fluctuations in comparison to the minority carrier diffusion length.

This chapter investigates the influence of this length-scale relationship on the absorption and emission spectra of semiconductors with band gap fluctuations. It presents an analytical statistical model that extends an earlier approach [97,98] in order to extract information about extent and length-scale of fluctuations from global absorption and photoluminescence (PL) measurements. Both, absorptance and emission spectra, are increasingly broadened by increasing band gap inhomogeneities. While the absorp-

tance spectra are not influenced by the length-scale of the band gap fluctuations, the length-scale affects the spectral position of the emission peak.

The chapter is structured as follows. To begin with, I shortly delineate the concept of band gap fluctuations as a form of spatial disorder in a semiconductor's lattice structure and clarify the correlation between band gap fluctuations and other forms of disorder.

The next part presents the theoretical model of the band gap fluctuations. First, the effect of fluctuations on the absorptance spectrum is analyzed, followed by the analysis of the effect on the emission spectrum. Whereas the effect on the absorptance spectrum is independent of the length-scale of the fluctuations, the length-scale significantly determines the emission spectrum. For a comprehensible analysis, I distinguish between fluctuations that occur on a small, a large, and an intermediate length-scale. A numerical simulation reveals that the minority carrier diffusion length is the critical parameter on which the categorization of the fluctuations as being 'small-scale' or 'large-scale' is based.

The last part of the chapter applies the model to experimental data from polycrystalline $\text{Cu}(\text{In}_{1-x}\text{Ga}_x)\text{Se}_2$ thin films commonly used as photovoltaic absorber material in $\text{ZnO}/\text{CdS}/\text{Cu}(\text{In,Ga})\text{Se}_2$ heterojunction solar cells [6]. Such $\text{Cu}(\text{In}_{1-x}\text{Ga}_x)\text{Se}_2$ films are likely to display band gap inhomogeneities due to the high degree of disorder caused by structural defects, spatial fluctuations of stoichiometry and/or alloy composition [86, 99, 100]. Band gap inhomogeneities (see section A.1 and Ref. [98]) or inhomogeneities of the electronic properties [101–103] in such polycrystalline thin films result in reduced power conversion efficiency for solar cells made from such absorbers.

The quantitative statistical analysis of luminescence/absorption spectra yields band gap fluctuations expressed by standard deviations σ_g in a range of $\sigma_g = 15 \text{ meV}$ up to $\sigma_g = 65 \text{ meV}$. In the composition range $x = 0.2$ to $x = 0.5$ that is technologically relevant for $\text{Cu}(\text{In}_{1-x}\text{Ga}_x)\text{Se}_2$ thin film solar cells these inhomogeneities would lead to losses in the open circuit voltage of up to 80 mV. From the analysis I find that the observed band gap fluctuations have a length-scale that is at least ten times smaller than the minority carrier diffusion length in the material.

4.1 Disorder and band gap fluctuations

The well-defined band gap energy of a crystalline semiconductor results from the perfect spatial order, i.e. from the periodicity in the semiconductor's lattice. Any symmetry-breaking disorder in the lattice, i.e. disruption in the crystal's periodicity, splits degenerate electronic states such as the band edges into separate levels and leads to the formation of states in the forbidden gap [104]. These states are observable in the optical absorptance and emission spectra and are commonly described as Urbach tails [105]. The classical interpretation regards band tail states as the result of local disorder leading to localized states in the forbidden gap. However, tail-like absorption and emission can also result from spatial fluctuations of the fundamental band gap [106–108], which can in principle occur on any length-scale.

4.2 Band gap fluctuations model

This section develops a model that describes the absorptance and emission spectra of inhomogeneous semiconductors with lateral fluctuations of the fundamental band gap. Note that besides the band gap fluctuations, inhomogeneities due to a spatially inhomogeneous distribution of charges (electrostatic potential fluctuations) have an additional influence on the final performance of the material in the finished solar cell [86]. However, only band gap fluctuations are detectable by the optical analysis performed in this paper.

Figure 4.1 depicts the general situation of a semiconductor with band gap fluctuations under illumination. The valence band energy E_V^{loc} and the conduction band energy E_C^{loc} fluctuate independently as a function of the spatial coordinate x . As a consequence, the local band gap energy $E_g^{\text{loc}} = E_C^{\text{loc}} - E_V^{\text{loc}}$ fluctuates as well. In the simplest case, the local absorptance a^{loc} will only depend on E_g^{loc} .

In contrast to the previous chapter, the current approach neglects the spatial resolution in the direction normal to the surface of the semiconductor. Since charge carrier transport is assumed to be sufficiently ideal to result in a constant chemical potential throughout the whole absorber depth, the generation profile of carriers is of no interest. Instead of the microscopic absorption coefficient $\alpha(E)$ only the macroscopic absorptance $a(E)$ is needed.

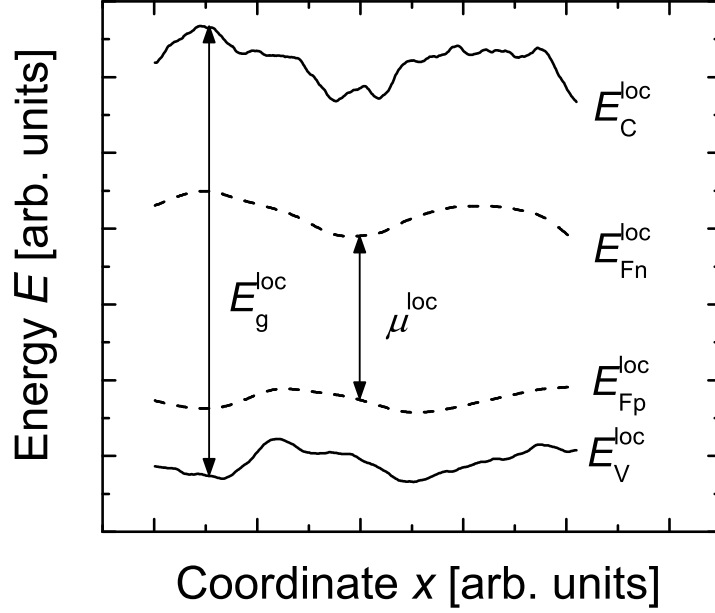


Fig. 4.1: Band diagram of a semiconductor with fluctuations of the local band gap $E_g^{\text{loc}} = E_C^{\text{loc}} - E_V^{\text{loc}}$. These fluctuations of E_g^{loc} lead to fluctuations of the chemical potential $\mu^{\text{loc}} = E_{Fn}^{\text{loc}} - E_{Fp}^{\text{loc}}$.

The illumination of the semiconductor causes a splitting of the local quasi-Fermi levels E_{Fn}^{loc} and E_{Fp}^{loc} of electrons and holes. Because of the spatial variations of the band edges, the excess electrons and holes will move within their lifetime towards the minima or maxima of their respective bands. Therefore, E_{Fn}^{loc} and E_{Fp}^{loc} will have a dependence on x that differs from that of the band edges. This difference is especially important when considering the local chemical potential $\mu^{\text{loc}} = E_{Fn}^{\text{loc}} - E_{Fp}^{\text{loc}}$ that defines the photon emission by radiative electron/hole recombination.

For the sake of simplicity, I neglect tunnelling. Therefore, the radiative recombination of electron/hole pairs is a strictly local process. Moreover, this chapter assumes that the fluctuations of the band edges are small enough that even in regions with small band gap, the quasi-Fermi levels are more than a couple $k_B T$ away from the band edges. Therewith, all emission of radiation remains spontaneous and stimulated

emission of light can be neglected.

4.2.1 Light absorption

Let us assume a locally well-defined band gap E_g^{loc} . In a first order approach, the local absorptance a^{loc} will be given by the step-function $a^{\text{loc}}(E, E_g^{\text{loc}}) = 1$ for photon energies $E \geq E_g^{\text{loc}}$ and $a^{\text{loc}} = 0$ for $E < E_g^{\text{loc}}$. Note that I use the term 'local' for a small region with well-defined constant band gap E_g^{loc} . The term 'global' applies to a considerably larger region comprising a statistically significant number of regions with different local band gaps.

Following the statistical approach of Refs. [97, 98], I use a Gaussian distribution $P_G(E_g^{\text{loc}})$ of the local band gaps E_g^{loc} around a mean band gap \bar{E}_g with a standard deviation σ_g as given by

$$P_G(E_g^{\text{loc}}) = \frac{1}{\sigma_g \sqrt{2\pi}} \exp \left(-\frac{(E_g^{\text{loc}} - \bar{E}_g)^2}{2\sigma_g^2} \right). \quad (4.1)$$

The spatially averaged, global, absorptance a^{glob} is given by the integral of the local absorptance spectrum over the surface area A

$$a^{\text{glob}}(E) = \frac{1}{A} \int_A a^{\text{loc}}(E, E_g^{\text{loc}}(\mathbf{x})) d\mathbf{x}. \quad (4.2)$$

Since the local band gap is the only independent variable determining the absorptance, the areal integral in Eq. (4.2) can be replaced by the integral over the probability distribution $P_G(E_g^{\text{loc}})$ [98]. The global absorptance is then calculated from

$$\begin{aligned} a^{\text{glob}}(E, \bar{E}_g, \sigma_g) &= \int_{-\infty}^{\infty} a^{\text{loc}}(E, E_g^{\text{loc}}) P_G(E_g^{\text{loc}}) dE_g^{\text{loc}} \\ &= \int_{-\infty}^E P_G(E_g^{\text{loc}}) dE_g^{\text{loc}} \\ &= \frac{1}{2} \operatorname{erfc} \left(\frac{\bar{E}_g - E}{\sqrt{2}\sigma_g} \right). \end{aligned} \quad (4.3)$$

Note that the complementary error function in Eq. (4.3) yields the step function at $E = \bar{E}_g$ in the limit $\sigma_g \rightarrow 0$. With increasing σ_g , i.e. with an increasing degree of non-uniformity, the absorptance spectrum is increasingly smeared out as depicted in Fig. 4.2a¹.

¹I use the lower integration limit $-\infty$ only to simplify the solution of the integral and to obey the normalization of the probability function. Assuming the Gaussian probability (4.1) for $E_g^{\text{loc}} < 0$ is justified as long as the mean band gap \bar{E}_g is much larger than the standard deviation σ_g .

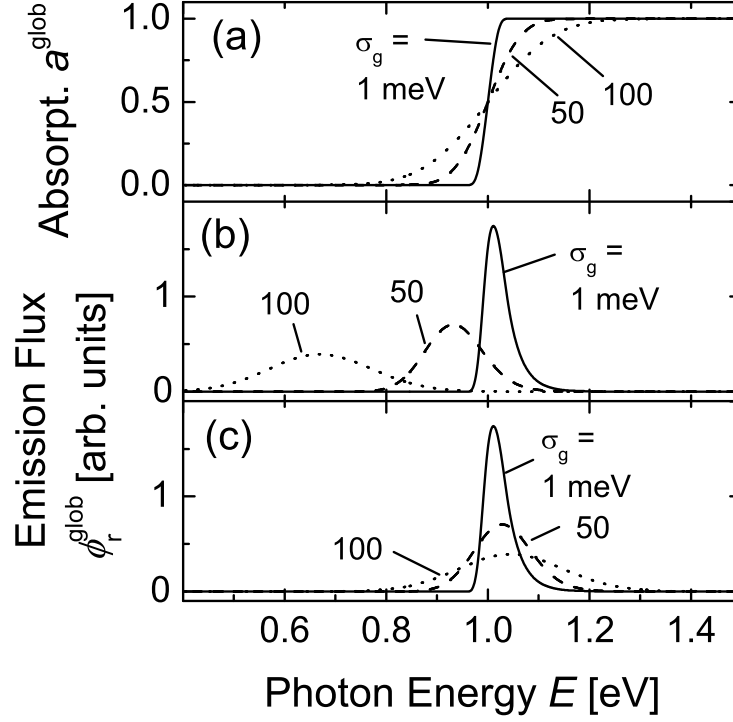


Fig. 4.2: Influence of the standard deviation σ_g on a) the global absorptance spectrum, b) the global spectrum in the case of small-scale fluctuations, and c) the global emission spectrum for large-scale fluctuations. The absorptance curves are calculated from Eq. (4.3). The emission curves are calculated from Eq. (4.28) with $\beta = 0$ in the case of small-scale fluctuations and with $\beta = 1$ in the case of large-scale fluctuations. The average band gap is $\bar{E}_g = 1$ eV. A higher degree of inhomogeneity in terms of higher σ_g leads to a broadening of the spectra. For small-scale fluctuations, the emission peak is shifted towards lower energies (b), whereas the maximum emission of large-scale fluctuations is at the mean band gap energy (c).

4.2.2 Light emission

Light emission of a homogeneous semiconductor is linked to its absorptance via Würfel's generalization of Planck's law [15]. In an inhomogeneous semiconductor, this relation holds on a local level. The locally emitted photon flux ϕ_r^{loc} per energy interval dE is

related to the local absorptance a^{loc} via

$$\phi_r^{\text{loc}}(E)dE = \frac{2\pi}{h^3 c^2} \frac{a^{\text{loc}}(E, E_g^{\text{loc}}) E^2}{\exp\left(\frac{E - \mu^{\text{loc}}}{k_B T}\right) - 1} dE, \quad (4.4)$$

where h is Planck's constant, c is the speed of light, k_B is Boltzmann's constant and T is the absolute temperature. Note that here and in the following all photon fluxes and electron currents are understood as particle current densities per unit surface area.

In analogy to the case of the absorptance spectrum, the global emission spectrum, i.e. the globally emitted photon flux per energy interval

$$\phi_r^{\text{glob}}(E)dE = \frac{2\pi}{h^3 c^2} dE \times \frac{1}{A} \int_A a^{\text{loc}}(E, E_g^{\text{loc}}(\mathbf{x})) E^2 \exp\left(-\frac{E - \mu^{\text{loc}}(\mathbf{x})}{k_B T}\right) d\mathbf{x} \quad (4.5)$$

is obtained by the areal integral over the local emission spectra. Note that Eq. (4.5) uses the Boltzmann approximation of Eq. (4.4), which is valid as long as $E - \mu^{\text{loc}} \gg k_B T$.

Unlike in Eq. (4.2), we now have *two* variables, $E_g^{\text{loc}}(\mathbf{x})$ and $\mu^{\text{loc}}(\mathbf{x})$ that depend on the spatial coordinate \mathbf{x} . Hence, to solve the integral in Eq. (4.5), we would have to calculate $\mu^{\text{loc}}(\mathbf{x})$ for an explicitly given distribution $E_g^{\text{loc}}(\mathbf{x})$. A rigorous treatment would have to solve the two- or three-dimensional continuity equation for the minority and majority charge carriers (cmp. for instance Ref. [109]).

This chapter chooses a different approach by postulating that μ^{loc} is reasonably well approximated by

$$\mu^{\text{loc}} = \mu^{\text{loc}}(E_g^{\text{loc}}). \quad (4.6)$$

Thus, we reduce Eq. (4.5) again to an integration over the band gap distribution according to

$$\phi_r^{\text{glob}}(E)dE = \frac{2\pi}{h^3 c^2} dE \int_{-\infty}^E P_G(E_g^{\text{loc}}) E^2 \exp\left(-\frac{E - \mu^{\text{loc}}(E_g^{\text{loc}})}{k_B T}\right) dE_g^{\text{loc}}. \quad (4.7)$$

Note that the assumption made in Eq. (4.6) is necessary to transform the geometrical transport problem hidden in Eq. (4.5) into the statistical integral of Eq. (4.7). I am aware that Eq. (4.6) is not strictly fulfilled for any pair of $E_g^{\text{loc}}(x)$, $\mu^{\text{loc}}(x)$ but represents a correlation that holds when averaging over large areas.

In the following, I introduce two limiting cases for which Eq. (4.7) provides the exact solution of Eq. (4.5). These limiting cases are defined by the comparison of the

characteristic length L_g of the band gap fluctuations with the characteristic length L_μ of the charge carrier transport. Note that the definition of L_μ is not straight forward in the general case where transport of both kinds of carriers is equally important. However, in the situation where one kind of carriers is clearly identified as minorities, L_μ equals the minority carrier diffusion length L_n . For the treatment of the general statistical problem, we define the quantities L_g and L_μ as the autocorrelation lengths of E_g^{loc} and μ^{loc} as shown in section 4.2.2.3. In analogy to Ref. [110], I distinguish three cases:

- i) *Small-scale fluctuations*, $L_g \ll L_\mu$: In this situation, the flow of carriers will lead to a complete flattening of the quasi-Fermi levels. Consequently, the chemical potential is constant as sketched in Fig. 4.3a.
- ii) *Large-scale fluctuations*, $L_g \gg L_\mu$: Here, transport of carriers within their lifetime can be readily neglected. All photo-generated carriers recombine at the location of their generation. Consequently, the chemical potential will follow the band gap energy as sketched in Fig. 4.3b.
- iii) *Intermediate length-scale*, $L_g \approx L_\mu$: In this situation, μ^{loc} only reproduces the features of E_g^{loc} that have a small spatial frequency as sketched in Fig. 4.3c.

4.2.2.1 Small-scale fluctuations

If the length-scale of band gap fluctuations is very small compared to L_μ , we have

$$\mu^{\text{loc}} = \mu_0 = \text{const.} \quad (4.8)$$

Consequently, the integration of Eq.(4.7) is carried out in analogy to Eq.(4.3) and we obtain the global spectral emission

$$\phi_r^{\text{glob}}(E)dE = \frac{\pi}{h^3 c^2} \text{erfc} \left(\frac{\bar{E}_g - E}{\sqrt{2}\sigma_g} \right) E^2 \exp \left(-\frac{E - \mu_0}{k_B T} \right) dE. \quad (4.9)$$

Steady state During PL measurements, the sample is in a global steady state. In steady state, no external currents are flowing and for the splitting of the quasi-Fermi levels it holds $\mu^{\text{loc}} = \mu = \mu_{\text{ss}}$ (cf. Fig. 4.3a). In this case, the sum of radiative and non-radiative recombination current $J_{\text{rec}} = \Phi_r^{\text{glob}} + J_{\text{nr}}$ is equal to the impinging photon flux

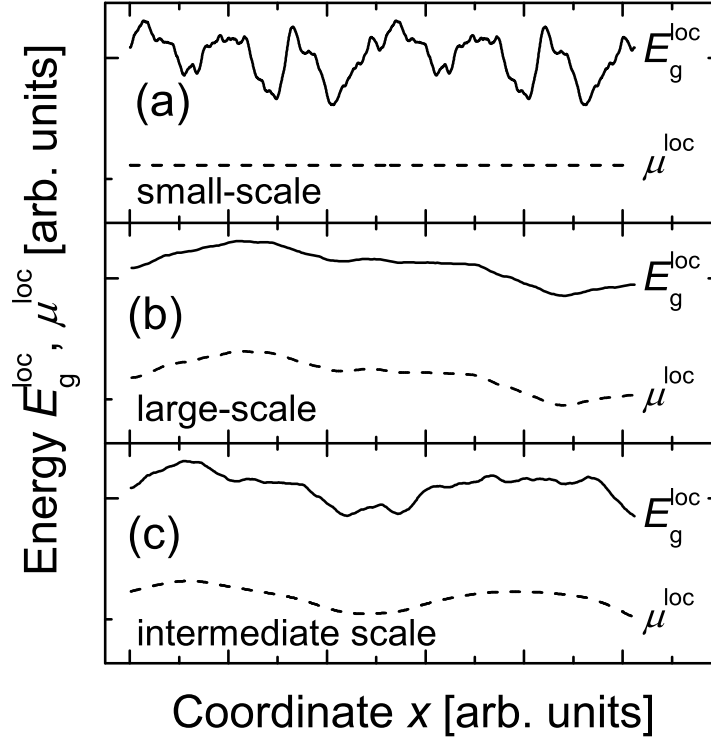


Fig. 4.3: Sketch of a semiconductor with spatial variations in the local band gaps E_g^{loc} under illumination. Also depicted are the resulting chemical potentials μ^{loc} for the case of a) small-scale fluctuations, where the typical fluctuation length L_g of the band gap fluctuations is much smaller than the characteristic transport length L_μ , b) large-scale fluctuations where L_g is much larger than L_μ , and c) fluctuations with intermediate length-scale. In the case of large-scale fluctuations (b), the variations in μ^{loc} reproduce the variations in E_g^{loc} . For smaller length-scales of the band gap fluctuations (c), compensating currents level out differences in the chemical potential. In case (a), μ^{loc} is constant throughout the entire semiconductor.

Φ_γ . If one type of carriers is clearly identified as minorities, the ratio of non-radiative and radiative recombination current is determined by the ratio $\vartheta_r = J_{\text{nr}}/\Phi_r^{\text{glob}} = \tau_r/\tau_{\text{nr}}$ of radiative lifetime τ_r and non-radiative lifetime τ_{nr} . Therewith, the steady state

condition $J_{\text{rec}} = \Phi_\gamma$ yields

$$\Phi_r^{\text{glob}} = (1 + \tau_r/\tau_{\text{nr}})^{-1} \Phi_\gamma \approx \frac{\Phi_\gamma}{\vartheta_r}, \quad (4.10)$$

where the last term holds if $\tau_r \gg \tau_{\text{nr}}$. Following [98], the global radiative recombination current

$$\Phi_r^{\text{glob}} = \int_0^\infty \phi_r^{\text{glob}}(E) dE = \frac{2\pi k_B T}{h^3 c^2} E_1^2 \exp\left(-\frac{2(\bar{E}_g - \mu) k_B T - \sigma_g^2}{2(k_B T)^2}\right), \quad (4.11)$$

where E_1^2 is given by

$$E_1^2 = (\bar{E}_g + k_B T)^2 + (k_B T)^2 - \sigma_g^2(2\bar{E}_g/k_B T + 1) + \sigma_g^4/(k_B T)^2, \quad (4.12)$$

is obtained from integrating Eq. (4.9) over the photon energy E . Using the steady state condition Eq. (4.10) and solving for $\mu = \mu_{\text{ss}}$ allows us to derive an expression for $\mu = \mu_{\text{ss}}$ under steady state conditions

$$\mu_{\text{ss}} = \bar{E}_g + k_B T \ln\left(\frac{c^2 h^3 \Phi_\gamma}{2\pi \vartheta_r k_B T E_1^2}\right) - \frac{\sigma_g^2}{2k_B T}. \quad (4.13)$$

By inserting Eq. (4.13) into Eq. (4.9) we obtain the spectral emission under steady state conditions

$$\begin{aligned} \phi_r^{\text{glob}}(E) dE &= \frac{\Phi_\gamma}{2\vartheta_r k_B T E_1^2} \exp\left(\frac{2\bar{E}_g k_B T - \sigma_g^2}{2(k_B T)^2}\right) \times \\ &\quad \text{erfc}\left(\frac{\bar{E}_g - E}{\sqrt{2}\sigma_g}\right) E^2 \exp\left(\frac{-E}{k_B T}\right) dE. \end{aligned} \quad (4.14)$$

4.2.2.2 Large-scale fluctuations

In the large-scale situation, the photogenerated charge carriers recombine before moving to (distant) regions with different band gap E_g^{loc} . Because of this lack of lateral interaction, each region has to be in a steady state condition, i.e. locally, the total recombination current $J_{\text{rec}}^{\text{loc}}$ equals the excitation flux Φ_γ ². Now, the steady state condition holds on a local as well as on a global level.

²During PL measurements the sample is illuminated with laser light at a wavelength $\lambda = 488 \text{ nm}$ which corresponds to a photon energy $E = 2.54 \text{ eV}$ that is much larger than the common average band gaps of approx. 1.2 eV . Therefore, the local excitation flux $\Phi_\gamma^{\text{loc}} = \Phi_\gamma$ is roughly independent of the local band gap E_g^{loc} .

Locally, radiative as well as non-radiative recombination currents depend on the band gap. However, in the case of bulk recombination both currents obey roughly the same dependency on the band gap. Therewith, the ratio of local radiative and non-radiative recombination current is independent of the band gap E_g^{loc} . For a doped semiconductor this ratio is determined by the ratio ϑ_r of radiative lifetime τ_r and non-radiative lifetime τ_{nr} , which are roughly independent of the band gap (cf. section 4.3.1).

The overall local radiative recombination current

$$\Phi_r^{\text{loc}} = \int_E \phi_r^{\text{loc}}(E, E_g^{\text{loc}}) dE = \frac{\Phi_\gamma}{\vartheta_r} = \text{const.} \quad (4.15)$$

is obtained by integrating Eq. (4.4) over the photon energy dE and equals a constant fraction of the excitation flux. This equation allows us to compute the hitherto unknown dependence of the local chemical potential μ^{loc} on E_g^{loc} under steady state conditions with $\mu^{\text{loc}} = \mu_{\text{ss}}^{\text{loc}}$. Inserting Eq. (4.4) into Eq. (4.15) yields

$$\Phi_r^{\text{loc}} = \frac{2\pi}{h^3 c^2} \int_{E_g^{\text{loc}}}^{\infty} E^2 \exp\left(-\frac{E - \mu_{\text{ss}}^{\text{loc}}}{k_B T}\right) dE. \quad (4.16)$$

Solving this integral and rearranging the result leads to

$$\begin{aligned} \mu_{\text{ss}}^{\text{loc}}(E_g^{\text{loc}}) &= E_g^{\text{loc}} + k_B T \ln\left(\frac{h^3 c^2 \Phi_\gamma}{2\pi \vartheta_r k_B T}\right) \\ &\quad - k_B T \ln\left(\{(E_g^{\text{loc}} + k_B T)^2 + (k_B T)^2\}\right). \end{aligned} \quad (4.17)$$

The knowledge of $\mu_{\text{ss}}^{\text{loc}}(E_g^{\text{loc}})$ now allows us to compute the spectral dependence of the global emission $\phi_r^{\text{glob}}(E)$ with help of Eq. (4.7). The resulting integral can only be solved numerically. However, approximating E_g^{loc} with \bar{E}_g in the logarithmic term in Eq. (4.17) leads to a simple linear relationship

$$\mu_{\text{ss}}^{\text{loc}}(E_g^{\text{loc}}) = E_g^{\text{loc}} - \text{const.} \quad (4.18)$$

In the next section I use a generalization of this approach to derive an expression for the emission under steady state conditions for any length-scale of the band gap fluctuations with respect to the characteristic transport length.

4.2.2.3 Intermediate length-scale

The last two sections have shown that the splitting of the quasi-Fermi levels is constant $\mu^{\text{loc}} = \mu_0$ in the case of small-scale fluctuations and that it is roughly equal to the local

band gap reduced by a constant according to $\mu_{\text{ss}}^{\text{loc}} = E_{\text{g}}^{\text{loc}} - \text{const}$ in the case of large-scale fluctuations. In the general case of intermediate length-scales, the simplest approach is to assume a linear superposition of these two cases namely to assume that μ^{loc} consists of a constant part and a part that depends linearly on the local band gap according to

$$\mu^{\text{loc}} = \mu_0 + \beta E_{\text{g}}^{\text{loc}} \quad (4.19)$$

where the local chemical potential consists of a constant part μ_0 and a part that is linearly fluctuating with $E_{\text{g}}^{\text{loc}}$. The constant factor β with $0 \leq \beta \leq 1$ is the quantity that contains the information about the length-scale of the fluctuations. In the following I will show that β is equal to the ratio $\sigma_{\mu}/\sigma_{\text{g}}$ of the standard deviations for band gap and chemical potential. Subsequently, I derive an expression that relates β to the ratio L_{μ}/L_{g} of the typical length-scales of the respective fluctuations.

Inserting Eq. (4.19) into Eq. (4.1) yields

$$\begin{aligned} P_{\text{G}}(E_{\text{g}}^{\text{loc}}) &= \frac{1}{\sigma_{\text{g}}\sqrt{2\pi}} \exp\left(\frac{-(\mu^{\text{loc}} - \mu_0 - \beta \bar{E}_{\text{g}})^2}{2\beta^2\sigma_{\text{g}}^2}\right) \\ &= \frac{\beta}{\sigma_{\mu}\sqrt{2\pi}} \exp\left(\frac{-(\mu^{\text{loc}} - \bar{\mu})^2}{2\sigma_{\mu}^2}\right) = \beta P_{\text{G}}(\mu^{\text{loc}}) \end{aligned} \quad (4.20)$$

and therewith the probability density $P(\mu^{\text{loc}})$ of the chemical potential which is determined by the mean chemical potential $\bar{\mu} = \mu_0 + \beta \bar{E}_{\text{g}}$ and the standard deviation $\sigma_{\mu} = \beta\sigma_{\text{g}}$. Thus, it follows

$$\beta = \sigma_{\mu}/\sigma_{\text{g}}. \quad (4.21)$$

Next, I derive an expression that relates $\sigma_{\mu}/\sigma_{\text{g}}$ to the length-scale of the band gap fluctuations. As pointed out above, I will not attempt to find the exact solution of the drift-diffusion equation. Instead I provide an approximate approach that makes use of the Fourier transforms for stochastic processes³.

Basically, the spatial distribution of the chemical potential can be regarded as a filtered distribution of $E_{\text{g}}^{\text{loc}}$ where the fractions with large spatial frequency have been cut off. By using some useful theorems of Fourier transforms for stochastic processes [111] we arrive at the desired relationships between standard deviations and fluctuation lengths.

³For details concerning Fourier transforms of stochastic processes, see, e.g., Ref. [111].

The spatial distribution of band gaps is not entirely uncorrelated but instead obeys an autocorrelation function R_g which states that the probability to find a certain band gap E_g^{loc} at a given position will also depend on the neighboring band gaps. This spatial correlation becomes immediately plausible by considering the origin of band gap fluctuations. For instance, the alloy composition may exhibit lateral fluctuations. However, there are always compensating processes that prohibit too steep variations.

Mostly, local interaction is restricted to the immediate vicinity of a given location. With increasing distance the correlation decreases strongly. To obtain integrable functions ⁴ I assume

$$R_g(\mathbf{x}) = \exp\left(\frac{-\mathbf{x}^2}{L_g^2}\right), \quad (4.22)$$

where \mathbf{x} is the distance vector between the two correlated locations and the correlation length L_g describes the length-scale of the fluctuations. Then the power spectrum of the distribution

$$\begin{aligned} S_g(\mathbf{k}) &= \int_{-\infty}^{\infty} \exp(-i\mathbf{k}\mathbf{x}) R_g(\mathbf{x}) d\mathbf{x} \\ &= \left(\frac{L_g}{\sqrt{2}}\right)^{\dim} \exp\left(\frac{-L_g^2 \mathbf{k}^2}{4}\right), \end{aligned} \quad (4.23)$$

where \mathbf{k} is the spatial frequency, is given by the spatial Fourier transform of R_g (cf. Ref. [111], p. 319). Depending on the dimension \dim of the fluctuations, the integral in Eq. (4.23) is multidimensional. Integrating over the whole power spectrum yields the standard deviation

$$\sigma_g^2 = \frac{1}{2\pi} \int_{-\infty}^{\infty} S_g(\mathbf{k}) d\mathbf{k} \quad (4.24)$$

as a measure for the overall power contained in the fluctuations (for a mean band gap $\bar{E}_g = 0$) [111, p. 106, 288].

The advantage of using Fourier transforms is that we are now able to deduce the power spectrum of the chemical potential μ^{loc} by applying a filter to the power spectrum S_g . If the length-scale of the band gap fluctuations is too short than the chemical potential does not reproduce the fluctuations exactly but only to an alleviated degree.

⁴Other approaches such as $R_g(\mathbf{x}) = \exp\left(\frac{-\mathbf{x}}{L_g}\right)$ qualitatively lead to equivalent results but do not provide analytic solutions for fluctuations that occur in more than one dimension.

In the spatial frequency space, this means that band gap fluctuations with high spatial frequency are not reproduced by the chemical potential. Effectively, the power spectrum of the chemical potential is the result of applying a low-pass filter to the power spectrum S_g of the band gap distribution. The relevant quantity determining the filter is the correlation length of the chemical potential L_μ . Band gap fluctuations with a higher spatial frequency can not be reproduced and are cut off by the filter. At the moment, L_μ is an unknown quantity. However, as will be shown in section 4.3, L_μ equals the minority carrier diffusion length L_n if one type of carriers is clearly identified as minorities. In analogy to Eq. (4.23) I assume a Gaussian filter

$$F(\mathbf{k}) = \exp(-L_\mu^2 \mathbf{k}^2 / 4) \quad (4.25)$$

and can thus compute the standard deviation of μ^{loc} as

$$\sigma_\mu^2 = \frac{1}{2\pi} \int_{-\infty}^{\infty} \exp\left(\frac{-L_\mu^2 \mathbf{k}^2}{4}\right) S_g(\mathbf{k}) d\mathbf{k}. \quad (4.26)$$

Performing the integrations in Eq. (4.24) and Eq. (4.26) and combining the two equations yields the length-scale coefficient

$$\beta = \frac{\sigma_\mu}{\sigma_g} = \frac{1}{((L_\mu/L_g)^2 + 1)^{dim/4}} \quad (4.27)$$

as a function of the length-scale ratio. Here, dim denotes the dimension of the band gap fluctuations, that is $dim = 2$ in the case of lateral fluctuations⁵. It is readily seen from Eq. (4.27) that we have $\beta = 0$ for $L_g \ll L_\mu$ (small-scale fluctuations) and $\beta = 0$ for $L_g \gg L_\mu$ (large-scale fluctuations). Thus, Eq. (4.19) represents a *general* approach that applies to all length-scales.

Inserting Eq. (4.19) into Eq. (4.7) and integrating over E_g^{loc} yields the global emission spectrum

$$\begin{aligned} \phi_r^{\text{glob}}(E) dE &= \frac{\pi}{h^3 c^2} \text{erfc}\left(\frac{\bar{E}_g - E + \beta \sigma_g^2 / k_B T}{\sqrt{2} \sigma_g}\right) \times \\ &E^2 \exp\left(-\frac{E - \mu_0 - \beta \bar{E}_g}{k_B T} + \frac{\beta^2 \sigma_g^2}{2(k_B T)^2}\right) dE. \end{aligned} \quad (4.28)$$

⁵Note that the choice of the auto-correlation function R_g and especially the filter for μ^{loc} is somewhat arbitrary and is not based on physical reasoning. The analytical expression Eq. (4.27) is an approximation that is not applicable if the actual autocorrelation function and filter function deviate significantly from the above assumptions.

After integration over the photon energy E and by using the global steady state condition Eq. (4.10) we find

$$\mu_0^{\text{ss}} = (1 - \beta)\bar{E}_g + k_B T \ln \left(\frac{h^3 c^2 \Phi_\gamma}{2\pi \vartheta_r k_B T E_2^2} \right) - \frac{(1 - \beta)^2 \sigma_g^2}{2k_B T} \quad (4.29)$$

with

$$E_2^2 = (\bar{E}_g + k_B T)^2 + (k_B T)^2 + (1 - \beta)^2 \sigma_g^4 / (k_B T)^2 + \sigma_g^2 (2\beta - 1 - 2\bar{E}_g(1 - \beta)/k_B T). \quad (4.30)$$

Inserting these expressions into Eq. (4.28) finally results in the global emission spektrum

$$\phi_r^{\text{glob}}(E) dE = \frac{\vartheta_r \Phi_\gamma}{2k_B T E_2^2} \exp \left(\frac{2\bar{E}_g k_B T - \sigma_g^2}{2(k_B T)^2} \right) \times \text{erfc} \left(\frac{\bar{E}_g - E + \beta \sigma_g^2 / k_B T}{\sqrt{2} \sigma_g} \right) E^2 \exp \left(-\frac{E}{k_B T} \right) dE. \quad (4.31)$$

With Eq. (4.31) we now have an expression that describes the emission spectrum for a semiconductor with inhomogeneous band gap for all possible length-scales of the band gap fluctuations. In the limit of small-scale fluctuations with $L_g \ll L_\mu$ and thus $\beta = 0$, Eq. (4.31) turns into Eq. (4.14). In the case of large-scale fluctuations with $L_g \gg L_\mu$ and $\beta = 1$, the approach (4.19) which results in Eq. (4.31) does not yield the exact situation as described by Eq. (4.17) where all subdomains are independently under steady state conditions. Even though the sample is under global steady state conditions, the local steady state conditions are not necessarily fulfilled. However, Eq. (4.31) provides a reasonable approximation which is valid as long as $\sigma_g \ll \bar{E}_g$. Figure 4.4 demonstrates that for a medium band gap $\bar{E}_g = 1 \text{ eV}$ the differences between the emission spectra according to the numerical solution of Eq. (4.7) with μ^{loc} given by Eq. (4.17) on the one hand and the analytical approximation Eq. (4.31) on the other hand are negligible for $\sigma_g < 100 \text{ meV}$.

4.2.3 Discussion

Figure 4.2b depicts the emission current in the case of small-scale band gap fluctuations according to Eq. (4.14) with $\bar{E}_g = 1 \text{ eV}$ and $\sigma_g = 50 \text{ meV}$ and 100 meV . The figure shows how band gap fluctuations with the resulting broadening of the absorption transition also broaden the emission peak. Due to the exponential dependence of the

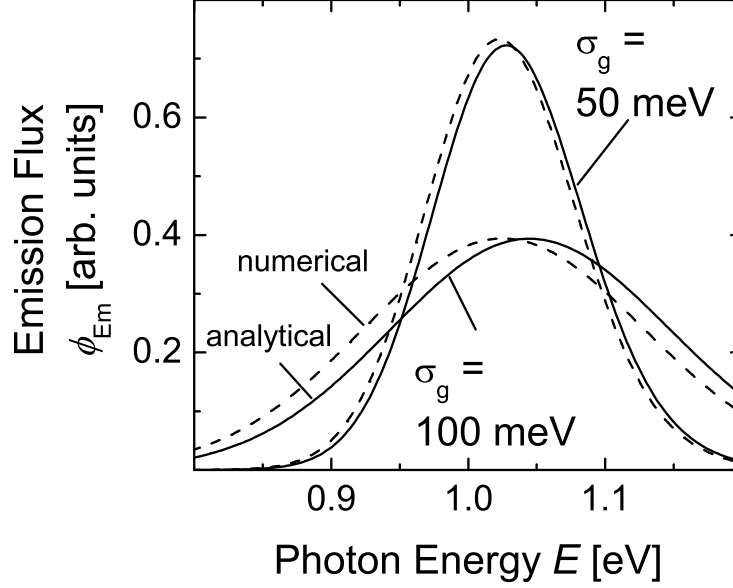


Fig. 4.4: Luminescence spectra in the case of large-scale fluctuations. Comparison between numerical solution of Eq. (4.7) with $\mu^{\text{loc}} = \mu_{\text{ss}}^{\text{loc}}$ according to Eq. (4.17) (dashed lines) and the analytical approximations Eq. (4.31) with $\beta = 1$ (solid lines) for $\bar{E}_g = 1$ eV and $\sigma_g = 50$ meV or 100 meV. For standard deviations σ_g larger than 100 meV the difference between the analytical approximation and the the numeric solution becomes more pronounced.

emission spectrum on the photon energy, a small increase of the absorption at lower energies results in an amplified increase of the corresponding emission, whereas a small increase of the absorption at higher energies results only in a reduced increase of the emission. Therefore, the position of the emission peak is shifted towards lower energies for more inhomogeneous samples.

Figure 4.2c displays the emission spectrum for large-scale fluctuations according to Eq. (4.31) with $\beta = 1$. As in the case of small-scale fluctuations, the emission peak of an increasingly inhomogeneous sample is broadened. But whereas small-scale band gap fluctuations lead to a shift of the emission peak towards lower photon energies, large-scale fluctuations leave the position of the peak unchanged at the average band gap \bar{E}_g .

Note that for identical σ_g the only difference between the spectra in Figs. 4.2b and 4.2c is the position of the peak. Spectral shape and magnitude of the spectra and, as a consequence, the integrated emission spectra are the same. Since both cases are under steady state conditions, the global recombination current is equal to the impinging photon flux and it holds in all cases $\Phi_r^{\text{glob}} = \Phi_\gamma/\vartheta_r$ according to Eq. (4.10).

Therefore, the position of the emission peak relative to the absorption edge yields information about the length-scale of the band gap fluctuations. Fitting Eq. (4.3) and Eq. (4.31) to a set of experimental absorptance and PL data yields the average band gap \bar{E}_g , the standard deviation σ_g , and the length-scale ratio L_μ/L_g . We can thus extract extent and length-scale of the measured inhomogeneities from experimental absorption and emission data, as will be shown in section 4.4. First, however, we need to analyze the relationship between the fluctuation length L_μ of the chemical potential and the minority carrier diffusion length L_n .

4.3 Numerical approach

In the previous sections I have only provided hand-waving arguments for the alleged agreement of the correlation length L_μ of the chemical potential μ with the diffusion length L_n in the situation where one type of carriers is clearly defined as minorities. As plausible as the reasoning might seem - the compensating lateral currents are not driven by carrier diffusion alone. The band gap fluctuations also lead to local quasi-electric fields that cause minority carrier drift currents. Drift and diffusion currents both depend on the strength and the length-scale of the band gap fluctuations, i.e. on σ_g and L_g . It is thus not completely clear, whether the resulting correlation length L_μ really is identical to the diffusion length L_n .

This section provides a numerical solution of the drift-diffusion equation to verify the results of the above analytical model and to show that the diffusion length indeed represents a very good indicator to approximate the correlation length L_μ of the chemical potential.

Osvald [109] investigates a very similar problem consisting of a Schottky diode with spatial variations of the Schottky barrier. However, while he needs to simultaneously solve the drift-diffusion equation and the Poisson equation to solve the problem, here, the band gap is not only preset as a boundary condition but throughout the entire

sample. Thus, the band diagram is already known and we do not need to additionally solve the Poisson equation.

4.3.1 Formulation of the problem

For the sake of simplicity, I assume that all band gap fluctuations occur in the conduction band as depicted in Fig. 4.5. The valence band features no variations and is constant throughout the entire semiconductor. Moreover, I treat the problem as a pure minority carrier problem. The quasi Fermi level E_{Fp} of the holes is invariant as well. Thus, the majority carrier concentration does not fluctuate and is given by the doping density N_{A} . Furthermore, the fluctuations of the conduction band are assumed to be sufficiently small, such that even in regions with small band gap, the electron concentration is still decisively smaller than the hole concentration.

The simplification of assuming that all band gap fluctuations occur in the conduction band, is only a special case of the general case depicted in Fig. 4.1. Therewith, the numerical results obtained in this section are not as general as the results obtained with the analytical model. However, the approximation is sufficient to show the relevance of the diffusion length for the length-scale of the chemical potential.

In general, the drift-diffusion equation for the minority carriers can be written as [112]

$$\nabla (n_0 \nabla u) - \frac{n_0 u}{L_{\text{n}}^2} = -\frac{g}{D_{\text{n}}}. \quad (4.32)$$

Here, D_{n} is the electron diffusion constant and $g(\mathbf{x})$ is the generation rate. The equilibrium electron concentration is determined by the local band gap according to

$$n_0(\mathbf{x}) = \frac{n_{\text{i}}^2}{p_0} = \frac{N_{\text{C}} N_{\text{V}}}{N_{\text{A}}} \exp \left(-\frac{E_{\text{g}}(\mathbf{x})}{k_{\text{B}} T} \right). \quad (4.33)$$

The normalized excess electron concentration is given by

$$u(\mathbf{x}) = \frac{n(\mathbf{x}) - n_0(\mathbf{x})}{n_0(\mathbf{x})}. \quad (4.34)$$

Equation (4.32) assumes a spatially constant lifetime τ_{n} and, therewith, a constant diffusion length L_{n} . Such an assumption is only valid if the lifetime is independent of the band gap.

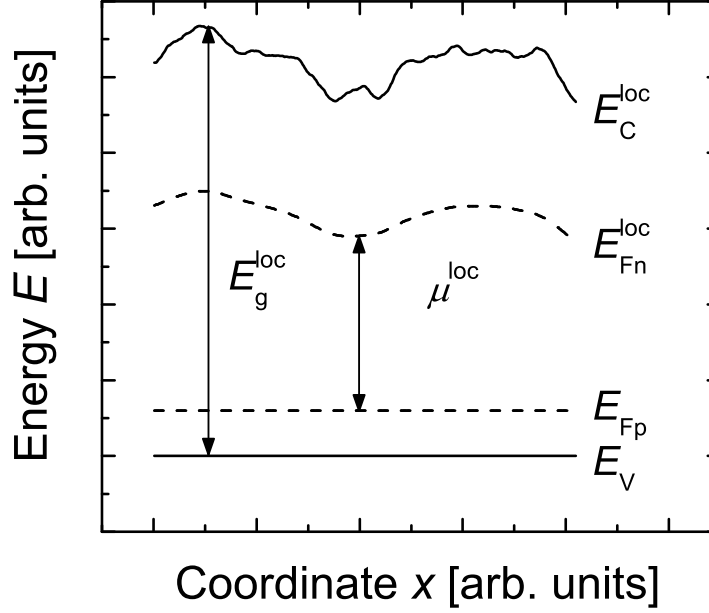


Fig. 4.5: Band diagram of a semiconductor under illumination with band gap fluctuations E_g^{loc} that occur only in the conduction band E_C^{loc} . These fluctuations of E_C^{loc} lead to fluctuations of the electron quasi Fermi level E_{Fn}^{loc} , i.e., to fluctuations of the chemical potential μ^{loc} . Both, the valence band edge E_V and the hole quasi Fermi level E_{Fp} , are constant.

The equilibrium electron concentration n_0 and the equilibrium radiative recombination rate R_0 (cmp. Eq. (B.19)) feature the same exponential dependence on the band gap. Apart from the small polynomial dependence in the denominator of Eq. (B.19), the radiative lifetime $\tau_r(\mathbf{x}) = n_0/R_0$ is therefore largely independent of the band gap. If we assume Shockley-Read-Hall (SRH) recombination through defects as the predominant non-radiative recombination mechanism, then the non-radiative lifetime is also mainly independent of the band gap as long as the defect level is situated not too close to one of the band edges (see for example [113, p. 15]). The Auger lifetime under low-level injection only depends on the doping and, thus, shows no dependence on the band gap [113, p. 10]).

Overall, the dependence of the lifetime on the band gap for different recombination

mechanisms is weak enough to justify the assumption of a constant lifetime.

In order to reduce the computational cost necessary for the solution of the problem, I restrict the discussion to the one-dimensional problem

$$\frac{dn_0}{dx} \frac{du}{dx} + n_0 \frac{d^2 u}{dx^2} - \frac{n_0 u}{L_n^2} = -\frac{g}{D_n}. \quad (4.35)$$

To solve this equation, I transform it to the spatial frequency domain via Fourier transform to obtain

$$\int_{-\infty}^{\infty} N_0(k-l) U(l) (klL_n^2 + 1) dl = \frac{2\pi G(k)L_n^2}{D_n} \quad (4.36)$$

where $N_0(k)$, $U(k)$, and $G(k)$ are the Fourier transforms of $n_0(x)$, $u(x)$, and $g(x)$, respectively. The use of finite fast Fourier transforms (FFT) leads to a Matrix equation. Solving this equation for $U(k)$ and subsequently transforming $U(k)$ back into the spatial domain yields $u(x)$ and also the local chemical potential

$$\mu_{ss}(x) = k_B T \ln(u(x) + 1). \quad (4.37)$$

4.3.2 Correlated band gap sequence

As input for the problem we require a stochastic distribution of band gaps that feature a Gaussian distribution with standard deviation σ_g and a specified spatial correlation function R_g . Such a band gap distribution is generated in the following manner [114, p. 61]:

The Fourier transform of an uncorrelated stationary sequence of random numbers with Gaussian distribution and standard deviation σ_g yields a stationary uncorrelated white noise sequence. Applying a filter $F(k)$ and transforming the filtered sequence back into the spatial domain results in a correlated sequence.

The filter has to be chosen in accordance with the desired auto-correlation function. As has been pointed out in Eq. (4.23) and Eq. (4.25), the Gaussian auto-correlation function

$$R_g = \exp\left(-\frac{x^2}{L_g^2}\right) \quad (4.38)$$

corresponds to the filter

$$F(\mathbf{k}) = \exp\left(-L_g^2 \mathbf{k}^2 / 4\right). \quad (4.39)$$

Using this filter allows the comparison between the numerical results and the results from the analytical model which is based on the Gaussian auto-correlation function.

Performing an inverse Fourier transform of the filtered sequence and adding the mean band gap \bar{E}_g finally yields the desired Gaussian band gap distribution with the mean value \bar{E}_g , the standard deviation σ_g , and the Gaussian auto-correlation function Eq. (4.38).

4.3.3 Discussion

Figure 4.6 exemplarily displays one-dimensional spatial fluctuations of the band gap energy E_g versus the spatial coordinate x normalized to the fluctuation length (correlation length) L_g (bold line). The fluctuations in Fig. 4.6 feature a Gaussian auto-correlation function and a standard deviation $\sigma_g = 50$ meV. For simplicity, the band gap is corrected by the mean band gap \bar{E}_g , i.e., the plot shows $E_g - \bar{E}_g$.

The figure also displays the resulting fluctuations of the chemical potential $\mu - \bar{\mu}$ corrected by the mean chemical potential $\bar{\mu}$ for different length-scale ratios L_n/L_g of diffusion length L_n and fluctuation length L_g .

For very small diffusion lengths $L_n < 0.3 L_g$ (large-scale fluctuations), the chemical potential essentially reproduces the spatial fluctuations of the band gap. With increasing diffusion length, lateral currents increasingly compensate the fluctuations of the chemical potential. For $L_n > 100 L_g$, i.e., small-scale fluctuations with a length-scale that is much smaller than the diffusion length, μ hardly features any fluctuations at all.

Figure 4.7 depicts the dependence of the ratio $\beta = \sigma_\mu/\sigma_g$ of the standard deviations σ_μ and σ_g on the length-scale ratio L_n/L_g for different magnitudes of the band gap fluctuations in terms of the standard deviation σ_g .

The analytical model Eq. (4.27) with the fluctuation length of the chemical potential $L_\mu = L_n$ being equal to the diffusion length L_n predicts that β is unity for $L_n < L_g$ and drops sharply once the diffusion length exceeds the fluctuation length (dashed line). This dependence is independent of the magnitude of σ_g .

In contrast, the numerical results unveil that β does depend on σ_g . While numerical and analytical results agree reasonably well for small fluctuations with $\sigma_g \leq 25$ meV, the numerically obtained curves exhibit a broadened decline.

At a small amplitude, fluctuations thus seem to enhance lateral compensating cur-

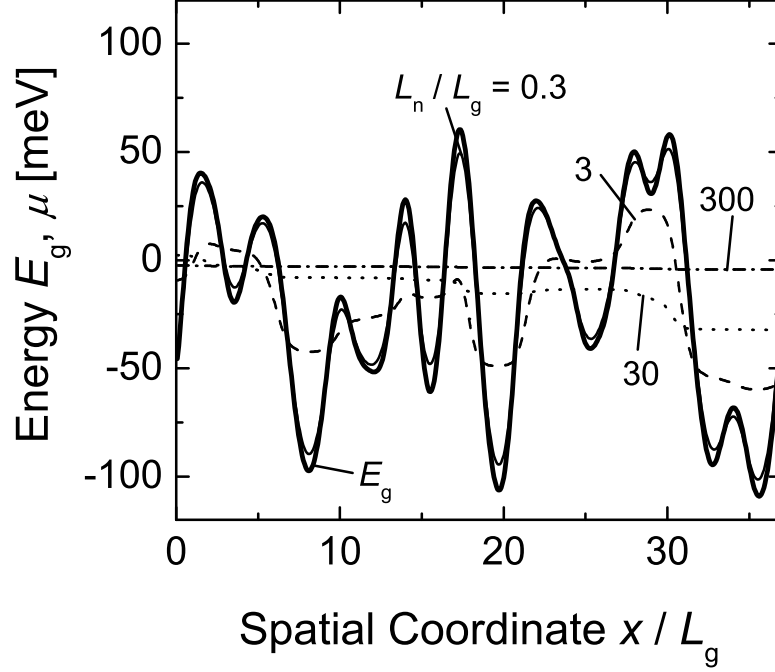


Fig. 4.6: Band gap fluctuations and resulting fluctuations of the chemical potential versus the spatial coordinate x normalized to the fluctuation length L_g for a standard deviation $\sigma_g = 50$ meV. The bold line represents the band gap fluctuations $E_g - \bar{E}_g$ corrected by the mean band gap \bar{E}_g . With increasing length-scale ratio L_n/L_g of diffusion length and fluctuation length, the chemical potential $\mu - \bar{\mu}$ corrected by the mean chemical potential $\bar{\mu}$ can not follow the band gap fluctuations.

rents, resulting in β being smaller than predicted by the analytical model. For increasing magnitude σ_g of the fluctuations, however, this effect is reversed and β is larger than the analytical β obtained with Eq. (4.27).

Overall, the simulations show that

- (i) the analytical model is a good approximation for the relation between the standard deviation ratio $\beta = \sigma_\mu/\sigma_g$ and the length-scale ratio L_n/L_g as long as the magnitude of the band gap fluctuations does not exceed $\sigma_g \approx 50$ meV, and that
- (ii) the diffusion length indeed is the crucial parameter that determines the fluctua-

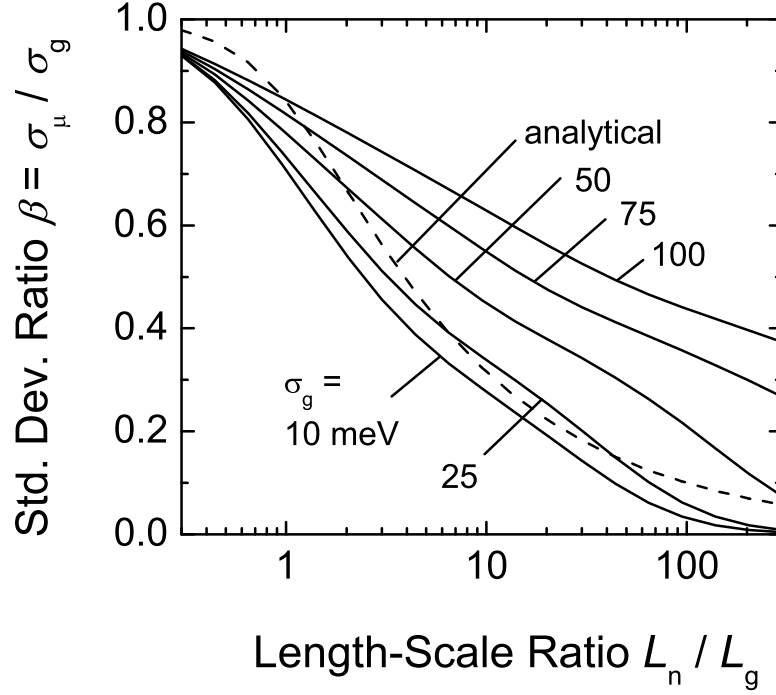


Fig. 4.7: Ratio β of the standard deviations σ_g and σ_μ versus the length-scale ratio L_n/L_g of diffusion length and fluctuation length for different standard deviations σ_g . The analytical model Eq. (4.27) is represented by the dashed line. Solid lines are the numerical results. For $\sigma_g \leq 25$ meV analytical model and numerical results show a high degree of agreement. For larger standard deviations however, the analytical model predicts a much steeper curve than the numerical simulations.

tion length $L_\mu = L_n$ of the chemical potential.

4.4 Experimental results

This section applies the above theory to absorptance and photoluminescence measurements in polycrystalline $\text{Cu}(\text{In}_{1-x}\text{Ga}_x)\text{Se}_2$ thin-films. The samples are fabricated by coevaporation of the individual elements onto soda-lime glass substrates with a substrate temperature $T_{sub} = 550^\circ \text{C}$. The films have a thickness $d \approx 2 \mu\text{m}$. The in-

vestigated samples are either prepared in a three-stage process described in detail in Ref. [115] or in a single-stage process which means coevaporation of all elements at constant rates. All samples have a slightly copper-poor final composition. I vary the relative Ga content x from $x = 0$ to $x = 1$. The three-stage samples are covered with a 50 nm thick CdS layer deposited from a chemical bath in order to reduce surface recombination during PL measurements. The CdS layer has a band gap of approx. 2.4 eV. It passivates the surface and therewith substantially improves the luminescence signals. The single-stage samples, which are only used for absorptance measurements, do not have such a protective layer.

Absorptance spectra are obtained from room temperature reflection and transmission measurements as described in Ref. [72]. Photoluminescence (PL) spectra are measured at room temperature under monochromatic excitation at $\lambda = 514$ nm with an areal power density of 300 mW/cm^2 as described in Ref. [116].

The fabricated three-stage CIGS thin films exhibit three different Ga contents $x = 0.3$, $x = 0.4$ and $x = 0.5$. Figures 4.8a-c show the measured absorptance and PL spectra. Also displayed are the theoretical curves obtained from simultaneously fitting Eq. (4.3) to the measured absorptance data and Eq. (4.31) to the measured PL data. The fit-parameters are the mean band gap \bar{E}_g , the standard deviation σ_g , the length-scale coefficient β and an additional factor for adjusting the magnitude of the emission spectra. In accordance with the literature [117], the average band gap increases with the Ga content. The obtained medium band gaps are $\bar{E}_g = 1.15, 1.19$, and 1.24 eV for $x = 0.3, 0.4$ and 0.5 . These results are consistent with the band gaps obtained from quantum efficiency measurements of solar cells fabricated from absorbers processed in the same run. The standard deviations resulting from the fits are $\sigma_g = 48, 50$, and 62 meV. Figure 4.9 displays the values as solid triangles. For the length-scale coefficient we obtain $\beta = 0$ in all cases, which means that the length-scale L_g of the observed band gap fluctuations is much smaller than the characteristic transport length L_μ . Since all prepared samples are p -type semiconductors, L_μ equals the electron diffusion length L_n . Note that some systematic deviations of the experimental in Fig. 4.8 are due to parasitic absorption as discussed in section 4.5.1 and to optical interference effects as discussed in section 4.5.3.1.

We have also fabricated CIGS thin films in a single-stage process with varying gallium content $x = \text{Ga}/(\text{In}+\text{Ga})$ from $x = 0$ to $x = 1$ from pure CuInSe_2 to pure

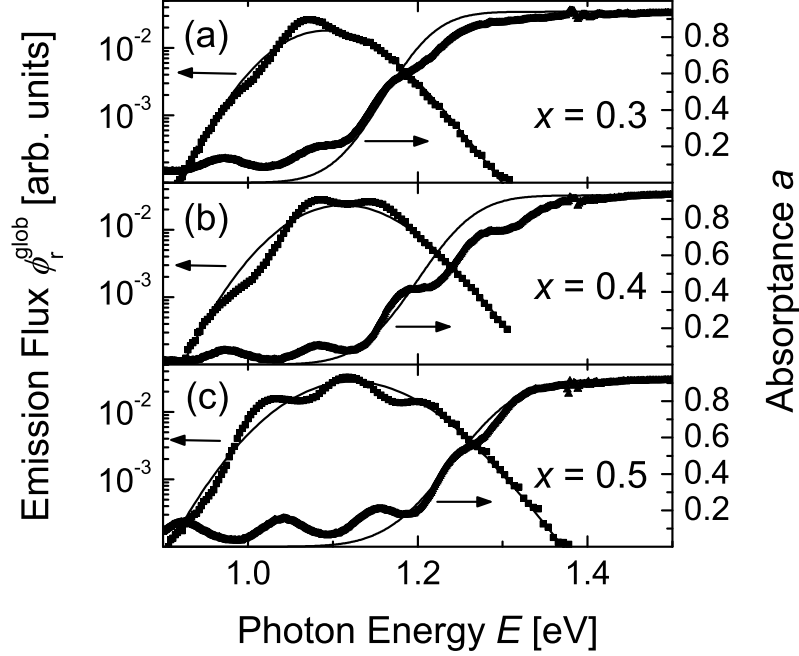


Fig. 4.8: Absorbance and photoluminescence spectra of CIGS thin films processed in a three-stage process with different gallium content x . Fitting Eq. (4.3) and Eq. (4.31) (solid lines) to the experimental data (symbols) simultaneously yields the fit-parameters $\bar{E}_g = 1.15$, 1.19, and 1.24 eV and $\sigma_g = 48$, 50, and 62 meV for $x = 0.3$, 0.4, and 0.5. All data-sets exhibit small-scale fluctuations with $\beta = 0$, i. e. $L_g \ll L_n$.

CuGaSe₂ and analyzed the absorbance spectra of these films by fitting Eq. (4.3) to the measured data. As for the three-stage samples, \bar{E}_g increases with x . We obtain $\bar{E}_g = 1.0$, 1.13, 1.29, 1.41, and 1.66 eV for $x = 0$, 0.25, 0.5, 0.75, and $x = 1$. The standard deviations obtained from fitting the measured absorbance spectra are displayed in Fig. 4.9 as solid squares.

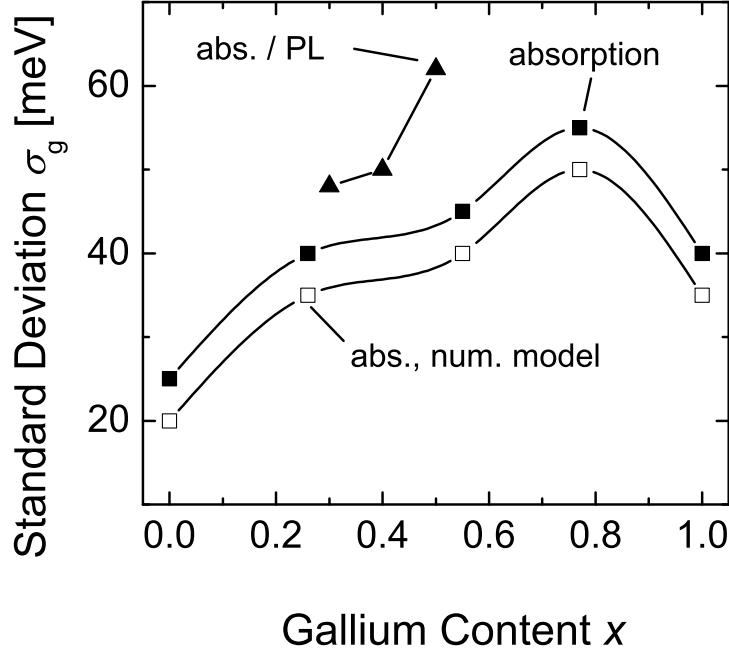


Fig. 4.9: Standard deviation σ_g of the local band gap energy E_g^{loc} in dependence of the relative gallium content x as obtained from the combined absorptance/photoluminescence fits displayed in Fig. 4.8 (solid triangles), and from fitting absorptance spectra of single-layer samples with either Eq. (4.3) (solid squares) or a numerical approach that considers coherent optics (open squares). The solid lines are a guide to the eye. For the ternary compounds CuInSe₂ and CuGaSe₂ the fluctuations are minimal. This finding indicates alloy disorder as one possible source of inhomogeneities.

4.5 Discussion

4.5.1 Length-scale of band gap fluctuations

The simultaneous analysis of absorptance and emission spectra relies on the assumption that light emission is associated with fundamental light absorption, i.e. that the dominant radiative recombination mechanism is band to band recombination. In general, the measured luminescence spectra are a superposition of all possible optical transitions. Especially donor-acceptor transitions are well-known in heavily compensated

semiconductors like CIGS [118–121]. However, such transitions are usually analyzed at temperatures below $T = 20$ K. At such low temperatures, the Fermi-distribution is very steep and therefore, the occupation probability of states below the conduction band edge is much higher than the occupation probability of higher energy levels. Consequently, transitions like donor-acceptor transitions gain importance at low temperatures. At room temperature, the Fermi-distribution is quite broad and it is reasonable to assume band to band recombination as the dominant radiative recombination path. Recently, Kirchartz et al. [122, 123] have shown in electroluminescence measurements that the dominant luminescent emission changes from a broadened donor-acceptor pair recombination at temperatures below $T = 140$ K to band to band recombination at temperatures above $T = 200$ K. Indications for this change are the higher peak energies of the emission peak as well as the absence of an intensity-dependent blueshift of the spectra at temperatures above 200 K. Another indication for the validity of this assumption is the consistency of the standard deviations σ_g obtained from absorptance and luminescence fits of the three-stage samples, which are obtained in different energy ranges. Whereas σ_g determines the slope of the absorption edge in an energy range around the mean band gap \bar{E}_g , it determines the low-energy flank of the luminescence peak which is located more than 100 meV below the absorption edge.

The experimentally observed shifts between luminescence peak and absorption edge displayed in Fig. 4.8 yield the length-scale coefficient $\beta = 0$ in all cases. Therefore, I conclude that all investigated samples feature fluctuations that occur on a length-scale which is much smaller than the electron diffusion length L_n of $L_n \approx 1 \mu\text{m}$. Reasonable fit results could only be obtained when using $\beta < 0.1$. Via Eq. (4.27) and assuming two-dimensional band gap fluctuations, this β -value corresponds to a diffusion length L_n that is at least ten times larger than the fluctuation length L_g . Moreover, comparison with the numerical results in Fig. 4.7 suggest that, with $\sigma_g \geq 50$ meV, the diffusion length needs to be more in the order of 100 times larger than the fluctuation length to obtain such low values for β . Therefore, even accounting for the influence of donor-acceptor pair recombination, which would also shift the emission peak towards lower energies, would not alter the result of $L_g \ll L_n$. The observed fluctuations are definitely small-scale fluctuations.

In the case of small-scale band gap fluctuations, the electron and the hole population in the entire semiconductor are each described by homogeneous quasi-Fermi levels.

Therefore, the chemical potential μ of photons is uniform throughout the sample and Wülfel's generalization of Kirchhoff's law holds for the global light emission spectrum. Local and global emission spectra are determined by the product of absorptance and black body spectrum according to Eq. (4.4).

In contrast, any departure from the small-scale limit leads to a spatially nonuniform $\mu(x)$ and Eq. (4.4) is only valid locally. Thus, a way to access the length-scale of inhomogeneities is to test the validity of Eq. (4.4) for global absorption/emission data. Figure 4.10 compares the measured absorptance data (open squares) of a three-stage sample with $x = 0.4$ to the data (open triangles) that are reconstructed from the PL spectra [124, 125] by inversion of Eq. (4.4) according to

$$a^{\text{loc}}(E) \propto E^{-2} \exp\left(\frac{E}{k_{\text{B}}T}\right) \frac{d\Phi_{\text{r}}^{\text{loc}}(E)}{dE}. \quad (4.40)$$

Additionally, Fig. 4.10 displays the theoretical fit to Eq. (4.3) (solid line) as performed in Fig. 4.8b. All three curves show a good agreement for $E > 1.1$ eV. In the case of fluctuations on a larger length-scale, the absorption data reconstructed with help of Eq. (4.40) and the measured absorption data would not show such an agreement. In that case, the luminescence is no longer the product of absorptance and black-body spectrum, but instead the modified spectrum according to Eq. (4.31) with $\beta \neq 0$.

To underline the inapplicability of Kirchhoff's law in the large-scale limit, I compute the large-scale emission spectrum according to Eq. (4.31) with $\beta = 1$ using the parameters $\bar{E}_{\text{g}} = 1.19$ eV and $\sigma_{\text{g}} = 50$ meV from the fit of the absorption data (cf. Fig. 4.8b). The spectral position of the large-scale emission peak is at higher energies than the measured PL peak and therewith, reconstructing the absorptance spectra with help of Eq. (4.40) results in a shifted absorption edge (dotted line in Fig. 4.10) that is not in agreement with the measured absorptance spectrum. Thus, the consistency of PL and absorption data at energies $E > 1.1$ eV unveils the small-scale nature of the fluctuations.

It is however also evident that at energies $E \leq 1.1$ eV the absorption of the sample is far larger than would be expected from the emission data. I observe such a parasitic absorption, which is also heavily influenced by interference patterns, in all our samples. Similar results were also reported earlier for samples from other sources [126]. Obviously, this absorption stems from parts of the samples that do not contribute at all to the radiative emission, i.e., parts with negligible chemical potential μ of the photons.

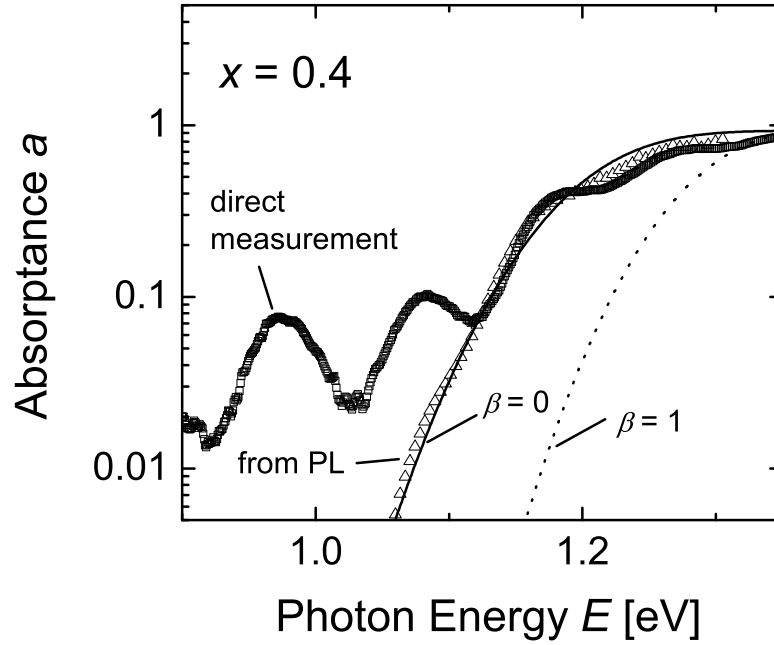


Fig. 4.10: Absorptance spectrum of a $\text{Cu}(\text{In}_{1-x}\text{Ga}_x)\text{Se}_2$ three-stage sample with a gallium content $x = 0.4$. The spectrum obtained from transmission and reflection measurements (open squares) exhibits pronounced sub-band gap absorption. The spectrum reconstructed from PL measurements (open triangles) does not show this parasitic sub-band gap absorption. The theoretical absorptance curve from Fig. 4.8b is displayed as well (solid line). It nicely represents the absorptance spectrum extracted from the luminescence measurements. The consistency of measured and reconstructed absorptance spectrum underlines the validity of Würfel's generalization of Kirchhoff's law, which only holds in the case of small-scale fluctuations. Assuming large-scale fluctuations would result in an absorptance spectrum which is substantially shifted towards higher energies (dotted line).

Most likely, this 'dark matter' corresponds to photovoltaically inactive phases with a broad-range absorption. Whether or not these phases play a significant role for the device performance is unclear up to now.

4.5.2 Origin of band gap fluctuations

The dependence of the standard deviations σ_g on the Ga/(In+Ga)-ratio x as depicted in Fig. 4.9 shows that the pure alloys CuInSe₂ and CuGaSe₂ are less inhomogeneous than the quaternary alloys. Thus, alloy disorder is clearly one source of the inhomogeneities detected by our experiments. This conclusion is also compatible with the fact that we are dealing with fluctuations on a length-scale of less than 100 nm because statistical alloy disorder occurs on a length-scale of a few unit cells of the crystal structure. Orgassa [72] analyzed the band tails of the absorption coefficient and reports an analogue dependence of the Urbach energy on the gallium content. Along a similar line, the broadening of the transition peaks in the admittance spectra in Cu(In,Ga)(S,Se)₂ solar cells was found to increase with increasing In/Ga and/or S/Se alloying [127].

The fact that maximum inhomogeneity is achieved at $x = 0.75$ instead of $x = 0.5$ and the fact that σ_g is larger in CuGaSe₂ than in CuInSe₂ points to a second source of inhomogeneities. In general, the material quality decreases in Cu(In,Ga)Se₂ alloys with increasing Ga content such that structural defects on a small length-scale contribute to the inhomogeneity of the Cu(In,Ga)Se₂ thin-films and significantly reduce the electronic film quality [128, 129].

Also, Cu-poor/Cu-rich nanodomains as recently found by transmission electron microscopy combined with x-ray energy-dispersive spectroscopy [100] might contribute to band gap fluctuations. Such a conclusion would fit to the observation that band gap fluctuations in CuInSe₂ films detected by absorption measurements increase with decreasing Cu-content [130].

In contrast to small-scale fluctuations, there are also variations of the electronic properties of Cu(In,Ga)Se₂ thin films on a length-scale of 3 – 20 μm as detected by spatially resolved PL measurements [131] and electron-beam induced voltage analysis [132]. These variations most likely originate from variations of the electronic material quality and are not or only slightly related to variations of the fundamental band gap. Grabitz finds V_{oc} variations with a standard deviation $\sigma = 70 - 85 \text{ mV}$. Looking at the local PL spectra measured by Gütay and Bauer (cf. Fig. 3c in Ref. [131]) unveils that the spectral position of the maxima of those peaks differs only slightly. The authors find that the associated band gap energies vary by at most 15 meV. In contrast, the width of each local spectrum (taken with a spatial resolution of less than 1 μm) corresponds to a standard deviation $\sigma_g \approx 35 \text{ meV}$ if analyzed by fitting the present Eq. (4.14) to the

data in Fig. 3c in Ref. [131]. We may thus conclude that in those sub-micron-resolution PL spectra the band gap fluctuations below the resolution limit are larger than those that are resolved in these measurements. Conversely, the chemical potential μ^{loc} in terms of the PL-yields, which varies by a factor of ten, shows significant fluctuations on a larger length-scale of $3 - 20 \mu\text{m}$ which are not caused by band gap fluctuations.

From the differences of the observed length-scales, I conclude that there are various types of inhomogeneities in CIGS absorber films. Localized disorder such as compositional or alloy disorder results in small-scale fluctuations of the band gap. On a larger length-scale the chemical potential μ^{loc} shows additional fluctuations due to variations in the local electronic quality of the absorber films.

In his PhD thesis [133, p. 97], Grabitz discusses different types of inhomogeneities in CIGS absorber layers and possible causes of the inhomogeneities. He also describes which method can be used to characterize different types of inhomogeneities. For the analysis of large-scale fluctuations of electronic material properties, he develops a multi-diode model that assigns different diode properties to regions with varying electronic material quality [133, p.33], [103,134]. However, such a model is only suited for large-scale inhomogeneities that do not require 2 or 3-dimensional device simulation. Applying the model to temperature-dependent current-voltage measurements of CIGS solar cells, Grabitz finds standard deviations $\sigma \approx 140 \text{ meV}$ in the activation energy that describes the local recombination behavior.

One important question arising from these different types of inhomogeneities is in how far fluctuations of the chemical potential that originate from causes other than band gap fluctuations influence the measured luminescence spectra.

The theoretical model developed in section 4.2 assumes that all regions with identical local band gap E_g^{loc} also exhibit identical local chemical potential $\mu^{\text{loc}}(E_g^{\text{loc}})$.

If μ^{loc} features additional fluctuations, this implies that for a given E_g^{loc} , different regions can still exhibit different μ^{loc} . The average chemical potential $\mu_{\text{av}}(E_g^{\text{loc}})$ of these regions differs from the chemical potential $\mu_{\text{model}}(E_g^{\text{loc}})$ which would have corresponded to that band gap if no additional fluctuations had been present. However, under the assumption that the additional fluctuations of μ^{loc} are completely uncorrelated to fluctuations in E_g^{loc} , the relationship between the average chemical potential $\mu_{\text{av}}(E_g^{\text{loc}})$ and $\mu_{\text{model}}(E_g^{\text{loc}})$ is independent of the band gap energy.

Therefore, the resulting global luminescence spectrum changes only in magnitude

but not in spectral position. This means that PL measurements on an arbitrary yield scale are not influenced by fluctuations of electronic material properties which cause fluctuations in the chemical potential. The spectral position of the luminescence peak is only determined by fluctuations of optical properties, e.g. fluctuations of the band gap energy which lead to fluctuations of the absorptance spectrum.

4.5.3 Model refinements

This section introduces some refinements of the relatively simple analytical model presented in section 4.2. The first section deals with fluctuations of the band gap over the film depth, incomplete absorption and optical interference effects. Subsequently, the implications of vertical gradings in the gallium content which lead to vertical band gap gradings are analyzed.

4.5.3.1 Coherent optical analysis

The presented analytical model only features lateral fluctuations and assumes a constant band gap throughout the film depth. Such an assumption is justified as long as the length-scale of the fluctuations is larger than the film thickness. However, the analysis of experimental data results in length-scales in the sub-micron regimes which is much smaller than the film thickness of approximately $2\ \mu\text{m}$. In addition, the absorptance and luminescence spectra feature pronounced interference patterns that hamper the interpretation of the data. A more accurate approach therefore requires the treatment of vertical band gap fluctuations and a coherent optical approach that accounts for non-ideal absorption and interference effects.

In direct semiconductors the absorption coefficient α obeys a square root-dependence on the photon energy E according to $\alpha(E) = \alpha_0 \sqrt{(E - E_g)/k_B T}$ where α_0 is the absorption coefficient at $E = E_g + k_B T$ (cmp. Tab. 3.2). In the small-scale limit of an inhomogeneous absorber with a band gap that is stochastically fluctuating over the absorber depth I define the effective absorption coefficient as

$$\alpha_{\text{eff}}(E) = \int_{-\infty}^{\infty} \alpha_0 \sqrt{(E - E_g^{\text{loc}})/k_B T} P(E_g^{\text{loc}}) dE_g^{\text{loc}}. \quad (4.41)$$

In this case, E_g^{loc} denotes the (fluctuating) band gap over the absorber depth. Note that laterally, the effective absorption coefficients are identical so that we do not need an additional lateral averaging.

For a system of plane-parallel thin layers, the absorptance can be calculated in a coherent optical analysis by making use of the matrix formalism for the propagation of electro-magnetic waves in stacks of homogeneous materials [72, 135]. With help of the effective absorption coefficient α_{eff} we thus numerically calculate the small-scale limit of the coherent absorptance. Note that the coherent optical analysis can also be carried out by calculating the coherent local absorptance with a locally well defined α^{loc} and inserting that value into Eq. (4.3).

Figure 4.11a exemplarily displays the measured absorptance data of a single-stage sample with $x = 0.5$ and the theoretical curves from fitting Eq. (4.3) or the coherent optical computation to the measured data. Accounting for non-ideal local absorption instead of the step-function utilized in Eq. (4.3) leads to far better fits to the experimental data. However, the standard deviations σ_g obtained from using the coherent optical model are only about 5 meV smaller than those obtained from the analytical model (cf. Fig. 4.9 (open squares)). This result demonstrates the reliability of the analytical model with respect to determining the extent of band gap fluctuations. For the reliability of the fit results it is crucial though, not to fit the whole data range but only a section that features no interference patterns.

4.5.3.2 Band gap grading

Another aspect to be discussed here is a nonuniform gallium content throughout the film depth. Samples grown in a three-stage process exhibit a gallium grading over the depth of the films [115, 136, 137]. The gallium content and therewith the band gap is larger at the back of the film than towards the film surface. Therefore, the absorption coefficient $\alpha(E)$ for a given energy E decreases towards the substrate [88, 91].

Figure 4.11b demonstrates the impact of a band gap grading on the absorptance spectrum. The figure depicts the absorptance for different $\Delta E_g = E_g(z = d) - E_g(z = 0) = 0$ meV, 50 meV, and 300 meV, where z is the spatial coordinate over the absorber depth⁶ and d is the absorber thickness. The parameters for the simulation are the surface band gap $E_g(0) = 1$ eV, the thickness $d = 2$ μm , and an absorption coefficient $\alpha(E, z) = 10^4 \text{ cm}^{-1} \sqrt{(E - E_g(z))/(k_B T)}$.

The effect of the grading is very similar to the effect of band gap fluctuation. At

⁶In contrast to the notation in chapter 3, the vertical coordinate is denoted as z because here, x already denotes the Ga content.

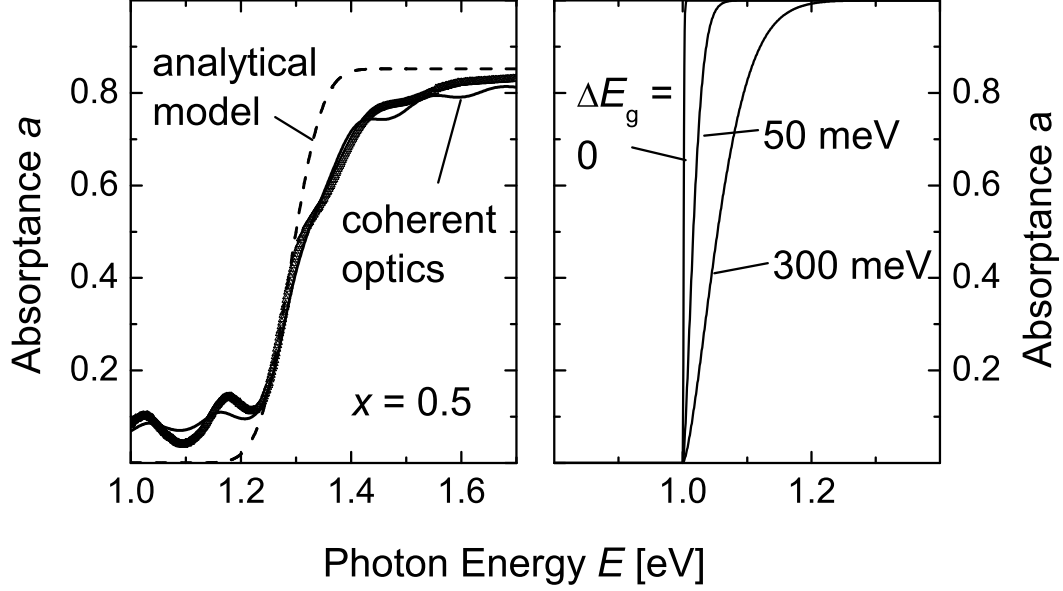


Fig. 4.11: a) Absorptance spectrum of a single-layer sample with Ga content $x = 0.5$. Fitting Eq. (4.3) to the measured data (open triangles) yields the dotted line. Accounting for optical interferences leads to the solid line. The fit parameters are $\bar{E}_g = 1.29$ eV and $\sigma_g = 45$ meV when using Eq. (4.3) and $\sigma_g = 40$ meV when accounting for interferences. b) Simulated absorptance spectrum for different gradings from $\Delta E_g = E_g(d) - E_g(0) = 0$, 50 meV, and 300 eV. The thickness is $d = 2 \mu\text{m}$, the surface band gap is $E_g(0) = 1$ eV, and the absorption coefficient is given by the square-root dependence of a direct semiconductor as described in the text. Particularly in the energy range $E_g(0) < E < E_g(d)$ the grading decreases the absorptance.

energies $E_g(0) < E < E_g(d)$, the absorption is reduced which leads to a broadening of the absorption edge. Three-stage samples that are grown at a constant Ga rate, typically feature band gap gradings $F \approx 25 \text{ meV}/\mu\text{m}$ [88, 115]. Such gradings result in a broadening which is comparable to the broadening induced by band gap fluctuations with standard deviations $\sigma_g \approx 15$ meV. The grading can be enhanced by intentionally decreasing the Ga rate during absorber deposition. Such samples feature gradings up to $F \approx 150 \text{ meV}/\mu\text{m}$ which correspond to standard deviations $\sigma_g \approx 40$ meV.

Obviously, this finding has serious consequences for the interpretation of the ob-

tained standard deviations in terms of lateral band gap fluctuations in the case of three-stage samples. The standard deviations displayed in Fig. 4.9 as solid triangles are obtained under the assumption that the complete broadening is a result of band gap fluctuations only. Thus, they represent maximum values for the band gap inhomogeneities. Taking into account the band gap grading would result in significantly smaller standard deviations. Therewith, the grading provides a qualitative argument why the standard deviations of three-stage samples are larger than the ones obtained from single stage samples.

4.5.4 Implications for solar cell performance

Inhomogeneous samples exhibit absorption at lower photon energies. Due to the exponential dependence of all recombination mechanisms that are governed by the band gap, the overall recombination current in an inhomogeneous semiconductor will thus be larger than in a homogeneous sample with a band gap E_g that equals the average band gap \bar{E}_g of the inhomogeneous sample. This increase of the total recombination current leads to a reduced open circuit voltage [98]

$$V_{oc}^{inhom} \approx V_{oc}^{hom} - \frac{\sigma_g^2}{2k_B T q} \quad (4.42)$$

of inhomogeneous solar cells in comparison to a uniform cell with a single band gap that is equal to the average band gap of the inhomogeneous cell. Therefore, it should be possible to see a correlation between the standard deviations obtained from the absorptance spectra in Fig. 4.9 and measured open circuit voltages of solar cells fabricated from these absorber films. However, the poorer cell-performance of wide-gap CIGS solar cells with $x > 0.4$ [128, 138–142] is only partially explained by band gap fluctuations. The standard deviations σ_g derived in the present work account for V_{oc} -losses in the range of 5 mV (for $\sigma_g \approx 15$ meV, CuInSe₂) up to 80 mV (for $\sigma_g \approx 65$ meV, Cu(In_{1-x}Ga_x)Se₂ with $x = 0.5$). Especially in the technologically relevant range of Cu(In_{1-x}Ga_x)Se₂ alloying with $0.2 < x < 0.5$, these losses are significant and making the devices more homogeneous would substantially improve their performance. However, the systematic degradation of the open-circuit voltage with increasing Ga-content $x > 0.3$ that hampers the development of efficient wide-gap Cu(In,Ga)Se₂ solar cells cannot be explained with the present data. The V_{oc} degradation of wide-gap Cu(In,Ga)Se₂ devices corresponds to V_{oc} losses of more than 250 mV when comparing

the V_{oc} of the best CuGaSe_2 devices to the V_{oc} that would be expected if the electronic quality of high efficiency $\text{Cu}(\text{In}_{0.8}\text{Ga}_{0.2})\text{Se}_2$ devices could be preserved for the wide-gap CuGaSe_2 solar cells [140]. Thus, the difficulty to produce high efficiency wide-gap chalcopyrite solar cells is not exclusively explained by the small-scale inhomogeneities detected in the present work. Rather, the overall poorer electronic quality of those wide-gap materials reflected in the larger concentration [143] or less favorable energetic position [129] of bulk defects plays a more decisive role. In addition, electrostatic potential fluctuations [86] that are superimposed on band gap fluctuations and that are not detected by room-temperature PL measurements might play a role in deteriorating the performance of wide-gap chalcopyrite solar cells.

Note at this point, that Eq. (4.42) holds only if all local chemical potentials μ^{loc} are equal to the global open circuit voltage. This is automatically the case for small-scale fluctuations but also for ideal front contacts that lead to a perfect parallel connection of the local subdomains which in turn levels out all voltage differences. However, in the case of large-scale fluctuations the lateral resistivity of the emitter decides about the resulting global open circuit voltage [103]. The emitter resistivity can thus be tuned to compensate V_{oc} losses due to large-scale inhomogeneities.

4.6 Conclusions

I have presented an analytical model that predicts the broadening and energetic position of absorptance and emission spectra for semiconductors with lateral band gap inhomogeneities. This model supplies information about the extent of the investigated band gap fluctuations from the broadening of absorption edge and emission peak. The length-scale of the fluctuations is determined by the position of the emission peak with respect to the absorption edge.

From fitting the model to experimental data of CIGS thin films with varying gallium content we extract standard deviations σ_g of the fluctuations in the range of 15 to 65 meV which would result in V_{oc} losses in the range of 5 to 80 mV for solar cells made of these films. As the ternary compounds CuInSe_2 and CuGaSe_2 show the smallest standard deviations we conclude alloy disorder as a possible source of band gap fluctuations. All investigated three-stage samples show a luminescence peak that is substantially shifted towards lower energies when compared to the absorption edge.

This shift means that the length-scale of the fluctuations is much smaller than the diffusion length. Hence, the fluctuations detected here result from rather local disorder on a length-scale below 100 nm.

Chapter 5

Outlook

The thesis on hand has focussed on the interplay of charge carrier transport and the detailed radiation balances of absorbed and emitted radiation fluxes.

The first focus was placed on the efficiency limits of *pn*-junction solar cells. This approach consisted of a pure low-level injection approach that neglected the behavior of majority carriers. However, as has been pointed out in section 3.10, in the radiative recombination limit, the low-level assumption is only valid for almost unrealistically high doping concentrations.

Consequently, the next step needs to extend the approach to the simultaneous treatment of minority and majority carriers. Since the differential equations of electrons and holes are coupled via the recombination term that includes the product of electrons and holes, such a problem can no longer be transformed into a linear matrix equation but needs to be solved iteratively.

As an additional advantage, such a general approach allows the inclusion of built-in electric fields as they occur in the space charge region of *pn*-junctions or in the intrinsic layer of *pin* structures. This approach is particularly important for the description of multiple quantum well structures. Such structures are investigated as third generation solar cells to use as top cells in tandem structures. The quantum confinement leads to increased band gaps and to potentially very high lifetimes. However, charge carrier transport in these structures is hampered by the tunnelling across the potential barriers [144].

Tunnelling also plays a role when it comes to extend the analysis of inhomogeneous semiconductors. In this thesis, I have assumed that the recombination of electrons and

holes is a strictly local process. However, this assumptions can hardly be maintained once fluctuations in the band gap or additional potential fluctuations are too steep and too abrupt. Then, tunnelling processes need to be considered that lead to non-local recombination.

Overall, the further development of new materials, such as organic semiconductors, or new solar cell device structures, such as fluorescent concentrator systems, requires further investigations of the interaction between electronic and photonic transport. The considerations performed in this thesis will gain importance whenever electronic transport is limited and increased radiative recombination enhances photonic transport. New generations of photovoltaic devices will encompass all kinds of combinations. Conventional solar cells feature near to perfect electronic transport but negligible photonic transport. New devices, however, might reverse this situation. An extreme case, for instance, consists of the fluorescent concentrator where transport is exclusively photonic. In systems with such fluorescent concentrators, conventional solar cells as we know them now only make up a very small part of the complete photovoltaic system.

Appendix A

Radiative efficiency limit with energy-dependent absorptance

A.1 Inhomogeneous band gap

Shockley and Queisser have performed their calculation of the maximum power conversion efficiency under the assumption of a homogenous band gap, which - provided that the solar cell is thick enough - leads to a step-like absorptance function.

Rau and Werner [98] have extended the SQ-approach to solar cells with lateral band gap fluctuations. Such fluctuations lead to a broadening of the absorption edge and consequently to a reduction of the radiative power conversion efficiency.

This is because radiative recombination is increased in the regions with small band gap and decreased in the regions with larger band gap. Due to the exponential dependence of the radiative recombination rate on the band gap, the overall radiative recombination rate is increased.

The following section shortly recapitulates the effect of band gap fluctuations on the power conversion efficiency. A detailed discussion of band gap fluctuations with different length-scales is given in chapter 4.

The simplest approach to model band gap fluctuations is to assume a Gaussian distribution of band gaps around a mean band gap \bar{E}_g with a standard deviation σ_g (cmp. Eq.(4.1)). As derived in Eq.(4.3), this approach yields the absorptance

spectrum

$$a(E, \bar{E}_g, \sigma_g) = \frac{1}{2} \operatorname{erfc} \left(\frac{\bar{E}_g - E}{\sqrt{2}\sigma_g} \right). \quad (\text{A.1})$$

A higher degree of inhomogeneity in terms of the standard deviation σ_g results in an increasingly broadened absorption edge when compared to a homogeneous semiconductor with band gap \bar{E}_g (see Fig. 4.2a).

In analogy to Eq. (2.10) and Eq. (2.11), the absorptance influences the emission. In total the broadened absorption edge results in the enlarged emission current

$$\begin{aligned} \Phi_{\text{em}}(\mu, \bar{E}_g, \sigma_g) &= \frac{\pi}{h^3 c^2} \int_0^\infty \operatorname{erfc} \left(\frac{\bar{E}_g - E}{\sqrt{2}\sigma_g} \right) E^2 \exp \left(-\frac{E - \mu}{k_B T} \right) dE \\ &= J_{00}(\bar{E}_g, \sigma_g) \exp \left(-\frac{\bar{E}_g - \mu}{k_B T} + \frac{\sigma_g^2}{2(k_B T)^2} \right), \end{aligned} \quad (\text{A.2})$$

where

$$\begin{aligned} J_{00}(\bar{E}_g, \sigma_g) &= \frac{2\pi k_B T}{h^3 c^2} \times \\ &\quad \left\{ (\bar{E}_g^2 + 2\bar{E}_g k_B T + 2(k_B T)^2) - \frac{\sigma_g^2}{k_B T} (2\bar{E}_g + k_B T) + \frac{\sigma_g^4}{(k_B T)^2} \right\}. \end{aligned} \quad (\text{A.3})$$

The chemical potential μ of the emitted photons is assumed to be constant throughout the depth of the solar cell. Also, lateral currents within the absorber layer or in the highly conductive emitter layer lead to a laterally homogeneous chemical potential. This case corresponds to the small-scale limit discussed in chapter 4.

As a result of the increased emission current, the radiative efficiency limit is significantly decreased by band gap fluctuations. Comparison of Eq. (A.2) with Eq. (2.9) reveals that the main contribution to the increase in the recombination current stems from the exponential factor.

The short circuit current is only slightly influenced by the fluctuations because the maximum of the solar spectrum is at energies larger than typical mean band gaps. Therefore, and by using Eq. (2.2) and Eq. (2.10), the drop in efficiency is almost exclusively caused by the decreased open circuit voltage

$$\begin{aligned} V_{\text{oc}}^{\text{inhom}} &= \frac{\bar{E}_g}{q} - \frac{\sigma_g^2}{2k_B T q} - \frac{k_B T}{q} \ln \left(\frac{J_{00}}{J_{\text{sc}}} \right) \\ &\approx V_{\text{oc}}^{\text{hom}} - \frac{\sigma_g^2}{2k_B T q}. \end{aligned} \quad (\text{A.4})$$

A.2 Optimal absorptance

For given solar irradiation $\phi_{\text{sun}}(E)$ and black body irradiation $\phi_{\text{bb}}(E)$, the maximum efficiency of a solar cell is given by the absorptance $a(E)$. Shockley and Queisser based their efficiency limit on the assumption of a step-like absorptance function. The previous section has shown that a deviation from the step function in the form of a broadened absorption edge according to Eq. (A.1) leads to a decreased power conversion efficiency. But does this result automatically mean that the step function is the optimal absorptance function leading to the ultimate maximum efficiency?

In this section, I show that for virtually any spectrum, the optimal absorptance is indeed given by a stepfunction. For uni-modal spectra $\phi_{\text{sun}}(E)$ and $\phi_{\text{bb}}(E)$, the stepfunction consists of only one step at the band gap energy E_g .

The underlying idea of the following proof is to consider a solar cell with a given arbitrary absorptance spectrum that is defined for all energies except an infinitesimally small interval dE at an energy E . By looking at the efficiency gain $d\eta$ implied by adding this interval dE with a certain absorptance $a(E)$, I determine the optimal absorptance that leads to maximized efficiency gain for all energies. A very similar proof is given by Araújo and Martí [70]. Their approach is slightly different as it considers the maximum power $P_{\text{max}} = V_{\text{mpp}} J_{\text{mpp}}$ and forms the derivative dV_{mpp}/dE_g . However, the results are essentially identical to the results obtained here.

For our consideration let us assume that the fill factor FF is independent of the voltage so that the efficiency can be approximated by

$$\eta = \frac{FF}{P_{\text{in}}} J_{\text{sc}} V_{\text{oc}} = \text{const} J_{\text{sc}} (\ln(J_{\text{sc}}) - \ln(J_0)). \quad (\text{A.5})$$

To simplify further, let us assume $\text{const} = 1$. The short circuit current is given by the integrated solar spectrum $\phi_{\text{sun}}(E')$ weighted with the corresponding absorptance $a(E')$ according to

$$\begin{aligned} J_{\text{sc}} &= \int_0^\infty a(E') \phi_{\text{sun}}(E') dE' \\ &= \int_0^E a(E') \phi_{\text{sun}}(E') dE' + \int_{E+dE}^\infty a(E') \phi_{\text{sun}}(E') dE' + a(E) \phi_{\text{sun}}(E) dE \end{aligned} \quad (\text{A.6})$$

By replacing $\phi_{\text{sun}}(E)$ with $\phi_{\text{bb}}(E)$ we obtain an identical equation for the radiative saturation current J_0 .

The currents depend on the absorptance at all energies. Since we want to determine the optimal absorptance $a(E)$ at the energy E , we have to split up the integral as performed in the last line of Eq. (A.6). Neglecting the term $a(E)\phi_{\text{sun}}(E)dE$ yields

$$J_{\text{sc}} \approx J'_{\text{sc}} = \int_0^E a(E')\phi_{\text{sun}}(E')dE' + \int_{E+dE}^{\infty} a(E')\phi_{\text{sun}}(E')dE' \quad (\text{A.7})$$

which is independent of $a(E)$. This approximation is valid as long as the absorptance is nonzero for most other energies, i.e. as long as the remaining integrals are much larger than the incremental contribution $a(E)\phi_{\text{sun}}(E)dE$. In the same way we define

$$J'_0 = \int_0^E a(E')\phi_{\text{bb}}(E')dE' + \int_{E+dE}^{\infty} a(E')\phi_{\text{bb}}(E')dE' \quad (\text{A.8})$$

Next, we determine the efficiency gain $d\eta(E)$ by looking at the derivative

$$\begin{aligned} \frac{d\eta}{dE} &= \frac{dJ_{\text{sc}}}{dE} \ln\left(\frac{J_{\text{sc}}}{J_0}\right) + J_{\text{sc}} \left(\frac{d\ln(J_{\text{sc}})}{dE} - \frac{d\ln(J_0)}{dE} \right) \\ &= \frac{dJ_{\text{sc}}}{dE} \ln\left(\frac{J_{\text{sc}}}{J_0}\right) + J_{\text{sc}} \left(\frac{1}{J_{\text{sc}}} \frac{dJ_{\text{sc}}}{dE} - \frac{1}{J_0} \frac{dJ_0}{dE} \right) \\ &= \frac{dJ_{\text{sc}}}{dE} \left(\ln\left(\frac{J_{\text{sc}}}{J_0}\right) + 1 \right) - \frac{J_{\text{sc}}}{J_0} \frac{dJ_0}{dE} \end{aligned} \quad (\text{A.9})$$

With $dJ_{\text{sc}}/dE = a(E)\phi_{\text{sun}}(E)$ and $dJ_0/dE = a(E)\phi_{\text{bb}}(E)$ and the approximations $J_{\text{sc}} \approx J'_{\text{sc}}$ and $J_0 \approx J'_0$ we rewrite Eq. (A.9) as

$$\frac{d\eta}{dE} \approx a(E)\phi_{\text{diff}} \quad (\text{A.10})$$

with

$$\phi_{\text{diff}}(E) = \phi_{\text{sun}}(E) \left(\ln\left(\frac{J'_{\text{sc}}}{J'_0}\right) + 1 \right) - \phi_{\text{bb}}(E) \frac{J'_{\text{sc}}}{J'_0}. \quad (\text{A.11})$$

This equation is the starting point of the following iterative argument. It consists of the product of the absorptance $a(E)$ and the photon flux difference $\phi_{\text{diff}}(E)$ which is independent of $a(E)$.

Let us now assume an arbitrary absorptance spectrum as depicted in Fig. A.1a. This spectrum determines J'_{sc} and J'_0 , which in turn determines $\phi_{\text{diff}}(E)$. An exemplary term $\phi_{\text{diff}}(E)$ is shown in Fig. A.1b. Then the maximum efficiency gain is obtained for $a(E) = 1$ if $\phi_{\text{diff}}(E) > 0$ and $a(E) = 0$ if $\phi_{\text{diff}}(E) \leq 0$. Therewith, we obtain a new absorptance spectrum according to Fig. A.1c, which leads to an efficiency that is larger

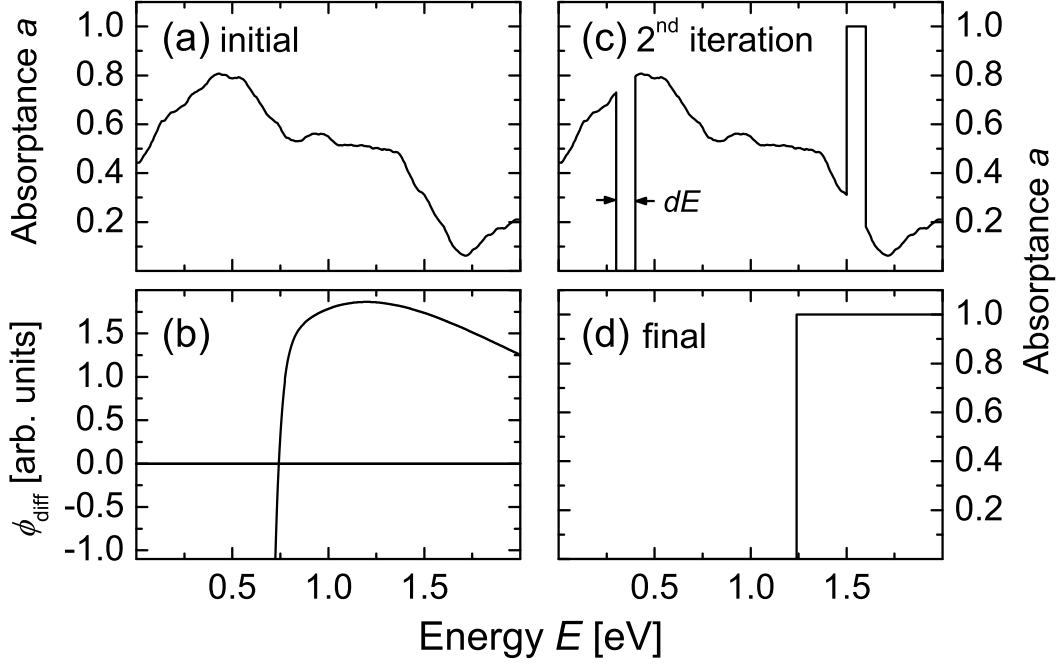


Fig. A.1: Iterative scheme to obtain the optimal absorptance. a) Initial random absorptance spectrum vs. photon energy E . b) Term $\phi_{\text{diff}}(E)$ in Eq. (A.11) resulting from the absorptance in a). c) Depending on the signum of $\phi_{\text{diff}}(E)$, the optimal absorptance at the energy E is either one (for $\phi_{\text{diff}}(E) > 0$) or zero (for $\phi_{\text{diff}}(E) \leq 0$). d) Optimal step-function absorptance spectrum under irradiation with a solar black body irradiation. The optimal band gap is $E_g^{\text{max}} \approx 1.24 \text{ eV}$.

or equal to the one obtained with the previous absorptance spectrum. Repeating these steps by randomly changing the energetic position E of the interval in question results in an absorptance spectrum that consists only of ones and zeros.

This digital optimal absorptance is only a consequence of the way the efficiency is defined in Eq. (A.5). The spectra Φ_{sun} and Φ_{bb} determine only if the signum $s_{\text{diff}}(E)$ of $\phi_{\text{diff}}(E)$ is positive or negative for a particular energy.

Next, we have to determine, whether the iteration will converge. With each new absorptance spectrum, the roots of the term in brackets will change as well. What is needed is an absorptance that reproduces itself at all energies. This absorptance will

consequently also reproduce the roots of ϕ_{diff} . Whether $\phi_{\text{diff}}(E)$ has one or more roots depends on the shape of the two spectra $\phi_{\text{sun}}(E)$ and $\phi_{\text{bb}}(E)$. For any two uni-modal spectra that feature at most one intersect, which is the case if both, solar cell and sun, are regarded as black bodies, the term has only one (or no) root. In particular, the approximation of the solar spectrum as a black body spectrum at $T = 5800$ K (normalized to an areal power density of 100 mW/cm^2) leads in combination with the black body spectrum Φ_{bb} at $T = 300$ K to $s_{\text{diff}} < 0$ for $E < E_g^{\text{max}} \approx 1.24$ and $s_{\text{diff}} > 0$ for $E > E_g^{\text{max}}$. Therefore, the iteration converges once the absorptance is given by the optimal absorptance $a(E) = 0$ for $E < E_g^{\text{max}}$ and $a(E) = 1$ for $E > E_g^{\text{max}}$ as depicted in Fig. A.1d. For this mono-step function, the efficiency reaches its ultimate maximum $\eta \approx 31\%$.

For a spectrum that can not clearly be classified as a uni-modal function such as the AM1.5g solar spectrum, the case is slightly different. In principle, ϕ_{diff} could feature more than one intercept, and, therefore, it would be feasible that the optimal absorptance would consist of a multiple step function to account for the different atmospheric absorption losses that lead to sharp recesses in the spectrum.

This reasoning becomes clear, if we consider a hypothetical spectrum consisting of multiple discrete peaks. Then, the optimal absorptance would be $a = 1$ at the peak energies and $a = 0$ everywhere else.

However, while the irregularities in the AM1.5g spectrum do lead to two optimal band gaps of $E_g = 1.15 \text{ eV}$ and $E_g = 1.34 \text{ eV}$ that each result in the ultimate maximum efficiency $\eta \approx 33\%$, the recesses are not deep enough to require an absorptance spectrum that deviates from the mono-step function. The SQ limit of 33% remains the ultimate efficiency for single junction solar cells.

The SQ limit can only be overcome by breaking the link between radiative recombination current and the absorptance. This can, for instance, be achieved by restricting the Fermi-levels governing certain energy regimes as has been conceptualized for the so-called intermediate band solar cell [145]. With such an arrangement, the theoretical maximum efficiency is increased to over 60% .

Appendix B

Derivation and numerical implementation of the photon recycling scheme

B.1 Exponential Integrals

This section provides the integrals needed for the derivation of various interaction terms for the internal and external generation rates. In general, the problem always consists of an integration of the term $\exp\left(-\frac{z}{\cos(\theta)}\right)$ over the angle θ in different combinations with the terms $\cos(\theta)$ and $\sin(\theta)$. Using the substitution $t = z/\cos(\theta)$ we obtain

$$d\theta = \frac{\cos^2(\theta)}{z\sin(\theta)}dt = \frac{\cos(\theta)}{t\sin(\theta)}dt = \frac{z}{t^2\sin(\theta)}dt = \frac{z^2}{t^3\sin(\theta)\cos\theta}dt. \quad (\text{B.1})$$

Since in the case of plane front surfaces the reflection coefficient at the front surface is different in the regime $0 \leq \theta \leq \theta_c$ and $\theta_c < \theta \leq \pi/2$, I divide the integral into two parts according to

$$\int_0^{\theta_c} f(\theta)d\theta = \int_0^{\pi/2} f(\theta)d\theta - \int_{\theta_c}^{\pi/2} f(\theta)d\theta, \quad (\text{B.2})$$

where $f(\theta)$ stands for any function depending on θ .

In the following, I only list the general cases with the lower integral boundary being θ_c that is also valid for the first integral when θ_c is replaced by zero and accordingly, $\cos(\theta_c)$ is replaced by one.

We need the following integrals:

- $\text{Ei}_1(z, \theta_c)$

$$\begin{aligned} & \int_{\theta_c}^{\pi/2} \exp\left(-\frac{z}{\cos(\theta)}\right) \frac{\sin(\theta)}{\cos(\theta)} d\theta \\ &= \int_{z/\cos(\theta_c)}^{\infty} \frac{\exp(-t)}{t} dt =: \text{Ei}\left(\frac{z}{\cos(\theta_c)}\right) =: \text{Ei}_1(z, \theta_c) \end{aligned} \quad (\text{B.3})$$

- $\text{Ei}_2(z, \theta_c)$

$$\begin{aligned} & \int_{\theta_c}^{\pi/2} \exp\left(-\frac{z}{\cos(\theta)}\right) \sin(\theta) d\theta \\ &= z \int_{z/\cos(\theta_c)}^{\infty} \frac{\exp(-t)}{t^2} dt = \cos(\theta_c) \exp\left(-\frac{z}{\cos(\theta_c)}\right) - z \text{Ei}\left(\frac{z}{\cos(\theta_c)}\right) \\ &=: \text{Ei}_2(z, \theta_c) \end{aligned} \quad (\text{B.4})$$

- $\text{Ei}_3(z, \theta_c)$

$$\begin{aligned} & \int_{\theta_c}^{\pi/2} \exp\left(-\frac{z}{\cos(\theta)}\right) \cos(\theta) \sin(\theta) d\theta \\ &= z^2 \int_{z/\cos(\theta_c)}^{\infty} \frac{\exp(-t)}{t^3} dt \\ &= \frac{1}{2} \left\{ (1 - z/\cos(\theta_c)) \cos^2(\theta_c) \exp\left(-\frac{z}{\cos(\theta_c)}\right) + z^2 \text{Ei}\left(\frac{z}{\cos(\theta_c)}\right) \right\} \\ &=: \text{Ei}_3(z, \theta_c) \end{aligned} \quad (\text{B.5})$$

These three exponential integrals are connected via the integration over the spatial variable ξ as performed in the following exemplarily for $\text{Ei}_1(z, \theta_c)$. The solution is best obtained by changing the order of integration over $d\theta$ and $d\xi$. We thus obtain the integral

$$\int_z^\infty \text{Ei}_1(\xi, \theta_c) d\xi = \int_z^\infty \int_{\theta_c}^{\pi/2} \exp\left(-\frac{\xi}{\cos(\theta)}\right) \frac{\sin(\theta)}{\cos(\theta)} d\theta d\xi \quad (\text{B.6})$$

$$= \int_{\theta_c}^{\pi/2} \int_z^\infty \exp\left(-\frac{\xi}{\cos(\theta)}\right) \frac{\sin(\theta)}{\cos(\theta)} d\xi d\theta \quad (\text{B.7})$$

$$= \int_{\theta_c}^{\pi/2} \exp\left(-\frac{z}{\cos(\theta)}\right) \sin(\theta) d\theta = \text{Ei}_2(z, \theta_c). \quad (\text{B.8})$$

Every integration of $\exp(\xi/\cos(\theta))$ over ξ yields the factor $\cos(\theta)$. Therefore, we also obtain

$$\int_z^\infty \text{Ei}_2(\xi, \theta_c) d\xi = \text{Ei}_3(z, \theta_c). \quad (\text{B.9})$$

For the transformation of the integro-differential equation into a finite differences scheme we need the double integration over the coordinates x_r and x_g given by

$$\int_{x_{i-1}}^{x_i} \int_{x_{j-1}}^{x_j} \exp \left(\frac{-\alpha x_{l,m} (s_g x_g, s_r x_r)}{\cos(\theta)} \right) dx_r dx_g \quad (\text{B.10})$$

$$\begin{aligned} &= -s_r \frac{\cos(\theta)}{\alpha} \int_{x_{i-1}}^{x_i} \left\{ \exp \left(\frac{-\alpha x_{l,m} (s_g x_g, s_r x_j)}{\cos(\theta)} \right) - \exp \left(\frac{-\alpha x_{l,m} (s_g x_g, s_r x_{j-1})}{\cos(\theta)} \right) \right\} dx_g \\ &= s_g s_r \frac{\cos^2(\theta)}{\alpha^2} \left\{ \exp \left(\frac{-\alpha x_{l,m} (s_g x_i, s_r x_j)}{\cos(\theta)} \right) - \exp \left(\frac{-\alpha x_{l,m} (s_g x_i, s_r x_{j-1})}{\cos(\theta)} \right) \right. \\ &\quad \left. - \exp \left(\frac{-\alpha x_{l,m} (s_g x_{i-1}, s_r x_j)}{\cos(\theta)} \right) + \exp \left(\frac{-\alpha x_{l,m} (s_g x_{i-1}, s_r x_{j-1})}{\cos(\theta)} \right) \right\} \\ &=: s_g s_r \frac{\cos^2(\theta)}{\alpha^2} f_{\text{exp}}^{ij} \end{aligned} \quad (\text{B.11})$$

B.2 Diffusion equation with reabsorption

This section starts by reformulating the diffusion equation as a linear matrix equation based on linear operators. Then it gives expressions for the transport operator and the recombination operator. Subsequently, it derives an expression for the internal generation rate, starting with the direct radiative interaction between two locations in the cell, and followed by the inclusion of multiple reflections. Finally, it derives expressions for the external generation rates G_{bb} and G_{sun} caused by black body and solar irradiation respectively.

B.2.1 Linear matrix formalism

Using methods from functional analysis allows us to rewrite the rather complex integro-differential Eq. (3.1) in a simple operator notation. On the one hand, this operator notation facilitates the derivation of certain theorems about for instance, the reciprocity of photovoltaic action and light emission, from basic properties of the operators [146]. On the other hand, linear operators in infinite spaces can be expressed as matrices in finite spaces since both describe linear transformations. This analogy directly points out the way to the numerical computation scheme, which transforms the integro-differential equation into a finite Matrix equation. This method is only possible due to the linearity of the operators. Otherwise, iterative numerical schemes would have to be used. In the following, I shortly discuss the properties of the operators.

Operators can only be defined on a certain normed space of functions with respect to a given norm. The electron concentration $n(x)$ is a function belonging to the Hilbert space L^2 of integrable functions on the set $0 \leq x \leq d$, where d is the thickness of the solar cell. A Hilbert space is a Banach space with a norm that is defined by the scalar product according to $\|u\| = \sqrt{\langle u, u \rangle}$ if u is real-valued [147, p.173, p.177]. In L^2 , the scalar product is defined as

$$\langle u, v \rangle = \int_{-\infty}^{\infty} u(x)v(x)dx, \quad (\text{B.12})$$

again, for real-valued functions u, v .

Transport operator The transport operator \underline{T} is the differential operator d^2/dx^2 , which is a linear and continuous operator [147, p.51]. In matrix notation, \underline{T} is given by (cmp. appendix B.4)

$$\underline{T} = \frac{D_n}{\Delta x^2} \begin{pmatrix} -2 & 1 & 0 & \dots & 0 & 0 & 0 \\ 1 & -2 & 1 & \dots & 0 & 0 & 0 \\ 0 & 1 & -2 & \dots & 0 & 0 & 0 \\ \vdots & \vdots & \vdots & \ddots & \vdots & \vdots & \vdots \\ 0 & 0 & 0 & \dots & -2 & 1 & 0 \\ 0 & 0 & 0 & \dots & 1 & -2 & 1 \\ 0 & 0 & 0 & \dots & 0 & 1 & -2 \end{pmatrix}. \quad (\text{B.13})$$

From the symmetric structure of the matrix one can directly tell the symmetry of the transport operator. An operator \underline{T} is symmetric if it holds $\langle v, \underline{T}u \rangle = \langle \underline{T}v, u \rangle$. Such a symmetric operator is also called Hermitian or self-adjoint¹.

Recombination operator The recombination operator \underline{R} simply consists of the multiplication of $n(x)$ with the scalar $1/\tau = 1/\tau_r + 1/\tau_{nr}$. Apart from this factor the operator is nothing else but the identity operator \underline{Id} , which maps a function onto itself.

¹Note that the transport operator would no longer be symmetric if drift currents were included in Eq. (3.1). However, the generalized drift-diffusion operator in Eq. (4.32) is self-adjoint and real-valued when applied to the normalized carrier concentration $(n - n_0)/n_0$, where n_0 is the equilibrium concentration. Therewith, the reciprocity relation between photocarrier collection and dark carrier distribution is still valid [67, 146].

It is evident that this operator is linear. In matrix notation \underline{R} reads as

$$\underline{R} = \frac{n_0}{\tau} \begin{pmatrix} 1 & 0 & \dots & 0 & 0 \\ 0 & 1 & \dots & 0 & 0 \\ \vdots & \vdots & \ddots & \vdots & \vdots \\ 0 & 0 & \dots & 1 & 0 \\ 0 & 0 & \dots & 0 & 1 \end{pmatrix}. \quad (\text{B.14})$$

The constant term n_0/τ_{nr} from non-radiative recombination that is not included in the recombination operator is shifted to the right-hand side of the equation as the equilibrium non-radiative generation term $G_{\text{nr}} = n_0/\tau_{\text{nr}}$.

Internal generation operator The photon recycling integral operator \underline{PR} in Eq. (3.2) is also linear, continuous and symmetric as long as the kernel function $f_{\text{r}}(x_{\text{g}}, x_{\text{r}})$ is continuous and symmetric [147, p.52]. As will be shown below, this is the case for the radiative interaction function derived in sections B.2.4 and B.2.5. Such an integral operator is called Fredholmian integral operator. In matrix notation, \underline{PR} is given by

$$\underline{PR} = \frac{R_0}{4\pi n_0} \begin{pmatrix} f_{1,1} & f_{1,2} & \dots & f_{1,N} \\ f_{2,1} & f_{2,2} & \dots & f_{2,N} \\ \vdots & \vdots & \ddots & \vdots \\ f_{N,1} & f_{N,2} & \dots & f_{N,N} \end{pmatrix}, \quad (\text{B.15})$$

where $f_{i,j}$ denotes the radiative interaction function $f_{\text{r}}(x_i, x_j)$.

Matrix equation With the operators as defined above, we are now able to rewrite the integro-differential Eq. (3.1) in the simple operator form

$$(\underline{T} + \underline{PR} - \underline{R}) n(x) = -G_{\text{sun}}(x) - G_{\text{bb}}(x) - G_{\text{nr}}(x) - I(x), \quad (\text{B.16})$$

where the injection vector $I(x)$ includes the boundary condition, i.e. the applied voltage. The matrix notation for the discretization scheme that is described in detail in appendix B is given by

$$(\underline{T} + \underline{PR} - \underline{R}) n(x_i) = -G_{\text{sun}}(x_i) - G_{\text{bb}}(x_i) - G_{\text{nr}}(x_i) - I(x_i), \quad (\text{B.17})$$

where x_i are the mesh points of the discretization.

Due to the simple form of the recombination operator, the equation can be multiplied with τ to obtain the operator $\tau\underline{T} + \tau\underline{PR} - \underline{Id}$. For $\underline{T} \in L^2$ and $\underline{PR} \in L^2$, this operator is isomorph and therewith explicitly invertible [147, p.56], such that the electron concentration is given by

$$n(x) = (\underline{T} + \underline{PR} - \underline{R})^{-1} (-G_{\text{sun}}(x) - G_{\text{bb}}(x) - I(x)). \quad (\text{B.18})$$

B.2.2 Transport

As pointed out above, transport is diffusive and defined by the transport operator \underline{T} . A general formulation of the transport operator in more than one dimension is given by the generalized expression in Eq. (4.32) derived in Ref. [112]. The generalized drift-diffusion equation also includes drift-currents caused by electric fields or variations of the material properties. Here, however, I only consider diffusive transport.

B.2.3 Recombination

Radiative recombination Radiatively recombining carriers emit radiation isotropically into all directions with a radiative recombination rate $R_r = R_0 np/n_i^2 = R_0 n/n_0$ with $n_0 = n_i^2/N_A$, where

$$R_0 = \int_0^\infty r_0(E) dE = \int_0^\infty \alpha(E) 4\pi \phi_{\text{bb},\bar{n}}^{\text{d}\Omega}(E, 0) dE \quad (\text{B.19})$$

is the radiative recombination rate in thermodynamic equilibrium, which is the integral over

$$\begin{aligned} r_0(E) &= 4\pi\alpha(E)\phi_{\text{bb},\bar{n}}^{\text{d}\Omega}(E, 0) = \frac{8\pi\alpha(E)\bar{n}^2}{h^3c^2} \frac{E^2}{\exp\left(\frac{E}{k_B T}\right) - 1} \\ &\approx \frac{8\pi\alpha(E)\bar{n}^2}{h^3c^2} E^2 \exp\left(\frac{-E}{k_B T}\right). \end{aligned} \quad (\text{B.20})$$

Here, the approximation in the last line again represents the Boltzmann approximation.

This expression was first derived by van Roosbroeck and Shockley in 1954 [148] and later generalized by Würfel [15]. The derivation is based on the detailed balance of absorbed and emitted photons in a semiconductor material with refractive index \bar{n} and absorption coefficient α . The semiconductor has infinite extensions in all directions and is in thermodynamic equilibrium. Then the radiative recombination rate has to

equal the generation rate caused by the thermal radiation within the sample. This generation rate is equal to the photon density per unit volume and the probability that a photon is absorbed per unit time. Via $R_0 = n_i^2 B$ the radiative recombination rate is related to the radiative recombination constant B .

The radiative recombination rate can also be expressed as a radiative lifetime

$$\tau_r = \frac{n_0}{R_0} = \frac{h^3 c^2 n_i^2}{8\pi \bar{n}^2 N_A} \left(\int_0^\infty \alpha(E) E^2 \exp\left(\frac{-E}{k_B T}\right) dE \right)^{-1} \quad (\text{B.21})$$

Note the similarity between Eq. (B.20) and Eq. (2.6). Only due to the identical spectral distribution of radiation emitted within the solar cell and thermal radiation outside the cell, can the radiation balance between the cell and its ambience be fulfilled.

For the analysis of the radiative interaction between two locations x_r and x_g , each photon energy needs to be considered separately because the absorption coefficient $\alpha(E)$ depends on the photon energy. Therefore, we require the spectral radiative recombination rate $r_r(E, x)$. With the chemical potential μ of the emitted photons being equal to the local splitting of the quasi-Fermi levels, the Boltzmann approximation of the spectral radiative recombination rate is given by

$$r_r(E, x) = r_0(E) \exp(\mu(x)/kT) = r_0(E) n(x)/n_0. \quad (\text{B.22})$$

Non-radiative recombination Non-radiative recombination includes Auger recombination or Shockley-Read-Hall recombination. Throughout the thesis I assume an injection independent non-radiative lifetime τ_{nr} . For Auger recombination, for instance, this assumption is justified as long as the doping level is not too high and the sample is operated in low-level injection conditions (see for example Ref. [76]).

Since all non-radiative recombination vanish in thermal equilibrium, the non-radiative recombination rate $R_{nr}(x) = (n(x) - n_0)/\tau_{nr}$ is proportional to the excess electron concentration $\Delta n(x) = n(x) - n_0$.

B.2.4 Direct internal generation

In the following, I derive the expression for the internal generation rate $\delta G_{\text{int}}(x_g, x_r)$ between two locations x_r and x_g . The derivation chosen here is based on the treatment presented by Mettler [29]. First I consider the generation $G_{\text{int}}^{\text{dir}}$ from direct paths of light,

then I extend the approach to the generation rate $G_{\text{int}}^{\text{ref}}$ caused by multiple reflections at front and back surface of the cell. The overall internal generation is then given by the sum $G_{\text{int}} = G_{\text{int}}^{\text{dir}} + G_{\text{int}}^{\text{ref}}$.

First, we have to consider the generation rate $\delta g_{\text{int}}(E, x_g)$ which is caused by the radiative recombination rate $r_r(E, x_r)$ at x_r . Let us consider the spherical symmetry around a recombination event at x_r according to Fig. B.1a. The relation between photon flux ϕ_γ and generation rate as well as recombination rate is given by $\nabla \phi_\gamma(\mathbf{x}) = r(\mathbf{x}) - g(\mathbf{x})$.² Recombining carriers emit radiation isotropically into all directions. The photon flux density per solid angle interval $d\Omega = \sin(\theta) d\theta d\varphi$ is obtained by dividing by 4π . Despite this three-dimensional photon emission, the calculation of the radial component $\phi_{\gamma,\rho}$ of the photon flux density per solid angle interval $d\Omega$ poses only a one-dimensional problem. This is because of the spherical symmetry of the emitted radiation.

With the radius $\rho = |x_g - x_r|/\cos(\theta)$ and the angle θ in accordance to Fig. B.1a, the photon flux $\delta\phi_{\gamma,\rho}$ per solid angle interval $d\Omega$ emitted by a thin layer with thickness δx_r at $x = x_r$ into the direction θ , reads as

$$\delta\phi_{\gamma,\rho}(E, x = x_r) = \frac{r(E, x = x_r)}{4\pi} \delta\rho. \quad (\text{B.23})$$

Since $\phi_{\gamma,\rho}(\rho)$ is attenuated exponentially according to Lambert-Beer's law $\phi_{\gamma,\rho}(\rho) = \phi_{\gamma,\rho}(\rho = 0)\exp(-\alpha(E)\rho)$, the generation rate caused at $x = x_g$ is given by

$$\begin{aligned} \delta g_{\text{int}}(E, \theta, \rho) &= -\frac{d\phi_{\gamma,\rho}}{d\rho} = \alpha(E)\delta\phi_{\gamma,\rho}(E, \rho) \\ &= \frac{\alpha(E)r(E, x = x_r)}{4\pi} \exp(-\alpha(E)\rho) \delta\rho. \end{aligned} \quad (\text{B.24})$$

We now change perspective and put the point x_g where the generation takes place in the center of the spherical coordinates as depicted in Fig. B.1b. This change of coordinates does not change the validity of Eq. (B.24). Using two different sets of coordinates is simply more descriptive to demonstrate the relevant spherical symmetries. In fact, by projecting the radius $\rho|x_g - x_r|/\cos(\theta)$ onto the x -axis we obtain cylinder coordinates with the coordinates x , θ and φ . We can therewith consider cylindrical plains and have the x -axis as an emphasized direction. On the other hand we could initially take advantage of the spherical symmetry of radiative photon emission which allowed for the one-dimensional treatment of the radial photon flux per solid angle described above.

²Vectors are indicated by bold symbols

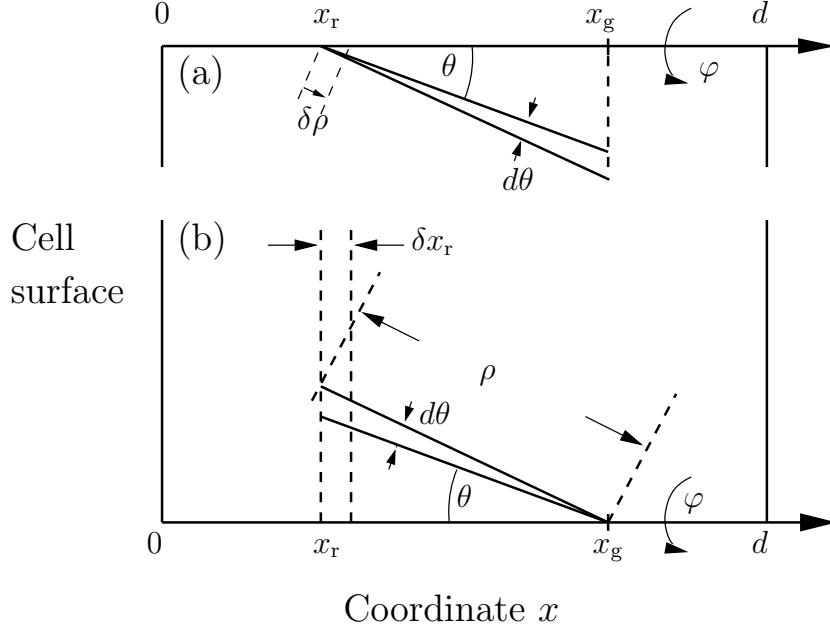


Fig. B.1: Geometry of the radiative interaction between x_r and x_g . (a) A radiative recombination event at $x = x_r$ emits radiation in a spherical symmetry. (b) To obtain the generation rate at $x = x_g$, coordinates are transformed so that x_g is in the center of the coordinate system.

To obtain the generation rate $\delta G_{\text{int}}(x_g, x_r)$ we have to integrate over all possible angles θ and φ and over all possible photon energies E . Thus, by inserting Eq. (B.22) into Eq. (B.24) and by making use of $\delta\rho = \delta x_r / \cos(\theta)$, the rate at which carriers are generated at $x = x_g$ by recombination between $x = x_r$ and $x = x_r + \delta x_r$ and subsequent direct radiative transfer to x_g reads as

$$\begin{aligned} \delta G_{\text{int}}^{\text{dir}}(x_g, x_r) &= \int_0^\infty \frac{\alpha(E) r_0(E)}{4\pi} \frac{n(x_r)}{n_0} \int_0^{2\pi} d\varphi \\ &\times \int_0^{\pi/2} \frac{\sin(\theta)}{\cos(\theta)} \exp\left(\frac{-\alpha(E)|x_g - x_r|}{\cos(\theta)}\right) d\theta dE \delta x_r. \end{aligned} \quad (\text{B.25})$$

With the substitution $t = \alpha(E)|x_g - x_r|/\cos(\theta)$ this becomes

$$\delta G_{\text{int}}^{\text{dir}}(x_g, x_r) = \int_0^\infty \frac{\alpha(E) r_0(E)}{2} \text{Ei}(\alpha(E)|x_g - x_r|) \frac{n(x_r)}{n_0} dE \delta x_r \quad (\text{B.26})$$

where the exponential integral $\text{Ei}(z)$ is given by Eq. (B.3) in appendix B.1.

Eventually, one has to carry out the integration over all possible recombination events at $0 \leq x_r \leq d$, i.e. over the whole thickness of the cell, as denoted in Eq. (3.2) to obtain the overall generation rate $G_{\text{int}}^{\text{dir}}(x_g)$.

B.2.5 Internal generation after multiple reflections

So far, we have only considered direct paths of light, but especially for thin cells and low photon energies with a corresponding low absorption coefficient $\alpha(E)$, the reflected rays have to be accounted for as well. This holds in particular for the black body radiation and the internally emitted radiation which contain a significantly larger fraction of low energy radiation than the solar spectrum emitted by the sun.

In this thesis, I consider two types of reflections, namely (i) reflections at plane surfaces, where the angle of reflection is equal to the angle of incidence and (ii) reflections at textured surfaces that lead to a complete randomization of the reflected light and therewith to a Lambertian radiation characteristic. Figure 3.1a depicts a solar cell with a plane front surface. Whereas all external rays enter the cell, only internally emitted rays that are emitted within the critical angle $\theta_c = \arcsin(1/\bar{n})$ are emitted through the front surface of the cell (ray 1). Rays emitted at larger angles are internally reflected by total internal reflection (ray 2). A textured surface randomizes all external and internal rays and emits radiation in all directions. Rays from within the solar cell are transmitted with the probability t_{lamb} (rays 3) and internally reflected with the probability $1 - t_{\text{lamb}}$ (rays 4).

As will be shown below, the textured surface especially enhances light absorption by means of light trapping in thin samples. For the sake of simplicity I restrict this distinction to the front surface. The back surface is always plane.

B.2.5.1 Plane front surface

To compute the internal generation caused by reflected rays that stem from radiation emitted by recombination in a thin plane at x_r , we have to consider four basic rays that reach the point $x = x_g$ where carriers are generated with an angle θ or $\pi - \theta$. Figure B.2 depicts the photon fluxes caused by recombination in the plane with thickness δx_r at x_r that reach the point x_g via multiple reflections.

Radiation is emitted at the location x_r either in the direction of the front surface or in the direction of the back surface. Accordingly, radiation reaches the location x_g either from the front side or from the back side. Combined this makes four possible combinations. I use the notation F for paths with a final reflection at the front side and B with a final reflection at the back side. For rays with an even/odd number of

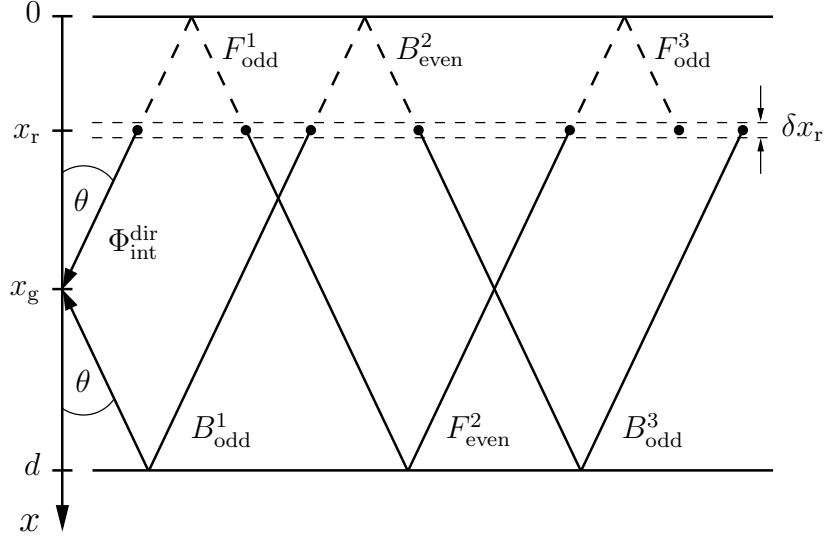


Fig. B.2: Multiple reflections in a solar cell with plane front surface. Radiation emitted by recombination events in the plane with thickness δx_r at the location x_r reaches the point x_g either directly or via multiple reflections. Four basic reflected paths are distinguished according to Tab. B.1. For all further reflections the path simply needs to be prolonged by $2d/\cos(\theta)$.

reflections, I use the subscript even and odd, respectively.

For all further reflections, the x -component of the path is simply prolonged by twice the thickness of the device. For instance, the path B_{odd}^3 is obtained by path B_{odd}^1 . For each reflection, the reflection coefficient ϱ_f of the front and ϱ_b of the back side has to be considered³. The x -components $\Delta x_{l,m}$ of the different paths and the corresponding reflection coefficients are displayed in Tab. B.1. Here, l is the number of reflections and m is the basic ray path type. The paths B_{odd} and F_{odd} are valid for odd numbers of reflections, and the paths B_{even} and F_{even} are valid for even numbers of reflections. Also displayed are the x -components of the direct rays. For the reflected rays, the term $|x_g - x_r|$ in Eq. (B.26) has to be replaced with $\Delta x_{l,m}$ from Tab. B.1.

Due to total internal reflection for $\theta \geq \theta_c$, radiative interaction between the solar cell and its ambience only takes place for angles $0 < \theta < \theta_c$. We obtain for $\theta > \theta_c$ the reflection coefficient for total reflection $\varrho_{\text{totref}} = 1$. Therefore, the integral over θ has to be split up into two separate integrals with $\varrho_{l,m}$ according to Tab. B.1 from $\theta = 0$ to $\theta = \theta_c$ and $\varrho_{l,m} = 1$ from $\theta = \theta_c$ to $\theta = \pi/2$. For each path m and reflection l we

³With no radiative interaction between the solar cell and its ambience through the back side, as is assumed throughout this thesis it holds $\varrho_b = 1$ for all angles. In contrast, ϱ_f can be chosen freely.

Tab. B.1: Components x_i normal to the cell surface of the four basic paths and corresponding reflection coefficients $\varrho_{l,m}$ after l reflections. Paths are termed B if the last reflection occurs at the back side and F if it occurs at the front surface. The indices even/odd indicate an even/odd number of reflections.

path m	# of refl. l	$\Delta x_{l,m}$	$\varrho_{l,m}$
0 - direct	$l = 0$	$ x_g - x_r $	1
1 - B_{odd}	$l = 1, 3, 5, \dots$	$(l + 1)d - x_r - x_g$	$\varrho_f^{\frac{l-1}{2}} \varrho_b^{\frac{l+1}{2}}$
2 - F_{odd}	$l = 1, 3, 5, \dots$	$(l - 1)d + x_r + x_g$	$\varrho_f^{\frac{l+1}{2}} \varrho_b^{\frac{l-1}{2}}$
3 - B_{even}	$l = 2, 4, 6, \dots$	$ld + x_r - x_g$	$\varrho_f^{\frac{l}{2}} \varrho_b^{\frac{l}{2}}$
4 - F_{even}	$l = 2, 4, 6, \dots$	$ld - x_r + x_g$	$\varrho_f^{\frac{l}{2}} \varrho_b^{\frac{l}{2}}$

thus obtain the internal generation at x_g

$$\begin{aligned}
 \delta G_{\text{int}}^{l,m}(x_g, x_r) &= \int_0^\infty \alpha(E) r_0(E) \frac{n(x_r)}{2n_0} \times \\
 &\left\{ \varrho_{l,m} \int_0^{\theta_c} \frac{\sin(\theta)}{\cos(\theta)} \exp\left(\frac{-\alpha \Delta x_{l,m}}{\cos(\theta)}\right) d\theta + \int_{\theta_c}^{\pi/2} \frac{\sin(\theta)}{\cos(\theta)} \exp\left(\frac{-\alpha \Delta x_{l,m}}{\cos(\theta)}\right) d\theta \right\} dE \delta x_r \\
 &= \int_0^\infty \alpha(E) r_0(E) \frac{n(x_r)}{2n_0} \times \\
 &\left\{ \varrho_{l,m} \text{Ei}(\alpha(E) \Delta x_{l,m}) + (1 - \varrho_{l,m}) \text{Ei}\left(\frac{\alpha(E) \Delta x_{l,m}}{\cos(\theta_c)}\right) \right\} dE \delta x_r.
 \end{aligned} \tag{B.27}$$

Summing up the direct ray and all reflected rays yields the total internal Generation in the plain x_g caused by recombination in the plain x_r

$$\delta G_{\text{int}}(x_g, x_r) = \sum_{m=0}^4 \sum_{l=0}^{\infty} \delta G_{\text{int}}^{l,m}(x_g, x_r). \tag{B.28}$$

For the special case with $\varrho_f = 0$, it holds $\varrho_{l,m} = 0$ except for $\varrho_{0,0} = 1$ and $\varrho_{1,1} = 1$. There is only one reflection at the back side and we obtain

$$\delta G_{\text{int}}(x_g, x_r) = \delta G_{\text{int}}^{\text{dir}}(x_g, x_r) + \delta G_{\text{int}}^{1,1}(x_g, x_r). \tag{B.29}$$

B.2.5.2 Textured front surface

For thin solar cells multiple reflections are of increasing importance to absorb the incident light. One means to increase the light confinement within the cell is by texturing

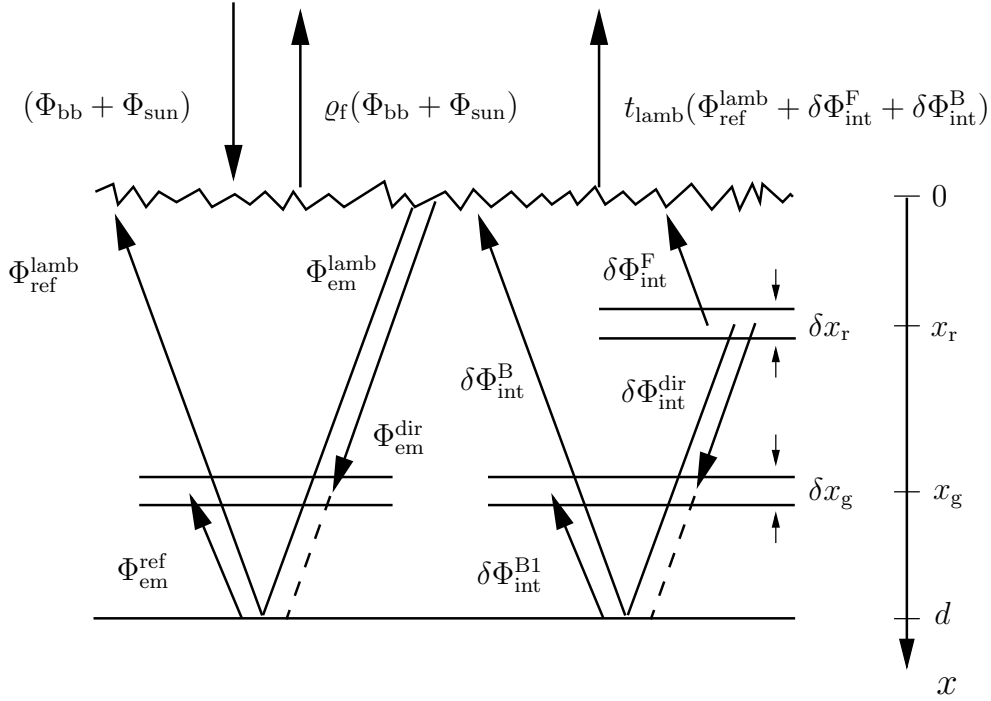


Fig. B.3: Photon fluxes in cell with textured front surface

the front surface as sketched in Fig. B.3. The texture leads to a randomization of the reflected light rays independent from the angle of the incident light ray. Completely randomizing surfaces have a Lambertian emission characteristic, which means that the emitted photon flux per solid angle interval $d\Omega$ is constant in all directions. A Lambertian source emits light isotropically in all directions, but also, a one-directional light beam impinging on a Lambertian surface is isotropically reflected into all directions⁴.

Upon being 'absorbed' and 'reemitted' by a Lambertian surface, a light beam loses all information about previous light reflections. Each time light impinges on a Lambertian surface, the cards are shuffled anew.

Therefore, we obtain an important difference to the case of a plane surface. In the case of a plane surface, each angle θ has to be treated separately. The integration over all angles has to be carried out over the complete path, the light travels before it is absorbed. Consequently, an analytical solution of the resulting integral does not exist. Instead, the contributions of all rays have to be summed up as performed in Eq. (B.28).

⁴The isotropic emission implies that the radial photon flux per solid angle interval is constant. The photon flux emitted from a unit surface area, however, follows Lambert's cosine law because the surface area element $dA = \cos(\theta) dA_\theta$ appears smaller from large angles.

This infinite series with the exponential integral function $Ei(z)$ as an argument has no analytical solution and thus brings along high computational costs when carried out numerically with a finite number of reflections (see appendix B).

In contrast, the case with Lambertian surface allows for an angular integration after each transition of the cell. Consequently, we obtain a closed-form expression for the generation rates including an infinite number of reflections. Especially for thin cells, where multiple reflections are increasingly important this enormously reduces computational costs and guarantees the accuracy of the computation.

Consider the solar cell with Lambertian surface in Fig. B.3.⁵ All incident radiation from the outside consisting of the photon fluxes $\Phi_{\text{bb}}^{\text{Eg}}$ and Φ_{sun} is initially reflected with reflection coefficient ϱ_{f} . Light beams impinging on the surface from the inside of the solar cell are transmitted with a transmission probability t_{lamb} which is independent of the angle of incidence. For a plane surface, the transmission probability is $(1 - \varrho_{\text{f}})$ for $\theta < \theta_{\text{c}} = \arcsin(1/\bar{n})$ and zero for $\theta_{\text{c}} \leq \theta \leq \pi/2$. The transmission probability through a Lambertian surface equals the average transmission probability through a plane surface and is given by [149]

$$t_{\text{lamb}} = \frac{(1 - \varrho_{\text{f}}) \int_0^{\theta_{\text{c}}} \cos(\theta) \sin(\theta) d\theta}{\int_0^{\pi/2} \cos(\theta) \sin(\theta) d\theta} = \frac{1 - \varrho_{\text{f}}}{\bar{n}^2}. \quad (\text{B.30})$$

This result is in accordance with the fact that the radiation density $\phi_{\text{bb},\bar{n}}^{\text{d}\Omega}$ in a medium with refractive index \bar{n} is \bar{n}^2 times higher than the ambient black body radiation density $\phi_{\text{bb},1}^{\text{d}\Omega}$ (cf. Eq. (2.6) in section 2.3.1). It is also in accordance with Snell's law of refraction which states $\sin(\theta) = \bar{n} \sin(\theta_{\text{r}})$, where θ is the angle of the incident light beam and θ_{r} is the angle of the refracted light beam.

The radiation flux $\Phi_{\text{em}}^{\text{lamb}}$ which is emitted from the surface to the inside of the solar cell is partially absorbed in the sample, partially transmitted through the back side (for $\varrho_{\text{b}} \neq 1$) and partially reaches the front surface again after one reflection at the back side, here denoted as the flux $\Phi_{\text{ref}}^{\text{lamb}}$. Both fluxes $\Phi_{\text{em}}^{\text{lamb}}$ and $\Phi_{\text{ref}}^{\text{lamb}}$ are connected via the energy-dependent transmission probability $t_{\text{cell}}(E)$ through the cell, which I derive in the following. The reasoning is similar to the above derivation of the internal generation and is identical to the derivation given by Green [150].

⁵Note again that I use capital letters $\Phi_{\text{sun}}, \Phi_{\text{em}}^{\text{int}}, \dots$ to denote fluxes integrated over energy and small letters $\phi_{\text{sun}}, \phi_{\text{em}}^{\text{int}}, \dots$ to denote fluxes per energy interval dE . The fluxes $\delta\phi_{\text{em}}^{\text{int}}, \delta\phi_{\text{int}}^{\text{F}}, \dots$ correspond to recombination in the infinitesimal plane δx_{r} at x_{r} .

The photon flux $\phi_{\text{em}}^{\text{d}\Omega}$ emitted into the solid angle interval $d\Omega = \sin(\theta) d\theta d\varphi$ per energy interval dE is constant as demanded from the Lambertian radiation characteristic. Upon traversing the sample to the back side, being reflected and traversing to the front side again, this photon flux is attenuated exponentially with the factor $\rho_{\text{b}} \exp(-2\alpha d / \cos(\theta))$. The total flux per unit surface area reaching the front side is then obtained by integrating over all angles as performed in Eq. (2.7). By normalizing this flux to the total flux that is emitted from each front surface unit area we obtain the transmission probability

$$\begin{aligned}
 t_{\text{cell}}(E) &= \frac{\phi_{\text{em}}^{\text{d}\Omega} \int_0^{2\pi} d\varphi \int_0^{\pi/2} \rho_{\text{b}} \exp\left(\frac{-2\alpha(E)d}{\cos(\theta)}\right) \cos(\theta) \sin(\theta) d\theta}{\phi_{\text{em}}^{\text{d}\Omega} \int_0^{2\pi} d\varphi \int_0^{\pi/2} \cos(\theta) \sin(\theta) d\theta} \\
 &= 2 \int_0^{\pi/2} \rho_{\text{b}} \exp\left(\frac{-2\alpha(E)d}{\cos(\theta)}\right) \cos(\theta) \sin(\theta) d\theta \\
 &= 2\rho_{\text{b}} \text{Ei}_3(2\alpha d, 0).
 \end{aligned} \tag{B.31}$$

With the transmission probability t_{cell} we know what fraction of the light that is emitted from the internal front surface returns to the front side. Therewith, we balance all photon fluxes across the front surface. Due to the linearity of the system, we can separate the contributions of external photon flux Φ_{sun} , the ambient photon flux Φ_{bb} , and the photon flux Φ_{int} from internal photon emission. We can subsequently superpose the generation terms just as in the case of flat surfaces.

To compute the internal generation rate we assume $\Phi_{\text{sun}} = \Phi_{\text{bb}} = 0$ and obtain the energetically resolved balance

$$\begin{aligned}
 \delta\phi_{\text{em}}^{\text{int}}(E, x_{\text{r}}) &= (\delta\phi_{\text{int}}^{\text{F}} + \delta\phi_{\text{int}}^{\text{B}} + \delta\phi_{\text{ref}}^{\text{int}}) (1 - t_{\text{lamb}}) \\
 &= \frac{(\delta\phi_{\text{int}}^{\text{F}} + \delta\phi_{\text{int}}^{\text{B}}) (1 - t_{\text{lamb}})}{1 - t_{\text{cell}} (1 - t_{\text{lamb}})}
 \end{aligned} \tag{B.32}$$

from balancing all photon fluxes at the front surface.

Note at this point that the denotations of the fluxes in Fig. B.3 are the overall stationary fluxes and include multiple reflections. The same result could be obtained by summing up all the contributions after each reflection. This leads to a geometric series which simplifies to Eq. (B.32).

The photon flux $\delta\phi_{\text{int}}^{\text{F}}$ that directly reaches each unit surface area from photon

emission in the plane at x_r with thickness δx_r reads as⁶

$$\begin{aligned}\delta\phi_{\text{int}}^{\text{F}}(E, x_r) &= \frac{r_0 n(x_r)}{4\pi n_0} \int_0^{2\pi} d\varphi \int_0^{\pi/2} \exp\left(\frac{-\alpha x_r}{\cos(\theta)}\right) \sin(\theta) d\theta \delta x_r \\ &= \frac{r_0 n(x_r)}{2n_0} \text{Ei}_2(\alpha x_r, 0) \delta x_r,\end{aligned}\tag{B.33}$$

where $\text{Ei}_2(z, \theta)$ is given by Eq. (B.4).

Accordingly, the flux $\delta\phi_{\text{int}}^{\text{B}}$ reaching the front surface after one reflection at the back side is given by

$$\delta\phi_{\text{int}}^{\text{B}}(E, x_r) = \frac{\varrho_b r_0 n(x_r)}{2n_0} \text{Ei}_2(\alpha(2d - x_r), 0) \delta x_r.\tag{B.34}$$

With Eq. (B.32) we can now compute the internal generation rate from rays that are reflected one or more times at the textured front surface, i.e., the generation rate caused by the photon flux $\delta\Phi_{\text{em}}^{\text{int}}$. Including direct beams $\Phi_{\text{em}}^{\text{dir}}$ and beams $\Phi_{\text{em}}^{\text{ref}}$ reflected once at the back side, it holds

$$\begin{aligned}\delta G_{\text{int}}^{\text{lamb}}(x_g, x_r) &\tag{B.35} \\ &= \frac{\int_0^\infty \alpha(E) \delta\phi_{\text{em}}^{\text{int}} \int_0^{2\pi} d\varphi \int_0^{\pi/2} \left\{ \exp\left(\frac{-\alpha x_g}{\cos(\theta)}\right) + \varrho_b \exp\left(\frac{-\alpha(2d-x_g)}{\cos(\theta)}\right) \right\} \sin(\theta) d\theta dE}{\int_0^{2\pi} d\varphi \int_0^{\pi/2} \cos(\theta) \sin(\theta) d\theta} \\ &= 2 \int_0^\infty \alpha(E) \delta\phi_{\text{em}}^{\text{int}}(E, x_r) \{ \text{Ei}_2(\alpha x_g, 0) + \varrho_b \text{Ei}_2(\alpha(2d - x_g), 0) \} dE \\ &= \int_0^\infty \frac{\alpha(E) r_0(E) (1 - t_{\text{lamb}})}{1 - t_{\text{cell}} (1 - t_{\text{lamb}})} \frac{n(x_r) \delta x_r}{n_0} \times \\ &\quad \{ \text{Ei}_2(\alpha x_r, 0) + \varrho_b \text{Ei}_2(\alpha(2d - x_r), 0) \} \{ \text{Ei}_2(\alpha x_g, 0) + \varrho_b \text{Ei}_2(\alpha(2d - x_g), 0) \} dE.\end{aligned}$$

The total internal generation rate is then given by the sum

$$\delta G_{\text{int}}(x_g, x_r) = \delta G_{\text{int}}^{\text{dir}}(x_g, x_r) + \delta G_{\text{int}}^{\text{B1}}(x_g, x_r) + \delta G_{\text{int}}^{\text{lamb}}(x_g, x_r),\tag{B.36}$$

where $\delta G_{\text{int}}^{\text{dir}}$ is specified in Eq. (B.26) and $\delta G_{\text{int}}^{\text{B1}}$ is given by Eq. (B.27) with $l = m = 1$. The internal generation caused by radiative recombination throughout the sample is obtained from the integral Eq. (3.2).

Independent of the nature of the front surface, the internal generation rate can be written as

$$G_{\text{int}}(x_g) = \int_0^d \int_0^\infty \text{const}(E) f_r(E, x_g, x_r) \frac{n(x_r)}{n_0} dE \delta x_r,\tag{B.37}$$

⁶Note that the $\cos(\theta)$ term from the projection to the front surface cancels out against the $\cos(\theta)$ term from $\delta\rho = \delta x_r / \cos(\theta)$.

where $f_r(E, x_g, x_r)$ (cmp. Eq. (B.27) is the radiative interaction function between x_r and x_g and Eq. (B.28) for a plane surface and Eq. (B.35) and Eq. (B.36) for a textured surface).

As can be seen from Tab. B.1 and Eq. (B.35), $f_r(E, x_g, x_r)$ is symmetric in x_r and x_g . The location of light emission and light absorption can be exchanged because the path of light is reversible. Due to the symmetry and linearity of the kernel-function f_r , the whole photon recycling operator as defined in section B.2.1 is linear and symmetric as well.

B.2.6 External generation

This section derives expressions for the external generation rates caused by the external photon fluxes Φ_{bb}^{Eg} and Φ_{sun} . As the light has to enter the cell through the front surface, the optical properties of the front surface play a role not only for reflected rays but also for direct rays. I use the same distinction between plane and textured front surface as in the previous section.

B.2.6.1 Plane front surface

Equilibrium irradiation The next step to obtain all generation rates in the integro-differential equation (3.1) is to give an expression for the equilibrium generation rate

$$\begin{aligned}
 G_{bb}(x) &= \sum_{m=0,1,4} \sum_{l=0}^{\infty} \int_0^{\infty} (1 - \varrho_f) \alpha(E) \phi_{bb,\bar{n}}^{d\Omega}(E, 0) \int_0^{2\pi} d\varphi \\
 &\quad \times \int_0^{\theta_c} \varrho_{l,m} \exp\left(-\frac{\alpha \Delta x_{l,m}}{\cos(\theta)}\right) \sin(\theta) d\theta dE \\
 &= \sum_{m=0,1,4} \sum_{l=0}^{\infty} \int_0^{\infty} 2\pi (1 - \varrho_f) \alpha(E) \phi_{bb,\bar{n}}^{d\Omega}(E, 0) \varrho_{l,m} \\
 &\quad \times \left\{ \text{Ei}_2(\alpha \Delta x_{l,m}, 0) - \text{Ei}_2(\alpha \Delta x_{l,m}, \theta_c) \right\} dE
 \end{aligned} \tag{B.38}$$

caused by the ambient black body radiation. The geometrical reasoning is analog to the derivation of G_{int} . We consider the thermal radiation $(1 - \varrho_f) \alpha(E) \phi_{bb,\bar{n}}^{d\Omega}(E, 0)$ entering the cell at $x = 0^+$, attenuate it by the factor $\varrho_{l,m} \exp((- \alpha(E) \Delta x_{l,m}) / (\cos(\theta)))$ and integrate over all possible angles. Here, ϱ_f is the reflection coefficient at the front surface. The ambient radiation from all directions at $x = 0^-$ is refracted into the cone within the critical angle $\theta_c = \arcsin(1/\bar{n})$ at $x = 0^+$.

Non-equilibrium irradiation For the external generation, I assume normal incidence and thus, the integration over all angles is unnecessary. The functional dependence of the photon flux on the coordinate x is therefore given by Lambert-Beer's exponential law. This has the advantage that it is possible to simplify the sum of all reflected rays in a geometrical series. Carrying out this series leads to the total non-equilibrium generation rate

$$\begin{aligned} G_{\text{sun}}(x_g) &= \int_0^\infty (1 - \varrho_f) \alpha \phi_{\text{sun}}(E) \\ &\quad \left\{ e^{-\alpha x_g} + (\varrho_b e^{-\alpha(2d-x_g)} + \varrho_f \varrho_b e^{-\alpha(2d+x_g)}) \sum_{l=0}^\infty (\varrho_f \varrho_b)^l e^{-2l\alpha d} \right\} dE \\ &= \int_0^\infty (1 - \varrho_f) \alpha \phi_{\text{sun}}(E) \left\{ e^{-\alpha x_g} + \frac{\varrho_b e^{-\alpha(2d-x_g)} + \varrho_f \varrho_b e^{-\alpha(2d+x_g)}}{1 - \varrho_f \varrho_b \exp(-2\alpha d)} \right\} dE \end{aligned} \quad (\text{B.39})$$

where ϕ_{sun} is the spectral density of the incoming photon flux so that the overall external photon flux reads as $\Phi_{\text{sun}} = \int_0^\infty \phi_{\text{sun}}(E) dE$ (cf. Eq. (2.12)).

B.2.6.2 Textured front surface

The derivation of the generation rates in the case of a textured front surface is identical to the derivation of the internal generation rate in section B.2.5.2.

Equilibrium irradiation For the generation rate caused by ambient black body radiation it holds $\Phi_{\text{int}}^F = \Phi_{\text{int}}^B = \Phi_{\text{sun}} = 0$ and from Fig. B.3 we derive the photon flux emitted from the front surface towards the inside of the cell

$$\phi_{\text{em}}^{\text{bb}} = \frac{(1 - \varrho_f) \phi_{\text{bb}}}{1 - t_{\text{cell}}(1 - t_{\text{lamb}})}, \quad (\text{B.40})$$

where $\phi_{\text{bb}}(E) = 2\pi/(h^3 c^2) E^2 \exp(-E/(k_B T)) = \pi \phi_{\text{bb},1}^{\text{d}\Omega}(E, 0)$ is the energy-resolved black body flux $\phi_{\text{bb},1}^{\text{d}\Omega}$ integrated over all angles as performed in Eq. (2.7). In analogy to Eq. (B.35) we thus obtain the black body generation rate

$$G_{\text{bb}}(x_g) = 2 \int_0^\infty \alpha \phi_{\text{em}}^{\text{bb}} \{ \text{Ei}_2(\alpha x_g, 0) + \varrho_b \text{Ei}_2(\alpha(2d - x_g), 0) \} dE. \quad (\text{B.41})$$

Non-equilibrium irradiation Accordingly, we assume $\Phi_{\text{int}}^F = \Phi_{\text{int}}^B = \Phi_{\text{bb}} = 0$ to calculate the generation rate contributed by solar irradiation and obtain

$$\phi_{\text{em}}^{\text{sun}} = \frac{(1 - \varrho_f) \phi_{\text{sun}}}{1 - t_{\text{cell}}(1 - t_{\text{lamb}})}. \quad (\text{B.42})$$

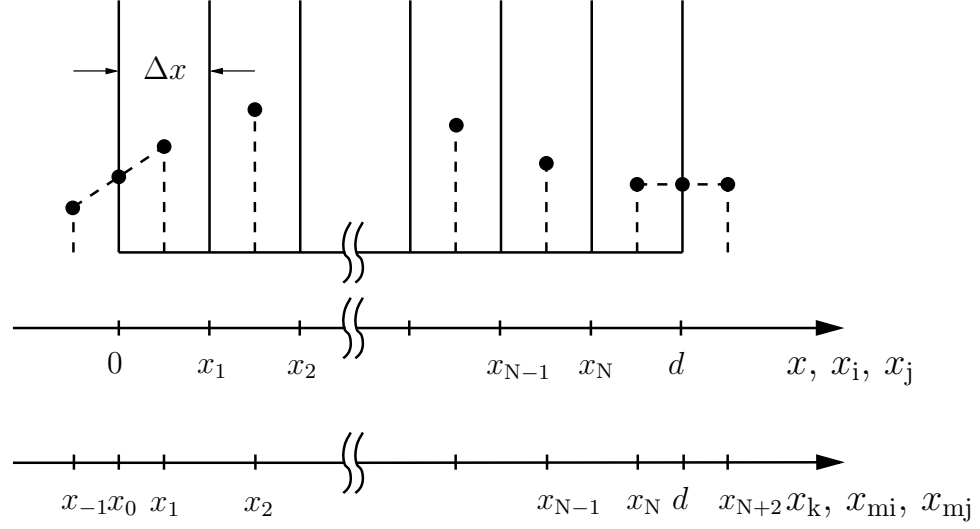


Fig. B.4: Discretization of the absorber into intervals with thickness Δx . The electron concentrations are computed in the middle x_{mi}/x_{mj} of each interval. To obtain equidistant spacing of the mesh points, the boundaries are extrapolated beyond the cell dimensions.

Therewith, it holds

$$G_{\text{sun}}(x_g) = 2 \int_0^\infty \alpha \phi_{\text{em}}^{\text{sun}} \{ \text{Ei}_2(\alpha x_g, 0) + \varrho_b \text{Ei}_2(\alpha(2d - x_g), 0) \} dE. \quad (\text{B.43})$$

Now, we have the expressions for all generation rates in Eq. (3.1). To solve the linear integro-differential equation, I transform it into a matrix equation as performed in appendix B. The numerical evaluation scheme is closely related to the procedure used by Durbin and Gray [52, 53]. In the next section I discuss the results of the computations.

B.3 Generation terms

The integro-differential Eq. (3.1) cannot be solved analytically. Therefore, I transform it into a finite differences equation by discretizing the absorber depth from $x = 0$ to $x = d$ into N intervals. The discretization I use is in accordance with the formulation given by Durbin and Gray [53], only that they use different coordinates. I restrict the following derivation to energetically resolved terms. The overall generation terms are obtained by integrating over the energy E .

B.3.1 Internal generation

In contrast to the differential equation, where we can consider the internal generation at one distinct point x_g caused by recombination within an infinitesimal interval δx_r at another distinct point x_r we now have to build a matrix where each element comprises the radiative interaction between two finite intervals around x_g and x_r with thickness Δx . Considering the radiative interaction between two finite intervals instead of between two discrete locations makes the approach self-consistent and ensures the conservation of photons and electrons.

The internal generation at a point x_g caused by recombination in the incremental plane with thickness δx_r at x_r is given by

$$\delta g_{\text{int}}(x_g, x_r) = \frac{\alpha r_0}{2} \frac{n(x_r)}{n_0} \int_0^{\pi/2} \exp\left(\frac{-\alpha x_{l,m}(s_g x_g, s_r x_r)}{\cos(\theta)}\right) \frac{\sin(\theta)}{\cos(\theta)} d\theta \delta x_r. \quad (\text{B.44})$$

Here, $x_{l,m}(s_g x_g, s_r x_r)$ is the path of the light which can either be a direct ray or a reflected ray. Depending on the path, the signum $s_g = \pm 1$ of x_g and the signum $s_r = \pm 1$ of x_r can be either positive or negative.

For the discretization, I divide the sample into finite intervals with thickness Δx . With the approximation that the electron density is constant throughout one interval we obtain the generation rate at x_g caused by recombination in the interval between $x_r = x_{j-1}$ and $x_r = x_j$ by integrating over δg_{int} according to

$$\begin{aligned} \Delta g_{\text{int}}(x_g, x_{mj}) &= \int_{x_r=x_{j-1}}^{x_r=x_j} \delta g_{\text{int}}(x_g, x_r) \\ &\approx \frac{\alpha r_0}{2} \frac{n(x_{mj})}{n_0} \int_{x_r=x_{j-1}}^{x_r=x_j} \int_0^{\pi/2} \exp\left(\frac{-\alpha x_{l,m}(s_g x_g, s_r x_r)}{\cos(\theta)}\right) \frac{\sin(\theta)}{\cos(\theta)} d\theta \delta x_r. \end{aligned} \quad (\text{B.45})$$

Note that here and in the following I use the index j for the discretization of the location x_r where the recombination process takes place and the index i for the discretization of the location x_g where we consider the generation. The electron concentrations are computed in the middle of each interval. I use the notation

$$x_{mj} = \frac{x_{j-1} + x_j}{2} \quad (\text{B.46})$$

when referring to the middle of the recombination interval and

$$x_{mi} = \frac{x_{i-1} + x_i}{2} \quad (\text{B.47})$$

when referring to the middle of the generation interval.

The internal generation rate at x_g caused by recombination in the whole sample is then given by the sum

$$g_{\text{int}}(x_g) = \sum_{j=0}^{N-1} \Delta g_{\text{int}}(x_g, x_{\text{mj}}). \quad (\text{B.48})$$

For a self-consistent treatment we require the average internal generation in a finite plane with thickness Δx between $x_g = x_{i-1}$ and $x_g = x_i$ which reads as

$$\begin{aligned} \overline{g_{\text{int}}^{\text{l,m}}}(x_{\text{mi}}) &= \frac{1}{\Delta x} \int_{x_g=x_{i-1}}^{x_g=x_i} g_{\text{int}}(x_g) dx_g \\ &= \frac{\alpha r_0}{2\Delta x} \sum_{j=0}^{N-1} \frac{n(x_{\text{mj}})}{n_0} \times \\ &\quad \int_0^{\pi/2} \int_{x_g=x_{i-1}}^{x_g=x_i} \int_{x_r=x_{j-1}}^{x_r=x_j} \exp\left(\frac{-\alpha x_{\text{l,m}}(s_g x_g, s_r x_r)}{\cos(\theta)}\right) \frac{\sin(\theta)}{\cos(\theta)} \delta x_r dx_g d\theta \\ &= \frac{\alpha r_0}{2\Delta x} \sum_{j=0}^{N-1} \frac{n(x_{\text{mj}})}{n_0} \int_0^{\pi/2} s_g s_r f_{\text{exp}}^{\text{ij}} \frac{\cos^2(\theta)}{\alpha^2} \frac{\sin(\theta)}{\cos(\theta)} d\theta \\ &=: \frac{s_g s_r r_0}{2\alpha \Delta x} \sum_{j=0}^{N-1} \frac{n(x_{\text{mj}})}{n_0} \text{Ei}_3^{\text{ij}}(\alpha, 0), \end{aligned} \quad (\text{B.49})$$

where

$$\begin{aligned} \text{Ei}_3^{\text{ij}}(\alpha, \theta_c) &:= \text{Ei}_3(\alpha x_{\text{l,m}}(s_g x_i, s_r x_j), \theta_c) - \text{Ei}_3(\alpha x_{\text{l,m}}(s_g x_i, s_r x_{j-1}), \theta_c) \\ &\quad - \text{Ei}_3(\alpha x_{\text{l,m}}(s_g x_{i-1}, s_r x_j), \theta_c) + \text{Ei}_3(\alpha x_{\text{l,m}}(s_g x_{i-1}, s_r x_{j-1}), \theta_c). \end{aligned} \quad (\text{B.50})$$

In general, the interval thickness Δx depends on x_{j-1} and x_j . However, I use an equidistant discretization mesh so that Δx is constant.

The energy integral of this general expression is the analogy to G_{int} from Eq. (B.26). For the final expression including direct and reflected rays we again have to distinguish the two cases of plane and textured front surface.

B.3.1.1 Plane front surface

For a plane front surface we obtain in analogy to Eq. (B.27) the internal generation caused by the reflection l along path m

$$\overline{g_{\text{int}}^{l,m}}(x_{\text{mi}}) = \frac{s_g s_r r_0}{2\alpha \Delta x} \sum_{j=0}^{N-1} \frac{n(x_{\text{mj}})}{n_0} \left\{ \varrho_{l,m} \text{Ei}_3^{\text{ij}}(\alpha, 0) + (1 - \varrho_{l,m}) \text{Ei}_3^{\text{ij}}(\alpha(E), \theta_c) \right\}. \quad (\text{B.51})$$

Summing up the direct ray and all reflected rays yields the total internal Generation in the finite plane $x_{i-1} \leq x_g \leq x_i$ caused by recombination throughout the sample

$$\overline{g_{\text{int}}}(x_{\text{mi}}) = \sum_{m=0}^4 \sum_{l=0}^{\infty} \overline{g_{\text{int}}^{l,m}}(x_{\text{mi}}). \quad (\text{B.52})$$

B.3.1.2 Textured front surface

The discretization has no influence on the transmission probability t_{cell} through the sample so that Eq. (B.31) still holds. We rewrite the photon flux balance Eq. (B.32) at the front surface to obtain the photon flux internally emitted from the front surface

$$\Delta\phi_{\text{em}}^{\text{int}}(x_{j-1}, x_j) = \frac{(\Delta\phi_{\text{int}}^{\text{F}} + \Delta\phi_{\text{int}}^{\text{B}}) \varrho_{\text{lamb}}}{1 - t_{\text{cell}} \varrho_{\text{lamb}}} \quad (\text{B.53})$$

caused by radiative recombination in the plane $x_{j-1} \leq x_r \leq x_j$. The fluxes $\Delta\phi_{\text{int}}^{\text{F}}$ and $\Delta\phi_{\text{int}}^{\text{B}}$ are obtained by integrating $\delta\phi_{\text{int}}^{\text{F}}$ and $\delta\phi_{\text{int}}^{\text{B}}$ from $x_r = x_{j-1}$ to x_j according to

$$\begin{aligned} \Delta\phi_{\text{int}}^{\text{F}}(x_{j-1}, x_j) &= \frac{r_0}{2} \frac{n(x_{\text{mj}})}{n_0} \int_0^{\pi/2} \int_{x_r=x_{j-1}}^{x_r=x_j} \exp\left(\frac{-\alpha x_r}{\cos(\theta)}\right) \frac{\sin(\theta) \cos(\theta)}{\cos(\theta)} \delta x_r d\theta \\ &= \frac{r_0}{2\alpha} \frac{n(x_{\text{mj}})}{n_0} \int_0^{\pi/2} \left\{ \exp\left(\frac{-\alpha x_{j-1}}{\cos(\theta)}\right) - \exp\left(\frac{-\alpha x_j}{\cos(\theta)}\right) \right\} \cos(\theta) \sin(\theta) d\theta \\ &= \frac{r_0}{2\alpha} \frac{n(x_{\text{mj}})}{n_0} \left\{ \text{Ei}_3(\alpha x_{j-1}, 0) - \text{Ei}_3(\alpha x_j, 0) \right\} \end{aligned} \quad (\text{B.54})$$

and

$$\Delta\phi_{\text{int}}^{\text{B}}(x_{j-1}, x_j) = \frac{r_0}{2\alpha} \frac{n(x_{\text{mj}})}{n_0} \left\{ \text{Ei}_3(\alpha(2d - x_j), 0) - \text{Ei}_3(\alpha(2d - x_{j-1}), 0) \right\}. \quad (\text{B.55})$$

Note that the $\cos(\theta)$ term in line one of Eq. (B.54) cancels out because in contrast to Eq. (B.45) the projection to the front surface unit area requires an additional $\cos(\theta)$

term (cmp. Eq. (B.31) and Eq. (B.33)). The $\cos(\theta)$ term in line two stems from the integration over x_r .

The emission caused by recombination throughout the sample is then given by the sum

$$\phi_{\text{em}}^{\text{int}} = \sum_{j=0}^{N-1} \Delta\phi_{\text{em}}^{\text{int}}(x_{j-1}, x_j). \quad (\text{B.56})$$

In analogy to Eq. (B.35) this photon flux causes the average internal generation in the plane $x_{i-1} \leq x_g \leq x_i$

$$\begin{aligned} \overline{g_{\text{int}}^{\text{lamb}}}(x_{\text{mi}}) &= \\ &= \frac{2\alpha\phi_{\text{em}}^{\text{int}}}{\Delta x} \int_0^{\pi/2} \int_{x_g=x_{i-1}}^{x_g=x_i} \left\{ \exp\left(\frac{-\alpha x_g}{\cos(\theta)}\right) + \varrho_b \exp\left(\frac{-\alpha(2d-x_g)}{\cos(\theta)}\right) \right\} \sin(\theta) dx_g d\theta \\ &= \frac{2\phi_{\text{em}}^{\text{int}}}{\Delta x} \int_0^{\pi/2} \left\{ \exp\left(\frac{-\alpha x_{i-1}}{\cos(\theta)}\right) - \exp\left(\frac{-\alpha x_i}{\cos(\theta)}\right) \right. \\ &\quad \left. + \varrho_b \exp\left(\frac{-\alpha(2d-x_{i-1})}{\cos(\theta)}\right) - \varrho_b \exp\left(\frac{-\alpha(2d-x_i)}{\cos(\theta)}\right) \right\} \cos(\theta) \sin(\theta) d\theta \\ &= \frac{2\phi_{\text{em}}^{\text{int}}}{\Delta x} \left\{ \text{Ei}_3(\alpha x_{i-1}, 0) - \text{Ei}_3(\alpha x_i, 0) \right. \\ &\quad \left. + \varrho_b \text{Ei}_3(\alpha(2d-x_{i-1}), 0) - \varrho_b \text{Ei}_3(\alpha(2d-x_i), 0) \right\}. \end{aligned} \quad (\text{B.57})$$

The total internal generation rate is then given by the sum

$$\overline{g_{\text{int}}}(x_{\text{mi}}) = \overline{g_{\text{int}}^{\text{dir}}}(x_{\text{mi}}) + \overline{g_{\text{int}}^{\text{B1}}}(x_{\text{mi}}) + \overline{g_{\text{int}}^{\text{lamb}}}(x_{\text{mi}}), \quad (\text{B.58})$$

where $\overline{g_{\text{int}}^{\text{dir}}}(x_{\text{mi}})$ and $\overline{g_{\text{int}}^{\text{B1}}}(x_{\text{mi}})$ are given by Eq. (B.51) with $l = m = 0$ in for the direct path and $l = m = 1$ for the ray reflected once at the back side. The overall internal generation rate $\overline{G_{\text{int}}}(x_{\text{mi}})$ is obtained by integrating over the energy.

B.3.2 External generation

This section derives expressions for the average external generation rates caused by the external photon fluxes Φ_{bb} and Φ_{sun} .

B.3.2.1 Plane front surface

Equilibrium irradiation In analogy to Eq. (B.38) the average black body generation rate reads as

$$\begin{aligned}
 \overline{g_{\text{bb}}}(x_{\text{mi}}) &= \sum_{m=0,1,4} \sum_{l=0}^{\infty} \frac{(1 - \varrho_f) 2\pi\alpha\phi_{\text{bb},\bar{n}}^{\text{d}\Omega}(E, 0)}{\Delta x} \\
 &\quad \times \int_0^{\theta_c} \int_{x_g=x_{i-1}}^{x_g=x_i} \varrho_{l,m} \exp\left(\frac{-\alpha\Delta x_{l,m}(s_g x_g)}{\cos(\theta)}\right) \sin(\theta) dx_g d\theta \\
 &= \sum_{m=0,1,4} \sum_{l=0}^{\infty} \frac{(1 - \varrho_f) 2\pi s_g \phi_{\text{bb},\bar{n}}^{\text{d}\Omega}(E, 0)}{\Delta x} \\
 &\quad \times \int_0^{\theta_c} \varrho_{l,m} \left\{ \exp\left(\frac{-\alpha\Delta x_{l,m}(s_g x_{i-1})}{\cos(\theta)}\right) - \exp\left(\frac{-\alpha\Delta x_{l,m}(s_g x_i)}{\cos(\theta)}\right) \right\} \cos(\theta) \sin(\theta) d\theta \\
 &= \sum_{m=0,1,4} \sum_{l=0}^{\infty} \frac{(1 - \varrho_f) 2\pi s_g \phi_{\text{bb},\bar{n}}^{\text{d}\Omega}(E, 0)}{\Delta x} \left\{ \text{Ei}_3(\alpha\Delta x_{l,m}(s_g, x_{i-1}), 0) - \text{Ei}_3(\alpha\Delta x_{l,m}(s_g, x_i), 0) \right\}.
 \end{aligned} \tag{B.59}$$

Non-equilibrium irradiation For the non-equilibrium irradiation, I assume normal incidence and, thus, from the integration of Eq. (B.39) we obtain the average solar generation rate at $x_{i-1} \leq x_g \leq x_i$

$$\begin{aligned}
 \overline{g_{\text{sun}}}(x_{\text{mi}}) &= \frac{(1 - \varrho_f) \alpha \phi_{\text{sun}}(E)}{\Delta x} \\
 &\quad \int_{x_g=x_{i-1}}^{x_g=x_i} \left\{ e^{-\alpha x_g} + \frac{\varrho_b e^{-\alpha(2d-x_g)} + \varrho_f \varrho_b e^{-\alpha(2d+x_g)}}{1 - \varrho_f \varrho_b \exp(-2\alpha d)} \right\} dx_g \\
 &= \frac{(1 - \varrho_f) \phi_{\text{sun}}(E)}{\Delta x} \left\{ \exp(-\alpha x_{i-1}) - \exp(-\alpha x_i) \right. \\
 &\quad \left. + \frac{\varrho_b (e^{-\alpha(2d-x_i)} - e^{-\alpha(2d-x_{i-1})}) + \varrho_f \varrho_b (e^{-\alpha(2d+x_{i-1})} - e^{-\alpha(2d+x_i)})}{1 - \varrho_f \varrho_b e^{-2\alpha d}} \right\}.
 \end{aligned} \tag{B.60}$$

B.3.2.2 Textured front surface

The derivation of the generation rates in the case of a textured front surface is identical to the derivation of the internal generation rate in section B.3.1.2. We obtain the average black body generation rate $\overline{g_{\text{bb}}}(x_{\text{mi}})$ and the average external generation rate $\overline{g_{\text{sun}}}(x_{\text{mi}})$ by simply replacing $\phi_{\text{em}}^{\text{int}}$ in Eq. (B.57) with $\phi_{\text{em}}^{\text{bb}}$ from Eq. (B.40) and $\phi_{\text{em}}^{\text{sun}}$ from Eq. (B.42) respectively.

B.4 Diffusion operator

The simplest discrete approximation of the second derivative of a function $n(x)$ at equidistant meshpoints with meshwidth Δx is obtained from the Taylor expansion of $n(x)$ at $x = x_k$ and reads as

$$\begin{aligned} \left. \frac{d^2 n(x)}{dx^2} \right|_{x=x_k} &= \frac{\frac{n(x_{k+1})-n(x_k)}{x_{k+1}-x_k} - \frac{n(x_k)-n(x_{k-1}))}{x_k-x_{k-1}}}{\Delta x} \\ &= \frac{n(x_{k-1}) - 2n(x_k) + n(x_{k+1}))}{\Delta x^2}. \end{aligned} \quad (\text{B.61})$$

However, in our case the meshpoints x_k are not equidistant. Instead, the x_k are given by the centerpoints of the equidistant intervals $x_{i-1} \leq x \leq x_i$. Therefore, The distance from $x_0 = x_k(k=0) = 0$ to $x_1 x_k(k=1) = \Delta x/2$ and the distance from x_N to $x_{N+1} = d$ is only $\Delta x/2$.

For a non-equidistant spacing of the meshpoints, the second derivative can again be obtained from the Taylor expansion [151]. In general, it holds

$$\begin{aligned} \left. \frac{d^2 n(x)}{dx^2} \right|_{x=x_k} &= \frac{2}{(x_k - x_{k-1})(x_{k+1} - x_{k-1})} n(x_{k-1}) \\ &\quad + \frac{-2}{(x_k - x_{k-1})(x_{k+1} - x_k)} n(x_k) \\ &\quad + \frac{2}{(x_{k+1} - x_k)(x_{k+1} - x_{k-1})} n(x_{k+1}) \end{aligned} \quad (\text{B.62})$$

However, in that case, the consistency error of the discretization is only of the order $O(\Delta x)$ compared to $O(\Delta x^2)$ for equidistant grids [151]. Therefore, the approximation of the second derivative is much worse than in the equidistant case and the solution of the differential equation will be much less exact.

To elude this problem, I extrapolate the electron distribution to the external points $x_{-1} = -\Delta x/2$ and $x_{N+2} = d + \Delta x/2$ as sketched in Fig. B.4 by assuming identical slopes

$$\frac{n(x_0) - n(x_{-1}))}{\Delta x/2} = \frac{n(x_1) - n(x_0)}{\Delta x/2} \quad (\text{B.63})$$

at x_0 and $(x_0 + x_1)/2$ and

$$\frac{n(x_{N+2}) - n(x_{N+1}))}{\Delta x/2} = \frac{n(x_{N+1}) - n(x_N)}{\Delta x/2} \quad (\text{B.64})$$

at x_{N+1} and $(x_N + x_{N+1})/2$. Therewith, we obtain the second derivatives

$$\begin{aligned} \left. \frac{d^2 n(x)}{dx^2} \right|_{x=x_1} &= \frac{\frac{n(x_2)-n(x_1)}{\Delta x} - \frac{n(x_1)-n(x_0)}{\Delta x/2}}{\Delta x} \\ &= \frac{2n(x_0) - 3n(x_1) + n(x_2)}{\Delta x^2} \end{aligned} \quad (\text{B.65})$$

at $x = x_1$ and

$$\begin{aligned} \left. \frac{d^2 n(x)}{dx^2} \right|_{x=x_N} &= \frac{\frac{n(x_{N+1})-n(x_N)}{\Delta x/2} - \frac{n(x_N)-n(x_{N-1})}{\Delta x}}{\Delta x} \\ &= \frac{n(x_{N-1}) - 3n(x_N) + 2n(x_{N+1})}{\Delta x^2} \end{aligned} \quad (\text{B.66})$$

at $x = x_N$.

B.5 Boundary conditions

Apart from the boundary conditions, we have all the components for calculating the electron (minority carrier) profile in the absorber by inverting the established matrix equation equivalent to Eq. (3.1). The electron profile in turn supplies the current/voltage characteristic of the solar cell. Since the voltage-dependence occurs only in the boundary condition Eq. (2.17) at the edge of the space-charge region, the recombination current exhibits the well known exponential voltage-dependence. With the linear dependence on the external excitation being unchanged the principle of superposition of recombination and short circuit current remains valid as well.

B.5.1 Back contact

In the ideal case of $S_n = 0$, the boundary condition Eq. (2.18) at the back contact simplifies to

$$\left. \frac{dn}{dx} \right|_{x=d} = 0. \quad (\text{B.67})$$

In conjunction with assumption Eq. (B.64), it holds $n(x_N) = n(x_{N+1}) = n(x_{N+2})$, and we rewrite the last row Eq. (B.66) of the diffusion matrix as

$$\left. \frac{d^2 n(x)}{dx^2} \right|_{x=x_N} = \frac{n(x_{N-1}) - 3n(x_N) + 2n(x_{N+1})}{\Delta x^2} = \frac{n(x_{N-1}) - n(x_N)}{\Delta x^2}. \quad (\text{B.68})$$

B.5.2 Junction

The boundary condition Eq. (2.17) at the junction depends on the applied voltage.

Short circuit current Under short circuit conditions with the applied voltage $V = 0$, the electron density at the junction, which according to Eq. (B.65) is needed for the first row of the diffusion matrix, reads as

$$n(x_0) = n(0) = n_0 \exp\left(\frac{qV}{k_B T}\right) = n_0. \quad (\text{B.69})$$

Solving the matrix equation under illumination with this boundary condition and computing the current density

$$J(V) = -qD_n \frac{dn}{dx} \bigg|_{x=x_0} \approx -qD_n \frac{n(x_1) - n(x_0)}{x_1 - x_0} \quad (\text{B.70})$$

at $x = 0$ yields the short circuit current density $J_{sc} = |J(V = 0)|$.

Saturation current I compute the saturation current density J_0 by solving the matrix equation in the dark under the applied bias $V = (k_B T/q) \ln(2)$ which leads to the boundary condition

$$n(x_0) = n(0) = n_0 \exp\left(\frac{qV}{k_B T}\right) = 2n_0. \quad (\text{B.71})$$

With this boundary condition it holds $\exp(qV/(k_B T)) - 1 = 1$ and the current becomes $J(V) = J_0(\exp(qV/(k_B T)) - 1) = J_0$.

B.6 Discussion

B.6.1 Reabsorption matrix

The computation of the photon recycling matrix \underline{PR} can be very time-consuming. This is because the computation of the exponential integral $\text{Ei}(z)$ is very expensive. For a sufficient accuracy of the computations, we need $N = 1000$ mesh points which results in a matrix with a million elements.

Fortunately, the matrix exhibits certain symmetries, namely the symmetry along the main diagonal because the interaction between two intervals at x_j and x_i equals the reverse interaction between the intervals at x_i and x_j .

Additionally, the radiative interaction depends only on the distance $\Delta x_{l,m}$ (cf. Tab. B.1). Since only the function $Ei_3(n\Delta x)$ occurs in the final equations, I only compute the array $Ei_3(n\Delta x)$ for $n = 1..(M+1)N-1$, where M is the maximum number of multiple reflections. The elements of the reabsorption matrix are then generated from this array without having to compute each element separately. Thereby, the computation cost is roughly reduced by a factor of N .

B.6.2 Energy superposition

With respect to the energy-dependence of internal, external and dark generation rate, the PR integral term evokes a fundamental difference between the differential equation Eq. (2.16) without PR and the integro-differential equation Eq. (3.1) with PR. In the former problem, energy-dependencies occur only in the right hand side generation terms which consist of the integrated generation rates at each energy. Due to this linear superposition, one can determine the exact solution for each energy and subsequently calculate the current from the convolution integral with the density of the incoming radiation fluxes. In the latter case with photon recycling, the radiation emitted by recombining carriers which causes the internal generation is always distributed according to Planck's law Eq. (2.6) regardless of the energy of the exciting photons. Consequently, in that case a linear superposition is not possible, the energy integration of the internal generation rate has to be carried out before inverting the matrix equation. However, for the external generation rate, the linear superposition is still valid.

B.7 Numerical error sources

Every numerical approximation scheme has its limits. The results delivered by the numerical program are only valid as long as the assumptions underlying the numerical approximations are not violated.

B.7.1 Optical limitations - absorption length

Optically, i.e., with respect to the absorptance of the solar cell, the reabsorption scheme is self-consistent. Due to the fact that I integrate the radiative interaction between two layers with finite thickness, no photons are lost in the computation, which makes the

Tab. B.2: Average absorption coefficients according to Eq. (B.74) and maximum thickness according to Eq. (B.73) for a numerical computation scheme with discretization $N = 1000$ and $E_g = 1$ eV.

$\alpha(E)$	$\bar{\alpha}(\Phi_{\text{sun}})$	$\bar{\alpha}(\Phi_{\text{bb}})$	$\alpha_0 d_{\text{max}}(\Phi_{\text{sun}})$	$\alpha_0 d_{\text{max}}(\Phi_{\text{bb}})$
α_0	α_0	α_0	2000	2000
$\alpha_0 \sqrt{\frac{E-E_g}{k_B T}}$	$5 \alpha_0$	α_0	400	2000
$\alpha_0 \left(\frac{E-E_g}{k_B T}\right)^2$	$1.4 \times 10^3 \alpha_0$	$2.4 \alpha_0$	1.4	840

computation almost insensitive to the resolution of the discretization. This means that the absorptance of the solar cell

$$a(E) = \int_0^d g(x) dx = \sum_{i=1}^N \bar{g}(E, x_{\text{mi}}) \Delta x \quad (\text{B.72})$$

as given by the integration over the generation profile is always exact.

However, if the generation profile is too steep, i.e. if the variation of $g(x)$ within one interval Δx is too large, then the average generation rate $\bar{g}(x_{\text{mi}})$ is not an accurate approximation of the real generation rate $g(x = x_i)$ anymore.

As a crude condition I postulate that the first interval length $d/(2N)$ should not exceed the average absorption length $1/\bar{\alpha}$, which leads to the condition for the maximum thickness of the solar cell

$$d \leq \frac{2N}{\bar{\alpha}}. \quad (\text{B.73})$$

Table B.2 lists the average absorption coefficients

$$\bar{\alpha} := \int_0^\infty \alpha(E) \phi(E) dE / \int_0^\infty \phi(E) dE, \quad (\text{B.74})$$

where $\phi(E)$ is either the solar spectrum $\phi_{\text{sun}}(E)$ or the black body spectrum $\phi_{\text{bb}}(E)$. The maximum thickness listed in the last column of Tab. B.2 shows the numerical restrictions for a discretization scheme with $N = 1000$ intervals for a band gap $E_g = 1$ eV.

B.7.2 Electrical limitations - diffusion length

The electrical current is calculated according to Eq. (3.10) which in the case of the normalized saturation current and with the discretization scheme of Fig. B.4 becomes

$$\frac{J_0}{\Phi_{\text{bb}}^{\text{Eg}}} = -\mu_{\text{norm}} \frac{d\nu}{d\xi} = -\mu_{\text{norm}} \frac{\nu(\xi = \Delta\xi/2) - \nu(\xi = 0)}{\Delta\xi/2}, \quad (\text{B.75})$$

where the normalized electron concentration at the junction $\nu(\xi = 0) = 2$ is determined by the boundary condition Eq. (B.71).

This approximation holds only if the carrier distribution $\nu(\xi)$ is not too steep. Let us assume an exponential decay $\nu(\xi) \approx 2\exp(-\xi/L_{\text{norm}})$, where $L_{\text{norm}} = \sqrt{\mu_{\text{norm}}\tau_{\text{norm}}}$ is the normalized diffusion length. Then reducing L_{norm} below $L_{\text{norm}} \approx \Delta\xi/2$ results in $\nu(\Delta\xi/2)$ approaching $\nu(\Delta\xi/2) = 1$. Consequently, the numerical approximation will be flawed and with $\Delta\xi = \alpha_0 d/N$ the erroneous saturation current approaches the low-mobility limit

$$\lim_{\mu_{\text{norm}} \rightarrow 0} \frac{J_0}{\Phi_{\text{bb}}^{\text{Eg}}} = -\mu_{\text{norm}} \frac{\nu(\xi = \Delta\xi/2) - \nu(\xi = 0)}{\Delta\xi/2} = \frac{2N}{\alpha_0 d} \mu_{\text{norm}} \quad (\text{B.76})$$

although in reality, the current follows the square root dependence $J_{\text{el}} \propto \sqrt{\mu_{\text{norm}}\tau_{\text{norm}}}$.

Thus, the numerical discretization scheme is only valid for $L_{\text{norm}} > \Delta\xi/2$, i.e.

$$\mu_{\text{norm}} > \frac{(\Delta\xi)^2}{4\tau_{\text{norm}}} = \frac{(\alpha_0 d)^2}{4N^2\tau_{\text{norm}}}. \quad (\text{B.77})$$

Summing up, the numerical computations are only valid below a maximum thickness defined by the average absorption length and above a minimum diffusion length.

Appendix C

Derivation of the two-layer model

This appendix performs the derivation of the two-layer model presented in section 3.7.2.

Region 1: $0 \leq \xi \leq \xi_{\text{pr}}$ In analogy to Eq. (3.3) without the PR term $\gamma_{\text{int}}(\xi)$ we obtain the following diffusion equation

$$\mu_{\text{norm}} \frac{d^2 \nu}{d\xi^2} - \frac{\nu(\xi)(1 + \vartheta_r)}{\tau_{\text{norm}}^r} = -\gamma_{\text{sun}}(\xi) - \gamma_{\text{bb}}(\xi) - \frac{\vartheta_r}{\tau_{\text{norm}}^r}. \quad (\text{C.1})$$

For both, plane and textured front surface, I approximate the non-equilibrium generation profile by the exponential profile

$$\gamma_{\text{sun}}(\xi) = \frac{k_\alpha F_0}{\Phi_{\text{bb}}^{\text{Eg}}} \exp(-k_\alpha \xi) + \frac{k_\alpha F_r}{\Phi_{\text{bb}}^{\text{Eg}}} \exp(-k_\alpha(2\alpha_0 d - \xi)) \quad (\text{C.2})$$

in order to guarantee an analytical solution. For the sake of simplicity, I assume that $\alpha(E) = \alpha_0$ for $E \geq E_g$. For a plane front surface, the profile is exact. The amplitudes F_0 and F_r and the path length enhancement factor k_α are determined by comparison with Eq. (B.39). For a textured surface, it holds $F_0 = J_{\text{sc}}^{\text{SQ}} / (1 - t_{\text{cell}}(1 - t_{\text{amb}}))$. I extract F_r and k_α from fitting γ_{sun} to the exact generation profile Eq. (B.43). For the case of a textured front surface and $\varrho_f = 0$ and $\varrho_b = 1$ we obtain for the thicknesses $\alpha_0 d = 0.1$ the coefficients $F_r = 1.02 F_0$ and $k_\alpha = 3.24$, and for the thickness $\alpha_0 d = 10$ $F_r = 0$ and $k_\alpha = 2$. The parameters are chosen in such a way that the integrated generation profile, i.e. the absorptance of the solar cell does not exceed the actual absorptance.

Since I assume that all emitted photons leave the cell, i.e. a constant emission probability of unity, I also assume a constant black body generation rate $\gamma_{\text{bb}}(\xi) = \text{const} = 1/\tau_{\text{norm}}^{\text{r}}$. Therewith, we obtain for the excess carriers $\delta\nu = \nu - 1$

$$\mu_{\text{norm}} \frac{d^2 \delta\nu}{d\xi^2} - \frac{\delta\nu(\xi)}{\tau_{\text{norm}}} = -\frac{k_{\alpha} F_0}{\Phi_{\text{bb}}^{\text{Eg}}} \exp(-k_{\alpha} \xi) - \frac{k_{\alpha} F_{\text{r}}}{\Phi_{\text{bb}}^{\text{Eg}}} \exp(-k_{\alpha}(2\alpha_0 d - \xi)) \quad (\text{C.3})$$

with the lifetime $\tau_{\text{norm}} = \tau_{\text{norm}}^{\text{r}}/(\vartheta_{\text{r}}+1)$. The general solution of this differential equation reads as

$$\delta\nu_1(\xi) = A \sinh\left(\frac{\xi}{L_{\text{norm}}}\right) + B \cosh\left(\frac{\xi}{L_{\text{norm}}}\right) + C \exp(-k_{\alpha} \xi) + D \exp(k_{\alpha} \xi), \quad (\text{C.4})$$

where $L_{\text{norm}} = \sqrt{\mu_{\text{norm}} \tau_{\text{norm}}}$ is the normalized diffusion length and the coefficients

$$C = \frac{k_{\alpha} F_0 \tau_{\text{norm}}}{\Phi_{\text{bb}}^{\text{Eg}} (1 - k_{\alpha}^2 L_{\text{norm}}^2)} \quad (\text{C.5})$$

and

$$D = \frac{k_{\alpha} F_{\text{r}} \exp(-2k_{\alpha} \alpha_0 d) \tau_{\text{norm}}}{\Phi_{\text{bb}}^{\text{Eg}} (1 - k_{\alpha}^2 L_{\text{norm}}^2)} \quad (\text{C.6})$$

are obtained from the particular solutions. The coefficients A and B will follow from the boundary conditions given below.

Region 2: $\xi_{\text{pr}} \leq \xi \leq \alpha_0 d$ Deep in the bulk the radiative lifetime is infinity due to the assumed complete reabsorption of all emitted photons. Along with radiative recombination the black body generation vanishes as well thereby guaranteeing the compliance of the internal detailed balance (zero emission is balanced by zero absorption). Therewith we arrive at the following differential equation for the excess carriers:

$$\mu_{\text{norm}} \frac{d^2 \delta\nu}{d\xi^2} - \frac{\delta\nu(\xi)}{\tau_{\text{norm}}^{\text{nr}}} = -\frac{k_{\alpha} F_0}{\Phi_{\text{bb}}^{\text{Eg}}} \exp(-k_{\alpha} \xi) \frac{k_{\alpha} F_{\text{r}}}{\Phi_{\text{bb}}^{\text{Eg}}} \exp(-k_{\alpha}(2\alpha_0 d - \xi)), \quad (\text{C.7})$$

which is identical to Eq. (C.3) in region 1, only that the lifetime is exclusively determined by the non-radiative lifetime $\tau_{\text{norm}}^{\text{nr}}$.

With the ansatz

$$\delta\nu_2(\xi) = E \sinh\left(\frac{\xi}{L_{\text{norm}}^{\text{nr}}}\right) + F \cosh\left(\frac{\xi - \alpha_0 d}{L_{\text{norm}}^{\text{nr}}}\right) + G \exp(-k_{\alpha} \xi) + H \exp(k_{\alpha} \xi), \quad (\text{C.8})$$

where $L_{\text{norm}}^{\text{nr}} = \sqrt{\mu_{\text{norm}} \tau_{\text{norm}}^{\text{nr}}}$ is the normalized non-radiative diffusion length, the coefficients G and H read as

$$G = \frac{k_{\alpha} F_0 \tau_{\text{norm}}^{\text{nr}}}{\Phi_{\text{bb}}^{\text{Eg}} (1 - (k_{\alpha} L_{\text{norm}}^{\text{nr}})^2)} \quad (\text{C.9})$$

and

$$H = \frac{k_{\alpha} F_{\text{r}} \exp(-2k_{\alpha} \alpha_0 d) \tau_{\text{norm}}^{\text{nr}}}{\Phi_{\text{bb}}^{\text{Eg}} (1 - (k_{\alpha} L_{\text{norm}}^{\text{nr}})^2)}. \quad (\text{C.10})$$

Boundary conditions As boundary conditions we obtain the well-known conditions $\delta\nu_1(\xi = 0) = \exp(qV/(k_{\text{B}}T)) - 1$ at $\xi = 0$ and $d\delta\nu_2/d\xi|_{\xi=\alpha_0 d} = 0$ at $\xi = \alpha_0 d$. At the Interface between the two regions the continuity of the electron concentration $\delta\nu(\xi)$ and the continuity of the diffusion current result in the conditions $\delta\nu_1(\xi = \xi_{\text{pr}}) = \delta\nu_2(\xi = \xi_{\text{pr}})$ and $\mu_{\text{norm}} d\delta\nu_1/d\xi|_{\xi=\xi_{\text{pr}}} = \mu_{\text{norm}} d\delta\nu_2/d\xi|_{\xi=\xi_{\text{pr}}}$.

Coefficients From these boundary conditions we obtain the coefficients

$$B = \exp\left(\frac{qV}{k_{\text{B}}T}\right) - 1 - C - D, \quad (\text{C.11})$$

$$E = \frac{k_{\alpha} G \exp(-k_{\alpha} \alpha_0 d) - H \exp(k_{\alpha} \alpha_0 d)}{\frac{1}{L_{\text{norm}}^{\text{nr}}} \cosh\left(\frac{\alpha_0 d}{L_{\text{norm}}^{\text{nr}}}\right)}, \quad (\text{C.12})$$

$$F = \frac{EK_3 - K_2 \sinh\left(\frac{\xi_{\text{pr}}}{L_{\text{norm}}}\right) + \frac{K_1}{L_{\text{norm}}} \cosh\left(\frac{\xi_{\text{pr}}}{L_{\text{norm}}}\right)}{K_4}, \quad (\text{C.13})$$

and

$$A = \frac{E \sinh\left(\frac{\xi_{\text{pr}}}{L_{\text{norm}}}\right) + F \cosh\left(\frac{\xi_{\text{pr}} - \alpha_0 d}{L_{\text{norm}}^{\text{nr}}}\right) + K_1}{\sinh\left(\frac{\xi_{\text{pr}}}{L_{\text{norm}}}\right)}, \quad (\text{C.14})$$

where the abbreviations K_1 , K_2 , K_3 , and K_4 are given by

$$K_1 = (G - C) \exp(-k_{\alpha} \xi_{\text{pr}}) + (H - D) \exp(k_{\alpha} \xi_{\text{pr}}) - B \cosh\left(\frac{\xi_{\text{pr}}}{L_{\text{norm}}}\right), \quad (\text{C.15})$$

$$K_2 = k_{\alpha} (C - G) \exp(-k_{\alpha} \xi_{\text{pr}}) + k_{\alpha} (H - D) \exp(k_{\alpha} \xi_{\text{pr}}) - \frac{B}{L_{\text{norm}}} \sinh\left(\frac{\xi_{\text{pr}}}{L_{\text{norm}}}\right), \quad (\text{C.16})$$

$$K_3 = \frac{1}{L_{\text{norm}}} \cosh\left(\frac{\xi_{\text{pr}}}{L_{\text{norm}}}\right) \sinh\left(\frac{\xi_{\text{pr}}}{L_{\text{norm}}^{\text{nr}}}\right) - \frac{1}{L_{\text{norm}}^{\text{nr}}} \sinh\left(\frac{\xi_{\text{pr}}}{L_{\text{norm}}}\right) \cosh\left(\frac{\xi_{\text{pr}}}{L_{\text{norm}}^{\text{nr}}}\right),$$

$$(C.17)$$

and

$$K_4 = \frac{1}{L_{\text{norm}}^{\text{nr}}} \sinh\left(\frac{\xi_{\text{pr}}}{L_{\text{norm}}}\right) \sinh\left(\frac{\xi_{\text{pr}} - \alpha_0 d}{L_{\text{norm}}^{\text{nr}}}\right) - \frac{1}{L_{\text{norm}}} \cosh\left(\frac{\xi_{\text{pr}}}{L_{\text{norm}}}\right) \cosh\left(\frac{\xi_{\text{pr}} - \alpha_0 d}{L_{\text{norm}}^{\text{nr}}}\right). \quad (C.18)$$

Layer thickness In order to comply the external detailed balance principle, we have to guarantee that the radiative recombination current does not exceed the absorptance a of the solar cell. Therefore, I choose the thickness ξ_{pr} of layer 1 in such a way, that the maximum radiative recombination current $J_0^{\text{rad}}(\mu_{\text{norm}} \rightarrow \infty)/\Phi_{\text{bb}}^{\text{Eg}}$ equals the absorptance and therewith the numerical result in section 3.4.1.

Radiative recombination only takes place in region 1. Therefore, and with keeping in mind that all photons emitted by radiative recombination are also emitted from the front surface by definition (no PR), we obtain the radiative saturation current

$$\frac{J_0^{\text{rad}}}{\Phi_{\text{bb}}^{\text{Eg}}} = \int_0^{\xi_{\text{pr}}} \frac{\delta\nu_1}{\tau_{\text{norm}}^{\text{r}}} d\xi \Big|_{V=k_{\text{B}}T/q\ln(2)}. \quad (C.19)$$

For $\mu_{\text{norm}} \rightarrow \infty$ and with $\delta\nu_1(\xi = 0) = 1$ for $V = (k_{\text{B}}T/q)\ln(2)$ it holds $\delta\nu_1(\xi) = \delta\nu_1(\xi = 0) = 1$. Therewith, we arrive at the condition

$$\lim_{\mu_{\text{norm}} \rightarrow \infty} \frac{J_0^{\text{rad}}}{\Phi_{\text{bb}}^{\text{Eg}}} = \frac{\xi_{\text{pr}}}{\tau_{\text{norm}}^{\text{r}}} \stackrel{!}{=} a \quad (C.20)$$

which with $\tau_{\text{norm}}^{\text{r}} = 1/(4\bar{n}^2)$ gives

$$\xi_{\text{pr}} = \frac{a}{4\bar{n}^2}. \quad (C.21)$$

The absorptance a is either given by Eq. (3.37) for a textured or Eq. (3.40) for a plane front surface.

With the above choice of the layer thickness ξ_{pr} , the model inherently predicts the correct high mobility limit for the saturation current in the radiative recombination limit. When non-radiative recombination is dominant, the model simply turns into the classical approach.

With respect to the low mobility limit the model also renders the correct result, namely the limit $\sqrt{\mu_{\text{norm}}/\tau_{\text{norm}}^{\text{r}}}$. But this limit is not the crucial point since it is

also correctly reproduced by the standard classical model. The high mobility limit makes up the much more critical issue, since the change from the limit $\alpha_0 d / \tau_{\text{norm}}^{\text{nr}}$ to the absorptance a with increasing non-radiative lifetime can not be captured with the classical approach.

The final step in the model is the calculation of the electrical current which is conducted in the usual manner according to

$$\frac{J_{\text{el}}(V)}{\Phi_{\text{bb}}^{\text{Eg}}} = \mu_{\text{norm}} \left. \frac{d\delta\nu_1}{d\xi} \right|_{\xi=0} = \mu_{\text{norm}} \left(\frac{A}{L_{\text{norm}}} - k_{\alpha} C + k_{\alpha} D \right). \quad (\text{C.22})$$

C.0.2.1 Radiative recombination limit

In the limit of radiative recombination, the two-layer model allows some simplifications. Without non-radiative recombination, i.e. with an infinite non-radiative lifetime, the lifetime in region 1 is simply given by the radiative lifetime and the diffusion length turns into $L_{\text{norm}} = \sqrt{\mu_{\text{norm}} \tau_{\text{norm}}^{\text{r}}}$. In region 2, recombination vanishes altogether. Without the recombination term $\delta\nu_2 / \tau_{\text{norm}}^{\text{nr}}$ in Eq. (C.7), the electron profile in region 2 is given by

$$\delta\nu_2(\xi) = E\xi + F + G \exp(-k_{\alpha}\xi) + H \exp(k_{\alpha}\xi) \quad (\text{C.23})$$

with the coefficients

$$G = \frac{-F_0}{\Phi_{\text{bb}}^{\text{Eg}} k_{\alpha}^2 \mu_{\text{norm}}}, \quad (\text{C.24})$$

$$H = \frac{F_{\text{r}} \exp(-2k_{\alpha}\alpha_0 d)}{\Phi_{\text{bb}}^{\text{Eg}} k_{\alpha}^2 \mu_{\text{norm}}}, \quad (\text{C.25})$$

and

$$E = k_{\alpha} G \exp(-k_{\alpha}\alpha_0 d) - k_{\alpha} H \exp(k_{\alpha}\alpha_0 d). \quad (\text{C.26})$$

From the boundary conditions at $\xi = \xi_{\text{pr}}$ we obtain

$$A = \frac{(E + K_2) L_{\text{norm}}}{\cosh\left(\frac{\xi_{\text{pr}}}{L_{\text{norm}}}\right)} \quad (\text{C.27})$$

and

$$F = A \sinh\left(\frac{\xi_{\text{pr}}}{L_{\text{norm}}}\right) - E \xi_{\text{pr}} - K_1. \quad (\text{C.28})$$

The coefficients B , C , D , and K_1 and K_2 remain unchanged.

Nomenclature

Physical constants

c	Speed of light	$3 \times 10^{10} \text{ cm s}^{-1}$
h	Planck's constant	$4.14 \times 10^{-15} \text{ eV s}$
k_B	Boltzmann's constant	$8.62 \times 10^{-5} \text{ eV K}^{-1}$
q	Elementary charge	$1.602 \times 10^{-19} \text{ As}$

Symbols

a^{loc}	Local absorptance	
α^{loc}	Local absorption coefficient	cm^{-1}
α_{sun}	Average absorption coefficient of the solar spectrum	cm^{-1}
a_{sun}	Average absorptance of the solar spectrum	
a_{bb}	Average absorptance of the terrestrial black body spectrum	
B_{even}	Reflected path coming from the back side with even # of reflections	
B_{odd}	Reflected path coming from the back side with odd # of reflections	
c_{μ}	Proportionality constant between the normalized short circuit current in the low mobility limit and the normalized mobility	
c_r	Radiative lifetime multiplication factor	
d_{crit}	Critical thickness for light absorption	cm
dim	Dimension of band gap fluctuations	

d_{\max}	Maximum thickness for numerical accuracy	cm
D_n	Electron diffusion constant	$\text{cm}^2 \text{s}^{-1}$
E_C	Conduction band	eV
E_C^{loc}	Local conduction band	eV
E_F	Fermi level	eV
E_{F_n}	Electron Fermi level	eV
$E_{F_n}^{\text{loc}}$	Local electron Fermi level	eV
E_{F_p}	Hole Fermi level	eV
$E_{F_p}^{\text{loc}}$	Local hole Fermi level	eV
E_g	Band gap	eV
E_g^{loc}	Local band gap	eV
E_V	Valence band	eV
E_V^{loc}	Local valence band	eV
\bar{E}_g	Mean band gap	eV
EQE	External quantum efficiency (spectral)	
EQE _{LED}	External LED quantum efficiency (integrated)	
η	Solar cell power conversion efficiency	
η_{SQ}	Shockley Queisser efficiency	
f_C	Collection efficiency	
FF	Fill factor	
F_0	Initial photon flux at the solar cell surface	$\text{cm}^{-2} \text{s}^{-1}$
F_r	Reflected photon flux	$\text{cm}^{-2} \text{s}^{-1}$
F_{even}	Reflected path coming from the front side with an even # of reflections	
F_{odd}	Reflected path coming from the front side with an odd # of reflections	
f_r	Radiative interaction function	
$\phi_{\text{bb}, \bar{n}}^{\text{d}\Omega}$	Spectral black body photon flux per solid angle in a material with refractive index \bar{n}	$\text{cm}^{-2} \text{s}^{-1} \text{eV}^{-1}$
ϕ_{bb}	Spectral black body photon flux projected on the cell surface	$\text{cm}^{-2} \text{s}^{-1} \text{eV}^{-1}$
Φ_{bb}	Integrated black body photon flux projected on the cell surface	$\text{cm}^{-2} \text{s}^{-1}$

$\Phi_{\text{bb}}^{\text{Eg}}$	Black body photon flux integrated from the band gap and projected on the cell surface	$\text{cm}^{-2} \text{s}^{-1}$
$\Phi_{\text{bb}}^{\text{abs}}$	Integrated black body photon flux absorbed by the cell	$\text{cm}^{-2} \text{s}^{-1}$
ϕ_{sun}	Spectral solar photon flux projected on the cell surface	$\text{cm}^{-2} \text{s}^{-1} \text{eV}^{-1}$
Φ_{sun}	Solar photon flux integrated over all energies and projected on the cell surface	$\text{cm}^{-2} \text{s}^{-1}$
$\Phi_{\text{sun}}^{\text{Eg}}$	Solar photon flux integrated over all energies larger than the band gap and projected on the cell surface	$\text{cm}^{-2} \text{s}^{-1}$
$\Phi_{\text{sun}}^{\text{abs}}$	Integrated solar photon flux absorbed by the cell per unit surface area	$\text{cm}^{-2} \text{s}^{-1}$
$\Phi_{\text{r}}^{\text{loc}}$	Local radiative recombination current	$\text{cm}^{-2} \text{s}^{-1}$
Φ_{em}	Integrated emitted photon flux per unit surface area	$\text{cm}^{-2} \text{s}^{-1}$
g_{bb}	Spectral black body generation rate	$\text{cm}^{-3} \text{s}^{-1} \text{eV}^{-1}$
G_{bb}	Black body generation rate	$\text{cm}^{-3} \text{s}^{-1}$
γ_{bb}	Normalized black body generation rate	
g_{int}	Spectral internal generation rate	$\text{cm}^{-3} \text{s}^{-1} \text{eV}^{-1}$
G_{int}	Internal generation rate	$\text{cm}^{-3} \text{s}^{-1}$
γ_{int}	Normalized internal generation rate	
g_{sun}	Spectral solar generation rate	$\text{cm}^{-3} \text{s}^{-1} \text{eV}^{-1}$
G_{sun}	Solar generation rate	$\text{cm}^{-3} \text{s}^{-1}$
γ_{sun}	Normalized solar generation rate	
J_{el}	Electrical current drawn from the solar cell	$\text{cm}^{-2} \text{s}^{-1}$
J_0	Reverse saturation current	$\text{cm}^{-2} \text{s}^{-1}$
J_0^{SQ}	Saturation current in the SQ limit	$\text{cm}^{-2} \text{s}^{-1}$
J_0^{rad}	Radiative saturation current	$\text{cm}^{-2} \text{s}^{-1}$
J_0^{nr}	Non-radiative saturation current	$\text{cm}^{-2} \text{s}^{-1}$
$J_{\text{nr}}^{\text{loc}}$	Local non-radiative recombination current	$\text{cm}^{-2} \text{s}^{-1}$
$J_{\text{rec}}^{\text{loc}}$	Local recombination current	$\text{cm}^{-2} \text{s}^{-1}$
$J_{\text{rec}}^{\text{nr}}$	Non-radiative recombination current	$\text{cm}^{-2} \text{s}^{-1}$
$J_{\text{rec}}^{\text{rad}}$	Radiative recombination current	$\text{cm}^{-2} \text{s}^{-1}$
J_{sc}	Short circuit current	$\text{cm}^{-2} \text{s}^{-1}$
$J_{\text{sc}}^{\text{SQ}}$	Short circuit current in the SQ limit	$\text{cm}^{-2} \text{s}^{-1}$

k_α	Absorption multiplication factor that contains the absorption spectrum and the nature of the cell surface	
k_{lam}	Absorption multiplication factor that contains the nature of the cell surface	
L_α	Absorption length	cm
$L_{\alpha,\text{norm}}$	Normalized absorption length	
L_n	Electron diffusion length	cm
L_{norm}	Normalized diffusion length	
L_{crit}	Critical diffusion length	cm
$L_{\text{crit}}^{\text{rad}}$	Critical diffusion length in the radiative limit	cm
$L_{\text{em,norm}}$	Normalized emission length	
L_g	Fluctuation length of band gap fluctuations	cm
L_g	Fluctuation length of the chemical potential	cm
μ	Chemical potential of photons	eV
μ^{loc}	Local chemical potential	eV
μ_{ss}	Steady state chemical potential	eV
$\mu_{\text{ss}}^{\text{loc}}$	Local steady state chemical potential	eV
$\bar{\mu}$	Mean chemical potential	eV
μ_n	Electron mobility	$\text{cm}^2(\text{Vs})^{-1}$
μ_{ref}	Reference mobility for normalization	$\text{cm}^2(\text{Vs})^{-1}$
μ_{norm}	Normalized mobility	
μ_{crit}	Critical mobility	$\text{cm}^2(\text{Vs})^{-1}$
$\mu_{\text{crit}}^{\text{norm}}$	Normalized critical mobility	
$\mu_{\text{crit}}^{\text{rad}}$	Critical mobility in the radiative recombination limit	$\text{cm}^2(\text{Vs})^{-1}$
$\mu_{\text{p}}^{\text{band}}$	Hole mobility in valence band	$\text{cm}^2(\text{Vs})^{-1}$
$\mu_{\text{p}}^{\text{eff}}$	Effective hole mobility	$\text{cm}^2(\text{Vs})^{-1}$
N_A	Acceptor concentration	cm^{-3}
n_i	Intrinsic carrier concentration	cm^{-3}
n	Electron concentration	cm^{-3}
ν	Normalized electron concentration	
\bar{n}	Real part of the refractive index	
p	Hole concentration	cm^{-3}
P_G	Gaussian probability	

ϱ_b	Reflection coefficient at the back contact	
ϱ_f	Reflection coefficient at the front surface	
r_r	Spectral radiative recombination rate	$\text{cm}^{-3} \text{s}^{-1} \text{eV}^{-1}$
R_r	Radiative recombination rate	$\text{cm}^{-3} \text{s}^{-1}$
R_{nr}	Non-radiative recombination rate	$\text{cm}^{-3} \text{s}^{-1}$
R_g	Autocorrelation function of the band gap fluctuations	
S_g	Power spectrum of the band gap fluctuations	cm^{dim}
σ_g	Standard deviation of the band gap fluctuations	eV^{-1}
σ_μ	Standard deviation of the chemical potential	eV^{-1}
S_n	Electron surface recombination velocity at the back contact	cm s^{-1}
τ	Minority carrier lifetime	s^{-1}
τ_{norm}	Normalized lifetime	
τ_r	Radiative minority carrier lifetime	s^{-1}
τ_{norm}^r	Normalized radiative minority carrier lifetime	
τ_{nr}	Non-radiative minority carrier lifetime	s^{-1}
τ_{norm}^{nr}	Normalized non-radiative minority carrier lifetime	
$\tau_{\text{norm}}^{\text{mod}}$	Normalized modified minority carrier lifetime	
$\tau_{\text{norm}}^{r,\text{mod}}$	Normalized modified radiative minority carrier lifetime	
θ_c	Critical angle of total internal reflection	
ϑ_r	Ratio of radiative and non-radiative lifetime	
V_{oc}	Open circuit voltage	V
$V_{\text{oc}}^{\text{inhom}}$	Open circuit voltage with inhomogeneous band gap	V
$V_{\text{oc}}^{\text{rad}}$	Open circuit voltage in the Shockley Queisser limit	V
w_{scr}	Width of the space charge region	cm
x	Spatial coordinate	cm
ξ	Normalized spatial coordinate	
x_g	Position of carrier generation	cm
x_i	Discrete position (interval) of carrier generation	cm
x_r	Position of carrier recombination	cm
x_j	Discrete position (interval) of carrier recombination	cm
ξ_{pr}	Normalized depth of the layer from where all emitted photons exit the cell	

Bibliography

- [1] H. QUEISSER, *Kristalline Krisen* (Piper, Münche, 1985).
- [2] A. SHAH, P. TORRES, R. TSCHARNER, N. WYRSCH, AND H. KEPPNER, *Science* **285**, 692 (1999).
- [3] A. GOETZBERGER, C. HEBLING, AND H.-W. SCHOCK, *Mat. Sc. Eng. R* **40**, 1 (2003).
- [4] K. L. CHOPRA, P. D. PAULSON, AND V. DUTTA, *Prog. Photovolt.* **12**, 69 (2004).
- [5] E. A. SCHIFF, *Sol. En. Mat. Sol. Cells* **78**, 567 (2003).
- [6] U. RAU AND H.-W. SCHOCK, *Appl. Phys. A* **69**, 131 (1999).
- [7] S. E. SHAHEEN, D. S. GINLEY, AND G. E. JABBOUR, *MRS Bulletin* **30**, 10 (2005).
- [8] M. GRAETZEL, *MRS Bulletin* **30**, 23 (2005).
- [9] M. A. GREEN, *Physica E* **14**, 65 (2002).
- [10] W. SHOCKLEY AND H. J. QUEISSER, *J. Appl. Phys.* **32**, 510 (1961).
- [11] W. SHOCKLEY, *Bell Syst. Tech. J.* **28**, 435 (1949).
- [12] M. A. GREEN, *Solar cells: operating principles, technology, and system applications* (Englewood Cliffs : Prentice-Hall, 1982).
- [13] R. HULSTROM, R. BIRD, AND C. RIORDAN, *Sol. Cells* **15**, 365 (1985).

-
- [14] T. TIEDJE, E. YABLONOVITCH, G. CODY, AND B. BROOKS, IEEE Trans. on Electr. Devices **ED-31**, 711 (1984).
 - [15] P. WÜRFEL, J. Phys. C **15**, 3967 (1982).
 - [16] U. RAU, Phys. Rev. B **76**, 085303 (2007).
 - [17] S. SZE, *Semiconductor devices: physics and technology* (Wiley, 2002).
 - [18] N. ARORA, S. G. CHAMBERLAIN, AND D. J. ROULSTON, Appl. Phys. Lett. **37**, 325 (1980).
 - [19] W. P. DUMKE, Phys. Rev. **105**, 139 (1957).
 - [20] T. S. MOSS, Proc. Phys. Soc. B **70**, 247 (1957).
 - [21] P. T. LANDSBERG, Proc. Phys. Soc. B **70**, 1175 (1957).
 - [22] W. N. CARR, Infrared Phys. **6**, 1 (1966).
 - [23] S. KAMEDA AND W. N. CARR, J. Appl. Phys. **44**, 2910 (1973).
 - [24] C. J. HWANG, Phys. Rev. B. **6**, 1355 (1972).
 - [25] F. STERN AND J. M. WOODALL, J. Appl. Phys. **45**, 3904 (1974).
 - [26] T. KURIYAMA, T. KAMIYA, AND H. YANAI, Jpn. J. Appl Phys. **16**, 465 (1977).
 - [27] H. C. CASEY JR., B. I. MILLER, AND E. PINKAS, J. Appl. Phys. **44**, 1281 (1973).
 - [28] P. ASBECK, J. Appl. Phys. **48**, 820 (1977).
 - [29] K. METTLER, Phys. Stat. Sol. (a) **49**, 163 (1978).
 - [30] R. J. ROEDEL AND V. G. KERAMIDAS, J. Appl. Phys. **50**, 6353 (1979).
 - [31] W. RÜHLE, L. HOFFMANN, AND S. LEIBENZEDER, J. Appl. Phys. **53**, 3765 (1982).
 - [32] V. V. ROSSIN AND V. G. SIDOROV, Sov. Phys. Semicond. **15**, 106 (1981).

- [33] V. V. ROSSIN AND V. G. SIDOROV, *Sov. Phys. Semicond.* **18**, 702 (1984).
- [34] T. KAMIYA, S. HIROSE, AND H. YANAI, *J. Luminescence* **18/19**, 910 (1979).
- [35] B. BENSÄID, F. RAYMOND, C. LEROUX, M. AND VÈRIÉ, AND B. FOFANA, *J. Appl. Phys.* **66**, 5542 (1989).
- [36] V. I. KOROL'KOV, E. P. ROMANOVA, V. S. YUFEREV, AND A. A. YAKOVENKO, *Sov. Phys. Semicond.* **14**, 1005 (1980).
- [37] E. VELMRE, B. FREIDIN, AND A. UDAL, *Physica Scripta* **24**, 468 (1981).
- [38] J. W. PARKS JR. AND K. F. BRENNAN, *J. Appl. Phys.* **82**, 3493 (1997).
- [39] P. ENDERS, *Phys. Stat. Sol. (b)* **137**, 353 (1986).
- [40] O. v. ROOS, *J. Appl. Phys.* **54**, 2495 (1983).
- [41] P. ENDERS, *Phys. Stat. Sol. (b)* **137**, 701 (1986).
- [42] P. ENDERS, *Phys. Stat. Sol. (b)* **141**, 317 (1987).
- [43] V. V. ROSSIN, A. L. VINKE, AND V. G. SIDOROV, *Sov. Phys. Semicond.* **13**, 647 (1979).
- [44] LASTRAS-MARTÍNEZ, *J. Appl. Phys.* **50**, 4156 (1979).
- [45] V. V. ROSSIN AND V. G. SIDOROV, *Sov. Phys. Semicond.* **14**, 1167 (1980).
- [46] O. v. ROOS, *J. Appl. Phys.* **54**, 1390 (1983).
- [47] O. v. ROOS, *Sol.-State El.* **27**, 913 (1984).
- [48] V. S. YUFEREV AND M. P. PROSKURA, *Sov. Phys. Semicond.* **18**, 530 (1984).
- [49] P. RENAUD, F. RAYMOND, B. BENSÄID, AND C. VERIE, *J. Appl. Phys.* **71**, 1907 (1992).
- [50] V. BADESCU AND P. LANDSBERG, *Semicond. Sci. Technol.* **8**, 1267 (1993).
- [51] J. E. PARROTT AND A. POTTS, in *Proc. 22nd IEEE Photovoltaics Specialist Conf.* (1991), p. 153.

-
- [52] S. M. DURBIN AND J. L. GRAY, in *Proc. 22nd IEEE Photovoltaics Specialist Conf.* (1991), p. 188.
- [53] S. M. DURBIN AND J. L. GRAY, *IEEE Trans. on Electr. Devices* **41**, 239 (1994).
- [54] V. BADESCU AND P. LANDSBERG, *Semicond. Sci. Technol.* **12**, 1491 (1997).
- [55] A. YAMAMOTO, M. KURIZUKA, M. M. MURSHID, M. OHKUBO, AND A. HASHIMOTO, *Sol. En. Mat. Sol. Cells* **50**, 259 (1998).
- [56] J. L. BALENZATEGUI AND A. MARTÍ, *Sol. En. Mat. Sol. Cells* **90**, 1068 (2006).
- [57] J. E. PARROTT, *Sol. En. Mat. Sol. Cells* **30**, 221 (1993).
- [58] R. J. NELSON AND R. G. SOBERS, *J. Appl. Phys.* **49**, 6103 (1978).
- [59] S. D. LESTER, T. S. KIM, AND B. G. STREETMAN, *Appl. Phys. Lett.* **52**, 476 (1988).
- [60] R. K. AHRENKIEL, D. J. DUNLAVY, AND T. HANAK, *J. Appl. Phys.* **64**, 1916 (1988).
- [61] R. K. AHRENKIEL, D. J. DUNLAVY, AND B. M. KEYES, *Appl. Phys. Lett.* **55**, 1088 (1989).
- [62] R. K. AHRENKIEL, B. M. KEYES, G. B. LUSH, M. R. MELLOCH, M. S. LUNDSTROM, AND H. F. MACMILLAN, *J. Vac. Sci. Technol. A* **10**, 990 (1992).
- [63] G. B. LUSH, H. F. MACMILLAN, B. M. KEYES, D. H. LEVI, M. R. MELLOCH, R. K. AHRENKIEL, AND M. S. LUNDSTROM, *J. Appl. Phys.* **72**, 1436 (1992).
- [64] M. J. KERR, A. CUEVAS, AND P. CAMPBELL, *Prog. Photovolt: Res. Appl.* **11**, 97 (2003).
- [65] E. P. ROMANOVA AND V. S. YUFEREV, *Sov. Phys. Semicond.* **14**, 1430 (1980).
- [66] V. V. ROSSIN AND V. G. SIDOROV, *Sov. Phys. Semicond.* **15**, 1056 (1981).
- [67] C. DONOLATO, *Appl. Phys. Lett.* **46**, 270 (1984).

-
- [68] J. I. PANKOVE, *Optical Processes in Semiconductors* (Prentice-Hall, Inc., Englewood Cliffs, N.J., 1971).
- [69] R. BRENDDEL AND H. J. QUEISSER, *Sol. Energy Mat. Sol. Cells* **29**, 397 (1993).
- [70] G. L. ARAÚJO AND A. MARTÍ, *Sol. En. Mat. Sol. Cells* **33**, 213 (1994).
- [71] L. LEY, in *The Physics of Hydrogenated Amorphous Silicon II*, edited by J. D. JOANNOPOPOULOS AND G. LUCOVSKY (Springer Verlag, Heidelberg, 1984).
- [72] K. ORGASSA, *Coherent optical analysis of the ZnO/CdS/Cu(In,Ga)Se₂ thin film solar cell*, Phd thesis, University of Stuttgart (2004).
- [73] T. TRUPKE, M. A. GREEN, P. WÜRFEL, P. ALTERMATT, A. WANG, J. ZHAO, AND R. COURKISH, *J. Appl. Phys.* **94**, 4930 (2003).
- [74] K. PUECH, S. ZOTT, K. LEO, M. RUCKH, AND H.-W. SCHOCK, *Appl. Phys. Lett.* **69**, 3375 (1996).
- [75] P. J. ROSTAN, U. RAU, V. X. NGUYEN, T. KIRCHARTZ, M. B. SCHUBERT, AND J. H. WERNER, *Sol. En. Mat. Sol. Cells* **90**, 1345 (2006).
- [76] M. J. KERR AND A. CUEVAS, *J. Appl. Phys.* **91**, 2473 (2002).
- [77] M. A. GREEN, *IEEE Trans. on Electron Devices* **ED-31**, 671 (1984).
- [78] J. ZHAO, A. WANG, M. A. GREEN, AND F. FERRAZZA, *Appl. Phys. Lett.* **73**, 1991 (1998).
- [79] M. TAGUCHI, H. SAKATA, Y. YOSHIMINE, E. MARUYAMA, A. TERAKAWA, M. TANAKA, AND S. KIYAMA, in *Proc. 31st IEEE Photovolt. Spec. Conf.* (IEEE, New York, 2005), p. 866.
- [80] J. MEIER, J. SITZNAGEL, U. KROLL, C. BUCHER, S. FAY, T. MORIARTY, AND A. SHAH, *Thin Solid Films* **451**, 518 (2004).
- [81] E. A. SCHIFF, R. I. DEVLEN, H. T. GRAHN, AND J. TAUC, *Appl. Phys. Lett.* **54**, 1911 (1989).

-
- [82] G. JUŠKA, K. ARLAUSKAS, J. KOČKA, M. HOHEISEL, AND P. CHABLOZ, Phys. Rev. Lett. **75**, 2984 (1995).
- [83] E. A. SCHIFF, J. Non-Cryst. Sol. **352**, 1087 (2006).
- [84] Q. GU, Q. WANG, E. A. SCHIFF, Y.-M. LI, AND C. T. MALONE, J. Appl. Phys. **76**, 2310 (1994).
- [85] J. LEE, J. D. COHEN, AND W. N. SHAFARMAN, Thin Solid Films **480**, 336 (2005).
- [86] J. H. WERNER, J. MATTHEIS, AND U. RAU, Thin Solid Films **480**, 399 (2005).
- [87] B. OHNESORGE, R. WEIGAND, G. BACHER, AND A. FORCHEL, Appl. Phys. Lett. **73**, 1224 (1998).
- [88] J. MATTHEIS, P. J. ROSTAN, K. ORGASSA, U. RAU, AND J. H. WERNER, Sol. En. Mat. Sol. Cells .
- [89] K. RAMANATHAN, M. A. CONTRERAS, C. L. PERKINS, S. ASHER, F. S. HASOON, J. KEANE, D. YOUNG, M. ROMERO, W. METZGER, R. NOUFI, J. WARD, AND A. DUDA, Prog. Photovolt: Res. Appl. **11**, 225 (2003).
- [90] T. KIRCHARTZ, U. RAU, J. MATTHEIS, AND J. H. WERNER, unpublished (2007).
- [91] M. TOPIČ, F. SMOLE, AND J. FURLAN, J. Appl. Phys. **79**, 8537 (1996).
- [92] B. A. GREGG, J. Phys. Chem. B **107**, 4688 (2003).
- [93] B. A. GREGG AND M. C. HANNA, J. Appl. Phys. **93**, 3605 (2003).
- [94] H. HOPPE AND N. S. SARICIFTCI, J. Mat. Res. **19**, 1924 (2004).
- [95] S. E. GLEDHILL, B. SCOTT, AND B. A. GREGG, J. Mat. Res. **20**, 3167 (2005).
- [96] N. K. PATEL, S. CINÀ, AND J. H. BURROUGHES, IEEE J. Sel. Topics Quantum El. **8**, 346 (2002).
- [97] J. H. WERNER AND H. H. GÜTTLER, J. Appl. Phys. **69**, 1522 (1991).

-
- [98] U. RAU AND J. H. WERNER, Appl. Phys. Lett. **84**, 3735 (2004).
 - [99] D. EICH, U. HERBER, U. GROH, U. STAHL, C. HESKE, M. MARSI, M. KISKINOVA, W. RIEDL, R. FINK, AND E. UMBACH, Thin Solid Films **361-362**, 258 (2000).
 - [100] Y. YAN, R. NOUFI, K. M. JONES, K. RAMANATHAN, AND M. M. AL-JASSIM, Appl. Phys. Lett. **87**, 121904 (2005).
 - [101] V. G. KARPOV, A. D. COMPAAN, AND D. SHVYDKA, Appl. Phys. Lett. **80**, 4256 (2002).
 - [102] V. G. KARPOV, A. D. COMPAAN, AND D. SHVYDKA, Phys. Rev. B **69**, 1 (2004).
 - [103] P. O. GRABITZ, U. RAU, AND J. H. WERNER, Phys. Stat. Sol. (a) **202**, 2920 (2005).
 - [104] P. A. FEDDERS, D. A. DRABOLD, AND S. NAKHMANSON, Phys. Rev. B **58**, 15624 (1998).
 - [105] F. URBACH, Phys. Rev. **92**, 1324 (1953).
 - [106] T. SKETTRUP, Phys. Rev. B **18**, 2622 (1978).
 - [107] D. J. DUNSTAN, J. Phys. C **30**, L419 (1982).
 - [108] M. ROBERTS AND D. J. DUNSTAN, J. Phys. C **18**, 5429 (1985).
 - [109] J. OSVALD, J. Appl. Phys. **85**, 1935 (1999).
 - [110] M. SCHÖFTHALER, U. RAU, AND J. H. WERNER, J. Appl. Phys. **76**, 4168 (1994).
 - [111] A. PAPOULIS, *Probability, Random Variables, and Stochastic Processes* (McGraw-Hill, Inc, 1991).
 - [112] M. A. GREEN, J. Appl. Phys. **81**, 268 (1997).
 - [113] S. DAUWE, *Low-Temperature Surface Passivation of crystalline Silicon*, Phd thesis, Universität Hannover (2004).

-
- [114] S. J. ORFANIDIS, *Optimum signal processing: An introduction* (MacMillan Publishing Company, New York, 1985).
- [115] A. GABOR, J. TUTTLE, D. S. ALBIN, M. CONTRERAS, R. NOUFI, AND A. HERMANN, *Appl. Phys. Lett.* **65**, 198 (1994).
- [116] K. BOTHE, G. H. BAUER, AND T. UNOLD, *Thin Solid Films* **403**, 453 (2002).
- [117] B. DIMMLER, H. DITTRICH, AND H.-W. SCHOCK, in *Conf. Rec. 19th IEEE Photov. Spec. Conf.* (IEEE, New York, 1987), p. 1454.
- [118] I. DIRNSTORFER, M. T. WAGNER, D. M. HOFMANN, M. D. LAMPERT, F. KARG, AND B. K. MEYER, *Phys. Stat. Sol. (a)* **168**, 163 (1998).
- [119] A. BAUKNECHT, S. SIEBENTRITT, J. ALBERT, AND M. C. LUX-STEINER, *J. Appl. Phys.* **89**, 4391 (2001).
- [120] N. REGA, S. SIEBENTRITT, I. E. BECKERS, J. BECKMANN, J. ALBERT, AND M. C. LUX-STEINER, *Thin Solid Films* **431**, 186 (2003).
- [121] N. REGA, S. SIEBENTRITT, J. ALBERT, S. NISHIWAKI, A. ZAJOQIN, M. C. LUX-STEINER, R. KNIESE, AND M. J. ROMERO, *Thin Solid Films* **480**, 286 (2005).
- [122] T. KIRCHARTZ, U. RAU, M. KURTH, J. MATTHEIS, AND J. H. WERNER, *Thin Solid Films* **515**, 6238 (2007).
- [123] T. KIRCHARTZ AND RAU, *J. Appl. Phys.* **102**, 104510 (2007).
- [124] E. DAUB AND P. WÜRFEL, *Phys. Rev. Lett.* **74**, 1020 (1995).
- [125] T. TRUPKE, E. DAUB, AND P. WÜRFEL, *Sol. En. Mat. Sol. Cells* **53**, 103 (1998).
- [126] T. UNOLD, D. BERKHAHN, B. DIMMLER, AND G. H. BAUER, in *Proc. 16th Europ. Photovolt. Sol. Energy Conf., Glasgow*, edited by H. SCHEER, B. MCNELLIS, W. PALZ, H. A. OSSENBRINK, AND P. HELM (James & James Ltd, London, 2000), p. 736.
- [127] M. TURCU, I. M. KÖTSCHAU, AND U. RAU, *J. Appl. Phys.* **91**, 1391 (2002).

- [128] W. N. SHAFARMAN, R. KLENK, AND B. E. MCCANDLESS, *J. Appl. Phys.* **79**, 7327 (1996).
- [129] J. T. HEATH, J. D. COHEN, W. N. SHAFARMAN, D. X. LIAO, AND A. A. ROCKETT, *Appl. Phys. Lett.* **80**, 4540 (2002).
- [130] T. SCHLENKER, J. MATTHEIS, M. BOGICEVIC, U. RAU, AND J. H. WERNER, in *Proc. 20th Eur. Photovolt. Solar Energy Conf.*, edited by W. PALZ, H. OSSENBRINK, AND P. HELM (WIP-Renewable Energies, München, 2005), p. 1775.
- [131] L. GÜTAY AND G. H. BAUER, *Thin Solid Films* **487**, 8 (2005).
- [132] P. O. GRABITZ, U. RAU, B. WILLE, G. BILGER, AND J. H. WERNER, *J. Appl. Phys.* **100**, 124501 (2006).
- [133] P. O. GRABITZ, Phd thesis, University of Stuttgart (2007).
- [134] P. O. GRABITZ, U. RAU, AND J. H. WERNER, *Thin Solid Films* **487**, 14 (2005).
- [135] O. S. HEAVENS, *Optical Properties of Thin Solid Films* (Butterworths, London, 1955).
- [136] T. DULLWEBER, U. RAU, M. A. CONTRERAS, R. NOUFI, AND H.-W. SCHOCK, *IEEE Trans. Electr. Devices* **47**, 2249 (2000).
- [137] T. DULLWEBER, O. LUNDBERG, J. MALMSTRÖM, M. BODEGÅRD, L. STOLT, U. RAU, H.-W. SCHOCK, AND J. H. WERNER, *Thin Solid Films* **387**, 11 (2001).
- [138] S. SIEBENTRITT, *Thin Solid Films* **403**, 1 (2002).
- [139] M. TURCU, O. PAKMA, AND U. RAU, *Appl. Phys. Lett.* **80**, 2598 (2002).
- [140] U. RAU, in *Proc. 3rd World Conf. Photovolt. Energy Conv., Osaka*, edited by K. KUROSAWA, L. L. KAZMERSKI, B. MCNELLIS, M. YAMAGUCHI, C. WRONSKI, AND W. C. SINKE (2003), p. 2847.
- [141] R. KNIESE, D. HARISKOS, G. VOORWINDEN, U. RAU, AND M. POWALLA, *Thin Solid Films* **431**, 543 (2003).

-
- [142] S. SIEBENTRITT AND U. RAU (EDS.), *Wide-Gap Chalcopyrites* (Springer Series in Materials Science 86, Springer, Berlin, Heidelberg, Germany, 2006).
- [143] G. HANNA, A. JASENEK, U. RAU, AND H.-W. SCHOCK, *Thin Solid Films* **387**, 71 (2001).
- [144] M. A. GREEN, E.-C. CHO, Y. CHO, Y. HUANG, E. PINK, T. TRUPKE, A. LIN, T. FANGSUWANNARAK, T. PUZZER, G. CONIBEER, AND R. CORKISH, in *Proc. 20th Eur. Photovolt. Solar Energy Conf.*, edited by W. PALZ, H. OSSENBRINK, AND P. HELM (WIP-Renewable Energies, München, 2005), p. 3.
- [145] A. LUQUE AND A. MARTÍ, *Phys. Rev. Lett.* **78**, 5014 (1997).
- [146] U. RAU AND R. BRENDL, *J. Appl. Phys.* **84**, 6412 (1998).
- [147] D. WERNER, *Funktionalanalysis* (Springer Verlag Berlin, 2002).
- [148] W. V. ROOSBROECK AND W. SHOCKLEY, *Phys. Rev.* **94**, 1558 (1954).
- [149] E. YABLONOVITCH, *J. Opt. Soc. Am.* **72**, 899 (1982).
- [150] M. A. GREEN, *Prog. Photovolt: Res. Appl.* **10**, 235 (2002).
- [151] C. GROSSMANN AND H.-G. ROOS, *Numerik partieller Differentialgleichungen* (Teubner Verlag Stuttgart, 1994).

Curriculum Vitae

Persönliche Angaben

Name	Julian Mattheis
Geburtsdatum	14.12.1975
Geburtsort	Hannover

Schulbildung und Zivildienst

07/1995	Allgemeine Hochschulreife am Grotefend Gymnasium Münden Abiturnote: 1,4
08/1995-07/1996	Zivildienst in einem Kindergarten des Roten Kreuzes für geistig und körperlich behinderte Kinder

Studium und Promotion

10/1996-07/2002	Studium der Elektrotechnik an der Technischen Univer- sität Braunschweig und der Universität Stuttgart Diplomnote: Sehr Gut
10/2002-04/2006	Studium der Politikwissenschaft mit Nebenfächern Volkswirtschaftslehre und Mathematik Magisternote: Gut
09/2002-10/2006	Wissenschaftlicher Mitarbeiter am Institut für Physikalische Elektronik, Universität Stuttgart

Berufliche Tätigkeit

seit 11/2006	Mitarbeiter im Produktmanagement und in Forschung & Entwicklung, Q-Cells AG
--------------	--

List of Publications

- (1) J. Mattheis, J. H. Werner, and U. Rau, *Finite mobility effects on the radiative efficiency limit of pn-junction solar cells*, Phys. Rev. B, in print
- (2) J. Mattheis, U. Rau, and J. H. Werner, *Light absorption and emission in semiconductors with band gap fluctuations - a study on Cu(In,Ga)Se₂ thin films*, J. Appl. Phys. **101**, 113519 (2007)
- (3) J. Mattheis, P. J. Rostan, K. Orgassa, U. Rau, and J. H. Werner, *Carrier collection in Cu(In,Ga)Se₂ solar cells with graded band gaps and transparent ZnO:Al back contacts*, Solar Energy Materials and Solar Cells **91**, 689 (2007)
- (4) T. Kirchartz, U. Rau, M. Kurth, J. Mattheis and J.H. Werner, *Comparative study of electroluminescence from Cu(In,Ga)Se₂ and Si solar cells*, Thin Solid Films **515**, 6238 (2007)
- (5) Philip Jackson, Roland Würz, Matthias Kurth, Julian Mattheis, Thomas Schlötzer, Kay Orgassa, Uwe Rau, Gerhard Bilger, and Jürgen H. Werner, *High Quality Baseline for High Efficiency Cu(In_{1-x}Ga_x)Se₂ Solar Cells*, Prog. Photovolt. **15**, 507 (2007)
- (6) A. Halverson, J. Mattheis, U. Rau, and J. D. Cohen, *Reverse bias induced metastable effects in Cu(In,Ga)Se₂ photovoltaic devices* in Proc. 4th World Conference on Photovoltaic Energy Conversion, edited by: (IEEE, New York, USA, 2006), 519 - 522 (2006)
- (7) J. Mattheis, U. Rau, and J. H. Werner, *Finite mobility effects on the radiative efficiency limit of pn-junction solar cells* in Proc. 4th World Conference on Photovoltaic Energy Conversion, edited by: (IEEE, New York, USA, 2006), 95 - 98 (2006)

-
- (8) J. H. Werner, J. Mattheis, and U. Rau, *Efficiency limitations of polycrystalline thin film solar cells: case of Cu(In,Ga)Se₂*, Thin Solid Films **480-481**, 399 - 409 (2005)
 - (9) P. J. Rostan, J. Mattheis, G. Bilger, U. Rau, and J. H. Werner, *Formation of transparent and ohmic ZnO:Al/MoSe₂ contacts for bifacial Cu(In,Ga)Se₂ solar cells and tandem structures*, Thin Solid Films **480-481**, 67 - 70 (2005)
 - (10) J. Mattheis, T. Schlenker, M. Bogicevic, U. Rau, and J. H. Werner, *Band gap fluctuations in Cu(In,Ga)Se₂ thin films*, Mat. Res. Soc. Symp. Proc. 865, F16.4.1, San Francisco (2005)
 - (11) H.-D. Mohring, U. Heckmann, J. Mattheis, and U. Rau, *High efficiency CIS modules for PV concentrator systems*, in Proc. 20th European Photovoltaic Solar Energy Conference, 1796 - 1799, Barcelona (2005)
 - (12) T. Schlenker, J. Mattheis, M. Bogicevic, U. Rau, and J. H. Werner, *Optical analysis of band gap inhomogeneities in CuInSe₂ thin films*, in Proc. 20th European Photovoltaic Solar Energy Conference, 1775 - 1778, Barcelona (2005)
 - (13) J. Mattheis, P. J. Rostan, U. Rau, and J. H. Werner, *Carrier collection in Cu(In,Ga)Se₂ solar cells with transparent ZnO:Al back contacts*, in Technical Digest of the 14th international Photovoltaic Science and Engineering Conference, Bangkok (2004)
 - (14) G. Hanna, J. Mattheis, V. Laptev, Y. Yamamoto, U. Rau, and H. W. Schock, *Influence of the selenium flux on the growth of Cu(In,Ga)Se₂ thin films*, Thin Solid Films **431-432**, 31 - 36 (2003)
 - (15) U. Rau, V. X. Nguyen, J. Mattheis, M. Rakhlin, and J. H. Werner, *Recombination at a-Si:H/c-Si heterointerfaces and in a-Si:H/c-Si heterojunction solar cells*, in Proc. 3rd World Conf. Potovolt. Energy Conv., Osaka (2003)

Danksagung

Mein Dank gilt ganz besonders meinem Doktorvater Prof. Jürgen H. Werner, der mit seiner Mischung aus Forderungen und Lob genau den richtigen Ton getroffen hat, um mich maximal zu motivieren. Ihm verdanke ich viele grundlegende Einsichten in Bezug auf die Berechnung maximaler Wirkungsgrade und in Bezug auf die Modellierung von Bandlückenfluktuationen. Ohne ihn wäre diese Arbeit gar nicht ins Rollen gekommen. Ich wäre gar nicht auf die Idee gekommen, über Inhomogenitäten nachzudenken. Bei allen meinen Wünschen - sei es flexible Arbeitseinteilung für mein Zweitstudium oder die finanzielle Unterstützung eines Auslandsaufenthaltes - habe ich stets seine vollste Unterstützung bekommen.

Ein bombastisches Riesen-Dankeschön an meinen Gruppenleiter Dr. habil. Uwe Rau. Dieser geniale Kopf und Inbegriff des zerstreuten Physikers hat einen ganz erheblichen Anteil an sämtlichen Modellen in dieser Arbeit. Ich war ziemlich stolz, dass es ihn immerhin fast eine ganze Woche gekostet hat, das Photon Recycling Modell in Matlab zu programmieren, für das ich ein ganzes Jahr gebraucht habe. Denn unter Umständen kann es durchaus vorkommen, dass er an einem Nachmittag macht, wofür normale Menschen die vollen drei Jahre ihrer Promotion benötigen.

Vielen Dank auch an

- Martin Wagner für die Prozessierung von Proben,
- Martin Bogicevic für Absorptionsmessungen,
- Saioa Tardon von der Universität Oldenburg für Photolumineszenzmessungen,
- Thomas Gustav Schlenker und Peter Grabitz für intensive Diskussionen über Bandlücken- Potenzial- und sonstige Fluktuationen,
- Kay Orgassa für die Einführung in die Optik von Cu(In,Ga)Se_2 Solarzellen,

- Thomas Kirchartz, Peter Grabitz und Hannes Rostan für das kritische Korrekturlesen meiner Arbeit,
- George Hanna für die super Betreuung meiner Studienarbeit, die darin gipfelte, dass ich einfach nicht mehr vom *ipe* losgekommen bin,
- Werner Wille für alle Arten der Computerunterstützung, selbst als ich meine Grafikkarte mit meinem Ficus Benjamini verwechselt habe sowie
- Gerda Gläser, Mawuli Ametowobla, Hannes Rostan, Thomas Schlenker, Peter Grabitz, Thomas Kirchartz, George Hanna und Michael Reuter für die unzähligen spannenden Diskussionen über Solarzellen jeglicher Art und das Leben an sich.

Außerdem danke ich allen Mitarbeitern am *ipe*, insbesondere allen meinen Mitdoktoranden, für die grandiosen fünf Jahre, die ich insgesamt am Institut verbracht habe. Ich kann nur hoffen, dass meine zukünftigen Kollegen genauso gnadenlos herzliche, kompromisslos witzige, heillos chaotische, und hilflos hilfsbereite Charakterköpfe sein werden wie die Protagonisten des *ipe* Kollegiums.

Den Mitbewohnern meiner WG Noah und Lena Lindhorst, Jessica Klauke, Hanna Single, Conny Kühne und Walid Mehanna danke ich für das schönste Zuhause, das ich seit der Entwöhnung von Mutters Busen gehabt habe.

Außerdem danke ich den Jungs und Mädels vom Klettern und Turnen, die mich all die Jahre so erfolgreich und tatkräftig von der Doktorarbeit abgelenkt haben.

Und zu guter letzt geht natürlich ein exorbitantes DANKE an meine Eltern Walli und Nesto, die mich immer uneingeschränkt unterstützt haben, sich entgegen allen thematischen Widrigkeiten selbst inhaltlich für meine Promotion interessiert haben und die nie wirklich gejamert haben, dass ich sie so selten besuche und Monate brauche, um auf emails zu antworten.

Erklärung

Hiermit erkläre ich, dass ich die vorliegende Dissertation "Mobility and homogeneity effects on the power conversion efficiency of solar cells" selbstständig verfasst und nur die angegebenen Hilfsmittel verwendet habe.

Leipzig, den 04.05.2008

Julian Mattheis